Cosmic Radiation

Reconstruction of Cosmic-Ray Properties from Radio Emission
of Extensive Air Showers

Johannes Schulz

Cosmic Radiation
Thesis, Radboud University Nijmegen, The Netherlands
Illustrated; with bibliographic information and English, Dutch, and German summaries

ISBN: 978-94-028-0017-3
Printed by Ipskamp Drukkers, Enschede

This work was supported by the Netherlands Research School for Astronomy (NOVA).

Cosmic Radiation

Reconstruction of Cosmic-Ray Properties from Radio Emission
of Extensive Air Showers

Proefschrift

ter verkrijging van de graad van doctor
aan de Radboud Universiteit Nijmegen
op gezag van de rector magnificus,
volgens besluit van het college van decanen
in het openbaar te verdedigen op donderdag 11 februari 2016
om 14:30 uur precies

door

Johannes Schulz

geboren op 23 oktober 1986
te Lemgo, Duitsland

PROMOTOR:	Prof. dr. H. D. E. Falcke
COPROMOTOR:	Dr. habil. J. R. Hörandel
MANUSCRIPTCOMMISSIE:	Prof. dr. S. J. de Jong (voorzitter)
	Prof. dr. S. C. M. Bentvelsen Universiteit van Amsterdam
	Prof. dr. M. Erdmann RWTH Aachen University, Duitsland
	Prof. dr. P. J. Groot
	Dr. T. Huege Karlsruher Institut für Technologie, Duitsland

Cosmic Radiation

Reconstruction of Cosmic-Ray Properties from Radio Emission
of Extensive Air Showers

Doctoral Thesis

to obtain the degree of doctor
from Radboud University Nijmegen
on the authority of the Rector Magnificus
according to the decision of the Council of Deans
to be defended in public
on Thursday, February 11, 2016 at 14:30 hours

by

Johannes Schulz

born on October 23, 1986
in Lemgo, Germany

SUPERVISOR:	Prof. dr. H. D. E. Falcke
SUPERVISOR:	Dr. habil. J. R. Hörandel
DOCTORAL THESIS COMMITTEE:	Prof. dr. S. J. de Jong (chair)
	Prof. dr. S. C. M. Bentvelsen University of Amsterdam
	Prof. dr. M. Erdmann RWTH Aachen University, Germany
	Prof. dr. P. J. Groot
	Dr. T. Huege Karlsruhe Institute of Technology, Germany

Contents

Introduction

The Large Hadron Collider can accelerate charged particles to enormous energies of more than 10^{14} eV [1]. However, the existence of particles with more than one-hundred-thousand times higher energies has already been known for more than 50 years [2]. The discovery of these ultra highly-energetic particles, which are called *cosmic rays*, marks about half time between the first observations that radiation of high penetration power enters the atmosphere from above (*"Strahlung von sehr hoher Durchdringungskraft von oben her in unsere Atmosphäre eindringt"*) [3] by Victor Hess in 1912 and today where the understanding of its nature is still incomplete. During these 100 years, the scientific impact of cosmic rays rapidly developed to a large field of fundamental research. Major steps were taken in measuring the flux, the composition, and the arrival direction of the cosmic rays over a broad range of energies, but nevertheless the sources and the acceleration processes remain unknown.

Most of the contemporary ultra high-energy cosmic-ray observatories employ a ground based detector array which is sensitive to the particle cascade of millions of secondary particles developing when a cosmic ray collides with a nucleus in the Earth's atmosphere. These particle cascades are called *extensive air showers* and were first described by Pierre Auger and Werner Kolhörster [4, 5]. The particles can be detected with 100% duty cycle and a good resolution in reconstructing the energy and the arrival direction of the original cosmic ray can be achieved.

A key to improve the understanding of the sources of the cosmic rays is however to identify the nature of these particles. This information will improve the picture of their acceleration and propagation and will help to exclude possible sources. Nowadays, optical detectors are used to measure the shower development and extract information about the composition of cosmic rays. These detectors are sensitive to the fluorescence afterglow of the atmosphere when nitrogen is excited by the particle cascade. The amount of light produced is very low and only extremely sensitive cameras are able to detect a signal. Already moonlight is outshining the fluorescence light by orders of magnitude which limits the duty cycle of these optical detectors. Therefore, they can only provide information about the particle type for a fraction of the cosmic rays arriving at Earth.

Shifting from observations in the optical regime to MHz radio frequencies allows to detect the particle showers as well. This method is independent of almost all environmental conditions and thereby allows for a close to 100% duty cycle. After being introduced in the 1960s with promising results but many technological limitations, the radio technique hibernated for decades until being revived to help answering the still remaining questions about cosmic rays. One of these modern radio air-shower detectors is the Auger Engineering Radio Array (AERA) built in the heart of the Pierre Auger Observatory, which is the world's largest air shower observatory.

Coexisting with a classical particle detector array and a fluorescence light detector, the radio technique has been developed and calibrated towards the necessary precision to provide high resolution air shower data with 100% duty cycle. The development of methods for the reconstruction of the interesting air shower properties from data recorded with AERA is the main subject of this thesis. During the last 3 years, AERA was also extended twice and parts of the necessary hardware work are presented as well.
In this thesis, an overview of cosmic-ray and air-shower physics is given in the beginning, followed by the description of hardware and software tools for simultaneous multi-detector air-shower measurements as well as the discussion of the measurements of the energy and the trend of the cosmic-ray composition as determined from the radio data, and future prospects on coming developments in the end. In chapter 1, an introduction to cosmic rays and extensive air showers is given together with information about the current detection techniques. Chapter 2 is a description of the Pierre Auger Observatory in general and AERA in particular. Here, additional information about the topic of system integration for the upgrades of AERA is presented. The design of the wireless communication system and the tests for the system integration are discussed in detail (original work). The third chapter contains a presentation of the data acquisition of AERA and the reconstruction of radio, Surface, and Fluorescence Detector data. Additionally, new simulation strategies are introduced and discussed together with new functionality added to the reconstruction framework (collaborative work). In chapter 4, the reconstruction of air shower parameters based on small particle counters installed in the radio stations for triggering purposes is discussed. Data from these detectors are reconstructed and analysed for the first time (original work). Chapter 5 contains a detailed discussion about simulation studies of the lateral distribution of the radio signal produced for the geographical position of AERA and its sensitivity to air shower parameters (original work). The results are used in chapter 6 and 7 to extract information about air shower properties. This information with respect to the cosmic-ray energy is employed in chapter 6 to perform a calibration between the Surface Detector array of the Pierre Auger Observatory and AERA (collaborative work). Furthermore, this procedure opens the door towards an individual energy calibration of cosmic-ray detector arrays based on first principle calculations. In chapter 7, two methods for the determination of the depth of maximum air-shower development based on radio measurements are presented. This depth is an indicator for the particle type of the cosmic ray. Both approaches are discussed and for the first time, the two methods are compared to an independent measurement taken from the Fluorescence Detector of the Pierre Auger Observatory. Additionally, the results of the two methods are compared among each other and one of them is used to determine the average depths of the shower maximum for air showers measured with AERA as a function of the energy (original work). These values are compared to experimental data from other experiments for the given energy range as well as to theoretical predictions. The presented work is concluded in chapter 8 and an outlook on future short, mid, and long term developments is given.

1

Cosmic Rays and Extensive Air Showers

A cosmic ray is an energetic particle travelling through outer space. Even though this definition applies to photons the same way as to neutrinos and charged particles, mostly the latter are referred to as cosmic rays. The Earth is constantly hit by cosmic rays and various research projects are measuring these particles to identify their origin. The most energetic cosmic rays are subject of the studies in this thesis. This chapter gives an overview of the main observable properties of cosmic rays: energy, arrival direction, and particle type. Furthermore, the propagation and possible sources are discussed, followed by a description of the phenomenon of extensive air showers and its experimental observation.

1.1 Cosmic Rays

The energy spectrum of cosmic rays fascinates by the wide range it spans over tens of decades in decreasing flux with increasing energy. Covering these ranges experimentally is only possible by using multiple detection strategies. A complication of measuring cosmic rays is their interaction with nuclei in the Earth's atmosphere, which makes direct detection of the cosmic rays at ground impossible. For the lower energetic particles ($E < 10^{12}\,\mathrm{eV}$), every square meter is exposed to several hundred cosmic rays per second. This high rate allows for space or air borne experiments on satellites or balloons to directly detect the particles and measure their energy, charge/mass, and arrival direction e.g., [6, 7, 8, 9, 10]. As the maximum payload on space- and airborne carriers is limited, large sensitive areas cannot be instrumented above the Earth's atmosphere and ground based detector systems are employed to detect cosmic rays with energies above 10^{15} eV corresponding to a flux of less than one particle per square meter per year. These detectors detect the cascade of secondary particles produced in the interaction between the cosmic ray and the atmosphere, called *extensive air shower* (EAS) [4, 5, 11] (see section 1.2).

1.1.1 Energy Spectrum

A great achievement is the determination of the energy spectrum up to energies of 10^{20} eV by several ground based experiments despite the indirect nature of the measurements at energies higher than 10^{15} eV. The spectrum is shown in figure 1.1. For energies below 10^{10} eV, the flux is suppressed by solar magnetic fields and modulated by solar activity [12]. Above this limit,

the flux decreases monotonously and the spectrum is close to a single power law

$$\frac{\mathrm{d}N}{\mathrm{d}E} \propto E^{-\gamma} \tag{1.1}$$

with a spectral index $\gamma = 2.7$. For energies above 10^{15} eV, the spectral index exhibits changes at certain energies. Around $4.5 \times 10^{15}\,\mathrm{eV}$, the spectrum steepens to $\gamma = 3.1$. This break is called the "knee" and it is followed by the "second knee" around $4 \times 10^{17}\,\mathrm{eV}$ where the spectral index further increases to $\gamma = 3.3$. Close to the end of the energy range, the spectrum flattens again at the "ankle" at around $4 \times 10^{18}\,\mathrm{eV}$. These features are displayed in the inset of figure 1.1. At the end of the spectrum around $10^{20}\,\mathrm{eV}$, a steep cut-off in flux is observed. The exact origin of this cut-off and the spectral breaks remain unexplained. However, many observations, such as different spectral breaks for different primary particle types [13] suggest a connection between the shape of the spectrum and the sources and propagation mechanisms of the cosmic rays, e.g., [14, 15]. Especially, the transition from galactic to extra galactic cosmic rays and the end of the maximal reachable acceleration at the sources are favoured explanations. For the cut-off at the highest energies, propagation effects are also considered as explanation which will be discussed later.

1.1.2 Composition

Cosmic radiation is mainly composed of nuclei of the elements of the periodic table. The most abundant species are protons and helium nuclei. The relative abundances of these elements however change with energy. At low energies ($1 - 100 \times 10^9\,\mathrm{eV}$), the cosmic radiation shows relative abundances of elements similar to what is found in the solar system. Some elements are however more abundant in cosmic rays. Most of these elements have slightly smaller atomic numbers than the CNO elements, iron, or lead. They are believed to be produced in spallation reactions of cosmic rays of the named groups with interstellar matter [24].
For higher energy measurements above 10^{15} eV, the determination of the atomic number of an individual cosmic ray is not possible any more as these cosmic rays are only detected through the extensive air showers they initiate in the atmosphere. Therefore, our knowledge about the composition of the cosmic radiation at higher energies is based on composition-sensitive observables of the air showers such as the ratio between different particle types or the atmospheric depth of the air shower maximum. These observables are interpreted using Monte Carlo simulation techniques and different hadronic interaction models which are extrapolations from interaction cross sections measured at particle accelerators. Changes in the composition appear around the same energies as where the spectral index changes and are likely to be linked to each other.
The depth of the air shower maximum X_{max} is used as the standard quantity in the experimental composition determination. In a simplified picture, the cross section σ for cosmic-ray interactions in the atmosphere is proportional to the mass number of the cosmic ray ($\sigma \propto \mathrm{A}^{2/3}$).

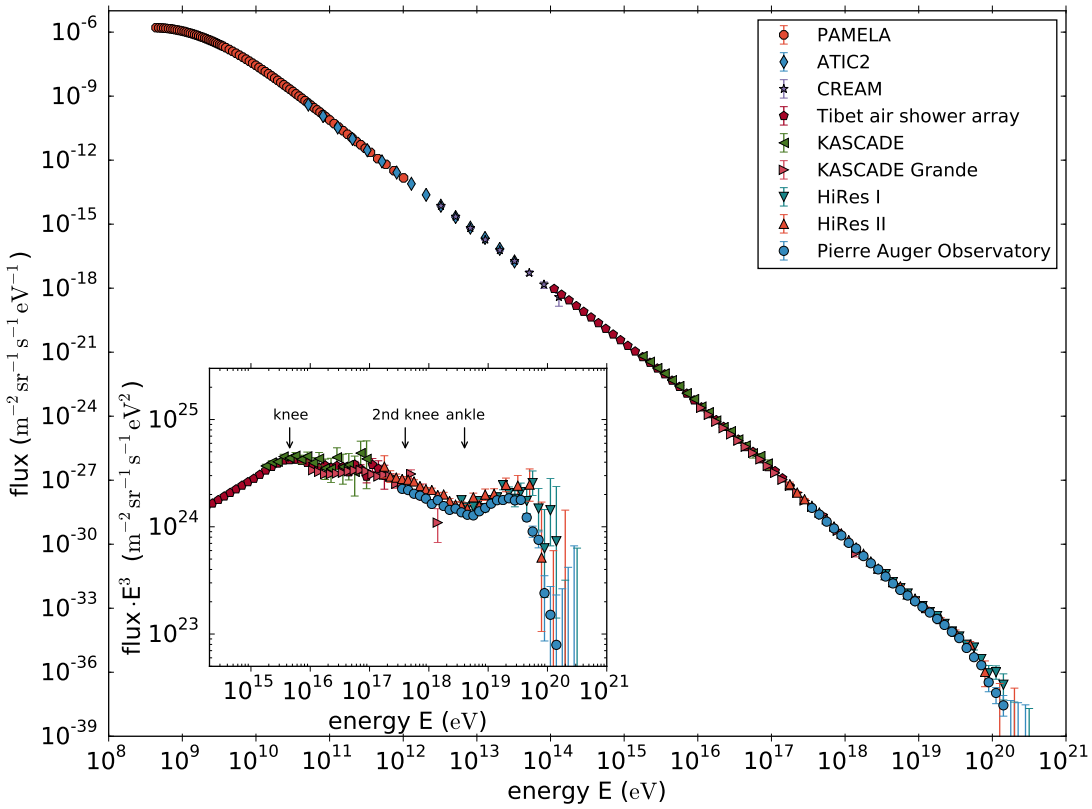

Figure 1.1: The energy spectrum of cosmic rays measured by various space- and airborne as well as ground based experiments. The flux multiplied by the energy to the power of 3 is shown in the inset revealing the breaks in the spectrum above an energy of $E = 10^{14}\,\mathrm{eV}$. The data is taken from [16, 17, 18, 19, 20, 21, 22] and the figure is modified from [23].

Therefore, iron nuclei interact higher up in the atmosphere and the initiated shower develops at a smaller atmospheric depth leading to a smaller X_{max}. Results from different experiments for which the average depth of the shower maximum $\langle X_{\mathrm{max}} \rangle$ is plotted as a function of the energy together with different model predictions for protons and iron nuclei from the knee to the highest energies are displayed in figure 1.2. The comparison with the different models suggests a light composition at the knee which then changes from light to heavy below the second knee. From the second knee to the ankle an opposite change towards a lighter composition is indicated. For the highest energies, the $\langle X_{\mathrm{max}} \rangle$ accuracy is affected by the low flux, but a trend towards a mixed composition can be observed.

The transition from light to heavy above the knee is often suggested to be caused by a mass- or rather charge-dependent cut-off starting with protons at around $5 \times 10^{15}\,\mathrm{eV}$ and going up to iron at around $10^{17}\,\mathrm{eV}$. Two main causes which might coincide are usually discussed. One is the rigidity dependent leakage from the galaxy and the other is the rigidity dependent maximum acceleration power of the sources (e.g., [15, 25, 26]). Both interpretations are suggesting a change from galactic to predominantly extra galactic cosmic rays around $10^{17} - 10^{18}\,\mathrm{eV}$.

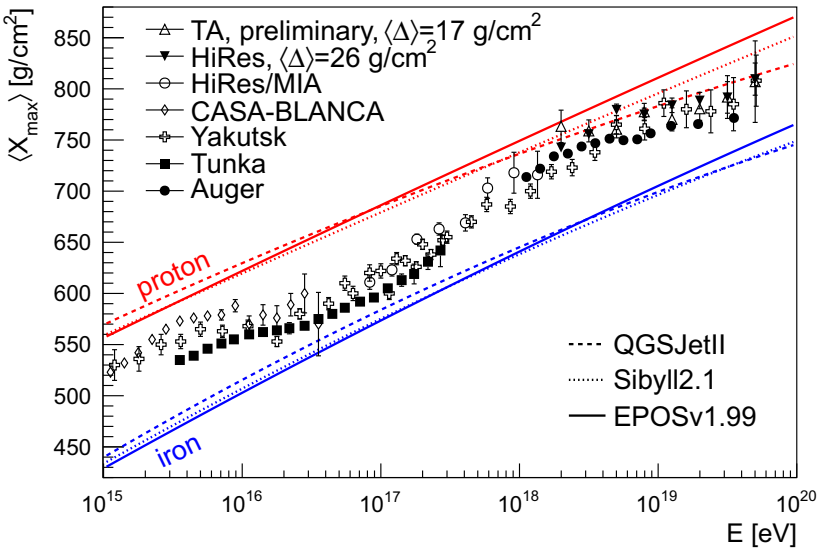

Figure 1.2: Measurements of the average depth of the shower maximum $\langle X_{\max} \rangle$ from different experiments for energies above the knee. The lines indicate the predictions from different hadronic interaction models for protons and iron nuclei. The data from the HiRes and the TA experiment are corrected for detector effects as discussed in [25] where the figure is taken from.

Particle interactions at energies up to $3 \times 10^{16}\,\mathrm{eV}$ (lab frame) are still accessible at the Large Hadron Collider (LHC) and predictions for the hadronic interactions from the current models have been found to be in good agreement with the data [27]. Therefore, changes in the underlying particle interaction processes are unlikely to cause the composition changes. For higher energies up to the end of the known spectrum, the interpretation of the observed composition transitions is challenging due to the increasing uncertainties. However, an explanation for a changing composition at the highest energies analogue to the changes at the knee might be an energy dependent maximum in acceleration power of the extragalactic sources [28]. Other explanations are employing propagation effects to explain the observed behaviour.

1.1.3 Arrival Direction

The arrival direction of ultra high-energy cosmic rays (UHECR) at Earth can be measured within about 1° [29]. This however does not mean that the position of the sources can be determined within 1°. Magnetic fields change the direction of charged particles during their propagation. The measured arrival directions of cosmic rays are nevertheless fundamental to understand the origin of these particles. If emitted by a few extremely powerful sources within a relativity small distance of the order of tens of Mpc, the skymap of the measured arrival directions should show a clustering of cosmic rays emitted by the same source. The recent skymap of UHECR measured by the Pierre Auger Collaboration is shown in figure 1.3. The plot also contains the positions of active galactic nuclei (AGN) taken from the Swift-BAT

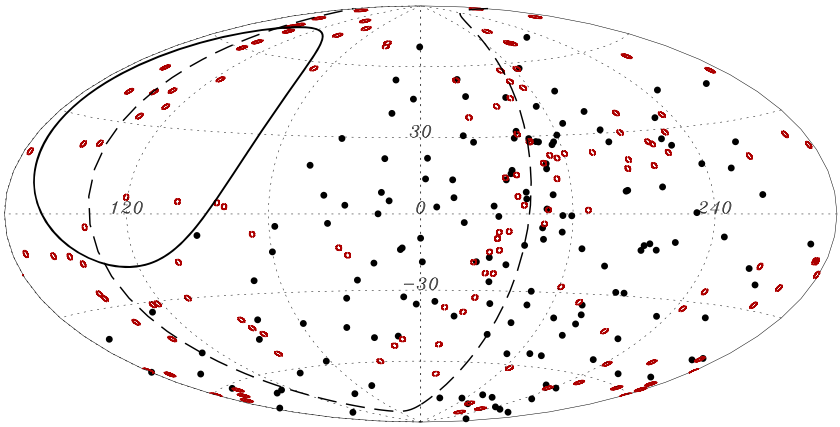

Figure 1.3: Arrival direction of cosmic rays with energies above 58 EeV as measured with the Pierre Auger Observatory (dots). In addition, the positions of AGNs with distances less than 80 Mpc are taken from the Swift-BAT catalogue and indicated with circles of 1° radius. The solid line represents the edges of the field of view of the Pierre Auger Observatory and the dashed line corresponds to the Super-Galactic plane. Figure taken from [31].

catalogue [30]. Various detailed studies have been performed as for example in [31] and an excess of cosmic rays with arrival directions pointing back to the Centaurus A region and bright close-by AGNs has been found. The statistical studies show however no significant evidence for anisotropy and more data need to be acquired for further investigation of the excesses observed so far.

1.1.4 Propagation

To interpret the composition and arrival direction measurements in the context of the sources, the propagation of the particles needs to be taken into account as the composition of cosmic rays detected at Earth might not be the same as emitted by the sources. Especially for ultra high-energetic cosmic rays ($E > 10^{17}\,\mathrm{eV}$), the universe is not transparent [32]. Interactions with photons (γ) from the cosmic microwave background (CMB) or the UV/optical/IR background photons are predicted to significantly attenuate cosmic rays. Several different types of interactions are expected with varying energy thresholds. For protons with energies below $5 \times 10^{18}\,\mathrm{eV}$ for instance, the dominant interaction process is the electron (e^-) positron (e^+) pair production which can occur for every nucleus N as

$$N + \gamma \rightarrow N + e^+ + e^-. \tag{1.2}$$

For larger nuclei also the photo-disintegration contributes significantly to the attenuation as

$$N + \gamma \rightarrow N^* + X, \tag{1.3}$$

where N^* is the remainder of the initial nucleus and X the split up fragment. The cross section for photo-disintegration depends on the type of nucleus and can be the dominant interaction

process for cosmic rays with energies above $10^{17}\,\mathrm{eV}$. For the most energetic cosmic rays (e.g., $E_{\mathrm{proton}} > 5 \times 10^{19}\,\mathrm{eV}$) interactions with CMB photons have a significant cross section and can produce pions via the delta resonance [33, 34] as

$$\begin{aligned} p + \gamma_{CMB} \rightarrow \Delta^{+} &\rightarrow p + \pi^{0} \\ &\rightarrow n + \pi^{+}. \end{aligned} \tag{1.4}$$

The pions decay further according to

$$\begin{aligned} \pi^{0} &\rightarrow \gamma\gamma \\ \pi^{+} &\rightarrow \mu^{+} + \nu_{\mu} \end{aligned} \tag{1.5}$$

and the neutron decays according to

$$n \rightarrow p + e^{-} + \bar{\nu_{e}}. \tag{1.6}$$

This process is called *GZK-effect* after Greisen, Zatsepin, and Kuzmin, who independently proposed a cut-off in the cosmic-ray energy spectrum for protons around $10^{20}\,\mathrm{eV}$. For heavier nuclei, the energy threshold for photo-pion production is significantly higher, however the photo-disintegration also leads to a cut-off in the spectrum of these elements. Therefore no conclusions about the composition can be drawn from observations of a cut-off only. The influence of the propagation effects are summarized in figure 1.4 for the case of nitrogen and iron nuclei.

During the propagation, charged particles are not only experiencing interaction, but also deflection magnetic fields. Except for the highest energetic protons in the cosmic radiation, the detected arrival direction can therefore be far from pointing back to the source. Extra- and intergalactic magnetic fields of different strengths are deflecting the cosmic rays during their propagation. The mechanism is the same as for confining the particles in their sources as discussed in section 1.1.5, but the magnetic fields which the particles encounter during their propagation are much smaller. Therefore, the particles are not trapped, but deflected proportional to their rigidity

$$R = \frac{pc}{Ze}, \tag{1.7}$$

where p is the momentum and Z is the number of elementary charges e. The rigidity of a particle depends on its charge which means iron nuclei of the same energy as protons will be effected much stronger by deflections during propagation. Unfortunately, the charge of individual high-energy cosmic rays cannot be measured. The degree of deflection also depends on the strengths and directions of the magnetic fields the particles encounter which are not know in detail either.

1.1.5 Sources

Cosmic rays must originate from objects which are able to accelerate individual particles to enormous energies. The acceleration however does not need to take place in one go. It can be

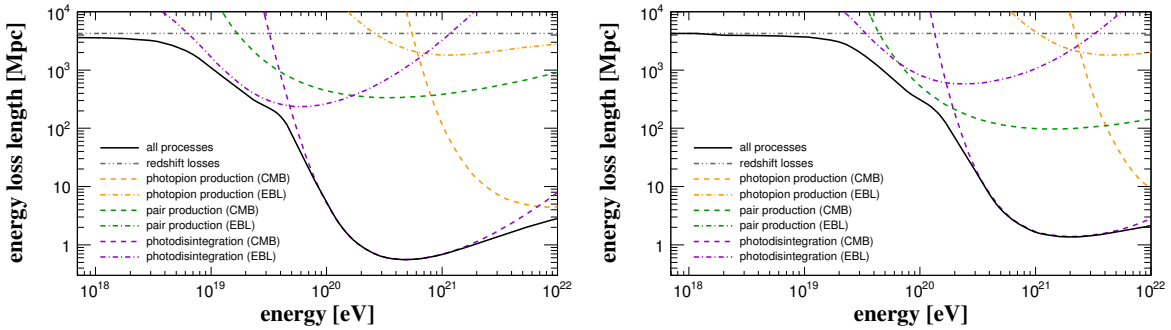

Figure 1.4: Propagation lengths of ^{14}N (left) and ^{56}Fe (right) as a function of initial primary cosmic ray energy. The energy loss length is defined as the travelled distance over which the particle energy decreases by 1/e due to the shown energy loss processes. Figure taken from [35].

distributed in multiple steps as long as the particles encounter enough of these accelerations, as it is also the case for man-made ring accelerators. A meanwhile established mechanism for the acceleration process based on multiple acceleration steps is called *Fermi acceleration* [36]. The idea is that charged particles can gain energy by statistical acceleration due to multiple scattering processes in strong turbulent magnetic fields. These fields occur in shock waves of the interstellar plasma such as the expanding shells of supernova explosions or around active galactic nuclei. The particles are accelerated when crossing the shock wave heads on. For each encounter, the energy gain is equal to

$$\frac{\Delta E}{E} \approx \frac{4}{3}\beta_{\text{shock}}, \tag{1.8}$$

where $\beta_{\text{shock}} = v_{\text{shock}}/c$ is the shock velocity. To encounter enough shock front crossings to gain the observed energies of UHECR, the particles must be trapped long enough in the source region. Charged particles can be confined by magnetic fields forcing the particles on a circular trajectory (in a simplified picture). The size of the trajectory is characterized by the Larmor radius

$$r_L = 1.08\,\frac{1}{Z}\,\frac{E}{10^{15}\text{eV}}\,\frac{B}{\mu\text{G}}\text{pc} \tag{1.9}$$

with the number of elementary charges of the cosmic ray Z, the magnetic field of the source B, and the cosmic ray energy E [37]. The requirement of containing particles that travel on such radii puts constrains on the properties of possible sources and also on the composition of the cosmic rays they emit. As the Larmor radius is proportional to $1/Z$, light particles will leak from the sources first, followed by heavier and heavier particles. This picture can be used to explain the spectral break and the changing composition around the knee for galactic and above the ankle for extra galactic cosmic rays [38]. Based on these arguments, a condition for the maximum energy to which a source can accelerate particles is given by the *Hillas* criterion

$$\left(\frac{B}{\mu\text{G}}\right)\left(\frac{L}{\text{pc}}\right) > \frac{2}{Z\;\beta_{\text{shock}}}\left(\frac{E_{\text{max}}}{10^{15}\text{eV}}\right), \tag{1.10}$$

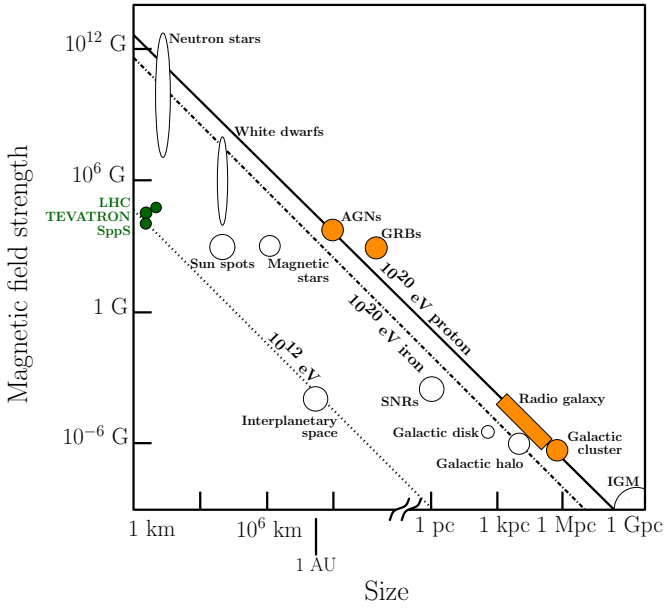

Figure 1.5: The *Hillas Plot*. In this figure, the maximum energy which particles can be accelerated to (according to equation 1.10) in various astronomical objects is shown. The velocity β_{shock} is assumed to be equal to 1. The regions of the diagonal lines indicate the parameter space allowing for particle acceleration to a certain energy. For protons with an energy of 10^{20} eV, only very few sources fulfil the criteria. Man made accelerators are shown as well for reference. Figure taken from [39], originally published in [37].

where L is the size of the shock region and E_{max} is the maximum energy for cosmic rays from the particular source. To accelerate particles to ultra high-energies, the sources need to be either very large, have a very strong magnetic field, or the combination of both needs to be sufficiently large. Figure 1.5 gives an overview of the maximum reachable energy in particle acceleration for known astronomical objects as well as some man-made accelerators as reference.

As supernova explosions are known to produce shock fronts expanding in the interstellar medium, they are a typical candidate for particle acceleration [40]. Following the *Hillas criterion*, they could accelerate protons up to around 10^{15} eV. Other objects such as pulsars or the galactic disk are also reasonable candidates at energies between the knee and the ankle. For the highest energies above the ankle, only a few sources are powerful enough. The termination shocks associated with jets of active galactic nuclei (AGN) for example are suited sites for the acceleration of cosmic rays up to the highest energies. Gamma-ray bursts (GRB) are also proposed to be good candidates for shock acceleration initiated by the burst. Furthermore, radio galaxy lobes, and shocks originating fom collisions of galaxy clusters fulfil the Hillas criterion for UHECR acceleration. All these sources are isotropically distributed on the largest distance scales. By taking propagation effects as discussed in subsection 1.1.4 into account, the particle horizon however shrinks significantly and the source candidates are not distributed isotropi-

cally within this volume. The deflections of the charged particles are also on these scales not negligible. In order to further constrain the type of possible sources, a multi messenger approach can be employed by combining results from gamma-ray observation as well as high-energy neutrino detections with cosmic-ray measurements. High energetic gamma rays and neutrinos are produced in interactions of charged cosmic rays with matter (e.g., around the sources) or background light photons (see equations 1.4 and 1.5). Both particle types are not deflected in magnetic fields and point back to their sources. Gamma rays with energies of more than 10^{14} eV have been observed from supernova remnants (SNR) supporting their role as particle accelerators at energies around the knee [41, 42]. For higher cosmic-ray energies, no corresponding gamma rays have yet been detected in the PeV range. A couple of neutrinos with energies exceeding 10^{15} eV were recently detected by the IceCube collaboration hinting at astrophysical high-energy neutrino sources [43, 44].

1.2 Extensive Air Showers

Primary cosmic rays cannot reach the surface of the Earth because of their interactions with atmospheric molecules. In the collisions, secondary particles are produced which undergo further interactions thereby creating a particle cascade. Depending on the type of the primary particle, different kinds of shower developments occur. In the following, the air shower development will be discussed for the case of a primary proton. Based on this, the description of an electromagnetic shower is given and the results are transferred to also extract information about heavier primaries.

1.2.1 Longitudinal Development

Nuclei in the cosmic radiation are interacting hadronically with atmospheric nuclei. For cosmic ray energies up to about $10^{17}\,\mathrm{eV}$ interactions have been studied at accelerators and extrapolations are used for higher energies where no experimental data are available. In general, the development of the initiated particle cascade can be characterized by three main components referred to as the *hadronic*, the *muonic*, and the *electromagnetic component*. In the first interaction of the primary particle, mainly pions (π) and kaons (K) are produced and also the remainders or fragments (p, X) of the collision partners (p, N) are available for further interactions as in

$$p + N \rightarrow p + X + \pi^{\pm} + \pi^{0} + K^{\pm} + K^{0} + \dots \,. \tag{1.11}$$

After the first interaction, the primary particle (here p) is called *leading particle* and still carries about 50% of its initial energy on average. In the next step, the produced particles can either interact again or decay. The high energetic charged pions and kaons live long enough to undergo further interactions continuing the hadronic cascade. After several interactions, the energy of the kaons and charged pions has decreased so much that it becomes more likely for

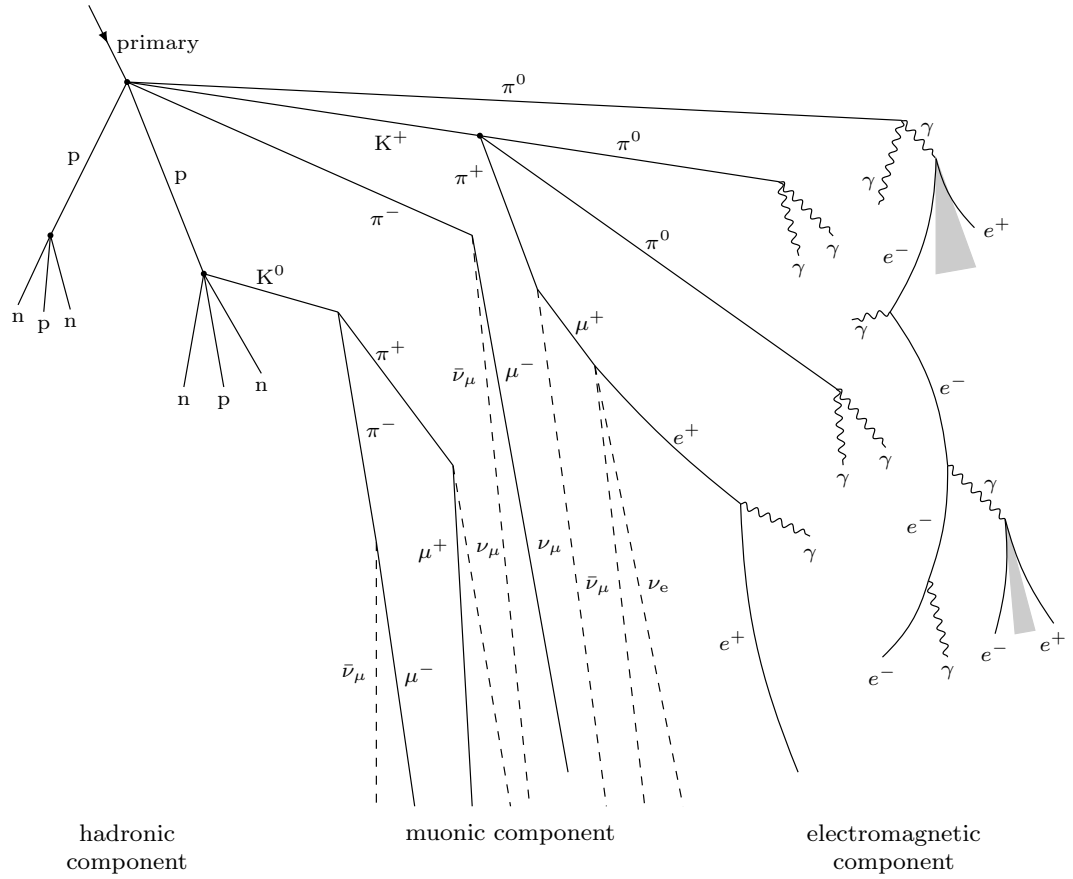

Figure 1.6: Three components of an extensive air shower initiated by a high-energy hadronic primary particle. Figure taken from [23].

them to decay than to interact again. The kaons decay into all three kinds of pions and the charged pions decay according to $\pi^\pm \rightarrow \mu^\pm + \overset{(-)}{\nu}_\mu$ into muons and (anti)-neutrinos building up the muonic component. The neutral pions however are decaying into two photons ($\pi^0 \rightarrow \gamma\gamma$) after a very short lifetime ($\tau_0 \approx 10^{-16}\,\mathrm{s}$). These photons are the starting point of the electromagnetic cascade as they undergo electron-positron pair production and the generated $e^\pm$ subsequently emit photons through bremsstrahlung which again generate high energy $e^\pm$. A small number of the muons also decays ($\mu^\pm \rightarrow e^\pm + \overset{(-)}{\nu}_e + \overset{(-)}{\nu}_\mu$) and the electrons enter the electromagnetic cascade. The first steps in the air shower development and the building up of the three shower components are depicted in figure 1.6. During the development of the cascade, the particles are confined in a relatively thin but laterally extended disk, referred to as the shower front.

1.2.2 Heitler Model

An analytic description of the physics involved in the development of electromagnetic cascades in the atmosphere was developed by Heitler [45] and later extended to the hadronic cascade

by Matthews [46]. Following the latter, the basic principle of the model is a repeated doubling of the particle number in each interaction by either emission of bremsstrahlung or electron-positron pair production. The atmosphere is thereby described in layers spaced by the splitting distance d which is related to the radiation length λ_{em} in the ambient medium by $d = \lambda_{\mathrm{em}} \ln 2$. After each step, every outgoing particle is carrying half the initial energy and after n steps the cascade has developed over a distance

$$x = n\lambda_{\mathrm{em}} \ln 2 \tag{1.12}$$

containing $N = 2^n$ particles, each with a fraction of the primary energy E_0/N. Once this fraction is smaller than the critical energy, splitting stops and energy losses due to ionization start to dominate. The critical energy $E_{\mathrm{c}} = 85\,\mathrm{MeV}$ in air sets a limit on the maximum number of particles

$$N_{\mathrm{max}} = \frac{E_0}{E_{\mathrm{c}}} = 2^{n_{\mathrm{c}}} \tag{1.13}$$

with n_{c} as the number of interaction steps until the particles reach the critical energy. Thereby, the depth of the maximum shower development X_{max} considering equation 1.12 can be formulated as

$$X_{\mathrm{max}} = n_{\mathrm{c}}\lambda_{\mathrm{em}} \ln 2 = \lambda_{\mathrm{em}} \ln \frac{E_0}{E_{\mathrm{c}}}. \tag{1.14}$$

With this simple model it can be shown that X_{max} depends on the primary energy. Its increase is called the *elongation rate* and is given by

$$\Lambda \equiv \frac{\mathrm{d}X_{\mathrm{max}}}{\mathrm{d}\log_{10} E_0}. \tag{1.15}$$

In order to be compatible with results from accelerator experiments, the maximum number of particles needs to be multiplied by a correction factor $g \approx 1/13$ [47]. This is caused by a number of simplifications, e.g., ranging out of the charged particles is not taken into account and neither is radiation of multiple photons during a bremsstrahlung process. Nevertheless, even in its simple form, the model allows for the general description of electromagnetic cascades. Also, its predictions for the relation between number of particles and energy as well as the elongation rate are qualitatively in agreement with observations and full Monte Carlo models of the shower development [46].

In figure 1.7 a sketch of the described model for electromagnetic showers is displayed on the left hand side. On the right hand side, the application of the modified model to hadronic cascades in extensive air showers is sketched. The basic idea is that hadrons also interact after travelling one hadronic interaction length $d = \lambda_{\mathrm{H}}\ln 2$. After this distance, the hadron produces a number of pions of which 1/3 are neutral and 2/3 are charged. While neutral pions decay immediately, charged pions interact again after travelling a distance d producing new pions. Similar to the critical energy for the electromagnetic cascade, charged pions below a certain "critical" energy decay to muons before they can interact. After n steps the energy in the

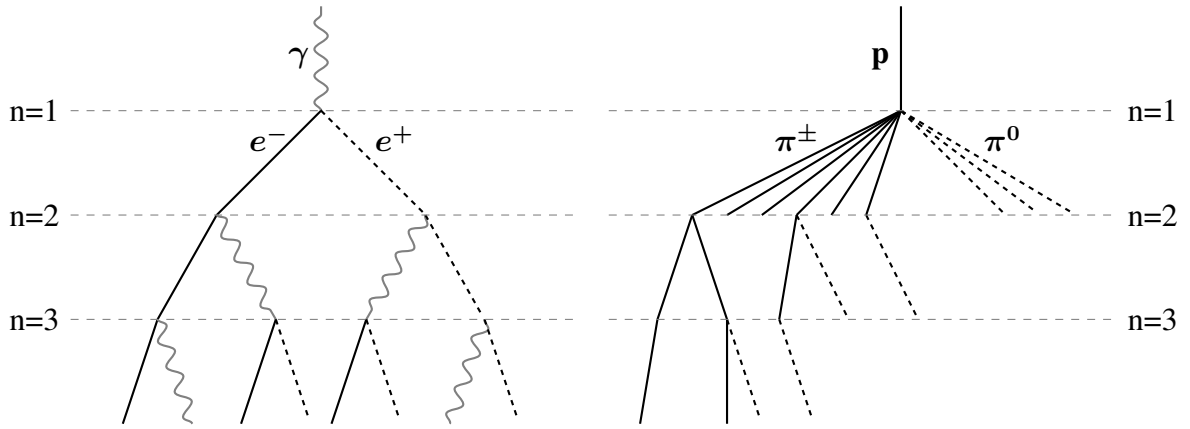

Figure 1.7: Sketches of the Heitler model for the development of extensive air-showers. Left: Electromagnetic cascade initiated by a photon. Right: Hadronic cascade initiated by a proton. The layers stand for one interaction distance in both sketches. After the second layer not all resulting particles are plotted. Figure adapted from [46].

hadronic cascade is equal to

$$E_{\mathrm{had}} = \left(\frac{2}{3}\right)^{n} E_0 \tag{1.16}$$

and the energy per pion is given by

$$E_{\pi} = \frac{E_{\mathrm{had}}}{(N_{\pi^{\pm}})^n} = \frac{E_0}{(\frac{3}{2}N_{\pi^{\pm}})^n}. \tag{1.17}$$

When E_{π} drops below the "critical" energy for pions ($E_{\mathrm{c}} = 20\,\mathrm{GeV}$), the charged pions decay to muons and their number can be estimated from

$$\ln N_{\mu} = \ln\left(\frac{E_0}{E_{\mathrm{c}}}\right) \frac{\ln N_{\pi^{\pm}}}{\ln(\frac{3}{2}N_{\pi^{\pm}})}. \tag{1.18}$$

In contrast to the electromagnetic shower, the number of muons does not scale linearly with the energy. This fact provides information about the type of the primary particle under the assumption of the superposition principle introduced in [48]. The superposition principle describes an air shower initiated by a nucleus with mass A as a superposition of A showers initiated by protons with an energy of $E_{\mathrm{A},0}/A$ each. This assumption is reasonable as long as the energy regime is significantly above the binding energy of the primary nucleus. Another application is the calculation of X^{A}_{max} for a nucleus based on $X^{\mathrm{p}}_{\mathrm{max}}$ for a proton initiated shower with the same energy which is

$$X^{A}_{\mathrm{max}} = X^{\mathrm{p}}_{\mathrm{max}} - \lambda_{\mathrm{em}} \ln A\,. \tag{1.19}$$

The interaction cross section however scales with $A^{2/3}$ as mentioned in section 1.1.2. Both statements in equations 1.18 and 1.19 provide keys to determine the mass A of the primary particle. One observable is N_{μ} which is a factor $A^{0.15}$ larger for nuclei with mass A than for protons. The second observable is X_{max} which is a factor of $\lambda_{\mathrm{em}} \ln A$ smaller (i.e., higher up in

the atmosphere) for nuclei compared to protons. Both statements are in qualitative agreement with extensive Monte Carlo simulations for air showers but they are only applicable on a statistical sample and not on a shower-by-shower basis.

1.2.3 Monte Carlo Simulations

The Heitler model is very successful in describing the phenomenology of particle cascades and extensive air showers. However, it does not allow for precise calculations and predictions of air shower observables such as the shower development or the particle distribution on the ground as they are needed for e.g., cross checks with measured air showers or to define initial parameters for air-shower reconstruction. These challenges are addressed by Monte Carlo simulations which are able to track every particle that is created during the air shower development. The interactions and decays of all particles are stochastically generated based on measured cross sections and life times. For higher energies, the cross sections are extrapolated from the measured values and are therefore a source of increasing uncertainties. Frequently used interaction models are EPOS-LHC [49], FLUKA [50], QGSJET-II [51] and SIBYLL [52]. Current air shower simulation codes like CORSIKA [53] and AIRES [54] have been proven to be valuable tools resampling the measured properties of extensive air showers. To generate simulated showers, the environmental conditions of the detector site such as height above sea level, atmospheric profile, and geomagnetic field can be loaded into or defined in the simulation codes.
An approach for air shower simulations using a combination of analytic descriptions and full Monte Carlo methods following every particle is realized in CONEX [55]. Here, only the most energetic particles in the shower are tracked as it is done in CORSIKA. For lower energetic particles, the further development of sub-cascades is calculated analytically following the cascades equations (e.g., [56, 57, 58]). This procedure is very advantageous in terms of computation time and CONEX is used for a wide range of applications to calculate the basic shower parameters or in cases where for example a detailed distribution of the particle distribution on the ground is not needed.

1.2.4 Radio Emission

A couple of years after the development of the Heitler model, Askaryan proposed the emission of radiation by electromagnetic cascades developing in a medium [59]. The origin of the radiation with frequencies in the MHz-regime is explained with an excess of negative charges in the air shower front and called *charge excess*. As the shower develops in the medium, electrons are dragged from molecules in the medium along with the shower particles leaving positively charged ions behind. This results in a charge separation along the shower axis. During the shower development, the number of particles first in- and then decreases and both effects together can be seen as a time varying net-current or a changing dipole moment. Additionally,

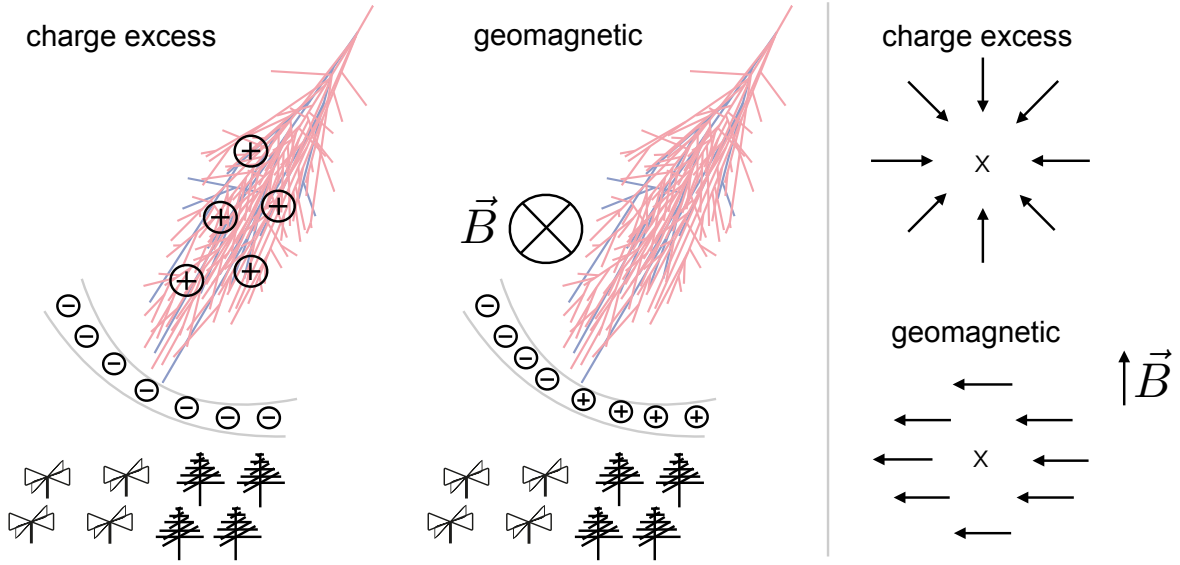

Figure 1.8: Illustration of the two emission mechanisms of coherent MHz pulses from extensive air showers. Left: The *charge excess emission* is produced as positive and negative charges are separated along the shower axis when electrons are dragged with the particles in the shower front. Center: The *geomagnetic emission* originates from the separation of mainly positrons and electrons based on their charge in the geomagnetic field. For both mechanisms, the changes in the particle number during the shower development are of main importance. Right: The polarisation of the radiation from the two emission mechanisms as seen in the shower plane around the shower axis (marked by the star) when the direction of the shower development goes into the paper plane.

positrons in the shower front can annihilate with electrons in the medium amplifying the charge separation. The radiation emitted by the dipole is coherent as long as the wavelength is larger than the thickness of the shower front. The polarization of the radiation is determined by the dipole moment and parallel to the shower axis. An observer at ground however sees it as being radially polarized with respect to the shower axis. The radiation is beamed in the direction of the shower development due to the boosted frame of the particles.

Another mechanism of generating radiation in extensive air showers was proposed by Kahn and Lerche [60]. The emission process in this case is based on the separation of electrons and positrons due to the Lorentz force in the geomagnetic field and therefore often referred to as the *geomagnetic emission*. As for the charge excess mechanism, the changing number of particles during the shower development leads to a varying net-current. The changing dipole moment is oriented in the direction of $\vec{v} \times \vec{B}$, i.e. perpendicular to the shower axis $\vec{v}$ and the direction of the geomagnetic field $\vec{B}$. The radiation measured on the ground is polarized in $\vec{v} \times \vec{B}$-direction and coherently emitted as it also originates in the shower front. A sketch of both emission mechanisms is shown in figure 1.8.

In general, the amplitude of the electric field scales with the number of electrons and positrons $N_{e^\pm}$ as the emission is coherent. The radiated energy then scales with $N_{e^\pm}^2$ which is directly

related to the energy of the primary particle by equation 1.13. The strength of the geomagnetic emission in addition scales with the sine of the angle between the shower axis and the geomagnetic field (geomagnetic angle) and the relation of the amplitude and radiated energy needs to be corrected accordingly. The shape of the emission pattern is further influenced by relativistic time compression effects due to the super-luminous particle speeds in the shower front. These compression effects extend the frequency content of the radio pulses from the MHz to the GHz range. The attenuation of electromagnetic radiation in this frequency regime in the atmosphere is negligible and the radio pulses from extensive air showers can be measured as broadband pulses of nanosecond scale duration. The exact shape of the pulse thereby depends on the shower development and geometry as described in [61].

The electric field measured at ground level is a superposition of the two electric fields emitted by the different emission mechanisms and the direction of the electric field vector depends on the strength of the individual components. Starting with the simple picture on the right side of figure 1.8, the vectorial addition of the two components yields an asymmetric pattern. Going along the $\vec{v} \times \vec{B}$-direction against the electric-field vector of the geomagnetic emission reveals an opposed polarization in the two components adding up destructively on this side of the shower axis. Going further in the $\vec{v} \times \vec{B}$-direction the charge excess emission experiences a sign-flip at the position of the shower axis and the two components start adding up constructively with an overall maximum on this side. For other positions, in the plane spanned by $\vec{v} \times \vec{B}$ and $\vec{v} \times (\vec{v} \times \vec{B})$, the interplay of the components works accordingly and a bean like shape of the measured amplitude pattern is expected. Note, that in this coordinate system, the overall bean shape of the pattern is always oriented in the same way.

More than 40 years ago, the first observations of radio pulses originating from extensive air showers (e.g., [62, 63, 64]) were reported, accompanied by the proposals of various theories to explain the phenomenons. But only recently, measurements of both, radially and linearly polarized emission in the radiation discussed above, support the theory of the two different emission mechanism as origins. The CODALEMA experiment [65] first reported results which were not in agreement with a sole geomagnetic emission mechanism [66]. The ratio of the amplitudes of the radially polarized electric field $|E_{\mathrm{C}}|$ originating from the charge excess mechanism and the linearly polarized electric field $|E_{\mathrm{G}}|$ originating from the geomagnetic mechanism, corrected for the influence of the geomagnetic angle α, is called charge excess fraction

$$a \equiv \sin(\alpha) \frac{|E_{\mathrm{C}}|}{|E_{\mathrm{G}}|}. \tag{1.20}$$

A quantification of the average charge excess in the measured radiation was presented by AERA [67] and amounts to $14 \pm 2\%$ [68] for the specific geographic site and the underlying data sample. The individual values for the measured showers are shown in figure 1.9 (left). With the high antenna density of LOFAR [69], the average contribution of radially polarized emission has been measured for different zenith angle bins and distances of up to 250 m in more detail, figure 1.9 (right). The results show a dependency of both parameters raising from

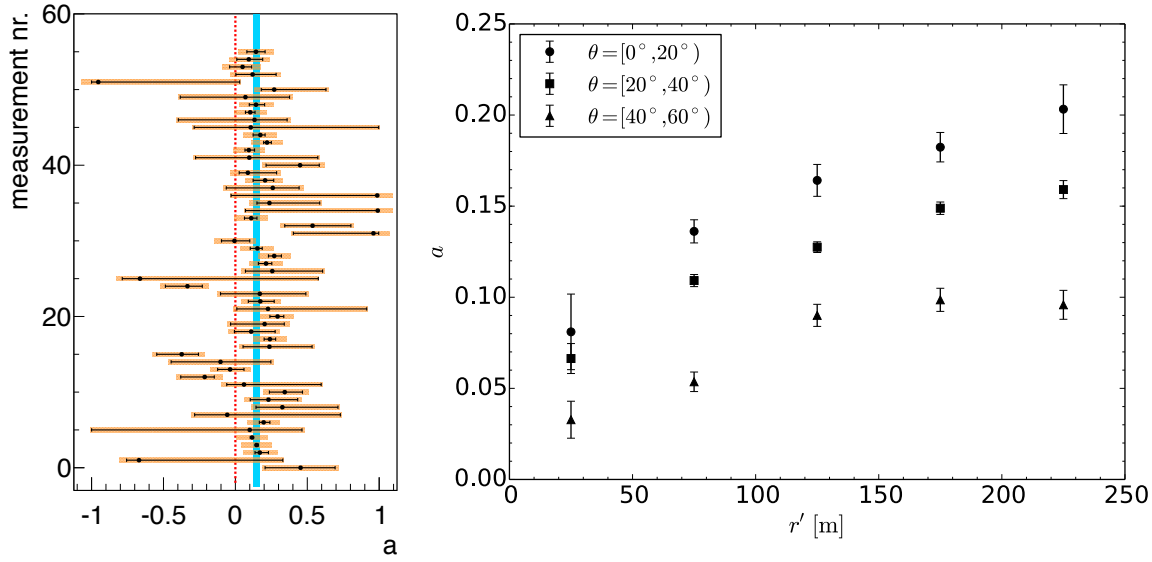

Figure 1.9: Charge excess fraction a as measured with AERA (left) for individual air showers and with LOFAR (right) for several bins in zenith angle θ and distance to the shower axis. Figures taken from [68, 70].

below 5% for inclined showers close to the shower axis to about 20% for vertical showers at large distances from the shower axis [70]. A rapid decrease of the charge excess fraction close to the shower axis is observed by LOFAR as expected due to the sign flip at the shower axis position.

In parallel to the experimental achievements, the theoretical description of the radio emission of extensive air showers has developed rapidly and simulation codes for the radio signals are in qualitative agreement with observations [67, 71]. These simulation codes can be categorized into *macroscopic* and *microsopic* descriptions.
Macroscopic models describe the phenomena in terms of dipole moments initiated by time varying charge separation on large scales as explained above. These dipole moments can be described in terms of classical electro-dynamics and allow for an analytic calculation of the resulting electric fields. The basic shower parameters needed as input for the calculations can be obtained from CONEX simulations of the corresponding air shower. Examples for such macroscopic models are MGMR [72] and EVA [73].
Microscopic models calculate the emission of every single particle in the cascade and the interference between their contributions. The complex interplay between different mechanisms of the radio emission and considerations of second order effects are thereby automatically included in the calculations. The radio simulations are mainly used as add-ons to full Monte Carlo codes determining the radio emission while the particles are tracked in the simulations. Example codes using the microscopic approach are ZHAires [74] and CoREAS [75].
For simulations produced in the context of this thesis, the CoREAS simulation code was em-

ployed which will be described in more detail here. The underlying principle to calculate the radio emission in CoREAS is the *end point formalism* [76]. In this approach, the trajectories of individual particles are described as a sequence of straight track segments with instantaneous acceleration processes (positive and negative respectively) occurring at the beginning and the end of each segment (endpoints). The radiation emitted during an instantaneous deceleration at the end of one segment mainly cancels out with the one emitted during the instantaneous acceleration at the beginning of the next track segment starting at the same endpoint. On a track, the momentum of the particles is constant and only at the endpoints of the track changes of momentum occur. Due to these changes of the particle momentum at the endpoints, some fraction of the radiation does not cancel out and contributes to the overall emission of the particle trajectory. The exact calculation for the emissions is derived directly from the Maxwell equations via the Liénard-Weichert potentials and therefore general and independent of any model of macroscopic particle motion. For the calculations of the electric field contributions of individual particles, the near-field term in the electric field equation is neglected as it gives only small corrections to the observed electric fields. According to [76], the radiation emitted from a charged particle under instantaneous acceleration to the velocity $\vec{\beta} = \vec{\beta}^*$ at time t_0' can then be calculated in terms of the electric field at a position $\vec{x}$ for a frequency ν, as

$$\vec{E}_{\pm}(\vec{x}, \nu) = \pm \frac{q}{c} \frac{e^{ikR(t_0')}}{R(t_0')} \frac{e^{2\pi i \nu t_0'}}{1 - n\vec{\beta}^* \cdot \hat{r}} \hat{r} \times [\hat{r} \times \vec{\beta}^*]. \tag{1.21}$$

Here, q is the charge of the particle in c.g.s. units, $\hat{r}$ is the unit vector to the observer position, R is the distance from the endpoint to the observer, n is the medium refracting index, and $k = 2\pi/\lambda = 2\pi\nu n/c$. The "$\pm$" accounts for the two directions of acceleration in the endpoint picture and is positive for acceleration from rest and negative for acceleration to rest. Analogues, the electric field averaged over a time bin Δt can be derived as

$$\vec{E}_{\pm}(\vec{x}, t) = \pm \frac{q}{\Delta t c} \left(\frac{\hat{r} \times [\hat{r} \times \vec{\beta}^*]}{(1 - n\vec{\beta}^* \cdot \hat{r})R} \right). \tag{1.22}$$

The width of Δt determines the time resolution of the resulting electric field trace at the observer position.

The decision which simulation code to use should be made according to the physics question to be answered. The CoREAS simulation code for example employs an approach of simulating the electric fields which is independent of models for the emission mechanisms and relies only on full Monte Carlo air-shower simulations. Every particle in the simulation is considered and the emission is calculated requiring considerably more computation time than e.g., macroscopic approaches. Furthermore the emission mechanisms cannot easily be simulated separately. One approach to nevertheless investigate the different origins of the radiation is to produce two simulations with the same start parameters except for the fact that the magnetic field is switched off for one of the cases. The radiation seen in the second simulation is then exclusively originated from the charge excess mechanism. The approach however requires an

additional air-shower simulation and the geomagnetic emission can only be singled out as the difference between the simulation with and without geomagnetic field [77]. The particle showers in these two simulations will also be slightly different which complicates the interpretation of the resulting radiation patterns. Aside from these considerations, an advantage of using the combination of CoREAS and CORSIKA is the detailed particle and radio hybrid output and the large number of additional options in both packages. Among others, CoREAS allows for the definition of atmospheric electric fields and has an option to just consider particles within a certain geometrical region for the calculation of the resulting electric fields.

1.2.5 Detector Systems

Since the discovery of extensive air showers, many different detection strategies have been developed. Pierre Auger for example used counters with various spacings operated in a coincidence mode. This technique of detectors placed in arrays on the ground is still the backbone of the majority of modern air shower experiments. However, by using this technique only a snapshot of the air shower at the time of arrival at ground is available. Therefore, various additional techniques addressing the measurement of the air shower development are also employed. These methods are based on the detection of radiation that is directly or indirectly produced by the charged secondary particles mainly in the electromagnetic component. The amount of radiation produced at a certain stage in the shower development is thereby related to the number of particles in the electromagnetic cascade at that stage. The three types of radiation observed from extensive air showers are fluorescence light, Cherenkov radiation, and (MHz-GHz) radio pulses.

Particle Detector Arrays

Ground based particle detector arrays sample the density of particles in the shower front at different distances from the shower axis. The lateral extent of the shower front depends on the energy of the primary particle as well as the stage of shower development and the types of particles considered. The discretely sampled lateral particle distribution can in general be continuously described by a lateral distribution function (LDF) developed by Nishimura, Kamata and Greisen (NKG-function) [78, 79] as

$$\rho(N_{\mathrm{ch}}, r) = \frac{N_{\mathrm{ch}}}{2\pi R^2} \left(\frac{r}{R}\right)^{(s-2)} \left(1 + \frac{r}{R}\right)^{(s-4.5)} \left(\frac{\Gamma(4.5-s)}{\Gamma(s)\Gamma(4.5-2s)}\right). \tag{1.23}$$

Here, N_{ch} is the total number of charged particles, r is the radial distance to the axis, R is the parameter of the characteristic radius, s is the shower age which accounts for the stage of shower development and Γ denotes the Gamma-function. For pure electromagnetic showers, the characteristic radius is the Molière radius. The exact form of this parametrization depends on the individual detector setup and different versions are used for different experiments [80]. An example of the lateral particle distribution as measured at the Pierre Auger Observatory

together with a fit of a modified NKG function is shown in figure 1.10 (left). The energy of the primary particle is in principle connected to the total number of charged particles N_{ch}. The exact relation between the two numbers however also depends on the type of primary particle and the shower development. This introduces further uncertainties in the reconstruction of shower parameters. Many experiments operate a certain type of detector and therefore the typical detector responses to different particle types have a large influence on the LDF, see section 4.3.2. As the number of muons in the air shower is an indicator for the primary particle type (section 1.2.2), the separation of the electromagnetic and the muonic component is a powerful tool for cosmic-ray composition studies. Modern particle detector arrays are employing differential techniques to realize a separation of the components. One approach is a layered detector structure, where an absorber is placed between two detector layers absorbing a large fraction of the electromagnetic particles in the shower front as realized in the KASCADE experiment [81]. Another approach is used for the upgrade of the Pierre Auger Observatory, AugerPrime. Here, two detector systems, water Cherenkov detectors and plastic scintillators will be stacked on top of each other to disentangle the shower components through the different detector responses. A somewhat different approach is the usage of underground muon counters which are shielded against all electromagnetic particles by meters of soil in combination with radio detection stations.

Following from the lateral particle distribution, the energy threshold for an air shower array is given by the spacing of the detectors, the sensitive detector area, and the type of detectors. The steep spectrum of cosmic rays additionally puts a lower limit on the size of the instrumented area to gain sufficient statistics in the desired energy range. Typical combinations of detector spacings and instrumented areas are e.g., 137 m and $700 \times 700\,\mathrm{m}^2$ in the KASCADE-Grande experiment [82] targeting cosmic rays of energies between $10^{16}\,\mathrm{eV}$ and 10^{18} eV or 1500 m and $> 3000\,\mathrm{km}^2$ at the Pierre Auger Observatory [29] targeting UHECR above 10^{18} eV.

The arrival direction of cosmic rays is inferred from the axis of the air shower which in terms can be reconstructed from the arrival times of the particles in the shower front at different detector positions on the ground. Efforts are ongoing in studying the correlations between the shape of the shower front and the shower development, mainly targeting X_{max} (e.g., [83]). Studies focussing on the reconstruction of the energy or the shower development based on the signal measured with a particle detector array depend on a calibration with either a different detector technique or Monte Carlo simulations. Particle detector arrays can reach a duty cycle of 100% and they are an established and cost effective tool in cosmic-ray research. Further information about particle detector arrays is given in the description of the Surface Detector array of the Pierre Auger Observatory in chapter 2.1 and in chapter 4 where an analysis based on the scintillation detectors of AERA is presented.

Fluorescence Detectors

The detection of fluorescence from extensive air showers allows for a detailed measurement of the longitudinal shower development. For a cosmic ray, the atmosphere acts like a calorimeter and a large part of the primary energy is deposited by creating cascades of secondary particles which are subsequently absorbed in the atmosphere. A part of the energy deposit is caused by the excitation of atmospheric nitrogen molecules which are de-exciting via the emission of UV photons. This fluorescence light is emitted isotropically and can be detected with special telescopes. The number of emitted photons is proportional to the energy deposited in the atmosphere. The ratio of photons emitted per unit of energy deposited in the atmosphere by an electron is called fluorescence light yield. For the measurement of this yield, a dedicated experiment named AIRFLY [84] was performed as the conversion factor is highly important for the energy calibration of the detector systems. The fluorescence yield depends on the pressure and temperature of the atmosphere, and the measured photon numbers need to be rescaled accordingly. To perform the correction, the atmospheric conditions and the emission region of the photons must be known. Atmospheric state variables are monitored continuously and fluorescence detectors can be equipped with multi-pixel cameras which allow actual spacial tracking of the shower development and geometric shower reconstruction. Furthermore, they are often combined with particle detector arrays providing additional information about the geometry. Therefore, the fluorescence light measurements can be corrected for propagation effects as scattering and absorption (this requires further calibration procedures as discussed in section 2.2). Including all these corrections, the longitudinal profile in terms of deposited energy $\mathrm{d}E(X)/\mathrm{d}X$ at an atmospheric depth X can be reconstructed from the detected photons. The shape of the profile can be parametrized with the Gaisser-Hillas function [85, 86] as

$$f_{\mathrm{GH}}(X) = \omega_{\max} \left(\frac{X - X_0}{X_{\omega_{\max}} - X_0} \right)^{(X_{\omega_{\max}} - X_0)/\lambda} e^{(X_{\omega_{\max}} - X)/\lambda}, \tag{1.24}$$

where $X_{\omega_{\max}}$ is the atmospheric depth where the maximum energy deposit $\omega_{\max}$ is reached and X_0 and λ are shape parameters. X_0 hereby represents the depth of the first interaction and λ represents the mean free path. The integral

$$E_{\mathrm{cal}} = \int_0^\infty f_{\mathrm{GH}}(X)\mathrm{d}X \tag{1.25}$$

over the profile gives the calorimetric energy deposit in the atmosphere. Besides a fraction of about 10% that goes into muons and neutrinos, the calorimetric energy E_{cal} corresponds to the energy of the primary particle if the shower is fully developed in the atmosphere. As the deposited energy on its part is proportional to the number of ionizing particles, $X_{\omega_{\max}}$ can also be seen as the atmospheric depth of maximum shower development ($X_{\omega_{\max}} = X_{\max}$). A measured longitudinal shower-profile is shown in figure 1.10 (right).

Examples of cosmic-ray experiments employing fluorescence detector systems are HiRES [87], the Telescope Array [88], and the Pierre Auger Observatory [89].

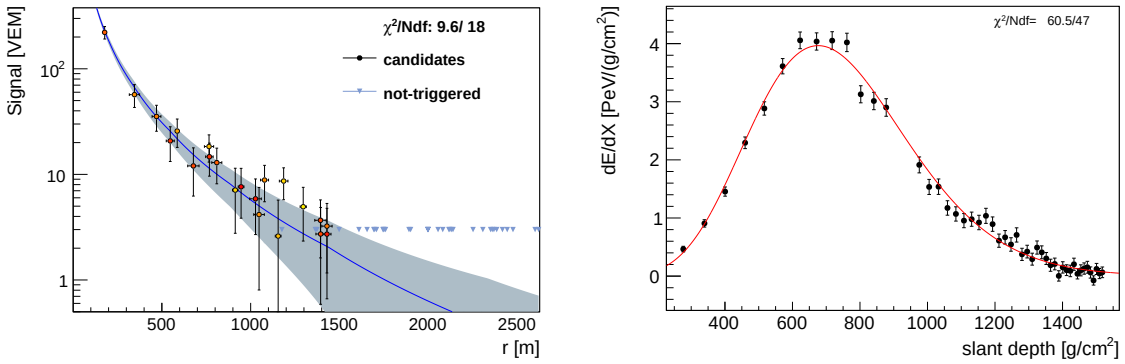

Figure 1.10: Hybrid detection of an extensive air shower. Left: Lateral particle density distribution as measured with the Surface Detector array of the Pierre Auger Observatory. The timing of the detected signals is color coded from yellow to red. Non-triggered stations are plotted as triangles.The distribution is fitted with a modified version of equation 1.23. Right: Longitudinal shower development in terms of energy deposit as function of the traversed atmospheric depth measured with the Fluorescence Detector of the Auger Observatory. The line indicates a fit with the Gaisser-Hillas function (equation 1.24). The reconstructed parameters of the displayed shower are $E = 2.7 \times 10^{18}\,\mathrm{eV}$, $X_{\max} = 676\,\mathrm{g/cm^2}$, and zenith angle $\theta = 58°$.

Air Cherenkov Detectors

Next to the fluorescence light, Cherenkov radiation is produced by the ultra-relativistic air-shower particles in the atmosphere with its non-unity index of refraction. The lateral pattern of the Cherenkov light contains information about the shower development and especially $X_{\max}$ which can be used in dedicated experimental setups. The TUNKA experiment [90] employs such a non-imaging Cherenkov detector array for extensive air showers.

As fluorescence and Cherenkov telescopes detect photons in the ultraviolet (UV) wavelength regime, they can only be operated during clear moonless nights which has a large impact on the duty cycle being limited to less than 15%.

Radio Detector Arrays

Besides fluorescence and Cherenkov light, the third type of radiation generated by an extensive air shower are MHz (and GHz) radio pulses as discussed in section 1.2.4. The observation of those pulses is not limited to any special atmospheric conditions and allows for almost 100% duty cycle only limited in case of strong atmospheric electric fields (e.g., during thunderstorm conditions). The signal distribution at ground level can be measured by arrays of radio detectors similar to particle detector arrays. The individual radio detection stations are thereby equipped with antennas (most often in two polarization directions) and fast digitizing electronics to sample the ultra-short pulses. Starting the renaissance of radio detection, LOPES [91] and CODALEMA proved that the developments in electronics were advanced enough

to allow observations of extensive air showers on large scales. Today's radio detectors like LOFAR, TUNKA-REX [92] and AERA are already approaching a competitive performance in the reconstruction of shower parameters such as arrival direction, energy, and $X_{\max}$, see e.g., [71, 93].
The reconstruction of the shower geometry is based on the arrival times of the radio pulses. By analysing this timing information, it has been found that the wave front of the radio signal has a hyperbolic shape [94] which is proposed to be related to the shower development [95].
The lateral distribution of the signals, which might be taken as the maximum amplitude of the electric field or the energy deposited per area (which we call energy density from here on) in the pulse, is more complex than in the case of the particle detectors due to the two emission mechanisms and cannot be properly described by a radially symmetric function. This became at latest obvious from the measurement of the densely populated antenna array of LOFAR. A new approach is using a two-dimensional function empirically developed on simulations accounting for the seen asymmetries [96]. This function describes the signal P at every position (x', y') in the $\vec{v} \times \vec{B}$ vs. $\vec{v} \times (\vec{v} \times \vec{B})$ plane as

$$\begin{aligned} P(x', y') &= A_+ \cdot \exp\left(\frac{-[(x' - X_+)^2 + (y' - Y_+)^2]}{\sigma_+^2}\right) \\ &\quad -A_- \cdot \exp\left(\frac{-[(x' - X_-)^2 + (y' - Y_-)^2]}{\sigma_-^2}\right), \end{aligned} \tag{1.26}$$

where $A_\pm$ are scaling parameters ($A_+ > A_-$), $X_\pm$ and $Y_\pm$ are location parameters, and $\sigma_\pm$ are shape parameters. Two examples of the fit of modified functions to LOFAR and AERA data are shown in figure 1.11. A detailed discussion about the function in its original and modified version and the correlation between function parameters and air shower properties is given in chapter 5 and the following.

Multi Hybrid Detector Setups

Even though most detection methods show some sensitivity to all relevant air shower properties, many cosmic-ray observatories are built in a way that allows measurements of the air showers with different techniques simultaneously. Thereby, the different advantages can be combined to an accurate air shower reconstruction. It is furthermore possible to cross calibrate various detector systems which can be used to reduce the systematic uncertainties of individual experimental setups. The major present radio detectors are used in combination with a ground based (particle) detector array. In the case of TUNKA-REX this array consists of air Cherenkov detectors. In addition to the acquisition of complementary information about the same air shower, trigger information can be provided to the radio detectors during run time. This guarantees efficient triggering and allows for a significant suppression of the detection of pulses from background sources.
The introduction of radio detectors to cosmic-ray experiments offers the measurement of the

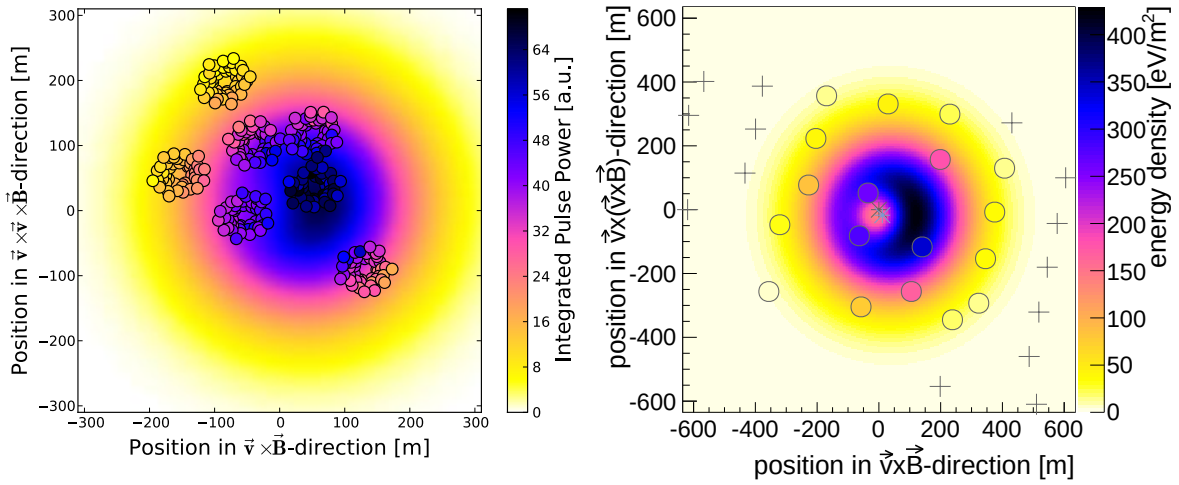

Figure 1.11: Measured intensity patterns of radio emission in the shower plane spanned by $\vec{v} \times \vec{B}$ and $\vec{v} \times (\vec{v} \times \vec{B})$. Left: Air shower footprint measured with LOFAR. Every coloured circle stands for the integrated pulse power in one radio antenna station. The background color shows the fit of a modified version of equation 1.26 to the data. Right: Air shower footprint measured with AERA. In addition to the signal stations with signals above the signal-to-noise threshold, sub-threshold antenna stations are indicated by a "+". The color scale in this case represents the measured energy density. The air shower displayed on the right side is the same as shown in figure 1.10.

depth of the shower maximum [71] with almost 100% duty cycle. One example is the Pierre Auger Observatory, where AERA is not only taking data together with the Surface Detector array, but it is operated in a multi-hybrid setup which also includes the Fluorescence Detector and underground muon counters. An example of a multi hybrid detection is already given in this chapter where the data in the figures 1.10 and 1.11 are taken from the same air shower measured by three different detectors. It should also be stressed, that the information gathered by the radio detectors might very well be used to improve the established techniques of particle and fluorescence air shower detection.

2

The Pierre Auger Observatory

Parts of this chapter have been published in:

J. Schulz for the Pierre Auger Collaboration
Status and Prospects of the Auger Engineering Radio Array
Proceedings of the 34th International Cosmic Ray Conference, The Hague, The Netherlands, (2015) [67]

J. Schulz, P. Dolron, R. Habraken, J. R. Hörandel, T. Wijnen
EMC-test of the AERA124 reference station
Auger Internal Publication, GAP2013_063 [97]

With an instrumented area of more than 3000 km^2, the Pierre Auger Observatory is leading in the field of ultra high-energy cosmic-ray research. It is located on the Argentinian high plain "Pampa Amarilla" ($\sim$ 1400 m a.s.l.) north of the city Malargüe in the province of Mendoza. The observatory consists of two main detector systems employing different methods to detect extensive air showers and extract complementary information (from the same shower). The two complementary detectors, which are described in the following sections (2.1 and 2.2), are the *Surface Detector* array and the *Fluorescence Detector*. Profiting from these two established and well calibrated baseline detectors, add-ons were introduced to the Observatory over time to extent the detection capabilities or to test new detection methods. The extensions relevant for this work will be introduced together with the Observatory's radio detector, the *Auger Engineering Radio Array* which this work is focussing on. Figure 2.1 gives an overview of the layout of the site with the two baseline detectors, AERA, and the low-energy extension *HEAT* (High Elevation Auger Telescope) with the associated dense Surface Detector region called *Infill*.

2.1 The Surface Detector Array

The Surface Detector array (SD) covers the $3000\,\mathrm{km}^2$ with more than 1600 individual water Cherenkov detector stations. The stations are deployed on a triangular grid with a spacing of 1500 m. This grid in combination with the station's technical specifications and the trigger conditions explained in the following allows for fully efficient air shower detection above a

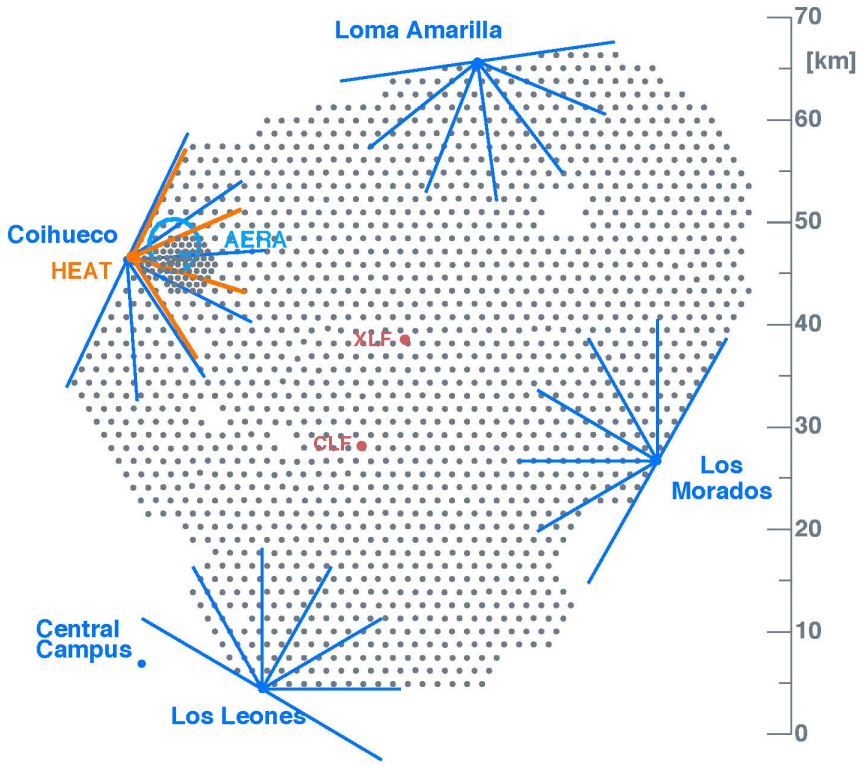

Figure 2.1: Map of the Pierre Auger Observatory. The individual stations of the Surface Detector array are indicated as dots. The Fluorescence Detector buildings are shown at the edges of the grid with the different field of views of the single telescopes. Close to the Coihueco Fluorescence Detector building where also HEAT is based, the densified region of the Infill as well as AERA are located. In the middle of the array, two laser facilities used for atmospheric monitoring (CLF, XLF) are shown. The central campus in the city of Malargüe is only a few kilometers south-west of the instrumented area. Figure taken from the Pierre Auger Collaboration.

primary particle energy of $3 \times 10^{18}\,\mathrm{eV}$.

The basic design of these detector stations was adapted from the Haverah Park experiment [98] and comprises a polyethylene tank of a diameter of 3.6 m and a height of 1.6 m. Each tank is filled to a height of 1.2 m with $12\,\mathrm{m}^3$ of purified water which is confined in a liner. All other station hardware, which is mainly the photomultiplier tubes (PMTs), analogue-to-digital electronics, wireless communication, global positioning system (GPS) antenna, and a solar power system, is attached to the main water compartment from the outside for easy access. With these components, every station forms a self-sufficient unit with all necessary hard- and software for power harvesting, data collection, and transmission. A photograph with indications of the components is shown in figure 2.2. Each station has a power consumption below 10 W and runs self-sufficient powered by a solar power system including two 55 Wp[1] solar panels.

[1] Wp = Output in (W) under 1000 W/m^2 irradiation and standardized test conditions.

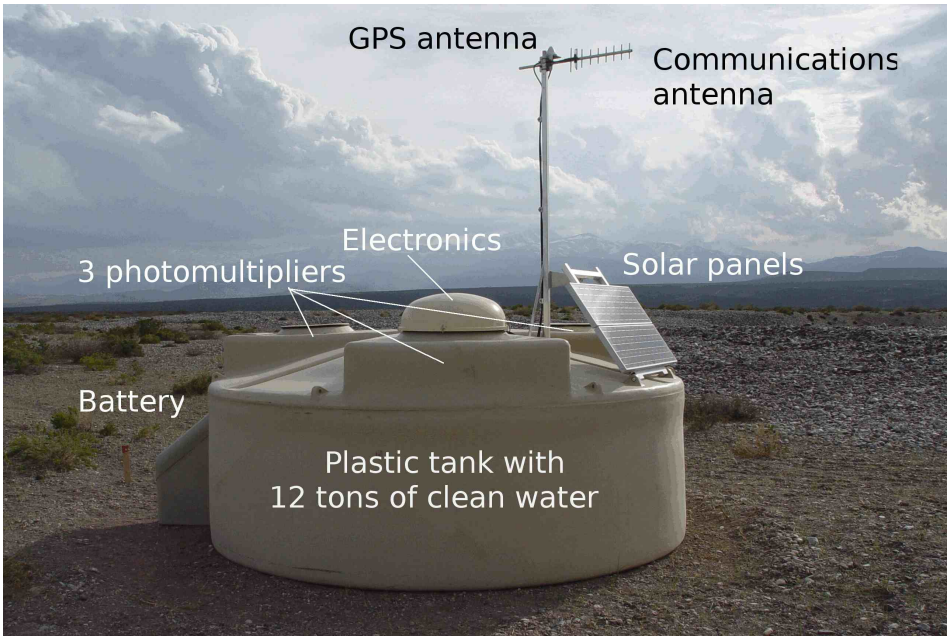

Figure 2.2: Photo of a Surface Detector station of the Pierre Auger Observatory. Indicated are the individual hardware components as water compartment, batteries, global positioning system (GPS), communication antenna, solar panel, photomultiplier tubes, and electronics. Photo courtesy of R. Smida.

The provided power is managed by a commercial charge controller connected to two 105 Ah 12 V-batteries allowing for 99% uptime [99].
All stations are connected via wireless Local Area Network (LAN) data links to the observatory's central data acquisition system (CDAS). Every Surface Detector station is equipped with a custom-designed wireless communication unit . The communication is handled according to the Time Division Multiple Access (TDMA) protocol, where each subscriber has a fixed time slot to send and receive data. The unit is connected to the station's main electronics on one side and a 12 dBi Yagi antenna on top of the solar panel support frame (3 m above ground) on the other side. The unit operates in the $902 - 928\,\mathrm{MHz}$ frequency band and has a power consumption of less than 1 W. The wireless connection allows for remote control of the station as well as software changes. A group of detector stations forms a unit connected to an access point (AP) located at one of the four Fluorescence Detector buildings. The typical number of stations connected to one AP is 57 (upper limit: 65) allowing for a single link bandwidth of 1.2 kbit/s. To provide predominantly line of site for the connections (even for the stations in the center of the array), the AP antennas are mounted at a height of $20 - 50\,\mathrm{m}$ on communication towers. The AP antennas are sector antennas with an acceptance of 90° and a gain of 17 dBi. In this configuration, the setup allows for long distance connections of more than 30 km between stations and their APs. The AP wireless unit is the same as in the stations with slight modifications to allow for the larger data throughput. In a second layer, all APs of one tower location are grouped together and connected to the other locations and to the central campus (where CDAS is based) with a backbone link. In this case, a commercial

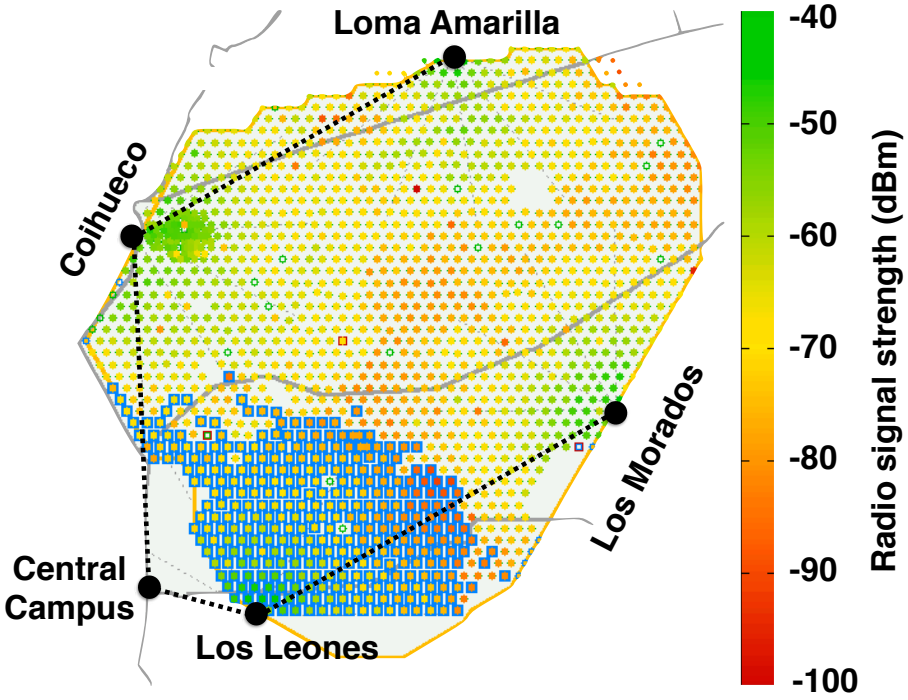

Figure 2.3: Map indicating the wireless communication layout of the Pierre Auger Observatory. The dots indicate the Surface Detector stations. Color coded is the radio signal strength of the connections between a station an its access point at one of the Fluorescence Detector sites. Exemplary marked by an additional square in the lower part of the array are those stations connected to the access points at Los Leones. The big dots denote the backbone wireless network stations at the central campus and the four Fluorescence Detector locations. These main wireless links are indicated as dotted line.

7 GHz wireless network with a bandwidth of 34 Mbps per link is used. The links are arranged in a U-shape with the central campus in the middle and two connections to both sides around the array (see figure 2.3). This network infrastructure as a whole allows the transmission of all necessary data packages between the individual SD stations and CDAS. Furthermore, data from the Fluorescence Detector and the Observatory's extensions can be handled. Detailed information about the wireless network can be obtained from [100].

The Surface Detector data emanates from three nine inch photomultiplier tubes (PMTs) which are installed at the top of the tank facing downwards through transparent windows in the liner. The PMT signals indicate Cherenkov light induced by super luminous particles traversing the water. The output is digitized by 40 MHz flash analogue-to-digital converters (FADCs) and stored in a ring buffer for 10 s. The data are automatically calibrated for the detector response on station level to the average signal induced by a vertical equivalent muon (VEM). This calibration is updated every minute and also added to the station data for later analysis.

To select interesting events, two different trigger conditions are defined on the single-station level (T1/T2). The time over threshold (ToT) condition requires 13 out of 120 FADC bins in a sliding window to be above a threshold of 0.2 VEM in two of the three PMTs. The thresh-

old crossing (TH) condition requires all three PMTs to have a signal larger than 3.2 times the VEM signal height. The local T2 triggers are sent to CDAS where the set of T2 triggers from different SD stations is checked for spatial and temporal coincidence. In case the requirements to form a trigger for the Surface Detector array (T3) are met by the combination of T2 triggers, the data are requested by CDAS and stored centrally for off-line analysis. The exact conditions for T3 triggers and further information about the T1 and T2 trigger settings are presented in [101].
For the data reconstruction the software framework $\overline{\text{Off}}\underline{\text{line}}$ [102] is used. A deeper insight to the framework is given in chapter 3. From the Surface Detector data, mainly the direction of the shower axis and the energy of the primary particle are determined. This energy is inferred from a cross calibration with the Fluorescence Detector discussed in the following section. The calibration reveals a resolution of 16% for low-energy showers and 12% for showers with the highest energies [29]. Additionally, 14% systematic uncertainty are inherited from the Fluorescence Detector energy scale, [103]. The resolution on the reconstructed incoming direction depends on the number of stations above the threshold (signal stations) and is 1.6° for showers detected with 3 stations and 0.9° for showers detected with more than 5 stations [29].

2.2 The Fluorescence Detector

The Fluorescence Detector (FD) covers the volume above the Surface Detector with 24 individual telescopes. Four observation sites at the edges of the SD array are hosting six of these telescopes each. The telescopes are arranged next to each other in a way that their individual coverage of $30^\circ \times 30^\circ$ gives each FD site a 180° azimuthal field of view (FOV) facing inwards to the center of the observatory. The elevation of the FOV is minimally 1.5° above the horizon. The FD sites and the fields of view in the North-South East-West plane are shown in figure 2.1. Inclined shower tracks can cross more than one individual FOV and in case of very high-energetic showers and depending on the geometry, "stereo" ("triple" and even "quadruple") events detected by telescopes at multiple FD sites can be observed.
The telescopes are installed in a closed, clean, and climate controlled room. The individual setups consist of an optical and an electronics system. The optical part comprises a shutter, an aperture system, an ultraviolet (UV) bandpass filter window, and a $10\,\text{m}^2$ mirror. For the readout, a 440 pixel (22×20) camera with one PMT per pixel is used and connected to fast digitizing electronics. A photograph of a FD building and a schematic drawing of a telescope are shown in figure 2.4. The shutter in front of the aperture system is closed during day time, in case of bad weather conditions (high winds, rain, etc.) or moonlight in the FOV. The bandpass of the UV filter window ranges from 310 nm to 390 nm (transmission above 50%) which covers the nitrogen fluorescence emission spectrum and limits the background from visible light photons. The other optical components are arranged in form of a Schmidt telescope. The segmented spherical mirror focusses the light onto a curved focal plane where the PMT cam-

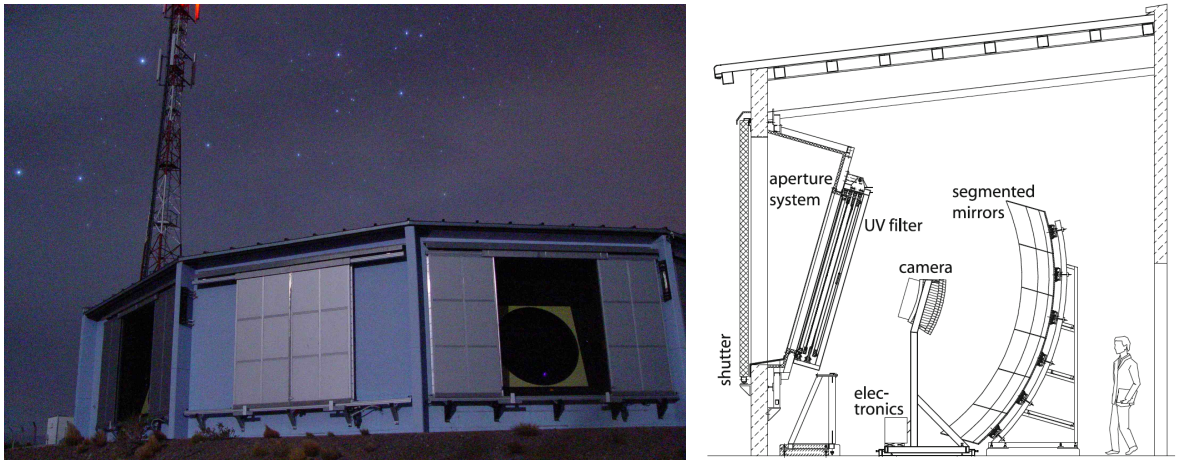

Figure 2.4: The Fluorescence Detector of the Pierre Auger Observatory. Left: Photograph of the Los Leones FD building during data acquisition. Three of the telescope bays are captured where one shutter is closed because the moon is in the FOV of the particular telescope. In the background, the communication tower is visible. Photo courtesy of R. Smida. Right: Sketch of a fluorescence telescope including the main components of the optical system. Figure taken from [89].

era is installed. Different types of mirrors are used, all providing a reflectivity (at 370 nm) of more than 90% in a clean state. The grid frame of the PMT camera is specially designed to guide photons to the PMTs using Winston cones. With the overall design of the telescopes, the angular spread of light from a distant point source falling onto the camera is well below the size of a single hexagonal pixel (40 mm side to side). This is important, as an imaged air shower activates a line of pixels on the camera.

The readout of the PMT signals is performed independently per telescope and the signals are filtered, digitized, and passed through a multiple stage trigger system (for details see [29, 89]). Additionally, a ground impact time is estimated for the shower candidate and a trigger is sent to CDAS. These triggers initiate the request for SD data recorded around this time to form a hybrid shower candidate. The threshold for full efficiency in hybrid detection of showers throughout the whole array is 10^{19} eV. However, depending on the geometry, hybrid detection of showers with much lower energies is possible. As a part of the SD array is readout after an FD trigger, valid hybrid events can also contain just a single SD station, lowering the energy threshold to 10^{18} eV. The average FD event rate is roughly $0.01\,\mathrm{s}^{-1}$ per FD site. Information about the reconstruction techniques of the data will be given in chapter 3.

The fluorescence technique has its main strength in determining the atmospheric (slant) depth of the shower maximum $X_{\max}$ and the energy of the shower (see section 1.2.5). The resolution on $X_{\max}$ is better than 20 g/cm^2 and the energy resolution is 7.6% with an additional 14% on the absolute energy scale for energies above $10^{18}\,\mathrm{eV}$ [29, 103]. For hybrid showers independently detected with the SD and the FD, the combined angular resolution improves to 0.6° and the resolution on the position of the shower axis is about 50 m.

In order to reconstruct the energy of a cosmic ray based on the measurement of the number

of fluorescence photons detected by an FD telescope, a precise calibration of the detectors is necessary in addition to the knowledge of the fluorescence yield. Furthermore, environmental influences on the measurement need to be eliminated or accounted for. The hardware of the telescopes is calibrated with a known light source that can be mounted to the aperture system of the telescope about once per year. More frequently, calibrations with a portable laser positioned at a few kilometer distance to the FD sites are performed shooting straight upwards into the field of view of the telescopes. In addition every telescope is relatively calibrated before and after each run with a fixed installed calibration light system. Details on the procedure of the fluorescence telescope calibration can be found in [89, 104, 105].
As for extensive air shower detection the whole atmosphere acts as a calorimeter, several properties need to be monitored in detail to be able to correct for the continuously changing detector medium. Exemplary, only a few key aspects will be mentioned here to demonstrate the complexity of the method.
The atmosphere is often not a clear detector medium and the produced fluorescence photons are scattered and absorbed by aerosols and clouds. To correct the measured light intensities at the FD sites, the amount and distribution of aerosols and their influence on the light propagation need to be measured in-situ and continuously during data acquisition. For this purpose, laser facilities (XLF and CLF, see figure 2.1) are centrally located in the Surface Detector array and used to provide a set of (vertical to inclined) UV-light pulses every 15 minutes. The photons of these laser shots are scattered by the aerosols and can be detected with the fluorescence telescopes at each site. As the laser beam power is calibrated, the amount of scattered light at the FD sites is used to correct for aerosols. The complete description of the method and further information can be found in [106]. Furthermore, the atmospheric state variables are influencing the shower development. Due to quenching effects, the temperature and pressure profiles of the atmosphere need to be taken into account to reconstruct the longitudinal shower development [84, 89]. After several years of direct airborne atmospheric measurements with weather balloons and radio soundings, the usage of atmospheric data based on the Global Data Assimilation System (GDAS) became the standard at the Pierre Auger Observatory in 2010 [107]. The influence on the reconstructed value of $X_{\max}$ is found to be smaller than 1 g/cm^2 [108] while it makes the great experimental efforts with balloon flights superfluous.

2.3 The Low-Energy Detector Extensions - Infill and HEAT

To extend the energy threshold of the SD to the second knee of the cosmic ray spectrum at $4 \times 10^{17}\,\mathrm{eV}$, two low-energy extensions to the baseline detector system were installed in 2011. One is a denser populated region in the SD additionally equipped with underground muon detectors, called the Auger Muon and Infill Ground Array (AMIGA) [109]. The other one is an extension of the FD consisting of three additional telescopes with an elevated field of view, the High Elevation Auger Telescopes (HEAT) [110]. Both extensions are depicted in figure 2.5

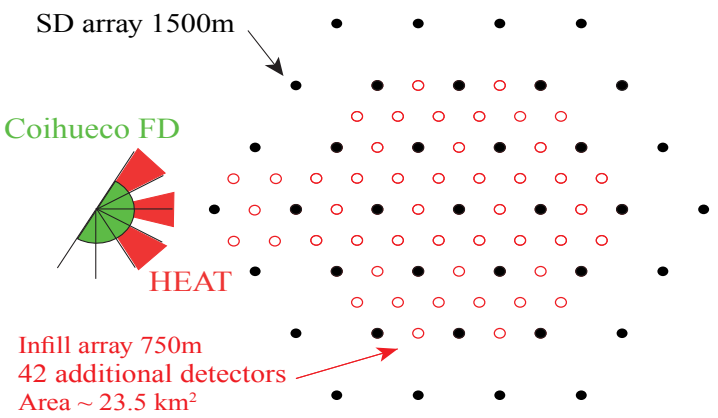

Figure 2.5: Sketch of the SD Infill array together with the position of the Coihueco FD and HEAT. The dots indicate regular SD station positions whereas the circles denote the positions of the additional tanks together forming the Infill. Also indicated are the fields of view for the Coihueco and HEAT telescopes. Figure adapted from [110].

and a photograph of the High Elevation Auger Telescopes is shown in figure 2.6.
The SD Infill array covers an area of 23.5 km^2 and is embedded in the regular SD 6 km to the East of the Coihueco FD building. Additional Surface Detector stations placed with a spacing of 750 m enable the Infill to be fully efficient at primary energies above 3×10^{17} eV for zenith angles smaller than 55°. To also profit from the hybrid approach of detecting air showers at these lower energies, the HEAT telescopes were designed to allow hybrid detections with the Infill array down to 10^{17} eV. These three telescopes are therefore based at the Coihueco FD side but work as an independent detector system. Their basic design does not differ significantly from the general FD telescopes, but the HEAT telescopes are installed separately from each other in individual shelters. These shelters can be tilted upwards by 29° so that their FOVs lay above the ones of the Coihueco FD telescopes and just slightly overlap. Taking both systems together, an elevation range from about 2° to 58° is covered. The same way an inclined shower track can range over the FOVs of neighbouring FD telescopes, a vertical shower can range over the FOVs of the HEAT and the baseline telescopes. In this case the Coihueco and the HEAT telescopes can be paired up in the reconstruction to one unit. For calibration and cross-checks with the baseline FD, the HEAT telescopes can be operated in the horizontal position as well. A special feature of the HEAT telescopes is the faster readout electronics which are optimized to measure air showers close to the telescope [29]. Both enhancements use the baseline detector hardware but work in a different parameter space in terms of e.g., geometry and energy, therefore the established reconstruction techniques can be used but need to be adapted to suit the Infill/HEAT data. As AERA is located within the SD Infill, the enhancements play a major role for the reconstruction as well as the analysis of radio data. From here on the term "Infill" will be dropped and the term SD denotes the SD Infill. In some cases the term Infill will however be recalled for clarification. Analogously, the term FD will also include HEAT if not explicitly stated otherwise.

Figure 2.6: The High Elevation Auger Telescopes. Left: Photograph of the 3 HEAT telescopes in the upwards orientation. Right: Sketches of a HEAT telescope in the horizontal orientation for calibration and maintanance (top) and the upwards orientation for data acquisition (bottom). Both figures are taken from [29].

2.4 The Auger Engineering Radio Array - AERA

AERA is an extension of the Pierre Auger Observatory designed to measure the radio emission of extensive air showers between 30 and 80 MHz. It is located inside the SD Infill array and underneath the FOV of the Coihueco and HEAT FD telescopes. The project is carried out in three phases. At first, an array of 24 radio detection stations (RDS) called AERA24 was deployed in September 2010 to proof the feasibility of hybrid air shower measurements and to develop the techniques to extract air shower parameters from the radio measurement. Based on the experience gained with AERA24, the second stage, AERA124, was deployed in May 2013 with a modified station and antenna design [111]. With different grid sizes, multiple improved hardware and trigger concepts and an instrumented area of 6 km^2, AERA124 is accumulating cosmic-ray data at a rate of a couple of thousand showers per year with energies ranging roughly from below 10^{17} eV up to exceeding 10^{19} eV. In the third stage deployed in April 2015, AERA153 now covers about 17 km^2. The targets of this extension are mainly horizontal air showers ($> 60°$ zenith angle). Their large footprint allows for the detection with a sparsely instrumented array and the hybrid measurements of these air showers contain complementary information in radio and particle signals. The layout of AERA including all three stages is shown in figure 2.7. The work for this thesis is mainly based on data from AERA24 and AERA124, therefore these two stages will be described in more detail in the following subsections.

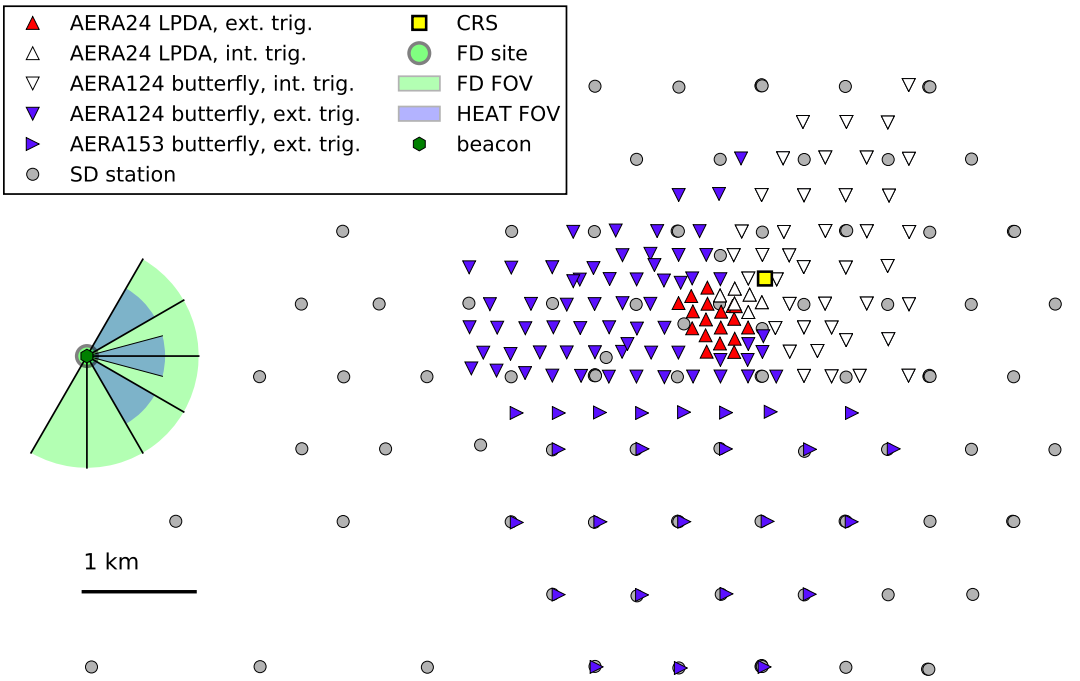

Figure 2.7: Schematic overview of the Auger Engineering Radio Array and part of the Infill region of the Surface Detector array. The Coihueco Fluorescence Detector telescopes and the HEAT extension are also indicated with their respective field of view (FOV).

2.4.1 AERA24

The AERA24 stations are arranged with a distance of 144 m from each other on a triangular grid covering 0.4 km^2. Each station operates self-sufficient and consists of five main components: the radio antenna, the fast digitizing electronics, the solar power system, the GPS timing system, and a communication unit. A photograph of an AERA24 station is shown in figure 2.8. The solar power system consists of four Isofóton solar panels with 60 W power each, two Victron Energy gel batteries with 150 Ah capacity each and a Morningstar SS-20L charge controller. The two panels are mounted on a triangular frame and all station electronics is housed in a water tight metal box underneath which also shields radio frequency interference (RFI) . The total power consumption of an AERA24 station is provided by the solar power system the whole year around.

The antenna is a logarithmic-periodic dipole antenna (LPDA), with two sensitive horizontal planes [111]. One is oriented in the direction of the magnetic field and the other is oriented perpendicular to it. For high-precision polarisation measurements, the alignment of the antennas has been carried out with an accuracy of better than 0.6° [112]. The antenna is optimized to operate in the frequency range from $27 - 84\,\mathrm{MHz}$ which was found to be relatively radio quiet in terms of terrestrial background radiation on site [113]. Connected to the foot of the antenna, a low-noise amplifier (LNA) is used to amplify the signals before they are introduced into a

Figure 2.8: Photograph of an AERA24 station. The logarithmic-periodic dipole antenna is mounted well above the ground with the solar panels on top of the electronics compartment underneath. The compartment houses the electronics as well as the batteries and the power controller.

filter-amplifier and digitization chain. There, they are bandpass filtered between $30 - 80\,\mathrm{MHz}$ and fed into a low-gain (+29 dB) and a high-gain (+49 dB) channel each extending the dynamic range. In the next step, the signals are digitized by 12-bit flash analog-to-digital converters (FADCs) and further processed by a field programmable gate array (FPGA) and a central processing unit (CPU). This chain is referred to as the "digitizer" and it exists in various forms to test and optimize the technical realization of different detection strategies. For AERA24, mainly two digitizer versions were deployed focussing on different triggering strategies. One has a sampling rate of 180 MHz and features a 4 GB ring buffer which can hold data from two channels for ~7 s or from four channels for ~3.5 s. The ring buffer allows for external triggering by other detectors of the Pierre Auger Observatory, mainly the SD and the FD. The time needed to form an external trigger from the SD or the FD via CDAS can be up to 7 s. Therefore, mostly only the high-gain channels are used for externally triggered data acquisition. In case of an external trigger, the ring buffer is read out, and a time series of $56.89\,\mu\mathrm{s}$ around the requested trigger time is sent to the central radio DAQ to be stored for offline analyses. In addition, running in a self-trigger mode is also possible with this hardware. The second type of digitizer has a sampling rate of 200 MHz and is designed for self-triggering and therefore features no large buffer medium. In case of self-triggering, a first trigger decision can be made in the FPGA based on the ADC values. This trigger information is then forwarded to the CPU where further processing and signal verification can be done. Remaining triggers are GPS timestamped and sent to the central radio DAQ where all timestamps of triggered stations are processed. In case of coincidences, the data are requested from the triggered stations. For further information on triggering, data aquisition and reconstruction see chapter 3.
The AERA24 stations use a fibre-based scheme to communicate with the central Radio DAQ [114]. Therefore, a media converter is used for the connection between the Ethernet and the

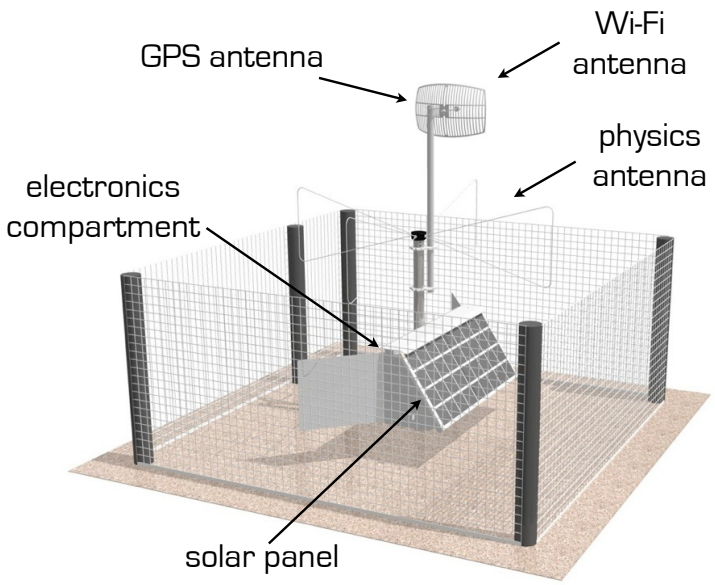

Figure 2.9: The AERA124 station. Technical drawing with indications of the main components.

fibre in the station electronics. The stations are daisy chained in two loops starting at the Central Radio Station (CRS). Compared to the 100 MBits/s Ethernet connections used on both ends, the fibre does not limit the bandwidth and therefore provides the opportunity for trigger development with high rates and data throughput. From the CRS, a wireless link is operated to the Coihueco FD building connecting to the Auger network, see also chapter 2.4.6.

2.4.2 AERA124

The AERA124 stations are arranged on a triangular grid with two different spacings of 250 m and 375 m around the dense core of AERA24. The spacings are chosen to enlarge the instrumented area and to increase statistics, but also to explore geometries for future cosmic-ray experiments. With a larger instrumented area and more stations, the challenges of semi-mass production, deployment, and operation become important. To account for that and also to include technical expertise from operating AERA24, the layout of the AERA124 stations was redesigned substantially. The new station design is shown in a rendered mechanical drawing in figure 2.9. The new setup includes various fundamental changes in the mechanical and electronic parts. The design was modified in such a way that all components are mounted to a central pole. The antenna for cosmic-ray measurements is mounted on top of this pole and all station electronics and the solar power system are housed in one compartment underneath. This electronics compartment also features an RFI tight Faraday cage as interior to prevent the station electronics from radiating to the outside. A test of the shielding capability of the Faraday cage is presented in section 2.5.2. On top of the physics antenna, a 5 GHz grid antenna for wireless communication and the GPS antenna are mounted on a secondary pole. For

cost effectiveness, the solar power system for the new setup consists of only one 135 W Kyocera KD140 solar panel in combination with one of the 150 Ah gel batteries already used for AERA24 and a new charge controller (IVT SCD-20). This limits the available power and puts constraints on the power consumption of all components. Part of the redesign goals of the new station electronics has therefore been a power consumption of less than 12 W.
The antennas used for the AERA124 stations are active bowtie antennas also called "Butterfly" [111, 115]. This antenna type has a simple design and has been tested successfully in the CODALEMA experiment [65] and in an earlier R&D setup at the Pierre Auger Observatory [116]. In contrast to the LPDA antenna, the Butterfly antenna is sensitive towards the ground which enhances the signal. This, on the one hand increases the antenna gain, but on the other hand leads to an influence on the antenna characteristic by the (changing) ground conditions.
The general layout of the digitizer chain is similar to the one used in AERA24 even though every component has been redesigned. In total, there are 60 AERA124 stations equipped with externally triggered hardware and 40 stations employing internal triggering. Two major changes were made to the digitizers without a ring buffer. A new FADC with a depth of 14- instead of 12-bits increases the dynamic range. Therefore, the duplication of data in high- and low-gain channels becomes unnecessary and the two anciently low-gain channels are used to introduce a new internal trigger next to the self-trigger on the radio signals. This internal trigger is based on scintillation counters in the electronics compartment of the radio station itself. Two (or one) small plastic scintillators are integrated in the 40 AERA124 stations that are not equipped with ring buffers (see figure 2.7). A detailed technical description of the digitizing electronics of the self-/scintillator-triggered AERA124 stations is given in [117]. More information about the scintillators and also their potential as a stand-alone cosmic-ray detector is given in chapter 4.
The stations communicate with the DAQ system via a wireless network operating in the 5 GHz range. The network was set up as part of this work and all components as well as the network scheme are presented in section 2.4.6. Tests for the system integration of the wireless system are presented in section 2.5.3. The DAQ system was changed from AERA24 to AERA124 to accommodate the additional stations and mainly moved to the Coihueco FD building. The DAQ of the internally triggered stations is still based at the CRS. A description of the data acquisition is given chapter 3.

2.4.3 AERA153

The AREA153 stations are technically very similar to the AERA124 stations equipped with a Butterfly antenna. Only the digitization electronics has been modified to account for technical improvements. The main difference to compared AERA124 is the increased station spacing. One row of seven stations has a spacing of 375 m and the other 18 stations are placed on a 750 m grid and the radio detection stations are located close to the Infill SD stations.

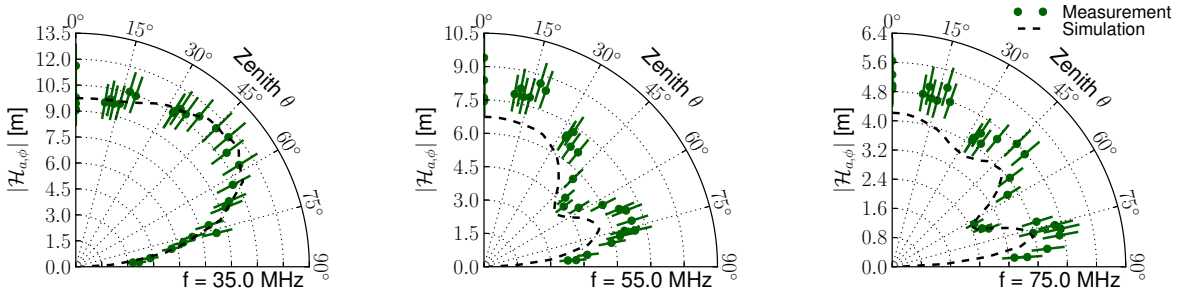

Figure 2.10: Comparison of the measured and the modelled vector effective length of the LPDA antennas of AERA24 for three different frequencies. The data were acquired in situ with a balloon-based reference source. Figure taken from [111].

2.4.4 Research and Development Stations

As an engineering array, AERA is also used to test new technologies and hardware components. Two subjects were addressed with dedicated test stations. One subject is the employment of an additional antenna sensitive to the vertical component of the electric field to measure the full three-dimensional electric-field vector. Extra stations equipped with an additional antenna are placed off grid in the middle of AERA124 and another 5 of the regular internally triggered stations in the South-East of AERA124 were modified accordingly with different vertical antenna types. The other subject is the detection of cosmic rays at low MHz frequencies. For this purpose, one additional radio detection station sensitive to frequencies of $1 - 10\,\mathrm{MHz}$ was installed in the field.

2.4.5 Calibration

Great efforts were made to calibrate the different AERA stations concerning the absolute signal response and relative timing. All components of the analogue signal processing chain were calibrated individually before being deployed and the production tolerances of the individual parts are small. The contribution of the uncertainty of the measured values induced by the signal chain components is estimated to be 2.5%. For the antennas, detailed electromagnetic simulations were performed and various air-borne calibration campaigns were carried out on-site to calibrate the direction and frequency-dependent responses on an absolute scale [111]. The simulated vector effective length (VEL) is shown in figure 2.10 for three different frequencies over the range of zenith angles compared to measurements taken in the field for the AERA24 LPDA antennas. The overall agreement between the measurements and the simulations is better $\pm 20\%$. Taking the average over all frequencies, the differences amounts to $\pm 5\%$. For the Butterfly antennas of AERA124, calibration measurements were performed and preliminary analyses of the data show a similar result. The calibration is however more challenging due to the sensitivity of the antenna towards the ground with its non constant properties. The exact modelling of the antenna pattern is work in progress and also aims at including changing en-

vironmental conditions.
For the reconstruction of air-shower properties, the arrival time of the signals is an important parameter. The reconstruction of the shower axis, interferometric approaches to enhance the detector sensitivity, and analyses based on the radio wavefront shape are depending on accurate timing. The commercial GPS systems however only provide a coarse resolution of a couple of nanoseconds and also experience drifting over time. Therefore, the relative timing of the AERA stations is continuously monitored via their phase offset measuring sine waves from a reference beacon [118]. The beacon is installed at the Coihueco FD site and emits four precisely defined sinusoidal signals. Additionally, signals from commercial aircraft detected by the AERA stations are used to determine the timing. In combination, a precise timing calibration of about 2 ns is possible, whereas the built-in GPS-clocks exhibit drifts of tens of nanoseconds. Further information on the timing calibration is available in [31].

2.4.6 Wireless Communication System

For AERA the step from a custom made wireless system as used for the SD to a commercial system manufactured by Ubiquity was made. The system operates in the 5 GHz regime and supports the standard Ethernet protocol as well as a TDMA protocol which is used in the AERA setup. As for the network of the Surface Detector array, the AERA network is set up in a point-to-multipoint configuration, where multiple RDSs are connected to a central base station access point (AP) .
A sketch of the AERA153 site including all RDSs and all AP locations is shown in figure 2.11. The network consists of two point-to-point and four point-to-multipoint wireless links and also includes the fibre-network of AERA24. The part of the AERA124 array to the East of the CRS (including all internally triggered stations) is connected to two APs at the CRS. There, 23 RDSs in the north-eastern part are connected to one AP (CRS East) and 17 RDSs in the south-eastern part are connected to the other AP at the CRS (CRS West). The part of the AERA124 array to the West of the CRS is connected to an AP at the Coihueco FD site. The same applies for the 25 stations deployed for AERA153 in the South of the AERA153 array for which an additional AP was installed at the Coihueco site. For the connection between the CRS and Coihueco, the two dedicated point-to-point links are used for data transmission and maintenance login.
Independently of the assigned AP, all RDSs using wireless communication are equipped with a combination of a Ubiquiti Bullet M5 and a 27 dBi L-COM grid antenna optimized for the 5 GHz range. For the APs at the CRS, the Ubiquiti Rocket M5 GPS is used in combination with an Ubiquiti Hi-Gain Airmax Sector 5G-90-20 antenna. For the two APs at Coihueco also Ubiquity Rocket M5 are used together with the Ubiquiti Hi-Gain Airmax sector antennas. Here, one of the used Ubiquity Rocket is a slightly modified Titanium version. The two point-to-point links are set up with Ubiquity Bullets M5 and 30 dBi Poynting high-gain grid-antennas. The 24 RDSs of AERA24 are connected to the CRS via a Draka Comteq Telecom

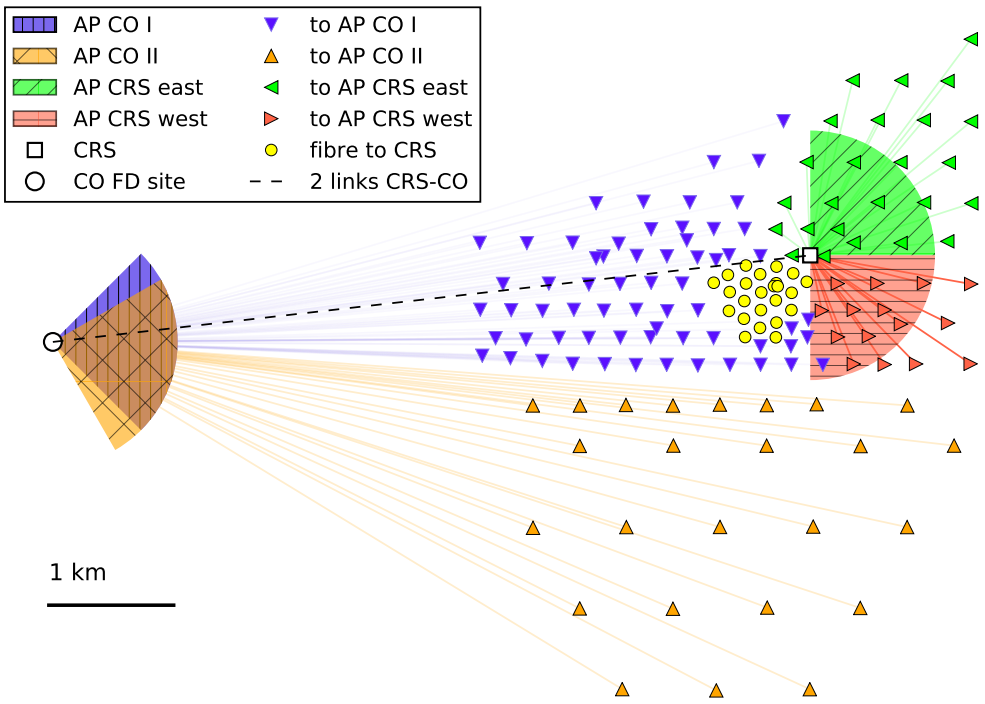

Figure 2.11: Overview of the AERA communication network. The AERA24 RDSs connected via fibre to the CRS are indicated by the red dots, AERA124 and AERA153 RDSs connected via wireless links by triangles. In addition the CRS and the Coihueco Fluorescence Detector building are represented by a square and a circle, respectively. At both of these two spots, two wireless access points are installed and their FOV is roughly indicated by the wedges. The color of the station marker corresponds to the AP the station is connected to. The two access points at the CRS are called *East* and *West* for historical reasons, even though this does not describe their orientation. Between the CRS and the Coihueco building, two point-to-point links are installed.

SM-LEJEN optical fibre [114]. Furthermore, an experimental system designed by the Institute for Data Processing and Electronics at the Karlsruhe Institute of Technology (KIT-COMs) also employing a TDMA protocol was temporarily installed in a part of the array [119]. After a successful test period, the experimental system was replaced by the commercial Ubiquity system. The experimental KIT-COMs system was realized as point-to-multipoint connection with one access point at the Coihueco communication tower and 29 subscriber units [119]. The system operated in the 2.4 GHz range and used a commercially available L-Com 27 dBi grid dish antenna at each RDS.

For completeness, it is mentioned here that for AERA24 only one point-to-point link between the CRS and Coihueco was operated using a 2.4 GHz system called Viper manufactured by Hopling Technologies. The Viper was taken down and replaced during deployment of AERA124.

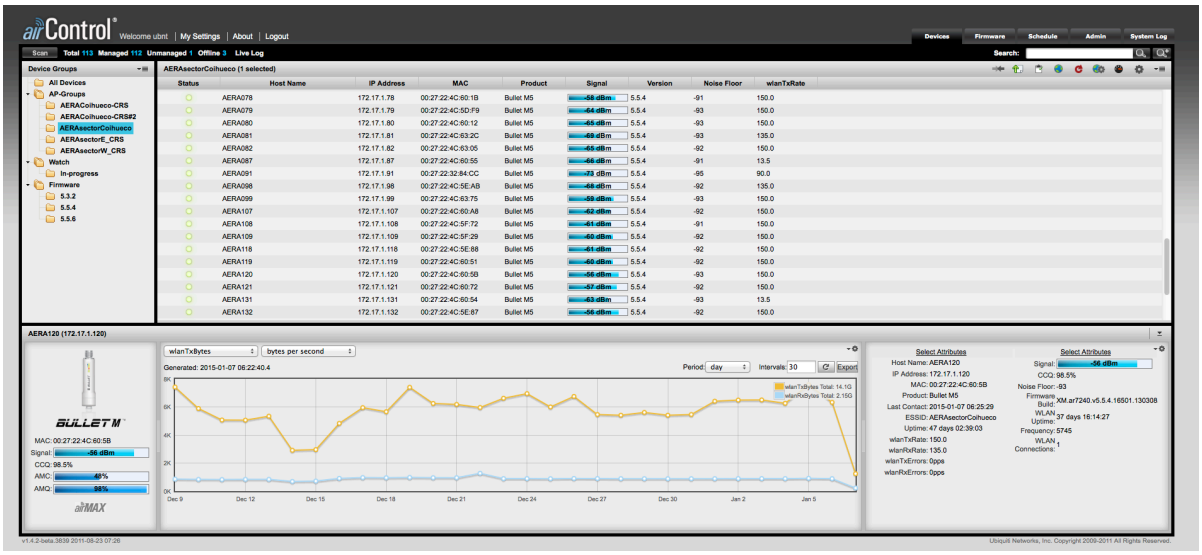

Figure 2.12: User interface of the Ubiquity web-based network management server application AirControl. The tool can be used to manage and monitor Ubiquity wireless devices.

Settings

The settings for the individual wireless hardware components are given in the tables in appendix A.1. In general, all links operate on not-overlapping frequency channels with 40 MHz width in the range of $5.600 - 5.805\,\mathrm{GHz}$. Each of the six wireless subnetworks has its own service set identification (SSID) and all components are locked to their sub-network SSID.

Monitoring

For monitoring and maintenance of the more than 150 wireless communication devices, the web-based Ubiquity network-management server-application called AirControl is used. With this tool, all components can be managed regarding local and global system settings. It is furthermore possible to send commands to all units simultaneously to e.g., upgrade the firmware or backup the system settings. The AirControl user interface is shown in figure 2.12.

System Performance

Due to the shifting focus in trigger strategies towards particle based triggers (internally or externally detected), the effective data-rates of the AERA153 setup are much below 200 kbps per station as predicted by Kelley [120]. For the externally triggered stations, the data transmission rate is about 40 kbps per station and the actual data receiving rates at the two APs at the Coihueco FD building are roughly 2.5 Mbps (CO I) and 1.0 Mbps (CO II). For the internally triggered stations, the data transmission rate is about 25 kbps and the receiving rates of the APs are roughly 570 kbps (CRS East) and 420 kbps (CRS West). For the point-to-point link between the CRS and Coihueco serving the AERA24 stations the rate is around 700 kbps.

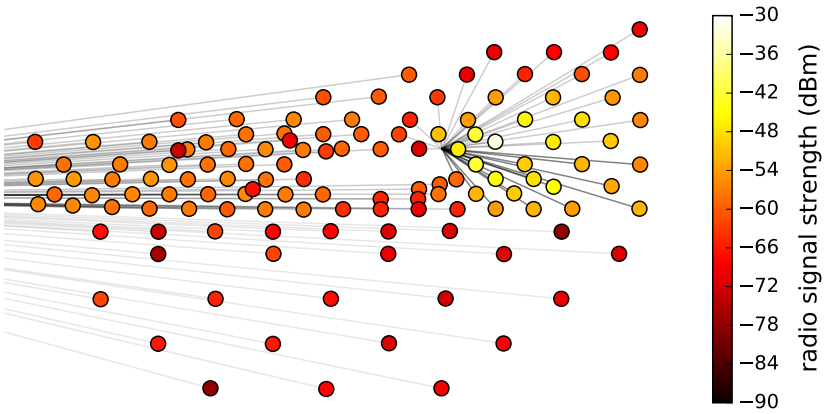

Figure 2.13: Overview of the signal strength for the connections of all AERA RDSs with wireless communication. The gray lines in the background indicate the directions of the links between the stations and the corresponding access points. The two dimensions of the plot are scaled arbitrarily.

In general, all stations have a stable and high-quality connection to their APs with signal strengths ranging from $-78\,\mathrm{dbm}$ to $-32\,\mathrm{dbm}$. The noise floor in the used frequency range is on average $-90\,\mathrm{dBm}$ which is well below the minimal signal strength reached by all stations. The causes for a lower signal strengths are various, the most obvious ones are not properly aligned grid antennas at the RDSs, disturbed line of sight, and link directions outside of the main acceptance region of the sector antenna as it is the case for one RDS connected to the CRS East access point. The signal strengths of the wireless subscriber units of all RDSs in the AERA153 array are shown in figure 2.13.

Due to the positive experience gained with the Ubiquity system, it has been suggested to also use this kind of hardware for the upgrade of the Pierre Auger Observatory: AugerPrime

2.5 System Integration for AERA124

The AERA124 station design was revised after the first stage of AERA to incorporated the gained experience concerning deployment and operation of the AERA24 stations. Due to these changes, the way of integrating every individual component such as e.g., the digitizer or the power control unit (PCU) into the station had to be reconsidered. Furthermore, tests of all individual hardware components and an efficient assembly and deployment scheme were necessary to build up the large number of new RDS. Most of these tests were performed with a complete prototype of the AERA124 station installed at the Radboud University in Nijmegen. In this section, three aspects of the system integration are discussed, namely the new solar power system, the electromagnetic compatibility (EMC) of the new electronics, and the wireless communication system.

2.5.1 Solar Power System

The power budget, i.e., the power consumption and the size of the solar power system is a crucial aspect for the design of self-sufficient detector stations. For AERA24, the requirements on the available power per station were formulated based on the combined power consumption of all individual units to be 20.4 W [121]. The size of the solar power system was planned based on simulations using different hardware combinations and considering the solar irradiation for the location of Malargüe, Argentina, calculated with the PVSYST software package [122]. In the final design, four 60 W solar panels and two 150 Ah batteries were installed.
Both, solar panels and batteries contribute significantly to the costs of an RDS. For larger scale arrays, the whole system should be cost optimized. Therefore, one of the design requirements for the new RDSs was to halve the size of the solar power system which in turn also means halving the power consumption. The simulations for AERA24 showed that the state-of-charge of the batteries should never be dropping below 40% during the whole year. To be able to resize the solar power system for AERA124, the design goal for the power consumption was set to 12 W encouraged by simulations. This load in combination with one 135 W solar panel and one 150 Ah battery were simulated and found to be sufficient to keep the battery at least 40% charged [123].
During tests with the prototype station, it turned out, that under normal conditions complete draining of the battery accrued leading to considerable downtime of the station. Therefore, a solar power test was performed with the goal to obtain the actual necessary solar irradiance to continuously operate the station given a constant load of 12 W and compare this to the expected minimum irradiance value at the AERA site. An overview of the values of the solar irradiance and the corresponding charge input during 42 days between the 21st of August and the 3rd of October 2012 is shown in figure 2.14 together with the average solar irradiance for the location of AERA during June of $3.7\,\mathrm{kW/m^2}$ [124] indicated by the vertical line (calculated for a panel with 50° inclination and including local cloud coverage). The solid line shown is a fit to the data in the interval $0-5\,\mathrm{kWh/m^2/d}$. The large fluctuations above that range were found to be caused by reaching a plateau in the charging state of the battery. From this, the minimum solar irradiance necessary to keep a steady-state charge level is $3.3\pm0.5\,\mathrm{kWh/m^2/d}$. Therefore the solar power system should be able to provide enough power to run a 12 W load continuously throughout the year, including a safety margin for periods of bad weather. Environmental conditions can however influence the situation. Dust and other dirt can decrease the performance of the solar panel and also the fences of the RDSs caste a slight shadow on the panel during some periods of the day. Low temperatures can decrease the capacity of the battery by 35% and also high temperatures influence the performance of the battery negatively. Even though the battery is explicitly made for deep discharging cycles, these have an impact on the lifetime. The used gel batteries are specified for a life time of 600 cycles of more than 50% discharging [125]. During the first 2 years of operation, the internally triggered stations have been found to stay in the provided power budget as expected from the simulations and the described tests.

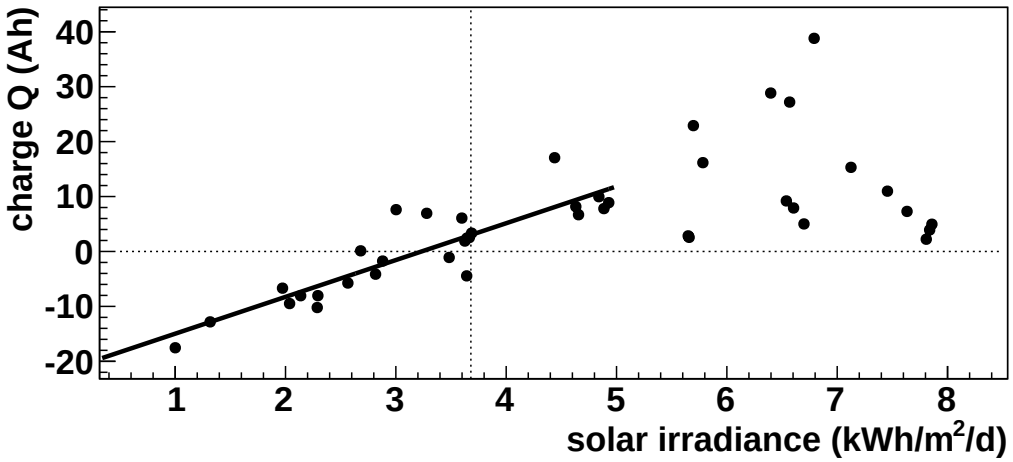

Figure 2.14: Charge input into the battery as a function of the solar irradiance. The horizontal line indicates a steady state and the vertical line indicates the average solar irradiance onto a surface with an inclination of 50° including modelled cloud coverage at the AERA site in June [124]. The fit to the data (solid line) is performed in the interval $0 - 5\,\mathrm{kWh/m^2/d}$.

For the externally triggered stations, the power consumption is slightly higher and a small amount of power related downtime has been experienced for these stations. The status of the batteries is continuously monitored for all RDS.

2.5.2 Radio Frequency Interference Tests

For AERA124, improvements on several parts were made changing the appearance of the RDS. Regarding these changes, the EMC of the AERA124 station had to be checked before commissioning. Similar tests were performed for the AERA24 station [126] and their results are taken as reference. During these tests, the monitoring hardware was found to produce a significant amount of RFI and was therefore disabled for later station operation. The resulting spectrum taken for the AERA24 station is shown in figure 2.15. In contrast to those tests, where just the electronics in the compartment were tested, it was now possible to assemble the complete AERA124 reference station inside the EMC chamber. This leads to a complete measurement of the emission produced by the station and allows to check to which amount the station picks up its own emissions.

Test Setup

The tests were performed in the ASTRON EMC test facility[2], which is a Faraday-chamber certified for measurements of full anechoic conducted immunity in the frequency range of

[2] www.astron.nl/r-d-laboratory/competence-and-support-groups/technical-support/rf-and-emc-test-facility/emc-test-fac

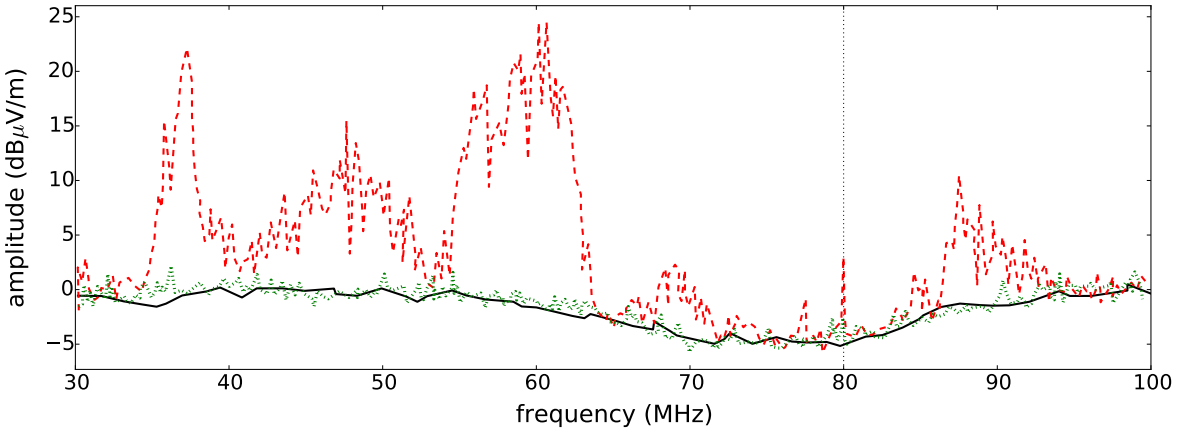

Figure 2.15: Measurement of the RFI emission of the AERA24 station tested at ASTRON in 2010. The noise floor (solid black), the station emission with monitoring (dashed red) and the situation with disabled monitoring (doted green) are shown in the $30 - 100\,\mathrm{MHz}$ range. Figure adapted from [126].

$150\,\mathrm{KHz} - 230\,\mathrm{MHZ}$ and full anechoic radiated immunity in the frequency range of $30\,\mathrm{MHz} - 3\,\mathrm{GHZ}$. The test object can be screened with a vertically aligned combination Yagi-bowtie antenna (Schwarzbeck biconilog VULB-9163), which is connected to a spectrum analyzer (Agilent Type E7405A). The setup acquires data during a sweep over the frequencies of 8.34 s.
For the tests, the complete station was mounted inside the test chamber, which included the Butterfly antenna, the main pole, the electronics compartment, the solar panel, the battery, the Wi-Fi grid antenna, two scintillators, the charge controller, and the digitizer together with all cables and the GPS antenna, see figure 2.16. The station was powered by the internal battery and connected to the DAQ system running outside the chamber via the build-in wireless communication module (Ubiquiti Bullet M5, see section 2.4.6). First, a Bullet inside the digitizer was connected to another one outside via an attenuated coaxial-cable. Later on, a point-to-point wireless link was established to check the emission of the communication hardware, see figure 2.16 (right).
Furthermore, it was checked whether activity in the solar panel as well as in the charge controller leads to emission. Therefore, a 500 W halogen light was placed in the chamber, illuminating the solar panel. This way, about 2 W electrical power were introduced into the system by the halogen lamp leading to the requested activity.

Tests and Results

To fully identify emitting parts and to characterize the circumstances under which RFI radiation is visible, the elements of the station were individually powered on. For some of the measurements, amplitude traces were acquired with the digitizer in addition to the taken spectra. This allows to check whether the emitted radiation is picked up by the station again. Furthermore, data traffic was generated on the connection between the components (e.g., RS232,

Figure 2.16: Test setup of the AERA124 EMC test in the Faraday-chamber at ASTRON. The whole station was set up inside the chamber (left). In addition, a halogen lamp illuminated the solar panel, and a wireless link was established for data transfer (right).

wireless link), as cables and connectors were found to be a substantial noise source for the AERA24 setup. The individual components were powered and tested one after another and the detailed results of these test can be found in [97].

In summary, none of the components was found to significantly emit radiation in the AERA frequency range from $30-80\,\mathrm{MHz}$. The internally triggered digitizers were found to show minor emission at 40 MHz of about $5\,\mathrm{dB}\mu\mathrm{V/m}$ above the baseline. The corresponding spectrum is given in figure 2.17 and represents the final emission of a fully running station equipped with an internally-triggered digitizer and two scintillator modules. As the 40 MHz emission lies in the region of interest, it was checked whether the radio station picks up the radiation coming from inside the digitizer itself. Therefore, traces were acquired with the digitizer and analysed in addition to the externally measured spectra. The resulting averaged frequency spectra of 1100 traces for all channels are shown in figure 2.18. Channel 1 and 2 are connected to the antennas, channel 3 and 4 are connected to one of the scintillator modules each. As expected, the two radio channels show the shape of the bandpass filter between $30-80\,\mathrm{MHz}$ in the noise floor whereas the two scintillator channels do not. Noticeable in all channels are the amplitudes at 40 MHz and 80 MHz. As the scintillator channels were connected to the PMTs via shielded cables, the emission is most likely picked up in the digitizer itself. In further tests with terminated signal inputs, it was discovered that the noise is picked up partly on the board. Even though the emission is pronounced in this test, it is only a problem if it has an amplitude

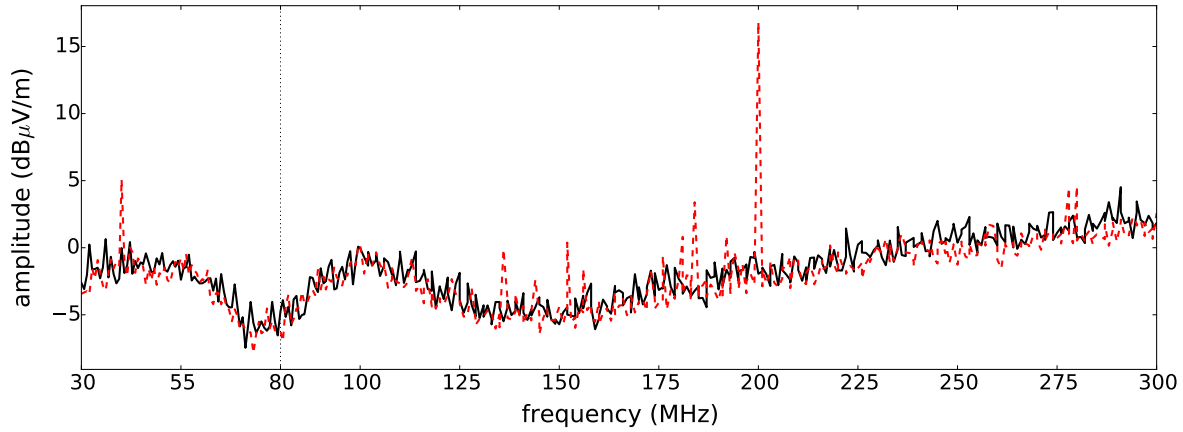

Figure 2.17: Result of the emission measurement of the final setup configuration with an internally triggering digitizer. In this measurement, all functionalities of the station were running and a wireless link for communication was established inside the Faraday chamber. The dashed red line represents the measurement of the emission of the station, the solid black line represents the noise floor baseline of the Faraday Chamber.

above the background noise level in the field. In figure 2.19, averaged spectra acquired at the AERA site with the stations equipped with an internally-triggered digitizer are shown. The corresponding traces were taken shortly after the AERA124 deployment. The lines at 40 MHz and 80 MHz are buried in the background noise. After zooming in, the emission at 80 MHz becomes barely visible. Compared to the amplitudes of background noise in other frequencies, it is negligibly small. The positions right at the edge of our range of interest makes them even less problematic.
In addition to the single-part test and the full-setup test with the internally triggered digitizer, a full-setup test was performed with the externally triggered digitizer as well. For this, the two scintillators were taken out of the system and the externally triggered digitizer was put into the Faraday cage inside of the electronics compartment. There are no major emission lines visible in the taken spectra shown in figure 2.20. At 40 MHz and 80 MHz, minimal peaks are present. Similar to the previews measurement, traces were taken with the complete with the digitizer which do not show self-induced noise.

Electromagnetic Compatibility Statement

The measurements show that a comparable or even lower level of emission is achieved with the new layout compared to AERA24. As the former results can be taken as a reference for the AERA124 station, the measured level of RFI emission is acceptable. The biggest improvement was made in shielding the monitoring hardware to read out currents, voltages, and temperatures from the charge controller. Summarizing the performed tests and the obtained spectra, no broad emission arises from any version of the digitizer in the range of interest of $30 - 80\,\mathrm{MHz}$. The station equipped with the internally triggered digitizer shows emissions at 40 MHz in the

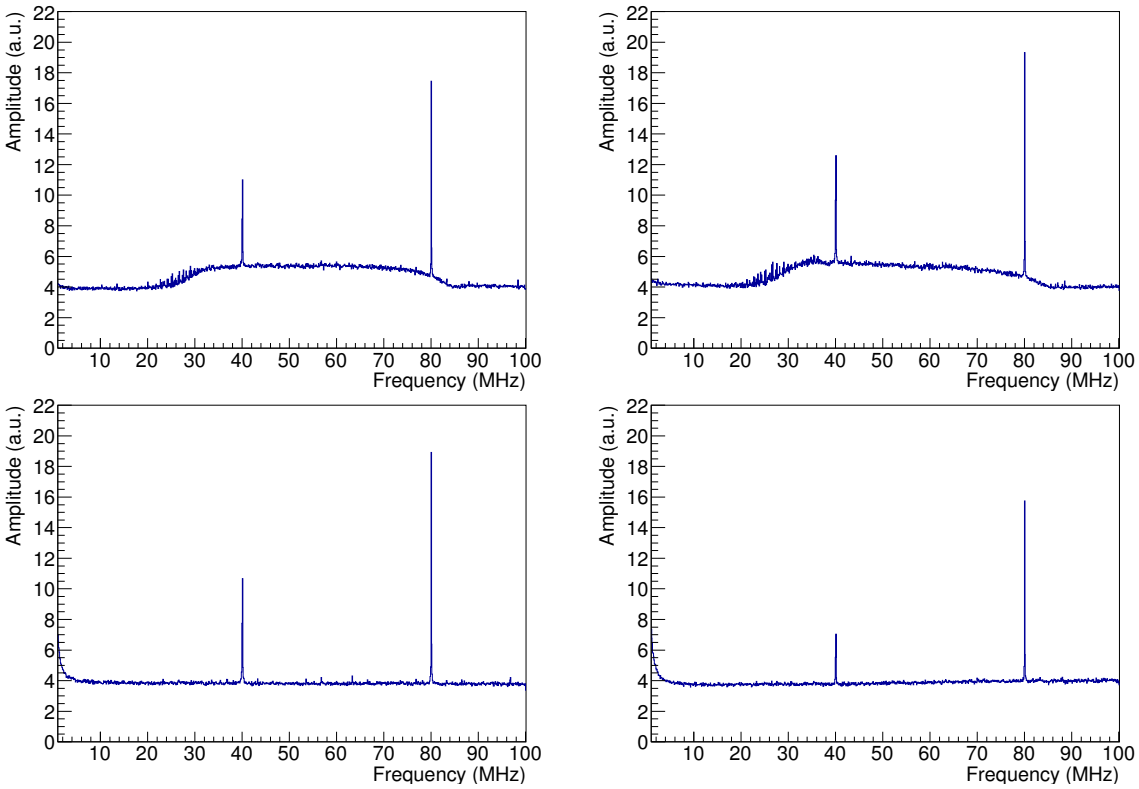

Figure 2.18: Averaged frequency spectra (1100 time traces) of the radio channels (top) and the scintillator channels (bottom) taken during the final full-setup test inside the Faraday chamber with the internally triggered digitizer. For the radio channels, the bandpass filter is imprinted in the spectrum.

recorded spectrum. Internally, 40 MHz and 80 MHz are visible in the recorded traces and are most likely generated by the internal clock of the FPGA. They are almost completely disappearing in the noise floor for measurements in the field. No influence on the emission was found by neither the wireless communication module nor the two scintillators.
The same conclusion holds true for the setup running with the externally triggered digitizer. There, emissions at frequencies of 40 MHz and 180 MHz are minimally visible in the recorded spectra. The traces recorded internally with the digitizer itself do not show an increased amplitude at 40 MHz. Here, the proper functioning of the Faraday-cage is crucial.

2.5.3 Tests of the Wireless Communication System

The Ubiquity wireless hardware has been tested in Europe and at the AERA site for about a year during AERA24 operation. The goal was the verification of the performance in terms of data throughput, power consumption, general reliability and project feasibility. The bandwidth requirements were based on the upscaled data rates of AERA24 and estimated to be 200 kbps/RDS. The maximum power budget was demanded to be $2 - 3\,\mathrm{W}$ for the wireless subscriber unit. Regarding reliability, an uptime fraction off 100% without maintenance was desired. A detailed description of the requirements and tests can be found in [120]. There, the

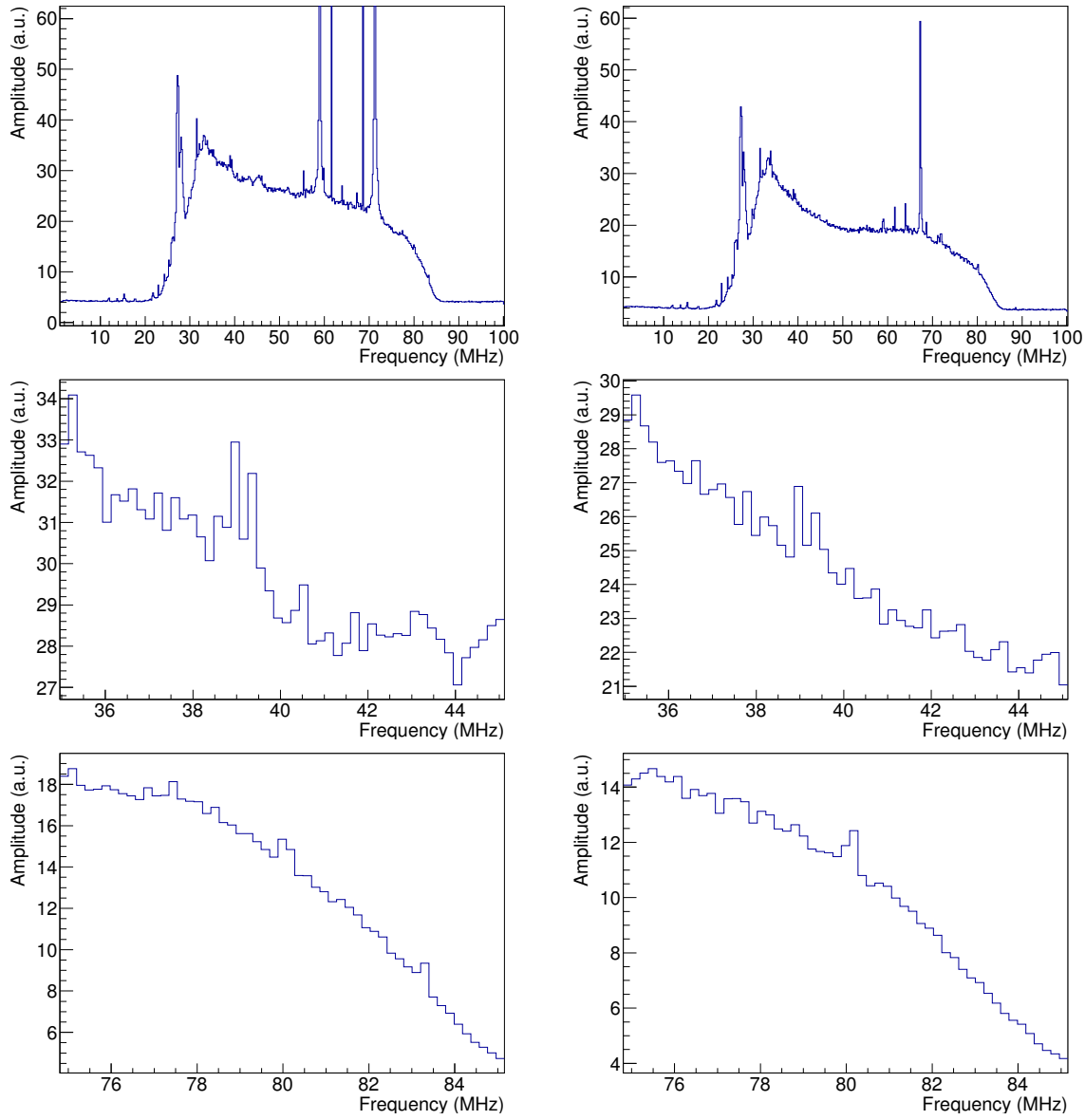

Figure 2.19: Averaged frequency spectra (1294 time traces) of the radio channels (Ch 1 and Ch 2) taken with the AERA124 stations after the deployment in the AERA field (top). Underneath are close-up views of the frequency ranges around 40 MHz and 80 MHz.

hardware was evaluated positively under the given requirements performing the tests with a 30 dBi Poynting K-GRID-003-06 antenna. As this antenna is rather heavy and expensive, Kelley already proposed to use a 27 dBi L-COM HG5827EG antenna [120]. From his link budget calculations, 27 dBi is the minimum gain of the antenna needed for AERA124. Therefore, two of the tests were repeated with the smaller antenna in Europe, as described in the following.
As a test base station, a Ubiquity Rocket M5 connected to an Airmax Sector 5G-90-20 antenna was set up at the Radboud University in Nijmegen. The height of the installation was approximately 90 m above ground and due to the flat landscape it was visible from relatively large distances. For the first test link, a Ubiquity Bullet M5 connected to a 27 dBi L-COM HG5827EG

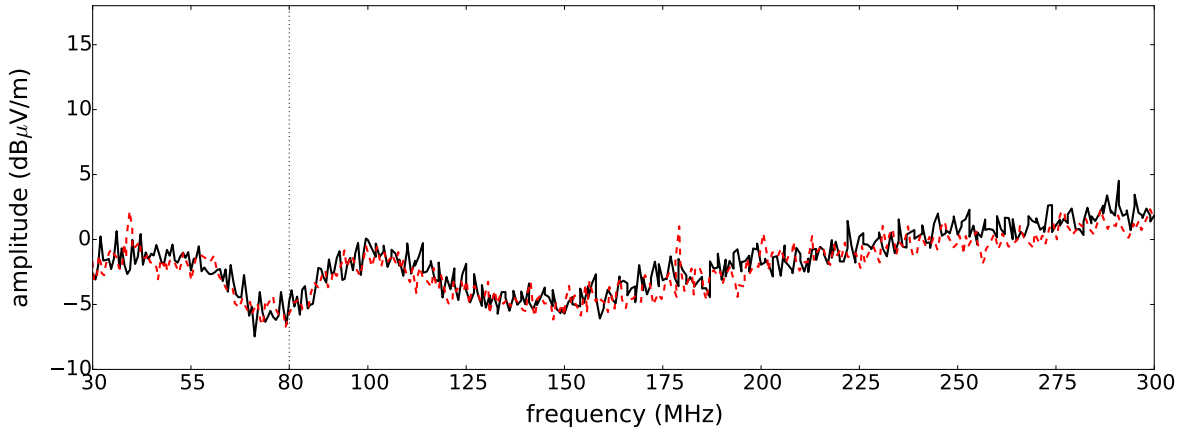

Figure 2.20: Result of the emission measurement of the final setup configuration with the externally triggered digitizer. In this measurement, all functionalities of the station were running and a wireless link for communication was installed inside the Faraday chamber. The dashed red line represents the measurement of the emission of the station, the solid black line represents the noise floor baseline of the Faraday chamber.

antenna via a 3 m TWS-400UF cable and a lightning protector (L-COM AL6-NFNFBW-9) was used. The device was connected to a laptop and powered via a power-over-Ethernet injector. The distance between the first test location and the base station was 2.4 km. The line of sight is outside of the main lobe of the gain pattern of the sector antenna as shown in figure 2.21 (short path, green squares). For this small distance, the smaller antenna gain is not an issue. The situation of smaller distances and directions outside of the nominal main lobe of the sector antenna is interesting to consider as the positive test increases the possible layouts for the connections at the AERA site. The transmission rate was tested via a build-in network speed test program. The reached transmission rate was 64 Mbps, while a signal-to-noise ratio of 30 dB and a link quality of 99% was measured.
For the second test link, the same test setup was used. A location close to the one used for earlier tests with the 30 dBi antenna was chosen which is 10.3 km away from the base station, see figure 2.21 (long path, marked violet). Here, the line of sight falls into the maximum of the gain pattern of the sector antenna. In this case, the transmission rate was 5.8 Mbps, while a signal-to-noise ratio of 13 dB and a link quality of 99% was measured. The power consumption was monitored during this measurement and had a value of 4.2 W at the maximum data transmission rate. The rates are significantly lower than for the larger grid antenna (TX speed: 74 Mbps at 10.7 km), however the performance is sufficient for the use at the AERA site with a modified link layout with four APs. By limiting the maximum distance between RDSs and access points to 6 km, as well as the total number of RDSs subscribed to one AP to 65, a sufficient bandwidth can be provided (only 50 kbps/RDS are necessary for AERA153 at the moment). Thereby, the advantages of the smaller and cheaper antenna concerning the wind load and deployment out-range the limited performance.

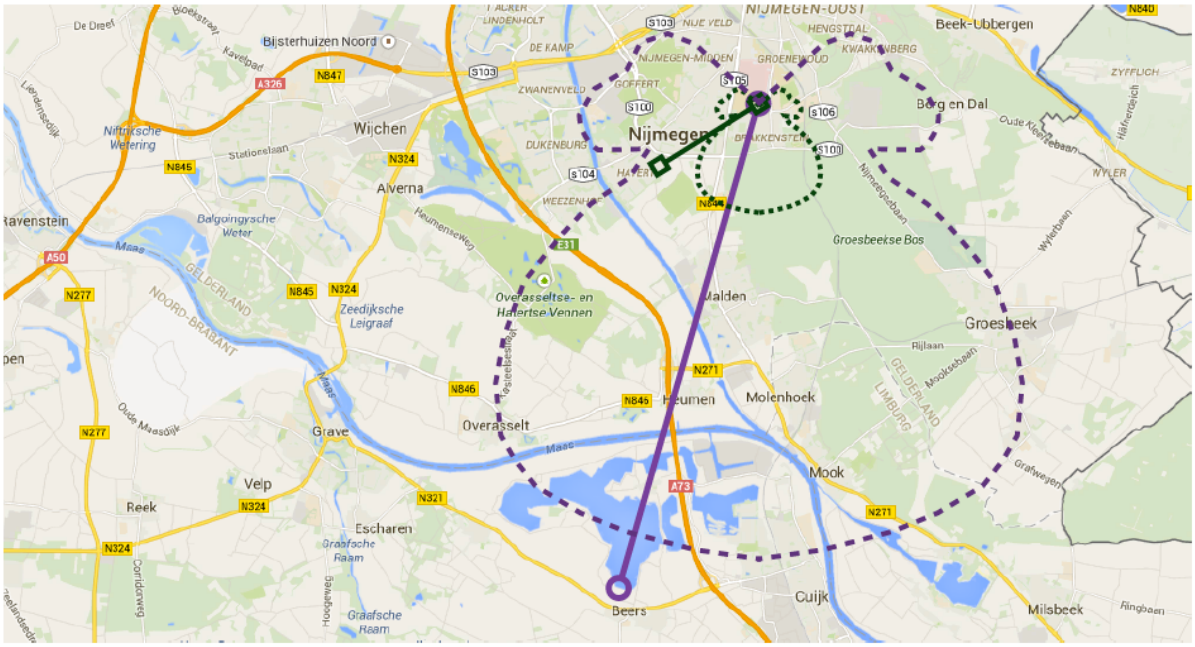

Figure 2.21: Indication of the two wireless test links. The short link (marked green) had a range of 2.4 km from Nijmegen Heyendaal to Nijmegen Hatert. The long link (marked violet) had a range of 10.3 km from Nijmegen Heyendaal to Beers. The two line of sights are plotted as solid lines. In addition, the gain pattern of the sector antenna at the base station is indicated by the dashed lines (for better readability the pattern is sketched in two sizes).

3

Data Acquisition and Hybrid Shower Reconstruction

Depending on the type of hardware and thereby the possible types of triggers, the radio data are acquired with two different systems. After acquisition, the radio data are merged with the data recorded by the other detectors of the Pierre Auger Observatory and reconstructed in a hybrid approach. Thereby, the reconstructed information from one detector can be used as input for the reconstruction of the data from the other detectors. The radio DAQ as well as the hybrid data reconstruction pipeline will be described in the following.

3.1 Background for Radio Air Shower Detection

The impact of broad- and narrowband noise differs for the specific steps in the acquisition and reconstruction pipeline. The overall noise floor for these measurements is set by the radio emission of the Galactic plane. This changes over time when the Galactic Center moves over the sky. Additionally, the anthropogenic emission which increases the background further varies over time, depending on its origin. In case of a threshold crossing trigger, the variations in the emission require a flexible threshold which can be adjusted e.g., based on the RMS of the background. More challenging is the appearance of pulsed broadband noise which can have a similar characteristic compared to the radio pulses from extensive air showers. This pulsed RFI originate from various sorts of electrical equipment, e.g., generators, broken power line isolators or transformers. Therefore, most of the pulsed emission is produced close to the horizon and in case events are recosntructed with zenith angles close to 90° they can easily be rejected in offline analyses. More troublesome are RFI pulses detected in single stations in coincidence with pulses from air showers in other stations. Various techniques have been developed to reject RFI pulses already during data acquisition or if that is not possible during offline analysis. These techniques are discussed in the following section 3.2 and in chapter 6.

3.2 Triggering and Data Acquisition

In the spirit of AERA as an engineering array, data are acquired with various triggering strategies. Self-triggers, external-triggers, and internal particle-triggers, are used for air shower de-

tection. Furthermore periodic-, random-, and airplane-triggers are used to collect background and calibration data.

3.2.1 Self-Trigger

For stand-alone operation of a radio cosmic-ray observatory, a reliable trigger mechanism needs to be implemented based on the radio measurements themselves. In principle, a basic signal-over-threshold trigger can be employed. Due to the background of broad- and narrow-band noise, a more advanced trigger strategy is necessary to be able to pre-select triggered pulses. Otherwise, the high frequency with which pulsed background noise appears challenges the data handling capacities of the stations, the network, and the DAQ systems. For this selection, the voltage time series are online processed in the FPGA and additional trigger conditions are applied. In principle, both types of digitizers are able to perform self-triggered data recording. The exact conditions of an additional pre-selection however differ for the two systems. The digitizers without ring buffers mainly select pulses based on their shape which is realized by e.g., the number of crossings of a secondary threshold. All self-trigger conditions for this type of hardware are discussed in [127]. For the digitizers with a ring buffer, a similar procedure is implemented as described in [128]. Once a pulse is selected in the RDS, the GPS timestamp of the pulse is sent to the central DAQ. There, it is checked for coincident timestamps from other RDSs and if found, a multi-station event is formed. Hereby, at least three stations need to participate. For the RDSs operating without a ring buffer, an additional requirement came in action after the deployment of AERA124. Now, at least two internally triggered (on the scintillation counters) RDSs need to participate in every event. An exception are event candidates were more than 10 RDSs are triggered simultaneously. In the central DAQ of the RDSs with ring buffer a basic direction reconstruction of the wave front is performed. Based on the direction, a cut on the maximum zenith angle and a cone algorithm are used to veto RFI background. The cone algorithm vetos events when there are multiple pulses coming from the same direction in a certain time window [128]. This can for example be used to reject RFI originating from airplanes. Finally, the voltage time trace data are requested from the RDSs by the DAQ and written to disk for offline analysis. AERA24 has proven that air-shower detection in a self-trigger mode is possible. Also, there are methods to further discriminate miss-triggered RFI pulses in an offline analysis [129, 130, 131].

3.2.2 External-Trigger

External-triggers from the other detector systems of the Auger Observatory are still the main source of successfully reconstructed multi-station radio air showers. An advantage is that data are only written to disk when an air shower has been confirmed externally as the coincidence requirement lowers the probability of selecting random noise pulses. Thereby, the data rate is kept at a manageable level. This does however not mean that all externally triggered events

contain a radio signal. Also noise pulses can occur in coincidence with an EAS which need to be identified and rejected in offline analyses. One of the limitations of employing the SD or the FD as trigger source is the time needed for the trigger to be formed in CDAS and sent to AERA. This can take up to about 7 s in case of an FD trigger and is usually of the order of 3 s for an SD trigger. To be able to use a trigger which is received a couple of seconds after measuring the radio signal, large ring buffers are necessary to store the data in the meantime. After a trigger, the whole buffer is read out and saved to disk leading to large data volumes. A second limitation is the poor knowledge of the signal position within the radio voltage trace. This leads to rather long radio traces, as the signal region can only be roughly determined by the external timestamps. In an offline analysis, the radio signal needs to be identified in a relatively large window of sometimes μs length which is placed with respect to the externally reconstructed core position and arrival direction and their uncertainties. This increases the chance to pick a random coincident pulse in the signal window.
After an external trigger, it is not known in which of the RDSs a radio pulse was measured, and therefore all stations are read out. In case of AERA153, this means 107 RDSs with ring buffers are read out simultaneously for every trigger, where most of them only contain noise. This is challenging due to the large data-volumes created for every event. At the same time this situation offers an increase in information as also stations that measured no or a sub-threshold signal contain useful information for high-level analysis, e.g., concerning the radio LDF.

3.2.3 Internal Particle-Trigger

A slightly different approach which is also interesting for possible future stand-alone radio detector arrays is the employment of an internal particle trigger. It combines advantages of external- and self-triggering, and allows self-sufficient and clear identification of the radio pulses associated with an EAS. Therefore, scintillation counters are designed as an integrated part of the radio stations and the particle detection on station level can directly trigger the radio DAQ of the station. Furthermore, the trigger time is very close to the time of the expected radio pulse in this station giving strong constrains on the radio signal-window. By triggering the stations individually, it is also not necessary to read out the whole radio array for every trigger. Details about the scintillation counters, the trigger settings, and the relative trigger efficiency are given in chapter 4.
As the internal particle-trigger also works on station level, a similar multi-stage trigger scheme is used as for self-triggering RDSs. After a particle detection in the scintillation counters, a time stamp is sent to the DAQ and there a search for coincidences is performed and if a multi-station event is found, the data are requested. The similarity between internal particle-trigger and self-trigger allows a combination of both to form a multi-station event. This is advantageous for air-shower detection without being dependent on the efficiency of non-radio detectors (e.g., the SD or the scintillation counters).

3.2.4 Periodic-, Random-, and Airplane-Triggers

Calibration and monitoring of the performance of AERA are important topics for the operation of the array. Furthermore, a realistic background library is extremely valuable for simulation studies. These aspects are addressed by using data acquired with special trigger settings. On periodic triggers, the full voltage time-trace data are requested from all RDSs every 100 s (every 10 s till July 2014). The data can be used as noise for simulations, allowing for studies with realistic background conditions. In case measured showers are simulated, noise traces are available from within 50 s around the time of the measured shower. The periodic data are also used for background studies. As the background is dominated by the Galactic emission, the amplitude levels of this background are used to relatively calibrate the stations among each other [61]. For random triggers, a station sending a GPS timestamp to the DAQ is chosen to send the time-trace data based on a trigger counter. For the internally triggered RDSs every 40000^{th} timestamp is selected by the random-trigger, for the RDSs equipped with a ring buffer it is every 999^{th} timestamp. In principle, commercial aircraft flying over the array often emit RFI and have to be seen as background sources. However, their emission can also be used for a timing calibration. To record this data in self-trigger mode, the cone algorithm is deactivated for a region of 5° around the position on the sky where the aircraft is located. This position is inferred from information broadcast by the aircraft as part of the ADS-B information [132]. In addition to these automatic triggers a manual-trigger can be invoked to request data at any time.

3.2.5 Data Handling and Merging

The data acquired with AERA are written to disk as binary files. To allow more flexibility, these binary data are converted in a following step to a ROOT-based file format [133, 134]. During the conversion it is possible to separate the different data streams based on the trigger flags. This allows for example to split up the files used for monitoring purposes or the airplane data and handle these files separately.

The data of every detector component of the Pierre Auger Observatory are written to individual ROOT-based raw files. For the SD and the FD, these raw files are merged directly in CDAS to a combined hybrid file on a daily basis. In the next step the hybrid files can be combined with the data from the AMIGA muon counters. The AERA data are merged with this SD-FD-AMIGA files, but they can also be merged with all individual detector raw files separately, e.g., to SD-radio hybrid files. For events where one or more of the detectors did not trigger, no information of the corresponding detector system is merged. The exact conditions of merging radio data depend on the DAQ these data were acquired with. The AERA data acquired with the DAQ system in Coihueco, including all stations with ring buffers, is directly merged at the FD site. The AERA data acquired with the DAQ system at the CRS is so far transferred to Europe and merged there. In the near future, the two radio DAQ systems will be combined

together in Coihueco.
For cosmic-ray data analysis daily multi-hybrid files (RD-SD-FD-AMIGA) are produced for the time from noon to noon of the next day. Thereby, the data of the nightly FD observations are contained in one file.

3.3 Shower Reconstruction Software Framework

The data of all detector systems at the Pierre Auger Observatory are processed with the software framework $\overline{\text{Off}}\underline{\text{line}}$ [102]. It was originally designed for (hybrid) reconstruction of the SD and the FD data and/or corresponding air shower simulations. The framework is structured in three separate parts. One part are the *event data* which contain the recorded raw data or the simulation output, respectively. During the reconstruction the data are processed and reconstructed information as well as results are added to the event data. The second part is the *detector description* which contains information about the detector configuration and performance at any given time of operation. This also includes calibration data as well as atmospheric monitoring data. The third part of the framework is the sequence of *analysis modules* which contain all the algorithms needed during the whole reconstruction procedure. In general, it links the event data and the detector description. Within the modules, information from the event data can be requested. For individual events, the detector description is used to infer the corresponding detector configuration, and reconstruct intermediate or final quantities of interest. These values are then also added to the event data. Modules cannot communicate with each other, which limits inter-module dependencies. The event data and the detector description differ conceptionally from each other. One allows read and write access from the modules and accommodation of reconstructed values on an event-by-event basis. The other is a read-only description of the detector. A schematic overview of the $\overline{\text{Off}}\underline{\text{line}}$ framework is shown in figure 3.1.

3.4 Baseline Detector Shower Reconstruction

During the hybrid reconstruction of the SD and the FD data, the SD information is processed independently of the FD information. The FD event reconstruction however relies on timing information of at least one SD station to reconstruct the shower geometry. A hybrid shower where the data from both detectors were reconstructable is displayed in figure 3.2. The reconstruction methods for both measurements are described in the following sections.

3.4.1 Surface Detector Array

The reconstruction of air-shower parameters from the measurements of the SD are based on the recorded signal traces from the PMTs in the SD stations. The information from the PMTs

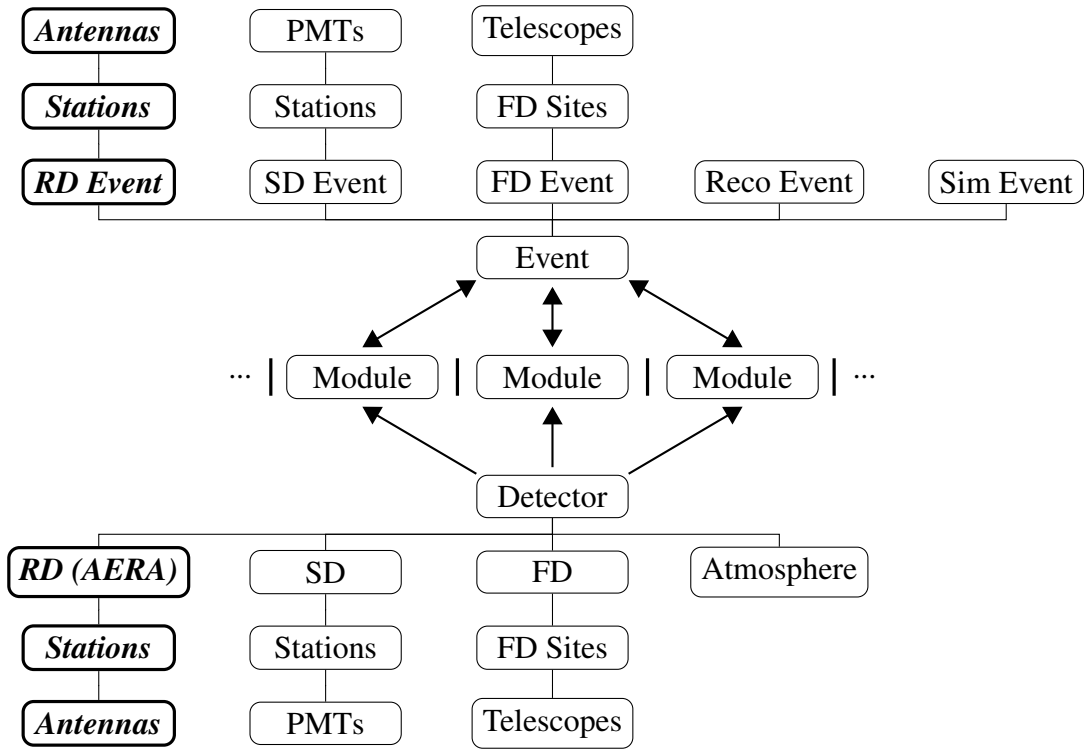

Figure 3.1: Structure of the $\overline{\text{Off}}\underline{\text{line}}$ framework. See text for details. Figure adapted from [135].

is combined to obtain the signal time as well as the signal size in vertical equivalent muon (VEM) per station. At the beginning of the reconstruction, quality criteria are checked in addition to the trigger requirements already presented in section 2.1. Here a stricter selection on the station timing is made to reject random stations which were triggered by muons not related to the air shower. Furthermore, only showers for which the ground impact point of the shower axis (shower core) is contained in the detector array are considered for highest level analysis. This is enforced by requiring that the detector station with the highest signal was surrounded by a hexagon of active detector stations at the time of the air shower (6T5 trigger). The arrival direction of the air shower can be reconstructed by fitting a wavefront model to the signal start times in the detector stations t_i. The most basic model is a plane wave front. This is e.g., used in case of low station multiplicity showers. The direction is then found by minimizing

$$\chi^2 = \sum_i \frac{[t_i - t(\vec{x}_i)]^2}{\sigma_{t_i}^2}, \tag{3.1}$$

where $\vec{x}_i$ are the detector positions, t_i and σ_{t_i} are the measured time and its uncertainty, and $t(\vec{x}_i)$ is the calculated time at position $\vec{x}_i$. For higher station multiplicity, the wavefront is approximated with an inflating sphere model as

$$c(t_i - t_0) = |\vec{x}_{\text{sh}} - \vec{x}_i|, \tag{3.2}$$

where $\vec{x}_{\text{sh}}$ and t_0 are a virtual origin and start time for the air shower development [29]. A sketch of the underlying model is shown in figure 3.3 (left) together with a measured footprint

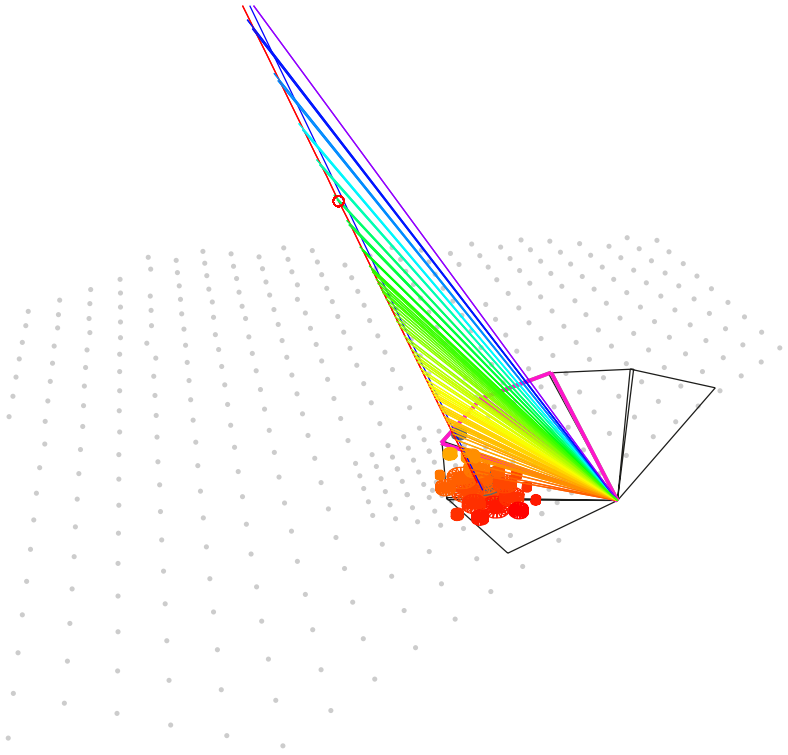

Figure 3.2: Hybrid shower geometry display, combing the measurements of the particle footprint on the ground with the observed longitudinal shower-profile. The signal times in the particle detectors are indicated by color (yellow = early, red = late) and the time distribution of the pulses in the FD pixels are indicated as lines to their emission region (purple = early, red = late). The triangles indicate the FOV of the individual FD telescopes and the gray dots indicate non-triggered SD stations. The circle on the reconstructed shower axis is the position of X_{max}.

where the timing distribution of the stations and the reconstructed direction is shown (right). The core position as well as the energy of the shower are inferred from fitting a modified NKG-function to the measured signals projected onto the shower plane. The LDF used for the SD reconstruction is a simplified version of equation 1.23,

$$S(r) = S(r_{\mathrm{opt}}) \left(\frac{r}{r_{\mathrm{opt}}} \right)^{\beta} \left(\frac{r + r_1}{r_{\mathrm{opt}} + r_1} \right)^{\beta+\gamma} . \tag{3.3}$$

Here, r_{opt} is the optimum distance, r_1 is a constant, $S(r_{\mathrm{opt}})$ is a fitted scaling parameter, and β and γ are shape parameters. The optimum distance is the distance from the shower axis at which $S(r_{\mathrm{opt}})$ on average shows the smallest sensitivity to the shower geometry and the shower development. This is important as the value of $S(r_{\mathrm{opt}})$ is also directly related to the energy and is used as an energy estimator. The values for r_{opt} and r_1 depend on the spacing of the detector stations. For the regular 1500 m grid the values are $r_{\mathrm{opt}} = 1000\,\mathrm{m}$ and $r_1 = 700\,\mathrm{m}$. For the Infill array the optimum distance is smaller, $r_{\mathrm{opt}} = 450\,\mathrm{m}$. The exponents can only be fitted if the station multiplicity is large enough to support the number of free parameters. Otherwise, parametrized values are used as $\beta = 0.9\mathrm{sec}(\theta) - 3.3$ and $\gamma = 0$, where θ is the zenith angle

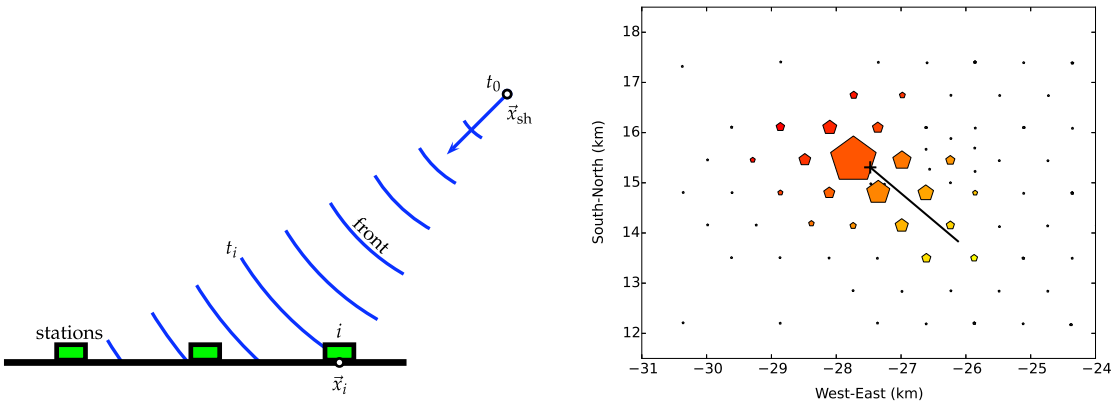

Figure 3.3: Direction reconstruction based on signal timing. Left: Sketch of the shower front model in the reconstruction of the direction of the air shower axis. See text for details. Figure taken from [29]. Right: Particle footprint of an air shower. The signal timing is indicated by the color coding (yellow = early, red = late). The size of the pentagons represents the measured signal size. The black cross and the black line represent the core position and the reconstructed azimuthal direction.

of the shower [136]. A display of the fitted lateral distribution of an air shower detected with the Infill array is shown in figure 1.10. Depending on the station multiplicity, the geometry of the shower can be reconstructed with an average uncertainty of 50 m for the core position [137]. The resolution on the reconstructed incoming direction depends on the number of signal stations and is 1.6° for showers detected with 3 stations and 0.9° for showers detected with more than 5 stations [29]. A complete description of the reconstruction of showers measured with the SD is given in [136].

3.4.2 Fluorescence Detector

For the reconstruction of the Fluorescence Detector data, first the ADC traces of all pixels of a camera are corrected for the background and then converted to photons at the aperture. In case multiple telescopes were triggered hosted at one FD site, the reconstructed data at the telescope level are merged to form a combined pixel array. The arrival times of the photons as a function of the viewing angle are combined with the timing of the highest-signal SD station to reconstruct the plane containing the shower axis and the FD telescope (visualized by the colored lines in figure 3.2). There is also work in progress to replace the SD station input with e.g., information from a RDS. An air-shower image as seen with two combined FD cameras is shown in figure 3.4. With the geometry information, every time bin in the recorded traces can be projected onto a segment of the shower axis. A segment in turn corresponds to a certain height and a certain atmospheric depth. The depth is inferred from the integration over the atmospheric density profile for the given direction. This allows to reconstruct the amount of light emitted along the shower axis from the number of photons at the aperture. The re-

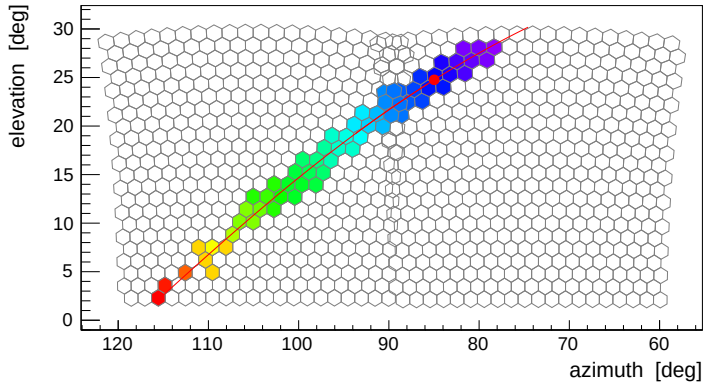

Figure 3.4: Combined camera image of an air shower detected by two of the Coihueco fluorescence telescopes. The color indicates the time distribution of the pulses in the shown pixels (purple = early, red = late). The line indicates the reconstructed plane spanned by the shower axis and the fluorescence telescopes.

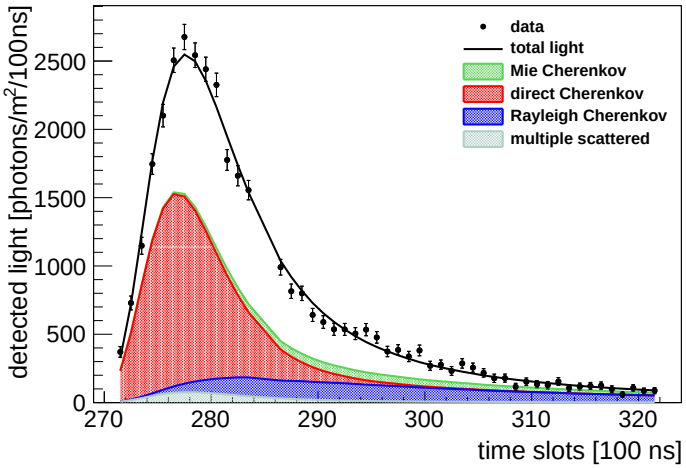

Figure 3.5: Reconstructed contributions of (scattered) fluorescence and Cherenkov light to the total amount of light detected. The displayed air shower is the same as shown in figure 1.10.

construction includes the response of the optical system as well as propagation losses due to Mie- and Rayleigh-scattering in the atmosphere. These corrections are based on the detailed calibration measurements of the atmosphere as well as of the detector system discussed in section 2.2. Depending on the geometry, a part of the detected photons is not originating from the fluorescence process, but from the Cherenkov radiation produced by the high-energetic air-shower particles. The two contributions are disentangled and handled independently [86]. An example of the detected light for a measured air shower including the different contributions can be seen in figure 3.5. The number of electrons and positrons in the air shower is proportional to the energy deposit in the atmosphere which is fitted by the Gaisser-Hillas function (equation 1.24). Similar to the procedure for the fit of the NGK-function to the SD data, the two shape parameters X_0 and λ are fixed for the reconstruction of air showers where a

four parameter fit to the longitudinal profile is not applicable (depending on the observed track length and the number of photons). For the Fluorescence Detector, these parameters are taken as the average values of detected air showers for which a four parameter fit was successfully performed. The values are $\langle X_0 \rangle = -121\,\mathrm{g/cm^2}$ and $\langle \lambda \rangle = 61\,\mathrm{g/cm^2}$.
In case telescopes at the Coihueco FD site are triggered in coincidence with telescopes of the HEAT extension, the data from both sites are reconstructed separately as well as in a combined approach.
The calorimetric energy (and from that the cosmic-ray energy) and the depth of shower maximum is obtained for the Gaisser-Hillas fit as discussed in section 1.2.5. The resolution on $X_{\max}$ is energy dependent and ranges from 30 g/cm^2 at 10^{17} eV to 15 g/cm^2 at 10^{20} eV [138, 139]. The energy resolution is discussed in the following section. The description of the FD reconstruction presented here is following [139].

3.4.3 FD-SD Energy Calibration with Hybrid Showers

The SD air shower reconstruction works independently from the FD reconstruction which needs a signal in one SD station and runs thereby in hybrid mode by default. A special category of high-quality hybrid showers where the measurements of both detectors fulfil certain quality criteria are called *golden events*. These quality cuts are e.g., applied on the fiducial FOV to ensure an equal trigger probability of both detectors independently of the primary particle. The golden events are used for a cross calibration between the two detector systems. Here, an additional criterion is a minimum energy reconstructed by the FD of $3 \times 10^{18}\,\mathrm{eV}$ for the calibration of the regular SD. In the following, the energy calibration of the Surface Detector array will be discussed briefly.
The values of $S(r_{\mathrm{opt}})$ are used as an energy estimator from the SD. The values of $S(r_{\mathrm{opt}})$ however show a strong zenith-angle dependency. A larger zenith angle corresponds to a longer development of the air shower in the atmosphere and therefore a larger attenuation of the shower particles. Additionally, there is an impact of the track length of the particles in the SD stations which also depends on the zenith angle. Both effects need to be corrected out during reconstruction. This can be done under the assumption that the total flux of cosmic rays at the top of the atmosphere is constant. The corrected values S_{38} (S_{35} for the Infill) for a specific shower can be seen as the value $S(r_{\mathrm{opt}})$ for the case that the shower axis would have had a zenith angle of 38° (35°). This corrected energy estimator is directly calibrated against the energy determined with the Fluorescence Detector. The calibration plots for both, the regular Surface Detector array and the Infill array are shown in figure 3.6. The data are fitted with a power law

$$E = A \cdot (S_{3\mathrm{x}})^B \tag{3.4}$$

and the fit values are given in table 3.1. The correlations between the energy measured by the FD and the energy estimators for the SD and the Infill array are almost linear. The resolution

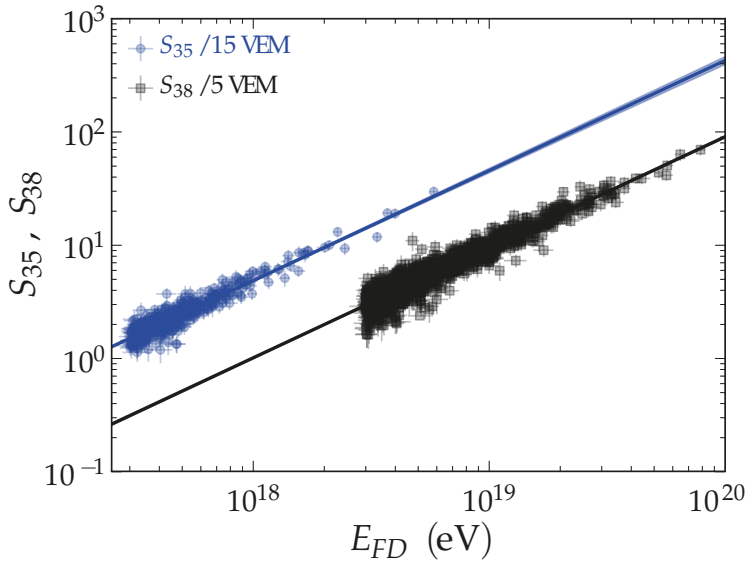

Figure 3.6: Calibration of the energy indicators S_{38} and S_{35} against the FD energy measurement. For the S_{38} calibration a minimum energy of 3×10^{18} eV is required leading to the sharp lower energy cut-off. Figure adapted from [140].

Table 3.1: Parameters of the energy calibration of the SD and the Infill array against the FD. Table adapted from [140].

detector	SD (S_{38})	Infill (S_{35})
A (EeV)	0.190 ± 0.005	$(1.21 \pm 0.007) \cdot 10^{-2}$
B	1.025 ± 0.007	1.03 ± 0.02
$E_{threshold}$ (eV)	3×10^{18}	3×10^{17}
dataset	01/2004-12/2012	08/2008-12/2012

of the FD energy determination is 7.6%. The systematic uncertainty is 16% at $10^{17.5}$ eV and decreases to 14% at 10^{18} eV and above [29, 103, 140]. The resolution of the SD energy measurements depend on the energy of the cosmic ray ranging from 22% at 10^{17} eV over 16% at 3×10^{18} eV to 12% at the highest energies and shows an additional direction dependence. The systematic uncertainty of the SD energy reconstruction is inherited from the FD reconstruction.

3.5 Radio Air Shower Reconstruction

For the reconstruction of the radio data recorded with AERA, the $\overline{\text{Off}}\underline{\text{line}}$ framework was extended to integrate the radio part in a multi-hybrid reconstruction procedure together with the SD and the FD (and their extensions) reconstruction and to make use of functionalities specifically interesting for the radio reconstruction [135]. These functionalities for example include operations on the recorded data in the frequency domain. The general structure is adapted from the SD, where the class for a Surface Detector station corresponds to the one for

a radio station and the class for the PMT signals corresponds to the one for the radio channels. The same holds true for the structure of the detector description which is similar to the one of the SD. The actually performed reconstruction can strongly depend on the planned analyses. A general description of the reconstruction steps on channel, station, and event level is given in the following. The standard multi-purpose reconstruction sequence used for AERA, the RdObserver, is described subsequently.

3.5.1 Radio Detector Description

To unfold the detector response from the measured data, every component in the signal chain needs to be corrected for. The values for the channel corrections as well as for the antenna pattern are available in the detector description. The responses of all individual components in the signal chain apart from the antenna and the LNA were measured in the laboratory before deployment. A time dependent detector description was introduced to the $\overline{\text{Off}}\underline{\text{line}}$ framework for AERA. The information is stored in a database and retrieved during run-time of the reconstruction. In addition, information about the status of the hardware and environmental conditions is stored in a separate database.

3.5.2 Initialisation

The first step in the radio reconstruction procedure is the initialization of the event. There, the shower-geometry source (SD, radio, simulation, etc.) and the signal and noise windows are set. Furthermore, the trigger source is read from the raw file and the events can be grouped according to this information.

3.5.3 Antenna Channel Level

The radio *channels* contain the recorded data from each antenna in ADC counts. The ADC values are converted to a voltage. Depending on the hardware version, the RDSs acquire data with two or three channels (four in case of high and low gain channels). In the further description the situation for two channels is discussed as most of the RDSs of AERA have two active channels. If data were recorded for the low and high gain channels, the low gain channels are selected in case of saturation in one or both of the other two.
The voltage time traces still contain the imprint of the detector response which needs to be corrected for during the reconstruction. This is partly done on channel level where all characteristics of the hardware parts like cables, filters, and amplifiers are taken into account.
For AERA a Beacon is used for an accurate timing calibration of the individual stations. The necessary steps for this calibration during reconstruction are performed on the channel data, a detailed description of the procedure can be found in [31]. The emission lines of the Beacon are useful for calibration, nevertheless they are RFI in terms of the detection of cosmic rays.

To clean the spectrum concerning narrowband RFI sources the corresponding frequency amplitude bins can be set to zero. This also affects information about the signal. Another more accurate but also computationally more expensive cleaning method is to fit the contributions of the Beacon lines in the time traces [141]. This fit is performed on parts of the trace which do not contain the air-shower signal with a superposition of four sine waves. The resulting amplitudes can then be subtracted from the data. In case of strong narrowband RFI from other sources e.g., radio or TV stations, the sine-wave suppression is less applicable due to the modulation in frequency. In those cases, the frequency bins are set to zero. To reduce leakage effects in the frequency spectrum, a window function is applied to the traces. If desired, the channel traces can be up-sampled by padding zeros to the frequency spectrum outside of the physical filter range. This allows to determine the positions of features in the traces as e.g., the pulse maximum or the rise time of the pulse with a higher precision. The corrected and to voltage converted channel-traces, are used to reconstruct the electric field measured on the *station* level.

3.5.4 Station Level

The measured channel data and the incoming electric field are linked by the antenna of the RDS. For AERA, the two antennas are aligned in east-west and north-south direction and the corrected data of the two channels represent the product of the electric field vector in these directions and the vector effective length (VEL) of the antenna. The effective antenna length depends on the incoming direction of the radiation as well as the frequency. To reconstruct the electric-field vector from the channel data, the antenna response is unfolded. The unfolding procedure requires knowledge of the incoming direction of the radiation, as the antenna pattern is directional sensitive. For a known direction of propagation $\hat{\mathbf{e}}_n$ from a source at position (θ, ϕ) on a sphere, the incoming electromagnetic wave $\vec{E}(t)$ can be described by the two components $\hat{\mathbf{e}}_\theta$, $\hat{\mathbf{e}}_\phi$ perpendicular to $\hat{\mathbf{e}}_n$. This so called on-sky coordinate system is depicted in figure 3.7. The radiation has no component in the direction of propagation when the far field approximation applies. The time dependent electric-field vector is then given as

$$\vec{E}(t) = \hat{\mathbf{e}}_\theta E_\theta(t) + \hat{\mathbf{e}}_\phi E_\phi(t)\,. \tag{3.5}$$

The conversion from the electric field to the generated voltage at the antenna base is given by a multiplication with the Jones matrix [142]

$$\mathbf{J} = \begin{pmatrix} J_{\mathrm{NS},\theta} & J_{\mathrm{NS},\phi} \\ J_{\mathrm{EW},\theta} & J_{\mathrm{EW},\phi} \end{pmatrix}. \tag{3.6}$$

Here, the components give the complex responses of the antennas orientated in the East-West (EW) and North-South (NS) directions for linearly polarized radiation in the $\hat{\mathbf{e}}_\theta, \hat{\mathbf{e}}_\phi$ directions at a given frequency f taken from the VEL ($\vec{H}(\theta, \phi, f)$). To use this relation to unfold the

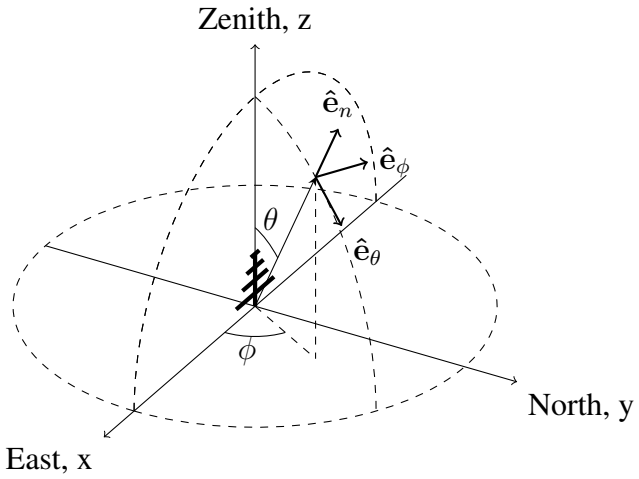

Figure 3.7: Geometry used for the reconstruction of the electric field from the measured voltage at the antenna bases. The on-sky coordinate system ($\hat{\mathbf{e}}_\theta, \hat{\mathbf{e}}_\phi, \hat{\mathbf{e}}_n$) allows to drop the $\hat{\mathbf{e}}_n$ component for the description of the incoming electromagnetic wave in the far field approximation. Additionally indicated is one of the two AERA antennas (East-West polarization).

antenna response, the channel data ($V_{\mathrm{NS}}, V_{\mathrm{EW}}$) are transformed to the frequency domain where the inverse Jones matrix is applied as

$$\begin{pmatrix} \hat{E}_\theta \\ \hat{E}_\phi \end{pmatrix} = \mathbf{J}^{-1} \begin{pmatrix} \hat{V}_{\mathrm{NS}} \\ \hat{V}_{\mathrm{EW}} \end{pmatrix}. \tag{3.7}$$

An inverse Fourier transformation results in the time dependent electric field vector of the incident wave $\vec{E}_{\theta,\phi,n}(t)$ which is then converted to the common coordinate system $\vec{E}_{x,y,z}(t)$. The antenna response is modelled with the software NEC2 [143]. The used model is generated according to the geometry of the RDS and ground effects are taken into account. The VEL is directly calculated by the software for excitation by a plane wave with a predefined polarization. An equivalent method is to simulate the antenna in transmission mode as in both cases the VEL is equivalent. This approach is used for the Butterfly antennas, where a sinusoidal current source is connected to the terminal of one of the two antennas and a load matching the input impedance of the LNA is connected to the terminal of the other antenna. The output of the simulation gives the electric field vector ($\vec{E}_{\mathrm{NEC}}(\theta, \phi, f)$) for a given frequency which can be converted to the VEL by

$$\vec{H}(\theta, \phi, f) = i \frac{2c}{I_t \nu f} \vec{E}_{\mathrm{NEC}}(\theta, \phi, f)\,. \tag{3.8}$$

Thereby, c is the vacuum speed of light, I_t is the current at the antenna terminal and ν is the vacuum impedance [111, 144]. The direction of the incoming wave is usually taken as the direction of the air shower axis which is a good approximation for radiation emitted far away from the antennas.

The direction of the shower axis however might not be known a priori depending on the reconstruction scheme. If not taken from the reconstruction of another Auger component, it is

calculated from the electric field data. Therefore, an iterative approach can be chosen were the electric field is first calculated based on an initial guess of the shower axis. Based on this, the antenna response is unfolded and stations with a signal above a certain signal-to-noise ration (SNR) are selected. From the timing of the selected stations, the direction of the shower axis is determined analogue to the procedure described for the SD reconstruction in section 3.4.1. With this direction information, the antenna response is again unfolded and the shower axis is recalculated. The procedure is terminated when the direction reconstruction converges to a final value.

In general, most parameters for higher-level analysis are derived from the electric field traces. The signal time as well as the signal amplitude are determined from the maximum of the Hilbert-envelop of the time traces which represents the instantaneous amplitude (see example in section 6.1.2). Depending on the analysis, the total electric-field trace, one of its components, or a projection is used. Another important quantity which is determined based on the electric-field trace is the energy deposited per area hereafter referred to as the energy density. This is calculated via the integral over the absolute values of the Poynting vector. In the reconstruction, the absolute electric-field traces are squared and integrated (summed for discrete sampling) in a window $[t_1, t_2]$ around the signal time. Outside of this signal window, the integral over the squared amplitude of the electric field in a window $[t_3, t_4]$ represents the background contribution which is subtracted from the integral over the signal region. The energy density u in units of eV/m^2 is then given as

$$u = \varepsilon_0 c \left(t_{\mathrm{bin}} \sum_{t_1}^{t_2} |\vec{E}(t_i)|^2 - t_{\mathrm{bin}} \frac{t_2 - t_1}{t_4 - t_3} \sum_{t_3}^{t_4} |\vec{E}(t_i)|^2 \right) . \tag{3.9}$$

Where ε_0 and c are the vacuum permittivity and the vacuum speed of light and t_{bin} is the size of a time bin. For a pure white noise background, the uncertainty of the energy density can be calculated. If the true background is not white noise a more practical approach is to approximate the uncertainty as the energy density of the noise scaled to the signal size window.

The polarization of the cosmic-ray pulse can be determined from the electric-field data as the direction of the electric-field vector. The polarization is a key to study the emission mechanisms but it can also be used to deselect false signal stations that have only measured a noise pulse. This method is applied and discussed in chapter 6.

From the quantities derived on station level for all RDSs, air-shower parameters are reconstructed on the event level.

3.5.5 Event Level

On the event level, the direction of the shower axis, the two-dimensional LDF, and the wavefront shape can be reconstructed. The direction reconstruction is performed as discussed above using either a basic plane wave or a more advanced model, depending on the station multiplicity and the required precision. The two-dimensional LDF is determined by fitting the

amplitudes or energy densities with a modified version of equation 1.26. The details on this procedure and the obtained air shower parameters which are energy, $X_{\max}$, and the shower core position are presented in detail in the following chapters. In addition, the shape of the wave front can be used to obtain the core position as well as an estimate of $X_{\max}$ [95]. Here, a hyperbolic wave front is used to fit the signal times of the RDSs. The opening angle of the hyperbola thereby shows a correlation with the position of the emission region.

3.5.6 Station and Event Pre-, Intermediate-, and Post-Selection

At the start of the reconstruction procedure R&D stations as well as stations with known hardware issues are excluded. During the reconstruction further RDSs might be excluded based on there timing residuals, the shower geometry, or the polarization of the measured electric field vector. In case of a non-sufficient number of signal stations or a failed reconstruction step the processing of the event is terminated. A selection of the events based on the quality of the reconstruction or certain parameter values is performed after the processing.

3.5.7 RdObserver

Despite the variety of possible reconstruction schemes tailored for certain analyses, the RdObserver is used as a standard reconstruction scheme for hybrid and multi-hybrid showers. Due to the hybrid approach, reconstructed shower parameters from the SD reconstruction can be used as input for the radio reconstruction. Thereby, the antenna model is directly unfolded with the actual arrival direction of the cosmic ray which saves a significant amount of computing time for the otherwise necessary iterative direction determination. For a successfully reconstructed shower, the SD reconstruction as well as the radio reconstruction must be successful. The FD reconstruction is optional if the event contains the corresponding data. A successful FD reconstruction is however not required in this case.
At present, the RdObserver is only run on data recorded with the externally triggered stations of AERA. Merged RD+SD (+FD) files are used as input and three types of output are created. First, steering files for simulations using the reconstructed parameters such as core position, energy, and arrival direction are generated. Second, the raw data of the reconstructed showers is written to a separate file for easier data transfer of the selected showers and the possibility to reconstruct these showers with a modified module sequence. At last, Advanced Data Summary Tree (ADST) files which are the standard output files of the $\overline{\text{Off}}\underline{\text{line}}$ framework containing all parameters of the reconstructed showers are created. If the RdObserver is run on all recorded raw data, the RFI is suppressed by setting the frequency amplitude bins to zero, if the RdOberserver is re-run on the selected events only, the sine wave fitting suppression of the Beacon emission lines is used to improve the reconstruction of shower parameters for some of the later presented analyses. A general overview of the steps in the RdObserver module sequence and the used settings is given in the tables 3.2 and 3.3. The complete sequence is given

Table 3.2: General overview of the reconstruction steps of the RdObserver.

Detector	Reconstruction step
General	Event read-in, preselection and quality checks
SD	PMT signal reconstruction
	Station signal reconstruction
	Direction and LDF fit
	Horizontal reconstruction if $\theta > 55^{\circ}$
Radio	Event initialisation, station selection, and signal window setting
	Electronic channel response correction
	Beacon timing calibration
	RFI cleaning
	Antenna response correction
	Station signal reconstruction
	Electric field vector calculation
	Top-down station selection and plane fit (loop)
	Event selection
	Radio LDF fit
FD (try)	Calibration and telescope data merging
	Coihueco and HEAT data merging
	Aperture light calculation
	Energy deposit reconstruction
	Longitudinal profile fit (Gaisser-Hillas)
Radio	Time trace cutting
	Radio simulation steering file preparation
General	Event file exporting (ROOT file format)
	Output file generation

in the appendix A.2. The dataset obtained from the RdObserver is presented in section 3.6. It is used in the analyses discussed in chapter 7.

3.6 AERA Dataset

AERA has recorded a large radio dataset of extensive air showers. Until beginning of August 2015, 6569 air showers were detected by three or more antenna stations equipped with a ring buffer in coincidence with the SD (RD+SD hybrid showers) and reconstructed with the RdObserver. The data recorded with the internally trigger stations is not yet considered in the RdObserver reconstruction. The arrival directions and the angular difference between the shower axis determined from the SD data and the axis determined from the radio data are

Table 3.3: Settings of the reconstruction parameters of the RdObserver.

Parameter	Setting
Signal window	determined from the SD geometry reconstruction
Noise window	$2000 - 5000\,\mathrm{ns}$
Shower geometry	taken from the SD reconstruction
Deselected R&D stations	87, 91, 98, 107
Up-sampling factor	4
Signal reconstruction	on Hilbert envelop, projection on XY direction
Minimum signal-to-noise ratio	10 - definition: $(\mathrm{Signal/RMS})^2$
Station is lonely	no signal station within 400 m or only one signal station within 800 m
Minimum number of signal stations	3
Maximum deviation RD-SD axis	20°
Energy density integration window	100 ns

shown in figure 3.8. The distribution has a mean of 1.69° and can be fitted with a Rayleigh function with $\sigma = 0.54^\circ$. Most of the air showers are detected with 3 RDSs, but there are also air showers which are detected with more than 40 RDSs. The distribution of signal stations per shower is shown in figure 3.9 (left). The event rate for the presented dataset is shown in figure 3.9 (right). During the stable operation of AERA24, about 50 air showers were recorded with three or more RDSs per month which has increased to about 250 air showers per month for AERA124 after a short commissioning phase. The energy distribution of the measured hybrid events is shown in figure 3.10 (left). In addition to the hybrid showers, 370 air showers were simultaneously detected with the Fluorescence Detector (RD+SD+FD multi-hybrid showers). For these showers, X_{max} is within the FD field of view and the measured profile allows for an FD-based energy reconstruction. The resulting X_{max} distribution is shown in figure 3.10 (right). Air showers in coincidence with the AMIGA muon counters were also detected. The dataset contains more than 500 RD+SD+AMIGA multi-hybrid showers and more than 50 RD+SD+FD+AMIGA multi-hybrid showers. The numbers are summarized in table 3.4. The reconstructed shower parameters obtained by using the RdObserver are used as basis for the analyses targeting the depth of the shower maximum presented in chapter 7. Also the results presented in chapter 6 are obtained with a very similar reconstruction sequence which however slightly differs in details for historical reasons. On top of the quality criteria applied to the data at the different stages of the reconstruction, additional quality cuts are necessary depending on the individual analysis carried out on the data. These selections are discussed in the corresponding chapters.

For the analysis targeting the reconstruction of X_{max}, the RD-SD-FD multi-hybrid showers are

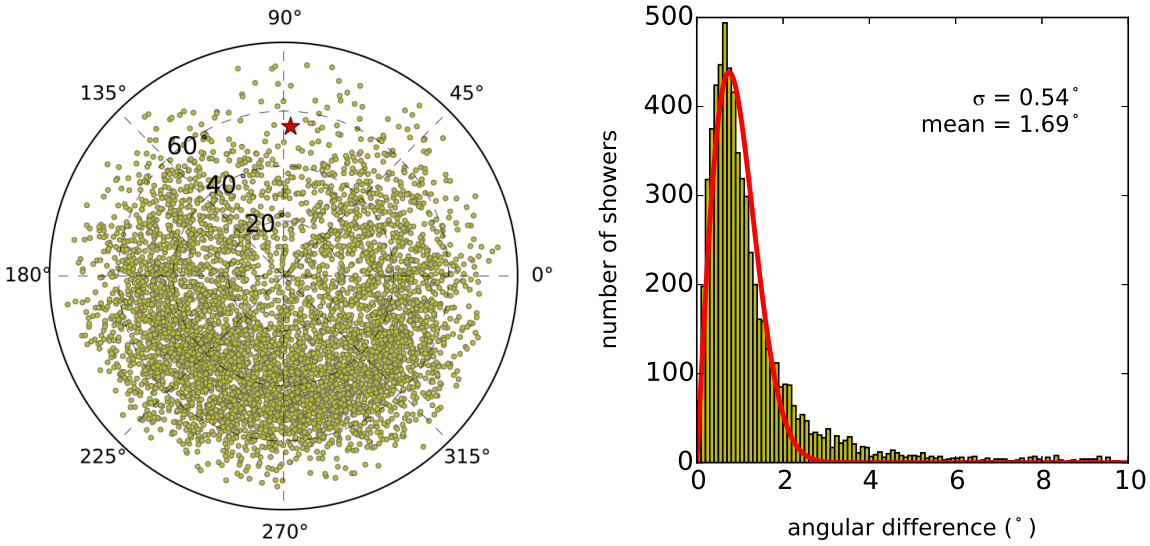

Figure 3.8: Air showers measured with AERA and reconstructed with the RdObserver. Left: Skyplot of all events. The shown arrival direction is taken from the SD reconstruction. The direction of the magnetic field axis is indicated with a star. Right: Distribution of the angular difference between the air-shower axis reconstructed from the SD and from radio data with a mean of 1.69°. The line indicates a fit of a Rayleigh function with $\sigma = 0.54°$.

Table 3.4: Air shower statistics for coincident detection with various detector combinations.

Detector combination	Number of air showers
RD-SD	6569
RD-SD-FD	370
RD-SD-AMIGA	> 500
RD-SD-FD-AMIGA	> 50

used for the calibration of radio observables against the Fluorescence Detector measurements. For these calibration the quality of the FD data is essential and therefore a high reconstruction quality and a reliable reconstruction of X_{max} are required. This is achieved by applying additional quality cuts corresponding to the ones used for the SD-FD energy calibration [140]. The most important ones needed to ensure a reliable reconstruction are given in table 3.5. The full list of used cuts can be found in appendix A.3. In total 105 reconstructed showers fulfil these criteria.

For the FD based X_{max} determination, the proper knowledge of the light scattering in the atmosphere is crucial. Therefore extended calibration efforts are made and the properties of the atmosphere concerning the scattering are incorporated during reconstruction. The databases for the calibration are filled once per year. Unfortunately this database is at the moment only filled until the end of 2013. Therefore, individual atmospheric conditions can not be consid-

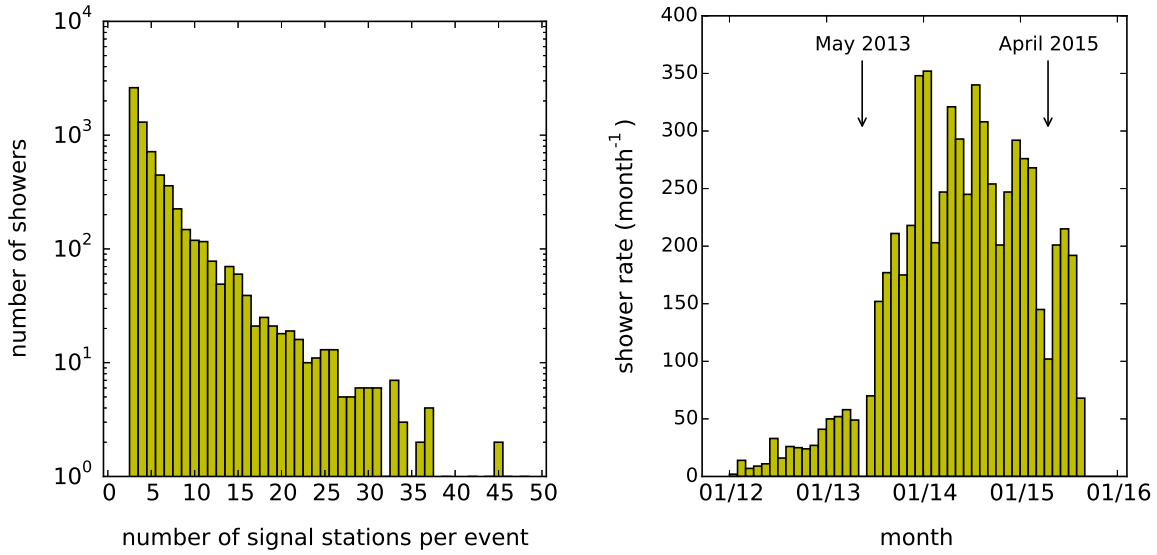

Figure 3.9: AERA showers reconstructed with the RdObserver. Left: Station multiplicity for all successfully reconstructed air showers. The y-coordinate is plotted in a log scale. Right: Shower rate in showers per month as of January 2012. Until the deployment of AERA124 in May 2013, data were acquired with AERA24. AERA153 was installed in April 2015.

Table 3.5: Most important quality cuts applied to the FD-SD data of the multi-hybrid event set.

detector	cut
FD	$X_{\max}$ in expected field of view
FD	$\sigma_{X_{\max}} \leq 40\,\mathrm{g/cm^2}$
SD	zenith angle $\geq 55°$
SD	rec-level ≥ 3
SD	minimum Trigger $= \mathrm{T5}$

ered in the reconstruction for most of the RD-SD-FD multi-hybrid showers. These showers are then reconstructed with a model for the scattering based on the atmospheric measurements in earlier years. This generic and less accurate description of the atmospheric condition introduces an uncertainty of 6.2 g/cm^2 on the reconstructed value of $X_{\max}$ [145]. This uncertainty is added to the uncertainty obtained from the FD reconstruction when no information about atmospheric conditions concerning the light scattering properties is available. This uncertainty obtained from the FD reconstruction is determined on shower-by-shower basis from the photon statistics, the shower geometry, and atmospheric conditions. The systematic uncertainty in the energy range of AERA is $8 - 11\,\mathrm{g/cm^2}$ [138].

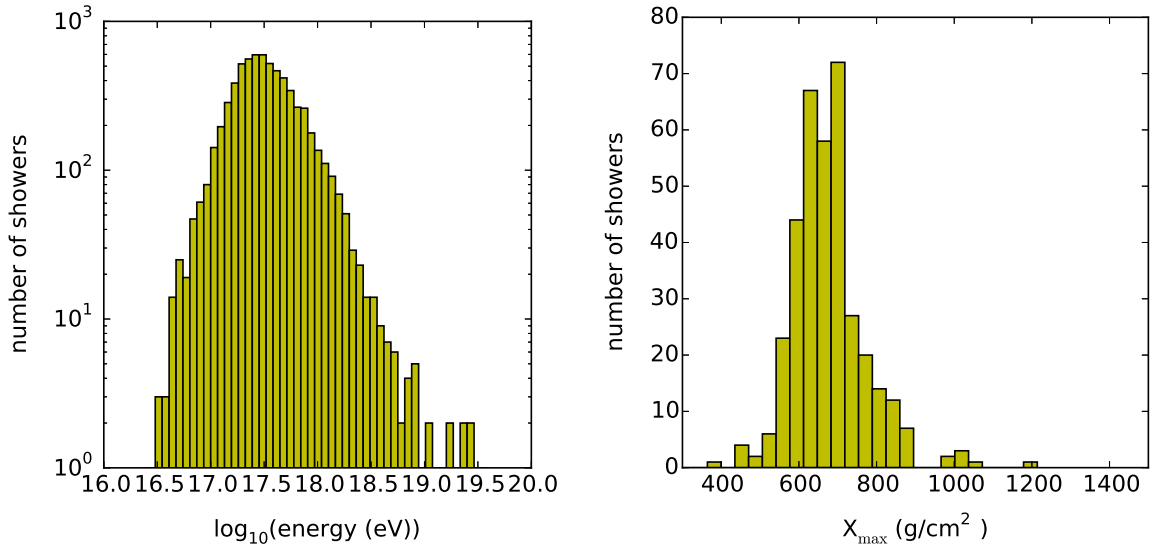

Figure 3.10: Air showers reconstructed with the RdObserver. Left: Energy distribution of the measured air showers as reconstructed from the SD data. Right: $X_{\max}$ distribution of the RD+SD+FD multi-hybrid showers.

3.7 Radio Simulations for the AERA Detector Geometry

For most of the air showers in the AERA124 dataset two simulations were produced using the measured arrival direction and energy as input parameters. One of the two simulations has a proton as primary particle, the other one an iron nucleus. The electric field is calculated for the actual AERA station positions and can in this case directly be read into $\overline{\text{Off}}\underline{\text{line}}$. There, the detector description is used to generate ADC time traces from the simulations including the imprint of the actual channel and antenna responses for the individual stations. This is achieved by applying first the antenna and then the channel response backwards. At this stage, noise recorded in the vicinity of the shower (maximum 50 s offset) is added to the simulated electric field traces. The reconstruction of the simulated data follows the steps outlined in section 3.5.7 except for the timing calibration which is not needed for simulations. As in the reconstruction of real data, at least three stations with signal above the SNR threshold are required. If the number is smaller, the shower is skipped and the reconstruction continues with the next shower. Stations for which no noise data of the time of the event are available are skipped as well. This allows accounting for the changing grid configuration when stations experience downtime. It should be noted that the simulated signals and the noise are added one to one and no scaling is applied, assuming the simulations give the correct absolute amplitude in the radio signals. This assumption is encouraged by the results presented in [146]. It is however in some tension with other observations [147].
For the simulations, CORSIKA 7.400 is used together with the hadronic interaction models FLUKA 2011.2b [50] and QGSJET-II-04 [148].

$\overline{\text{Off}}\underline{\text{line}}$ also provides a similar functionality to generate SD and FD data from air shower simulations which can be included in the reconstruction. For the presented dataset, simulated data are not generated for the SD and FD and the dataset is reconstructed only with the radio part of the RdObserver reconstruction. Simulations set up according to this scheme are used for calibration purposes in the $X_{\max}$ analysis in the chapter 7.

3.8 Generic Radio Simulations on a Star-Shape Pattern

In the classical approach of simulating radio emission of extensive air-showers, a shower-core location is set and the electric-field traces are simulated for fixed observer positions relative to this location. The observer positions are often chosen with respect to a regular grid on the ground. In the method introduced in [71], the positions of the observers are arranged in the plane spanned by $\vec{v} \times \vec{B}$ and $\vec{v} \times (\vec{v} \times \vec{B})$ and then projected onto the ground to determine the input for the simulations. Therefore, the grid on the ground is distorted but once transformed back into the shower plane, it always shows the same shape. A second innovation is the layout of the antenna grid in the $\vec{v} \times \vec{B}$ vs. $\vec{v} \times (\vec{v} \times \vec{B})$ plane which has a regular star-shape with eight arms and 20 antenna positions per arm with 25 m spacing. The arms are oriented in such a way that one of them is parallel and one antiparallel to the $\vec{v} \times \vec{B}$-direction and one is parallel and one antiparallel to the $\vec{v} \times (\vec{v} \times \vec{B})$-direction. In this way, the "bean"-shape of the lateral distribution pattern is always sampled in the regions where the polarizations of the geomagnetic and the charge excess emission are parallel/anitparallel and where they are perpendicular to each other. Thereby, it is guaranteed that the minimum and the maximum of the density pattern are sampled. Thus, parameters related to the signal strength can be interpolated. The simulated energy densities on the star shaped grid on the ground and in the shower plane are displayed in figure 3.11 (top row). The interpolation is performed with a radial basis function method employing a quintic function. The combination of the star-shape pattern and the interpolation was found to allow the prediction of the energy density at any point within the simulated star-shape with a difference of less than 2.5% of the maximum energy density compared to dedicated simulations at those positions [71]. This method is used throughout the work presented in this manuscript. The interpolated density pattern is illustrated in figure 3.11 (bottom). For the simulations, CORSIKA 7.4387 is used together with the hadronic interaction models FLUKA 2011.2b [50] and QGSJET-II-04 [148]. The CORSIKA showers are thinned at a level of 10^{-6} and optimized weight limitation [149] is used. The magnetic field is chosen according to the site of AERA. The energy density at each simulated position is determined according to equation 3.9 after filtering the simulated electric field traces to the frequency range of AERA of $30 - 80\,\mathrm{MHz}$. Simulations on the star-shape station-grid are used in two different analyses presented in chapter 5 and 7. The properties of the simulation sets used are discussed in the two chapters individually.

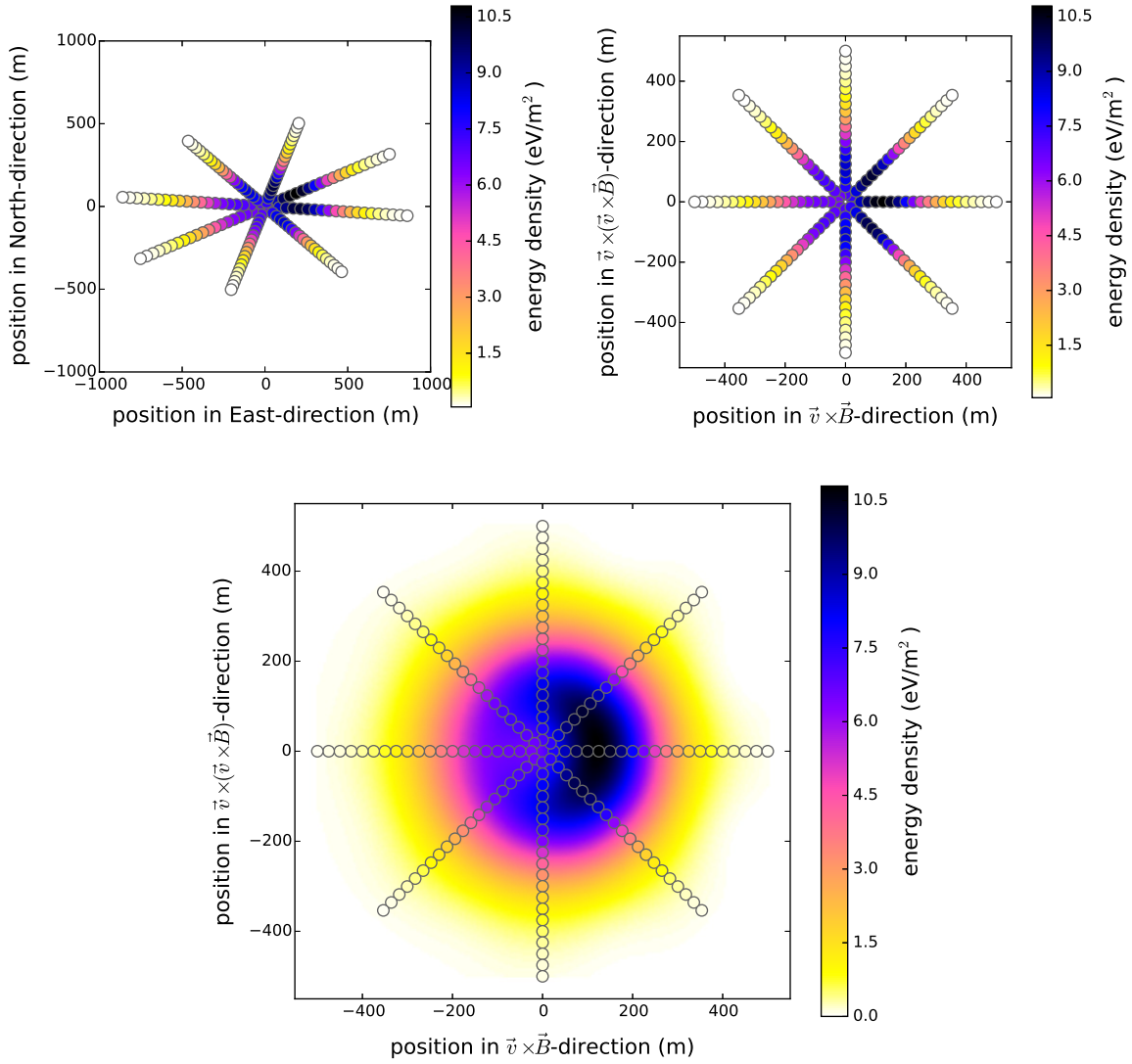

Figure 3.11: Simulation of the energy density of the radio emission of an extensive air-shower. Top left: Observer positions at which the electric-field traces are simulated on the ground. Top right: Observer positions transformed into the $\vec{v}\times\vec{B}$ vs. $\vec{v}\times(\vec{v}\times\vec{B})$ plane forming a regular eight-arm star. Bottom: Spatial interpolation of the simulated energy densities with a radial basis function (background color map). The simulated air shower has an energy of 4.4×10^{17} eV, the zenith angle is 56°, and the azimuth angle is 3°.

4

AERA Scintillators

Parts of this chapter have been published in:

J. Schulz, J. R. Hörandel, S. Jansen, A. Nelles, C. Timmermans

The Scintillators of the Auger Engineering Radio Array

Auger Internal Publication, GAP2014_122

With the deployment of the second stage of AERA not only 100 new radio detection stations were deployed, but also 75 small plastic scintillators were included in 40 RDSs. The scintillator modules are placed inside the station electronics compartment on top and underneath the lead battery (*Top-, Bottom-scintillator*). The distance between the detector stations is 250 m around and south of the CRS, whereas the stations further to the East and North are at 375 m distance from each other. The positions of the AERA scintillators are shown in figure 4.1.
Besides triggering, the particle density as function of the distance to shower axis (in the shower plane) can be utilized to determine the shower-core position. This is of interest due to the high dependency of nearly all radio analyses on the shower core position. Especially low-energy showers, triggering only 3 stations of the Surface Detector array suffer from relatively large uncertainties on the reconstructed core position. These uncertainties can be of the order of hundreds of meters in the worst cases.
A fit of the measured particle densities at ground with a NKG lateral distribution function (see equation 1.23) is used here to determine the core position purely based on the scintillator measurements using a maximum likelihood fit for showers sampled with high station multiplicity. For future analyses, the scintillator measurements can be included in a general reconstruction that combines core-sensitive data from the scintillators, the SD, and the radio measurements to constrain the shower geometry.

4.1 Scintillator Hardware

For a better understanding of the applied reconstruction, a short description of the hardware of the particle detectors is given in the following.

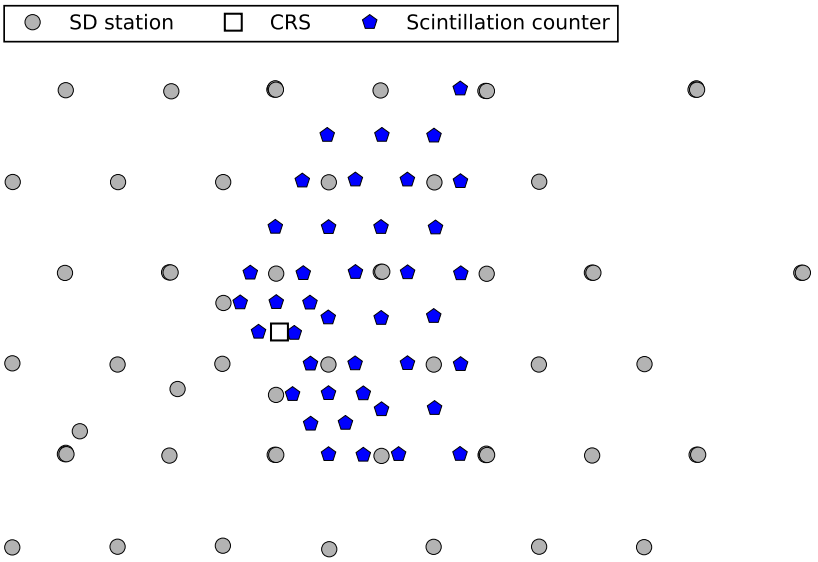

Figure 4.1: Overview of the AERA scintillation counters together with the SD stations and the Central Radio Station (CRS). The distance between the particle counters is 250 m around and south of the CRS, whereas further to the East and North the distance is 375 m.

4.1.1 Scintillator Module

The heart of the particle detectors is a $457 \times 172 \times 24\,\mathrm{mm}^3$ plastic scintillator [117]. From the scintillator, the photons are collected and guided to a SensTech P30CWS12-05 photomultiplier tube (PMT) by three BCF 91-A optical fibres that are glued into grooves in the scintillator surface. A technical drawing of the detector unit and the installed setup is shown in figure 4.2. The PMT base includes a high voltage (HV) generator which uses a 12 V input and a control voltage around 1 V to supply $300 - 1200\,\mathrm{V}$ to the photo cathode. The 12 V are provided from the charge controller and daisy-chained through the scintillator module(s) to the digitizer. The high voltage setting is controlled via the same cable which the signals are transmitted through. This, on the one hand simplifies connections and cabling, on the other hand requires an AC coupling of the signal introducing positive overshoots after a negative signal.

4.1.2 Scintillator Electronics

For the readout of the PMTs, the same electronic components as for the radio channels are used except for the analog filters. This provides a very flexible data-acquisition system, in which a scintillator channel can easily be exchanged for a third radio channel. It also provides powerful hardware with high sampling rate and good amplitude resolution for the particle detectors. Employing a 14 bit ADC with a resolution of about 13 μV/ADC-unit and 5 ns time binning, the scintillator pulses are recorded in great detail.

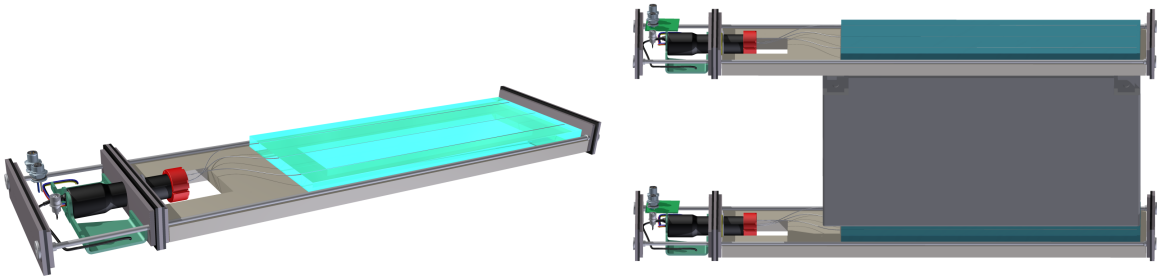

Figure 4.2: Technical drawing of the particle detector unit. Left: Visible are the plastic scintillator, the fibre connection as well as the PMT. In addition, parts of the housing are shown together with the PMT holder and electronics. Right: The combination of Top- and Bottom-scintillator with the lead-gel battery in between (gray).

4.1.3 Scintillator-Trigger

The trigger condition for the scintillator modules is a simple threshold crossing. After a short commissioning phase of the AERA124 stations, the trigger threshold for the scintillator modules was fixed to 150 ADC-units. In section 4.2.2, the distribution of signal pulse amplitudes and their corresponding integrated signals in units of vertical equivalent muons is presented verifying the chosen threshold.
Due to the slightly different propagation velocities of ultra-relativistic particles in the front of the air shower and the emitted electromagnetic radiation, one expects the radio signal to arrive with a delay at the observer with respect to the particle shower front. The hardware for particle and radio detection introduces additional time delays. On the one hand, the scintillator, the fibres, and the PMT have a specific rise time, on the other hand, the low-noise amplifier and the bandpass filters in the radio chain delay the signals. Different cables and cable lengths also have an influence. During the reconstruction of the radio signals, the responses of all components in the electronics chain are taken into account and the corresponding time delays are corrected for. These corrections are not applied to the scintillator chain, as its components were not measured individually. Therefore, the reconstructed radio signal usually appears ahead of the scintillator pulse in the station data. The trigger crossing of the scintillator signal is set to 2315 ns in the voltage time trace. In figure 4.3, the trigger time is shown as blue line together with the corresponding time distributions of radio pulses before (red) and after (black) correcting for the radio channel response. Only radio pulses with an amplitude more than 3.5 times above the full trace RMS are taken into account. To avoid possible biases from a too narrow signal time window, the period of acceptance is set between 2100 and 2500 ns.

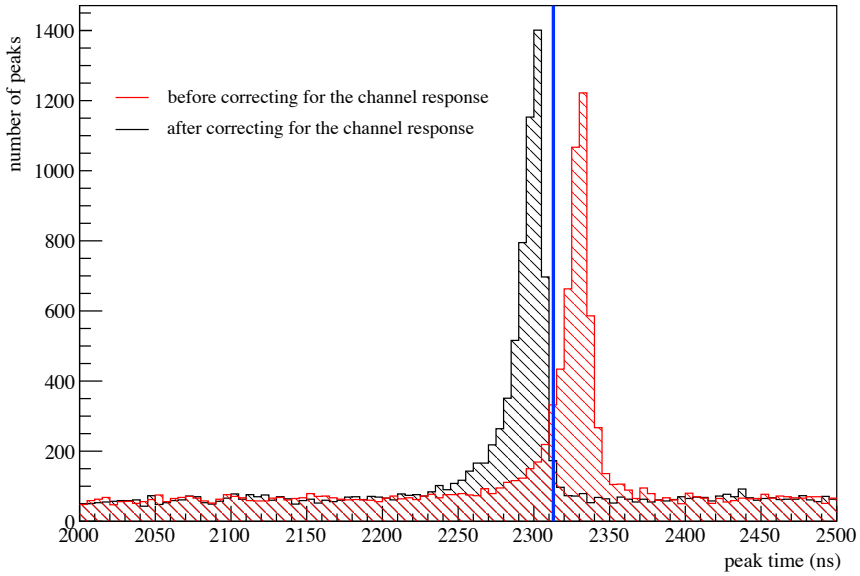

Figure 4.3: Distribution of radio pulse times for scintillator triggered signals with amplitudes 3.5 times above the full trace RMS. The vertical line indicates the time of trigger crossing in the particle detector. Corresponding to this, peak times of the radio pulses are shown in red (light) before correcting for the channel response and in black (dark) after the correction. After the correction for the channel response, the radio signals appear ahead of the particle signal as those are not corrected for the response of the electronics chain. Figure taken from [145].

4.1.4 Trigger Efficiency

Triggering individual radio stations only based on the detection of particles with the scintillators allows a precise determination of the signal windows. The efficiency in triggering however is lower compared to using an external trigger from the SD because of the small size of the particle detectors (100 times smaller effective area than a SD station). This effect is proportional to the cosine of the zenith angle due to the projection of the surface area. Therefore, the radio self-trigger was installed in addition to the scintillator trigger.
An absolute value for the efficiency cannot be given because the real number of showers falling into the instrumented aera of AERA is not known. Nevertheless, a comparison with the number of air showers detected by the SD Infill gives the relative efficiency compared to an external trigger. The number of showers detected with the SD together with the number of showers detected with both, the SD and the scintillators, as a function of the primary energies (left) and zenith angles (right) are presented in figure 4.4. In addition, the number of radio showers as reconstructed with the basic RdHybridReconstrution pipeline of the $\overline{\text{Off}}\underline{\text{line}}$ framework is shown in both plots. The datasets were acquired in 2013 and the considered time periods are set according to the uptime of AERA (downtimes of less than 6 hours are not accounted for). A large relative difference for the number of showers with energies below roughly 10^{17} eV

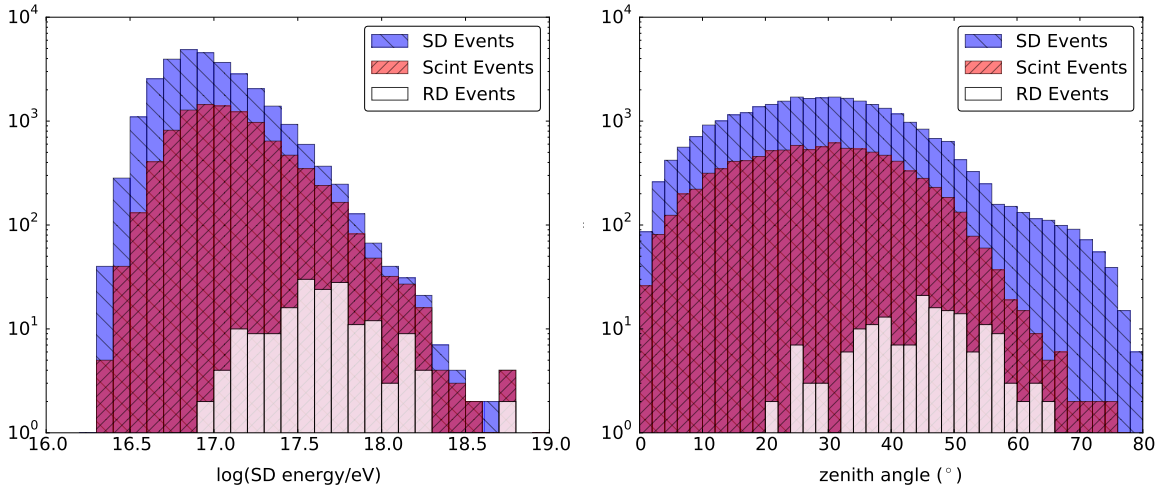

Figure 4.4: Number of air showers seen by the SD together with the number of those showers also seen by the scintillators and in the radio stations as a function of the energy (left) and the zenith angle (right). For the SD data, two different reconstruction schemes are used, depending on the zenith angle. The standard reconstruction is used up to 55°. For larger angles, a special horizontal air shower reconstruction is used.

detected with the scintillators compared to the SD is observed. The impact on the radio detection of air showers is however small as 10^{17} eV is the threshold for the radio detection in 3 or more stations for the given array configuration (see figure 4.4 left). For increasing energies, the efficiency of the scintillator array is also increasing almost reaches one at the highest energies. With increasing zenith angle, both distributions of the particle detectors increase due to the increasing solid angle up to a maximum around 30°. Larger angles lead to a dominant decrease of the projected detector area and thereby to a decrease in the distribution. The decrease of the distribution for the scintillators is steeper as their effective area decreases more rapidly than the one of the Surface Detector stations which are not flat detectors. Additionally, an asymmetry between the rise and the fall of the distributions is observed due to the increase in shower attenuation with growing zenith angles. For inclined showers (zenith angle larger than 60°), the small effective area of the scintillators combined with the attenuation of the electromagnetic cascade results in the detection limit for showers with these detectors. The SD data reconstruction employs two different methods depending on the zenith angle of the detected air shower. Up to 55°, the standard reconstruction as presented in section 3.4.1 is used. For more inclined air showers, a special reconstruction scheme is applied [150].
The distribution of radio events is roughly centred around 45°, but it is expected to continue to more inclined showers than observed here, as the footprint increases with the distance to the emission region enabling the detection with a relatively sparse grid.
As the efficiency is depending on energy as well as on the zenith angle, the fraction of showers detected by the scintillators and the SD compared to the fraction of showers which triggered

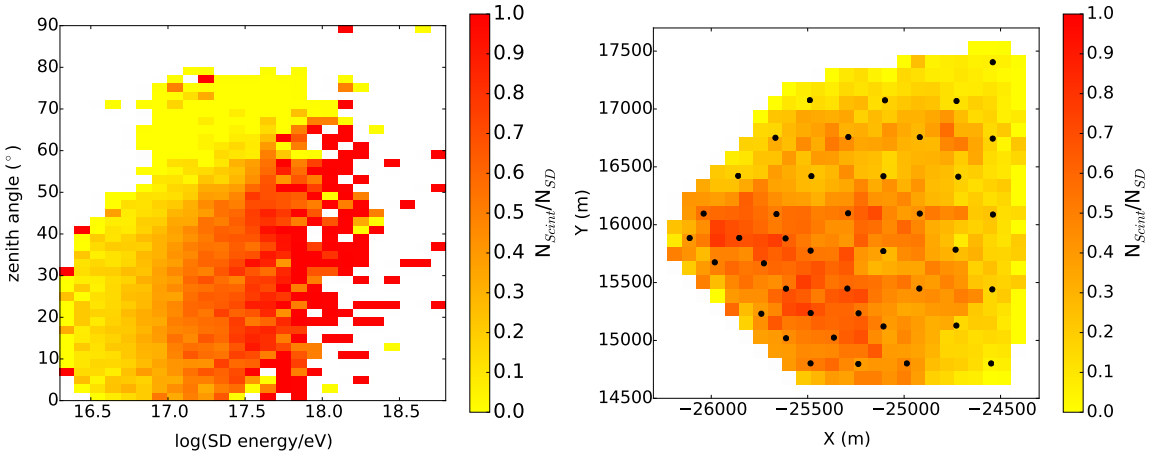

Figure 4.5: Fraction of the showers detected by the SD that also triggered the scintillators. Left: Fraction in bins of energy and zenith angle. Right: Fraction in bins of X (East) and Y (North) position of the shower axis position for energies above 10^{17} eV and zenith angles below $60°$. The positions of the radio stations are indicated as dots.

the SD (N_{Scint}/N_{SD}) is plotted as a function of both parameters in figure 4.5 (left). For energies below 10^{17} eV, the fraction is smaller than 0.5 increasing to $0.9 - 1.0$ for most of the bins above $10^{17.6}$ eV and below $60°$. Due to the irregular spacing of the radio stations, the efficiency changes over the scintillator array. In figure 4.5 (right) the fraction N_{Scint}/N_{SD} is shown depending on the core position of the showers as determined with the SD for energies above 10^{17} eV and zenith angles below $60°$. The fractions for the different array regions show a relation between the ratio N_{Scint}/N_{SD} and the grid size. For the region with a spacing of 250 m, the efficiency is between $0.5 - 1.0$ and decreases for the spacing of 375 m to < 0.1 at the outer edge.

4.2 Scintillator Calibration

An array of 40 scintillator stations spread over an area of about $3\,\mathrm{km}^2$ can be considered as a cosmic-ray detector on its own. Even though, this was never intended and also the size of the scintillators ($< 0.1\,\mathrm{m}^2$) makes the array unattractive for standalone detections, valuable information on the shower geometry as input for analyses of the radio emission of extensive air showers can be extracted.

4.2.1 Scintillator Signals

The two main observables in case of the scintillators are the signal time and the deposited energy in the detector. The time can directly be inferred from the signal trace itself according to the chosen definition. Here, the peak time of the signal is used. For the determination of the

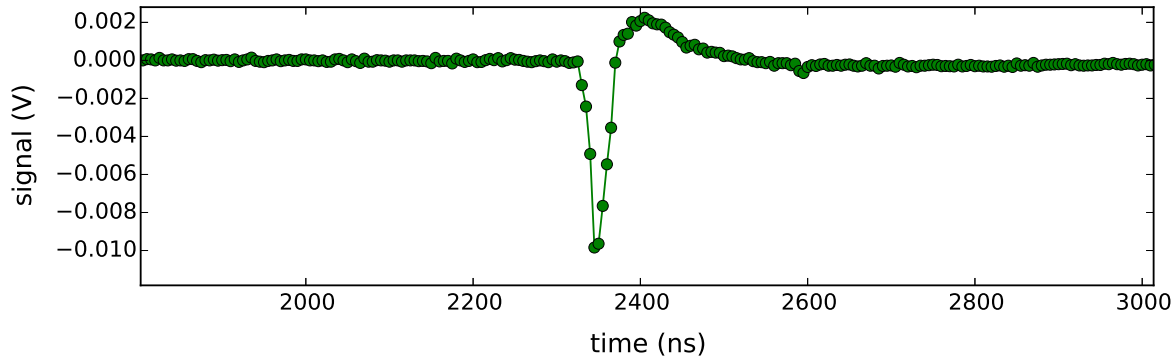

Figure 4.6: Typical time trace recorded with the scintillation detector. The negative signal is followed by a positive overshoot due to the AC-coupling of the signal line.

deposited energy, the linear proportionality between energy deposit, number of scintillation photons, and charge output of the PMT are used. This can be calculated from the measured signal trace by integrating the output voltage $U(t)$ over the sample time $\mathrm{d}t$ and accounting for the $50\,\Omega$ input impedance.

$$Q = \int_{t_i}^{t_f} \frac{U(t)}{R} \mathrm{d}t \tag{4.1}$$

For discrete sampling, this is equal to

$$Q = \sum_{i=1}^{n_{\mathrm{samples}}} \frac{U_i \Delta t}{R}. \tag{4.2}$$

Before the integration, the trace is corrected for a possible DC offset and fluctuations on smaller time scales that could influence the signal reconstruction. As mentioned in section 4.1.1, the control voltage for the HV setting on the photocathode is sent via the signal line. Therefore, the signal line is AC-coupled to the electronics. This leads to a positive overshoot following the negative signal due to the recharging of the coupling capacity. A signal time trace as it is typical for air shower particles traversing the scintillator is shown in figure 4.6. The signal integration window is defined as the range with negative signal around the first threshold crossing. For two consecutive signals, the second signal may fall within the overshoot of the first. These delayed pulses are not considered at present because the signals were not found to have a common pulse shape which can be parametrized and subtracted from the trace in order to recover delayed signals.

4.2.2 Detector Calibration

The detectors are calibrated with atmospheric muons. For this purpose, the double layer consisting of Top- and Bottom-scintillator is used in combination with the data acquired in the random trigger mode. In this mode, every 40000^{th} timestamp received by the central DAQ is selected and the station data are written to disk. This minimizes the chances to select signals

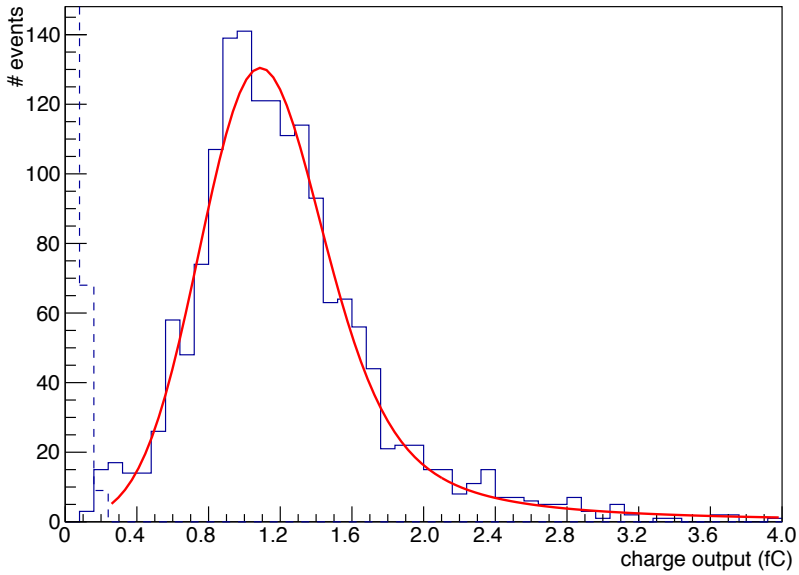

Figure 4.7: Histogram of charge output of one of the Top-scintillators exposed to single muons. The distribution is corrected for the impact of electronic noise indicated by the dashed line. The distribution is fitted by a convolution of a Landau and a Gaussian function and the charge output for 1 VEM is taken as the peak position of the Landau distribution.

affiliated with air showers which would be strongly influenced by the electromagnetic component.

In the next step, the calibration data for one scintillator are selected by taking events with a trigger crossing in the other scintillator of the station. From the resulting distribution, the background entries are subtracted. For that purpose, data taken every ten seconds are processed in the same way as the calibration data and the resulting distribution of the electronic noise is scaled to the same number of entries in the first bin. The cleaned distribution of the integrated signals is fitted with a convolution of a Landau and a Gaussian function for every individual scintillator. The integrated signal corresponding to one VEM is then defined as the peak position of the Landau distribution. A histogram showing the distribution of integrated single muon signals in one of the Top-scintillators is shown in figure 4.7. Stations which contain just one scintillator are not taken into account because it is not possible to select only almost vertical muons. For theses five stations, the combined distribution of the other 35 stations is used.

The distributions of the Landau-peak positions for all particle detectors placed on top and underneath the battery are shown in figure 4.8. The values for all Top- and Bottom-scitillators are similar within $10 - 20\%$. Between the Top- and the Bottom-scintillator, there is an overall shift of about 15%. The origin of this discrepancy is most likely the individual HV supplied to the PMTs. This voltage is software controlled to keep the trigger rate constant under changing temperature and pressure conditions and a lower HV-setting corresponds to a smaller inte-

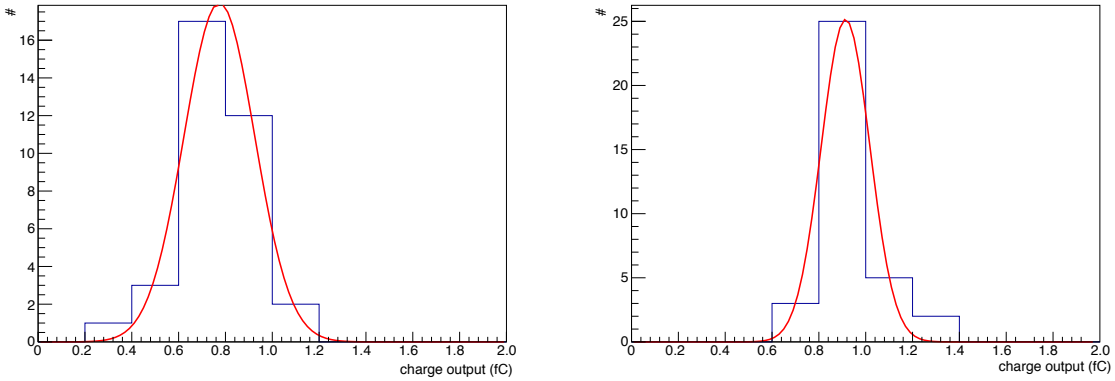

Figure 4.8: Distribution of the charge output corresponding to 1 VEM for all particle detectors. The variation between the individual detector units is $16 \pm 3\%$ for the scintillators at the bottom (left) and $12 \pm 2\%$ for the detectors placed on top of the battery (right). Note that the scintillators are not expected to have exactly the same signal output for single muons because of the different individual characteristics of the PMTs.

grated signals. A possible reason for an increased trigger rate in the Bottom-scintillator is pre-showering of particles in the lead battery.

Energy Calibration

To cross check the calibration of the vertical equivalent muon and to additionally obtain a calibration for the deposited energy, a GEANT4 [151] simulation of the scintillator modules is used. As a simplified model, two scintillator modules are implemented with a spacing given by the height of the battery. These modules contain the plastic scintillator block surrounded by styrofoam inside the metal housing. For the battery, a block of lead corresponding to the estimated amount of lead inside the battery is placed on top of the lower scintillator. In the real battery, the lead is arranged in vertical sheets but information about the exact construction details is not available. Therefore, the simplified implementation is chosen.
For the calibration, muons with a $\cos^2\theta$ zenith-angle distribution and an energy of 4 GeV are used. Analogue to the data driven calibration, only muons going through the bottom detector are selected for the top detector calibration and vice versa. The distribution of deposited energy can be seen in figure 4.9. Note that the plotted range does not include the noise peak. With 4.6 MeV energy deposit for single almost vertical muons, the simulations agree with the expected value of 2.02 MeV/cm of traversed scintillator material [152]. The observed difference between Top- and Bottom-scintillator is not reproduced in the simulations using single muons. However, detector simulations including also particles of the electromagnetic cascade show hints for pre-showering in the battery.
After fitting the distribution of simulated single-muon signals, a comparison between the

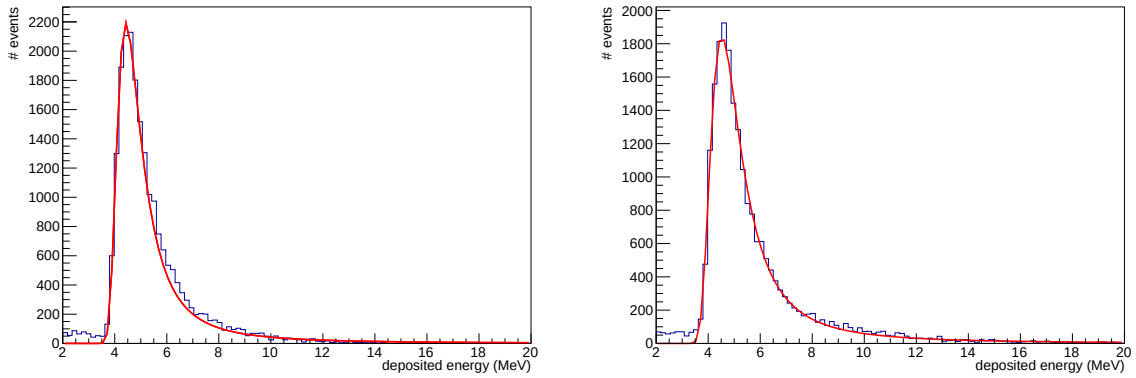

Figure 4.9: Distribution of deposited energy from single vertical muons as calculated with a simplified detector model in GEANT4 for Bottom-scintillators on the left and Top-scintillators on the right. The distribution is fitted with a Landau function leading to an energy deposit of $4.49 \pm 0.01\,\mathrm{MeV}$ for the Bottom- and $4.61 \pm 0.01\,\mathrm{MeV}$ for the Top-detector at the peak position.

model and the measurements can be made. The measured and the simulated single muon peak positions give the relation between the integrated signal and the deposited energy. To account for noise, a Gaussian-distribution is added to the simulation according to the width of the measured noise distribution in every individual detector. Normalizing both distributions to an area of one allows to match the measured and the simulated distribution. Both distributions as function of the deposited energy are in good agreement as shown in figure 4.10. For the Bottom-scintillators, varying deviations between the measurement and the simulation are seen. Given these issues, the Bottom-scintillators are not used in the reconstruction of air showers at the moment.
The presented calibration is used to convert integrated measured signals in VEM for all individual detector units of stations with two scintillators. For the stations containing only a Top-scintillator the combined calibration of all other Top-scintillators is used in this case. The results are shown in appendix A.4.

Cross Check of Trigger Settings and Silent Stations

To avoid unnecessary processing of data inside the CPU of the station, the scintillator trigger is implemented on ADC level as a threshold-crossing trigger. The deposited energy, however, is reconstructed from the integral of the pulse since it correlates with the charge output of the PMT. The distribution of signals from all Top-scintillators triggered on Top- or Bottom-scintillator in the random- and air-shower-trigger mode is shown in figure 4.11. The triggering on the Bottom-scintillators, allows the consideration of sub-threshold events. The trigger threshold is set to 150 ADC units, which corresponds to about 2 mV depending on the characteristics of the individual electronic components. With the chosen threshold setting, there are

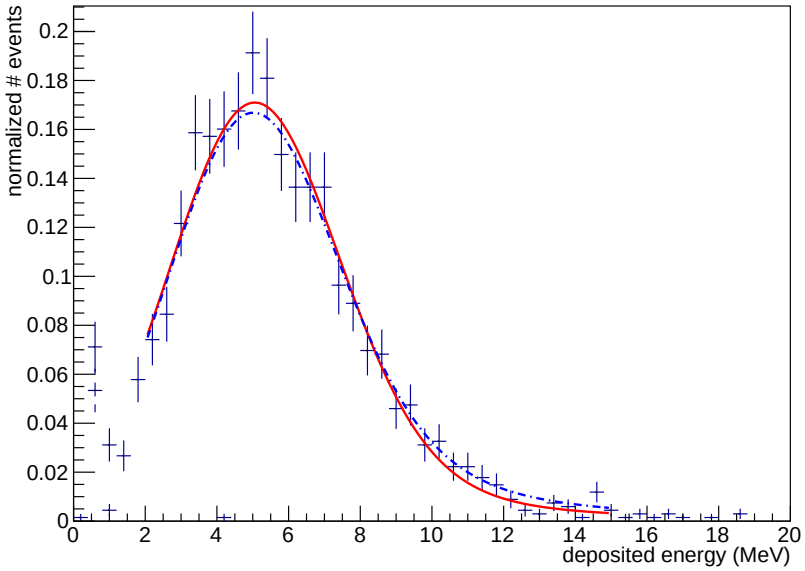

Figure 4.10: Histogram of single muon signals converted into the deposited energy in one of the Top-scintillators using the calibration obtained by GEANT4 simulations. The distribution is corrected for noise and normalized to an area of 1. The red solid line denotes the fit of a convoluted Landau-Gaussian function to the data. The blue dotted line shows the fitted distributions of the simulated single-muon signal combined with a Gaussian distribution according to the measured width and normalized to an area of 1.

only a few signals below threshold which were reconstructed to have an integrated signal of 1 VEM or more. The exact fraction of these events slightly varies due to the mentioned different electronic components. In figure 4.12, the same plot is shown for data taken every ten seconds. Here, the distribution of signal height as function of the corresponding reconstructed number of VEM is plotted, representing the background. For these data, almost all the signals are reconstructed noise fluctuations which are concentrated below 300 μV and 0.1 VEM with a tail to higher VEM fractions. A negligible number of signals is found in the expected signal region, representing particles measured in the periodically-triggered data by chance. Due to this, the electronic background does not need to be considered in terms of triggering. In addition to the previous results, the upper limit on the integrated signals in a station which did not trigger can also be inferred. Therefore, all sub-threshold signals are projected onto the x-axis and the bin content is summed up beginning with the low VEM values until the sum reaches 95.4% of the total number of entries. This procedure is repeated for all Top- and Bottom-scintillators individually and the results are given in table A.7 in the appendix. The mean values for Top- and Bottom-scintillators are 0.58 VEM and 0.70 VEM. Applying a similar procedure to the noise distributions reveals that more than 99% of all noise events have an integrated signal of less than 0.07 VEM giving no sign for a large influence of offsets and fluctuations. As the background fluctuations are well below 0.5 mV, the trigger threshold could be lowered in or-

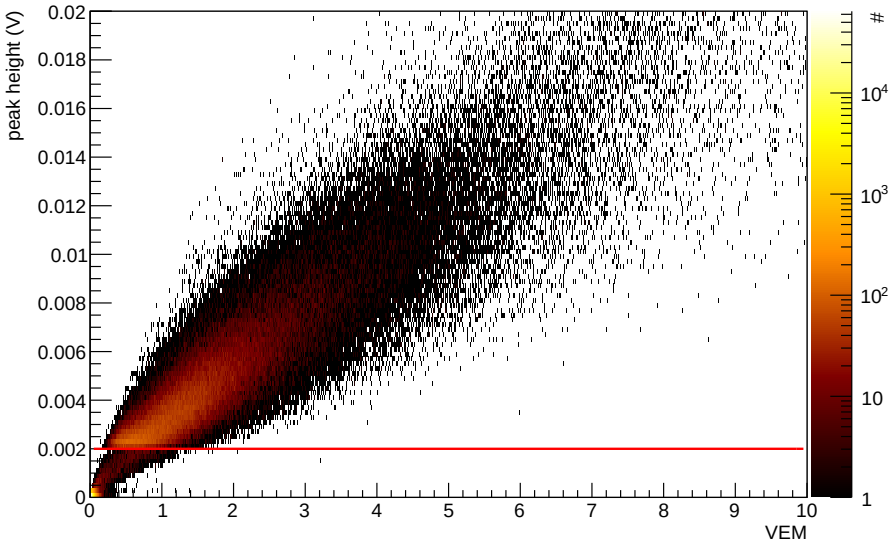

Figure 4.11: Distribution of the peak height and the corresponding integrated signal in vertical equivalent muon (VEM) for all Top-scintilltors. The data were taken in random- and air-shower-trigger mode. Per station a trigger in the Top- or Bottom-scintillator was required to also count sub-threshold events. The red solid line indicates the trigger-threshold of about 2 mV. Below the threshold, the number of events with signals corresponding to more than 1 VEM is negligible.

der to increase the sensitivity. Nevertheless, the higher threshold is justified as only very few signals above 1 VEM stay undetected and the trigger rate can be reduced.

4.2.3 Lateral Distribution Function

In order to reconstruct the core position of the air shower, the lateral distribution of the particles with respect to the shower axis is used. For the fit, the NKG function introduced in equation 1.23 is employed as lateral distribution function (LDF). Together with the two coordinates of the core position encoded in the radial distance r to the shower axis, the parametrization has five free parameters. The number of scintillators with a signal above threshold is normally not large enough to fit 5 free parameters and even if, the fitting procedure is rather unstable for these cases. Therefore, parameters are fixed as it is also done in other experiments, e.g., KASCADE [153]. To fit the core position, X, Y and N_{ch} are free parameters and R as well as s are fixed in the reconstruction presented here.

LDF Fit Parameters

To find appropriate values to fix the parameters, simulations are used. More than 400 showers simulated with the CORSIKA simulation package are used in combination with the GEANT4 model of the scintillators sketched in section 4.2.2. To generate a lateral distribution from

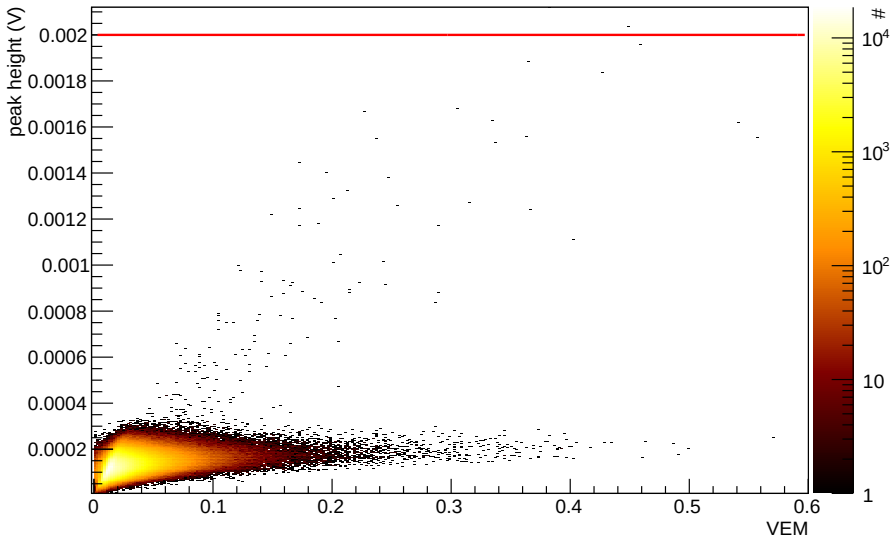

Figure 4.12: Distribution of the pulse height and the corresponding integrated signal in vertical equivalent muon (VEM) for all Top-scintillators. The data were taken in the 10 second trigger mode recording mostly electronic noise. The red line indicates the threshold of about 2 mV. The majority of the entries is concentrated below 300 μV and 0.1 VEM with a tail to higher VEM fractions.

the CORSIKA output, the particles are binned in rings of 5 m radial thickness in the shower plane. All particles are shot onto an area underneath the detector which is slightly bigger than the plastic scintillator. this procedure takes effects of edge cutting particles into account. The original directions of the shower particles are preserved. The deposited energy is weighted according to the particle weight assigned by CORSIKA and normalized to the area of the ring and the impact area. The resulting histograms are fitted with equation 1.23 and an example is shown in figure 4.13. Note that the distribution is fitted only in the range from $2 - 600\,\mathrm{m}$ as the asymptotic behaviour very close to the axis is unphysical and the function is known to deviate from the real particle distribution for larger distances to the axis. The distribution of the parameters from all fits can be used to fix the free parameters making also fits of measured data with only a handful of data points on a shower-by-shower basis possible. For R and s these distributions are shown in figure 4.14. Inclined showers with zenith angles above $45°$ show a large spread for both parameters. This might be due to the fact that the electromagnetic part of those showers dies out before reaching the detector leading to partly unphysical fit results. Therefore, a cut on the zenith angle of 45° is applied to the simulations. From both distributions, the mean values are taken as fixed values for the corresponding parameters: $R = 34.1 \pm 2.9\,\mathrm{m}$ and $s = 1.70 \pm 0.02$. In contrast to the theoretically calculated characteristic radius for purely electromagnetic showers which is of the order of 80 m, for hadronic showers a value of R around $30 - 40\,\mathrm{m}$ and a fixed shower age have been proven to be suitable fit conditions for various experiments [153, 154] and simulations.

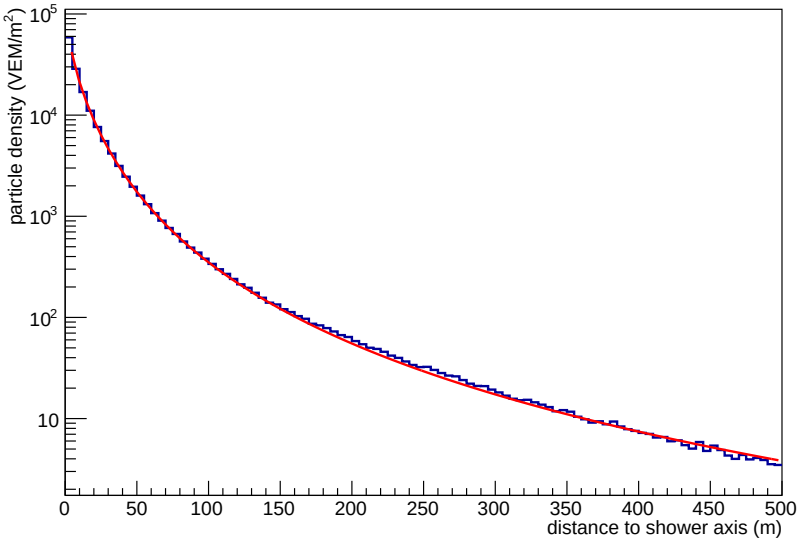

Figure 4.13: Simulated particle density as a function of the distance to the shower axis using a simplified model of the detector. The particles were generated with CORSIKA and the number of particles in VEM/m^2 per distance bin is inferred via the deposited energy given by a GEANT4 simulation and the detector calibration. The line indicates a fit with the NKG function (equation 1.23) in the range of $2 - 600\,\mathrm{m}$.

4.3 Reconstruction of Measured Air Showers

By applying the methods discussed in the previous section to data acquired with the particle detectors of AERA, the core position of air showers is reconstructed. The reconstruction of the arrival direction is analogous to the one for the SD. In the following sections, the used dataset is described and the reconstructed shower parameters are presented.

4.3.1 Dataset and Reconstruction

The data used were recorded with AERA124 from May 2013 until November 2014. During this time, data were acquired with different trigger conditions. Among those were the requirements to have at least 3 triggered scintillator stations, or 2 triggered scintillator stations and one radio self-trigger. In addition, variations of the acceptance for Bottom-scintillator triggers occur in the data.

In a basic coincidence check with the SD data, only scintillator events are selected which have an SD counterpart close to AERA within one second. The data are merged and reconstructed with the $\overline{\mathrm{Off}}\underline{\mathrm{line}}$ framework in a modified version of the example application *RdHybridReconstruction*. The used modules for the scintillator reconstruction can be seen in the following whereas the SD part of the reconstruction stays unchanged:

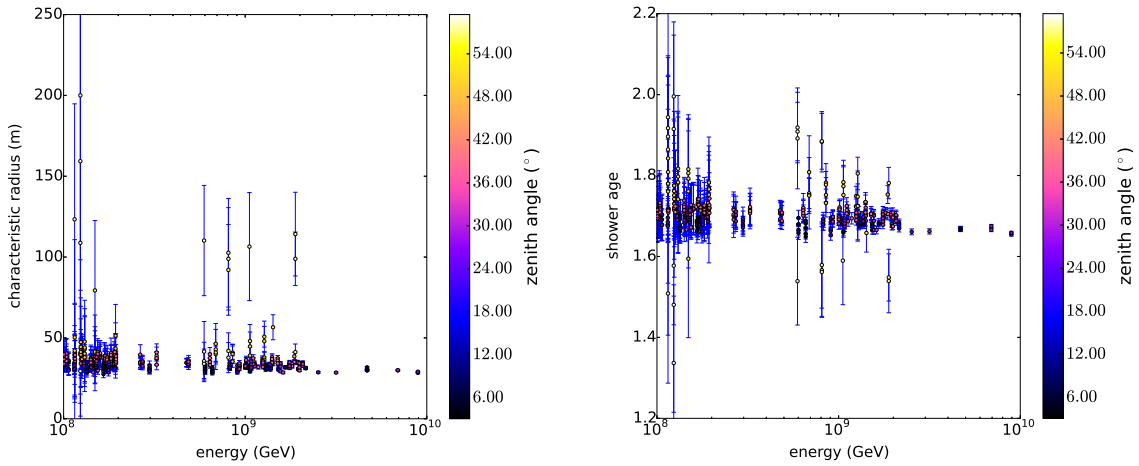

Figure 4.14: Fit parameters for the characteristic radius R (left) and the shower age s (right) for all simulated showers according to equation 1.23. The resulting mean values after applying a cut on the zenith angle of 45° are $R = 34.1 \pm 2.9\,\mathrm{m}$ and $s = 1.70 \pm 0.02$.

```
<module> EventFileReaderOG                    </module>
<module> RdEventPreSelector                   </module>
<module> RdEventInitializer                   </module>
<module> RdChannelADCToVoltageConverter       </module>
<module> RdChannelSelector                    </module>
<module> RdChannelPedestalRemover             </module>
<module> RdScintSignalReconstructor           </module>
<module> RdScintPlaneFit                      </module>
```

In case of triggering on Top- or Bottom-scintillators, the signal in the Top-scintillator could be below threshold and therefore a cut on the minimum signal height in the Top-scintillator of 2 mV is applied. After the determination of the integrated signal of the PMTs, the values are directly converted into units of VEM employing the calibration values obtained in section 4.2.2. In total, 23208 showers have been successfully reconstructed with this method.
For the reconstruction of the shower core position, the results from analysing simulated showers in section 4.2.3 are transferred to the data analysis. Before fitting individual showers, a few selection criteria on shower and station basis are applied. As for the simulations, a cut on the zenith angles reconstructed with SD of $45°$ is applied. Due to ambiguities concerning the scintillator direction reconstruction outlined in section 4.3.3, a cut on the difference in arrival direction between scintillators and SD is not applied in this analysis. To ensure reliable results from SD, a successful LDF reconstruction (RecLevel ≥ 3) and a 6T5-trigger are required. For the Top-scintillators, a minimum number of 4 stations with a measured signal of 1 VEM or more is necessary to consider the shower. In total 3908 showers are selected with these criteria. The number of cut showers for individual reasons is shown in table 4.1.

Table 4.1: Gerneral cuts on the used AERA scintillator dataset. The cuts select 3908 of the 23208 successfully reconstructed coincident showers.

cut	number of showers after cut
SD Quality (6T5 + RecLevel $\geq$3)	17455
SD zenith angle $< 45°$	15836
Number Top-scintillators with signal > 4	3908

4.3.2 Measured Particle LDF

The LDF of the SD differs from the one of the scintillators due to the different detector responses. The profiles of the measured signals in both detectors as function of distance to the SD shower axis and the SD energy are shown in figure 4.15. Water Cherenkov detectors are sensitive to charged particles with energies above the Cherenkov threshold and photons producing those charged particles in the detector. In comparison, scintillators are sensitive to charged particles that are stopped in the detector and also to minimum ionizing through-going particles. Therefore, close to the shower axis, the induced signal is higher in the scintillators, as there are many low-energy charged particles that deposit a large fraction of their energy in the detector. Further away from the axis, the muons dominate the particle content in the shower equalizing the measured signals [155]. Unfortunately, the small size of the scintillators does not allow measurements at low particle densities i.e., large distances. Also visible are the different behaviours of the detectors for different energies. Here, the water Cherenkov signals spread out with higher energy and larger distance, whereas the scintillators show a reversed pattern even though it is less pronounced due to low statistics.
For the case of reconstructing individual showers, it turns out that the number of showers with high enough station multiplicity to properly fit r_M is rather small and therefore, the characteristic radius is fixed together with the shower age to the values of $R = 34.1\,\mathrm{m}$ and $s = 1.70$ calculated based on simulations (see section 4.2.3). With these settings, the fit can be performed with only four stations maximizing the number of reconstructable showers. It should also be noted that the LDF shape changes with energy as shown in figure 4.15, which is not accounted for in the fixed parameter fit.

Maximum Likelihood Function for the LDF Fit

To determine the LDF, equation 1.23 is fitted to the data with fixed R and s in a maximum likelihood approach analogue to the SD reconstruction [136]. The likelihood function includes the contributions of small signal stations (f_{signal}) and sub-threshold stations (f_{silent}) in

$$L = \prod_i f_{\text{signal}}(n_i, \mu_i) \prod_i f_{\text{silent}}(n_i, \mu_i). \tag{4.3}$$

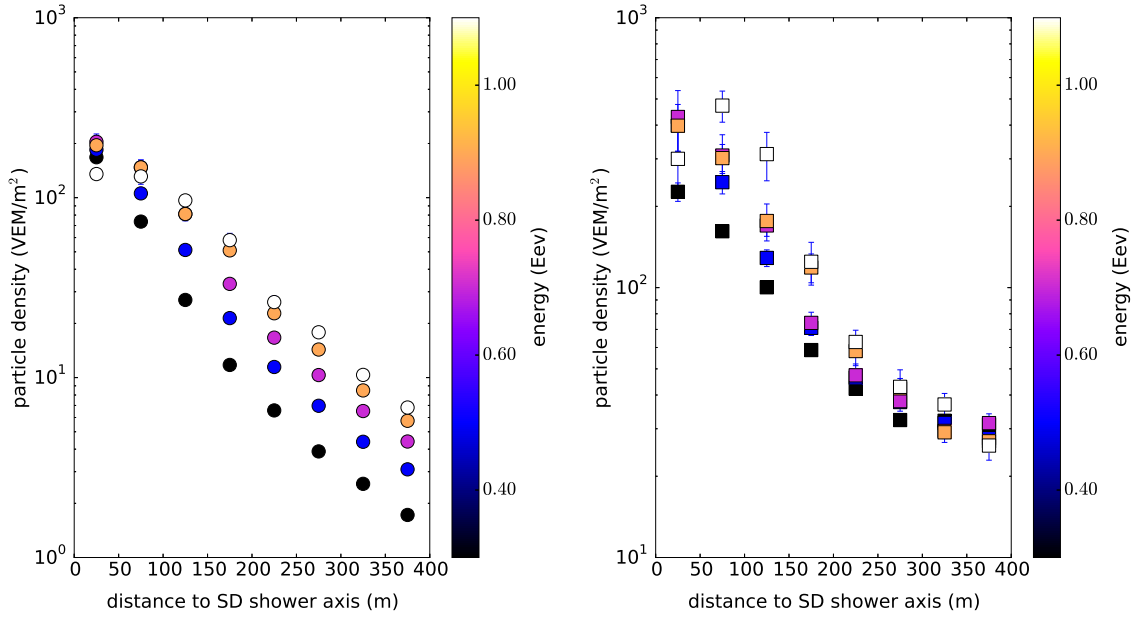

Figure 4.15: Particle density profiles as a function of the distance to the SD shower axis for SD (left) and Top-scintillators (right) for different shower energies (color code). The two plots show the different detector responses for the water Cherenkov detectors and the plastic scintillators. The measured signal in the scintillation detectors is higher, as they also measure a signal from low energetic particles below the Cherenkov threshold. These low-energetic particles are mostly concentrated around the shower axis.

Here, the product is calculated over station i at position (x, y) where n_i is the number of detected particles and μ_i is the expectation value from equation 1.23. The log-likelihood function is then

$$\ell = \sum_i \ln f_{\text{signal}}(n_i, \mu_i) + \sum_i \ln f_{\text{silent}}(n_i, \mu_i), \tag{4.4}$$

respectively.

Poissonian statistics is employed to calculate the likelihood contributions for signal stations with

$$\ln f_{\text{signal}}(n_i, \mu_i) = n_i \ln \mu_i - \mu_i - \sum_{j=1}^{n_i} \ln j. \tag{4.5}$$

For non-triggered stations below a threshold of 1 VEM, the contribution is:

$$\ln f_{\text{silent}}(1, \mu_i) = -\mu_i + \ln(1 + \mu_i). \tag{4.6}$$

In order to include non-triggered stations into the reconstruction, the precise status of all stations at the time of the shower is necessary to exclude non operational detectors. The technical framework in form of a bad-period database is work in progress. During the period of data

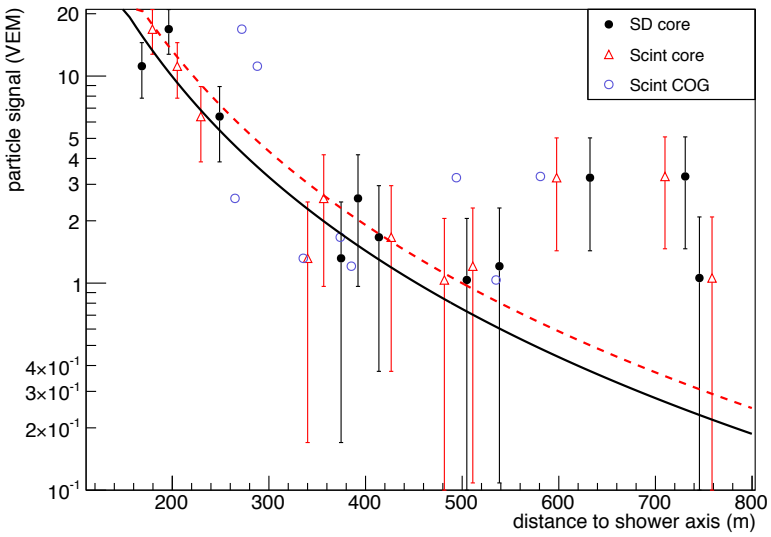

Figure 4.16: Lateral particle distribution in vertical equivalent muon (VEM) per detector of an individual air shower measured with the AERA scintillators. The line and points in black, are plotted using the SD core position. The red dotted line and triangles are plotted using the scintillator core position. The signals are fitted with equation 1.23 and with fixed shower age and characteristic radius in both cases. The purple circles indicate the distance to the scintillator center of gravity (COG) used as start values of the core position for the LDF fit. The distance between the SD core position and the found scintillator core position is 41 m.

acquisition, a significant number of stations have experienced downtime. Therefore, the following LDF fits will currently not include sub-threshold station contributions.

LDF Fits

In the approach presented here, the shower core position in (x, y) coordinates and the number of charged particles N_{ch} are fitted by maximizing the log likelihood function. Additionally, it was tried to include the shower-age parameter as a free parameter in an iterative procedure for high station-multiplicity events. However, no stable fit process could be established for this procedure and therefore the shower age is kept fixed as well. As start value for the core position, the reconstructed center of gravity of the Top-scintillator stations is used. The direction of the shower axis is taken from SD. An example of a fitted shower is shown in figure 4.16. The distribution of the distances between SD and scintillator core for all 2012 successfully fitted showers is shown in figure 4.17. Here, a distinction is made between showers where the reconstructed core is contained within the signal stations (dashed red, 410 events) and events where the core is not contained (blue, 1602 events). For not contained events, the core reconstruction can suffer from a weakly constrained geometry [101]. The fit does not converge for 1896 events. As the quality of the fit does not provide information about the absolute quality

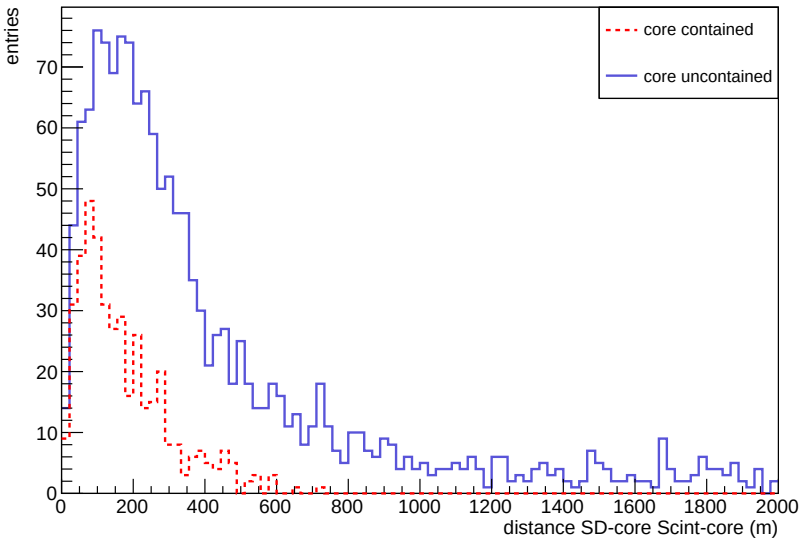

Figure 4.17: Distribution of the distances between the reconstructed SD and scintillator core-position for contained (dashed red) and uncontained (blue) showers.

of the core reconstruction, this has to be evaluated in future work by using air shower simulations and a detector simulation of the whole scintillator array. Far away from the axis, the particle density in the shower gets smaller than one particle per effective scintillator area and the chance increases that detected particles are not associated with the shower. Therefore, it is helpful to introduce a cut at the distance where the expected number of particles is one per scintillator. This distance is estimated as function of the energy based on the simulations used in section 4.2.3. The corresponding plot is shown on the left side of figure 4.18. The red line indicates a quadratic fit to the data shifted upwards by +150 m. This shift accounts for the fact that the SD core is used to calculate the distance of the stations during the reconstruction. On the right side of figure 4.18, the resulting distances between the reconstructed SD and scintillator core are shown. The number of events decreases as more events fail the four station cut (552 uncontained, 185 contained). The width of the distributions also decreases significantly. As for the reconstruction without a distance cut, the quality of the core reconstruction can however only be determined from detailed simulations.

4.3.3 Direction Reconstruction

The arrival direction of the air showers is reconstructed using the timing information of the signals. In a simple approach, a plane wave is fitted to the peak times of the minimum signal in the first negative peak below threshold. The reconstruction itself is analogue to the direction reconstruction for Surface Detector array discussed in section 3.4.1. In this analysis a plane-fit is chosen to maximize the number of reconstructed events as it only requires three stations detecting particles. The reconstructed directions are compared to those measured by the SD

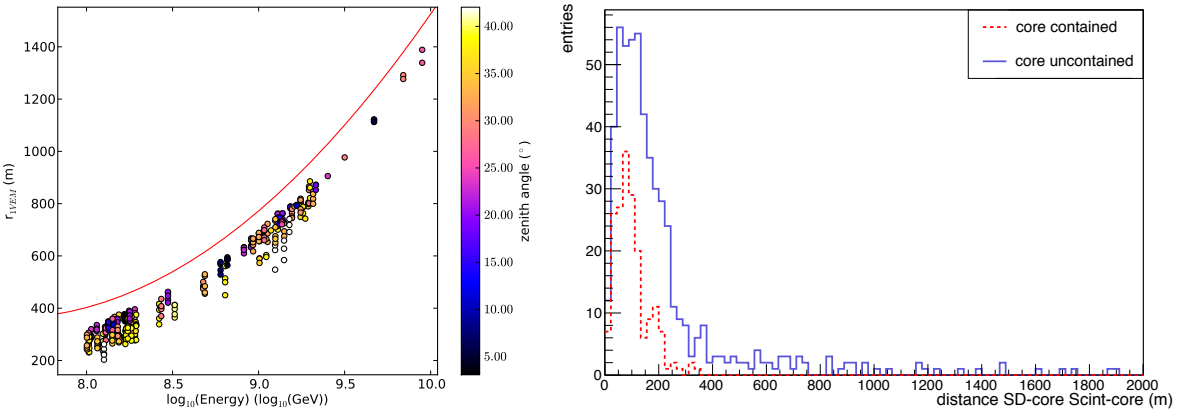

Figure 4.18: On the left site, the distance from the shower axis at which the particle density is equal to one particle per scintillator is shown as a function of the shower energy. The distance is determined from simulations. The red line indicates a quadratic fit to the data offset by +150 m taken as a quality cut on the distance. The right plot shows the corresponding distribution of the distances between the reconstructed SD and scintillator core for contained (dashed red) and uncontained (blue) showers after applying the distance cut.

and the resulting differences are displayed in the histogram in figure 4.19 (black dotted line). The distribution of the angular differences has a rather long tail which differs from a Rayleigh-like distribution. To check whether this is due to stations which were coincidentally triggered by single particles unrelated to the shower, the direction is fitted for various selections of stations. All distributions have a very similar shape and none of the selected cases improves the agreement to the SD direction significantly. Using the station trigger time instead of the peak time does also not alter the result. The seen differences are not dominantly caused by the GPS system as analysing the radio direction reconstruction employing the same GPS system, results in less deviation from the SD measurements. The small size of the scintillation detector is a likely reason as it only allows for a coarse sampling of the shower particles and thereby leads to fluctuations in the timing of the signals.

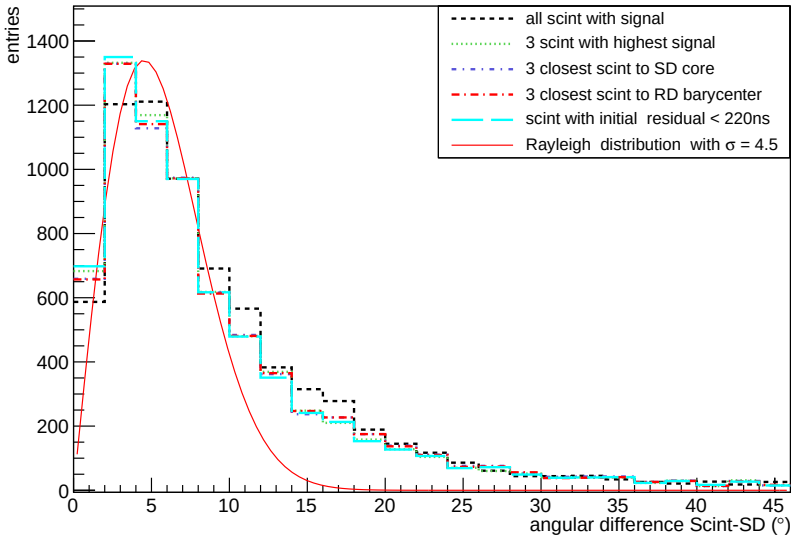

Figure 4.19: Distribution of the angular difference between the fitted direction of the shower axis derived from the SD and the scintillator data. The green dotted line shows the distribution based only on the plane-fit with the three highest signal stations, the blue dash-dotted line represents the fit with the three stations closest to the SD core position and the red dash-dotted line represents for the fit utilizing the three stations closest to the RD Barycenter. For the distribution shown with the dashed cyan line, a cut on the time residuals of 220 ns with respect to the initial plane-fit is made and the directions are refitted. The solid line indicates the fit of a Rayleigh function with $\sigma = 0.45$.

5

The Radio Lateral Distribution Function

Parts of this chapter are based on the publication:

A. Nelles, J. Schulz, J.R. Hörandel
A parameterization for the radio signal measured with AERA
Auger Internal Publication, GAP2014_073 [156]

The shape of the lateral distribution of the radio signals differs from the classical particle lateral distribution function. This is due to the superposition of radiation originating from the two different emission mechanisms as discussed in chapter 1. As a result of the interplay of the two mechanisms, the general shape of the radio footprint depends on the geometry which challenges modelling the data as well as the production of simulation libraries. This issue can be overcome by transforming the coordinate system into the $\vec{v} \times \vec{B}$ and $\vec{v} \times (\vec{v} \times \vec{B})$ plane, see section 1.2.4 and 3.8. In this coordinate system, the lateral distributions have a common overall shape for all geometries. Thereby, a general two-dimensional parametrization becomes feasible. Besides that, the approach is used to generate air-shower simulations in a generic way. In this chapter, the two-dimensional lateral distribution function is discussed, focussing on the application to AERA data and the correlation of function parameters with air-shower/cosmic-ray properties.

5.1 LDF Parametrization for AERA

From the shape of the density profiles generated with the air shower simulations described in section 3.8, the general two-dimensional function has been deduced as

$$u(\vec{r}) = A_+ \cdot \exp\left(\frac{-(\vec{r} - \vec{r_+})^2}{\sigma_+^2}\right) - A_- \cdot \exp\left(\frac{-(\vec{r} - \vec{r_-})^2}{\sigma_-^2}\right), \tag{5.1}$$

where $A_\pm$ are amplitude scaling parameters ($A_+ > A_-$), $\vec{r}_\pm$ are location parameters, and $\sigma_\pm$ are width parameters (rewritten from equation 1.26). To check the usability of the parametrization as fit function in an air-shower reconstruction, the function was first tested on LOFAR data as described in [96]. For the application, the number of free parameters was reduced to five by determining correlations between parameters based on the underlying simulation dataset. For the application of the function to AERA data, these correlations had to be redetermined on

Table 5.1: LDF parameters C_0 - C_4 of equation 5.2 for the corresponding zenith-angle range.

zenith angle	C_0	C_1(m)	C_2 (m)	C_3 (m)	C_4 (m^{-1})
$0° - 60°$	-	-	-	16.25	0.0079
$0° - 10°$	0.41	-8.0 ± 0.3	21.2 ± 0.4	-	-
$10° - 20°$	0.41	-10.0 ± 0.4	23.1 ± 0.4	-	-
$20° - 30°$	0.41	-12.0 ± 0.3	25.5 ± 0.3	-	-
$30° - 40°$	0.41	-20.0 ± 0.4	32.0 ± 0.6	-	-
$40° - 50°$	0.46	-25.1 ± 0.9	34.5 ± 0.7	-	-
$50° - 60°$	0.71	-27.3 ± 1.0	9.8 ± 1.5	-	-

simulations which include the height above see level and the direction and strength of the magnetic field at the AERA site. It is further desirable to decrease the number of free parameters in order to obtain a stable fit even for a low station multiplicity. Both aspects are addressed in work presented in [156]. After additional modifications, the AERA radio LDF is parametrized in the shower-plane by

$$u(\vec{r}) = A\left[\exp\left(\frac{-(\vec{r} + C_1\,\vec{e}_{\vec{v}\times\vec{B}} - \vec{r}_{\text{core}})^2}{\sigma^2}\right) - C_0\,\exp\left(\frac{-(\vec{r} + C_2\,\vec{e}_{\vec{v}\times\vec{B}} - \vec{r}_{\text{core}})^2}{(C_3 e^{C_4\,\sigma})^2}\right)\right]. \quad (5.2)$$

Here, A is the amplitude, σ is the width of the distribution, $\vec{r}_{\text{core}}$ is the position of the shower core and C_{1-4} are the constants arising from the simulation-based parameter reduction. The five parameters are given in table 5.1. Three of them are zenith-angle dependent and their values are given for bins of 10°. The ratio of the amplitudes of the two Gaussians C_0 can also be described as a function of the squared sine of the geomagnetic angle for zenith angles up to 50° as

$$C_0 = 0.337 \times \sin^2(\alpha)^{-0.218}\,. \quad (5.3)$$

As the energy in the geomagnetic emission scales with $\sin^2(\alpha)$ this is a physically motivated parametrization. The fit quality however does in general not improve in this case, most likely because the interplay between the two Gaussian functions is not only determined by the emission mechanisms but also accounts for relativistic beaming effects.

An example of the parametrization fitted to the simulated energy-density pattern is shown in figure 5.1 in the shower plane and in a one-dimensional projection of all points onto the $\vec{v} \times \vec{B}$ axis. The fit re-samples the asymmetry of the energy-density pattern and also the overall amplitude and fall off. The dip in the pattern due to the destructive interference of geomagnetic and charge excess emission is overestimated in this case due to the binned C-parameters. All together the distribution is sufficiently described and the method marks a significant improvement when compared to one-dimensional approaches.

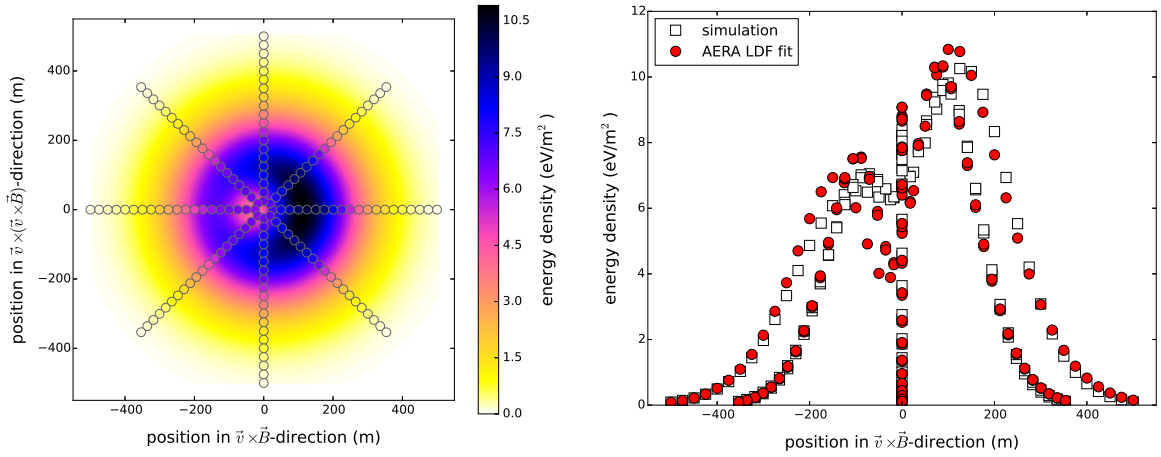

Figure 5.1: Application of the parametrized LDF used in AERA (equation 5.2) to a star-shape simulation. Left: Two-dimensional representation of the fitted LDF (background color) to the simulated energy-density pattern (circles). Right: Simulated and fitted values projected onto the $\vec{v} \times \vec{B}$ axis for different slices along the $\vec{v} \times (\vec{v} \times \vec{B})$ axis.

5.2 Relation between LDF Parameters and Air-Shower Properties

From the free fit parameters in the formulation of equation 5.2, air-shower parameters can be directly inferred. An alternative is the cross calibration with values obtained with a different detection technique or if this is not possible with values obtained from simulations.
The shower-core position is directly accessible from the fit result. The width of the energy-density distribution is determined by the beaming of the radiation from the emission region to the ground. Therefore, the width of the LDF σ is correlated with the distance to the emission region. This distance is approximated by the distance to X_{max}, defined as

$$D_{\mathrm{max}} = X_{\mathrm{total}} / \cos(\theta) - X_{\mathrm{max}}, \tag{5.4}$$

where X_{total} is the total thickness of the atmosphere above the Pierre Auger Observatory and θ is the zenith angle of the arrival direction. A simple sketch of the effect is shown in figure 5.2. In earlier work [96, 157], the amplitude parameter C_0 (or A_+ in the original equation 5.1) was found to be correlated with the primary energy when corrected with $\sin^2(\alpha)$ (the corrected parameter will be denoted by an asterisk in the following).

5.2.1 Air-Shower Simulation Set

To determine the resolution of reconstructed air shower parameters based on the two-dimensional LDF in a general way and also for the case of AERA, an extended set of simulations is used. In total 3150 simulated air showers with different incoming directions, energies, and X_{max}

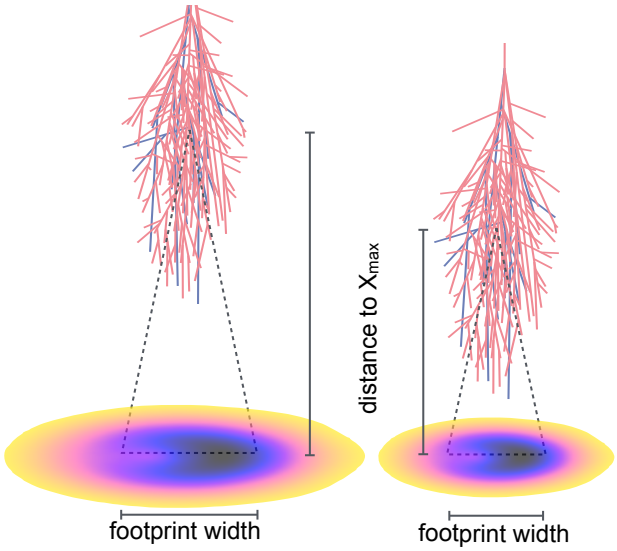

Figure 5.2: Sketch of the relation between the width of the footprint of the radio signal and the distance to the shower maximum.

values are used. The corresponding distributions are shown in figure 5.3. 896 simulations were performed for iron nuclei and 2254 initiated by protons. All simulated air showers have a geomagnetic angle of more than 10°. To study the resolution in general and for the case of the detector geometry of AERA, various analyses are performed for energy, core position, and X_{max} and presented in the following subsections.

5.2.2 Energy

The corrected fit parameter A_{+}^{*} is correlated with the simulated primary energy squared. The distribution as well as the resolution is shown in figure 5.4. In contrast to earlier work, the spread around the fit is asymmetric for the given simulation set and the resolution shows a rather long tail on one side. This discrepancy is most likely due to a shortcoming of the usage of A_{+}^{*} as an energy estimator. Depending on the geometry, e.g., the distance to the emission region, the emission pattern can be spread over a larger or smaller area due to projection effects. Therefore, two air showers with the same primary energy and the same arrival direction will show a spread in A_{+}^{*} because of the fluctuations in X_{max} which correspond to fluctuations of the distance to the emission region. An extreme example is shown in figure 5.5 where a proton and an iron simulation, for the same primary energy and incoming direction give almost a factor of 10 difference in the maximum energy-density A_{+}. Depending on the simulated shower geometries, primaries, and energies, this effect has more or less impact on the energy resolution. To improve the energy estimation it is necessary to take the amplitude of the energy density as well as the width of the pattern into account. Therefore, an improved estimator is

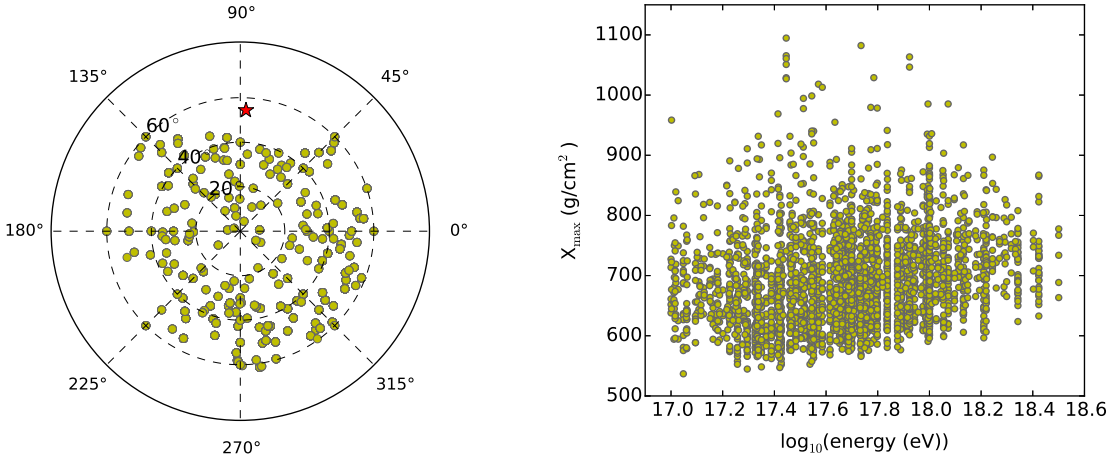

Figure 5.3: Distribution of parameters in the simulated dataset. Left: Skyplot of the incoming direction of the simulated showers. The star denotes the direction of the geomagnetic field. Right: $X_{\max}$ values as function of the simulated cosmic-ray energy in the set.

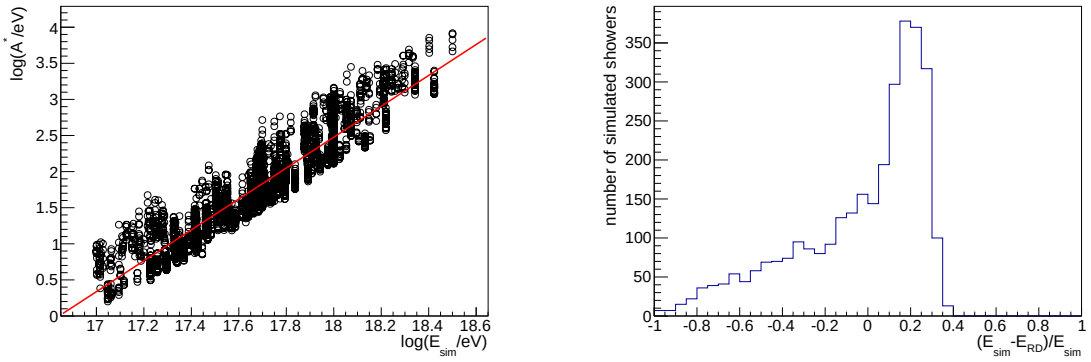

Figure 5.4: Correlation between A^*_+ and the simulated primary energy. Left: Linear fit to the distribution with a slope of 2.14±0.02. Right: Relative difference between the reconstructed energy based on A^*_+ and the simulated primary energy. The distribution has a RMS of 30.2% and a mean of -3.1%.

introduced which is the spatial integral over the distribution of the energy density $u(\vec{r})$,

$$E_{\mathrm{rad}} = \int u(\vec{r})\, \mathrm{d}^2\vec{r}. \tag{5.5}$$

The integrated energy density is also a well motivated quantity as it is the total energy radiated by the air-shower particles. This quantity, when corrected for the geomagnetic angle, is expected to be proportional to the primary energy of the cosmic ray as E_{rad} is expected to scale quadratically with the number of electrons and positrons in the shower due to the coherent emission. For a parametrization-independent determination of the total radiated energy, the interpolation of the simulated energy density on the star-shape antenna pattern is used. The interpolated profile is numerically integrated on a circle with a radius of 500 m which corresponds to the extend of the star-shape pattern. This energy in the radiation is taken as the

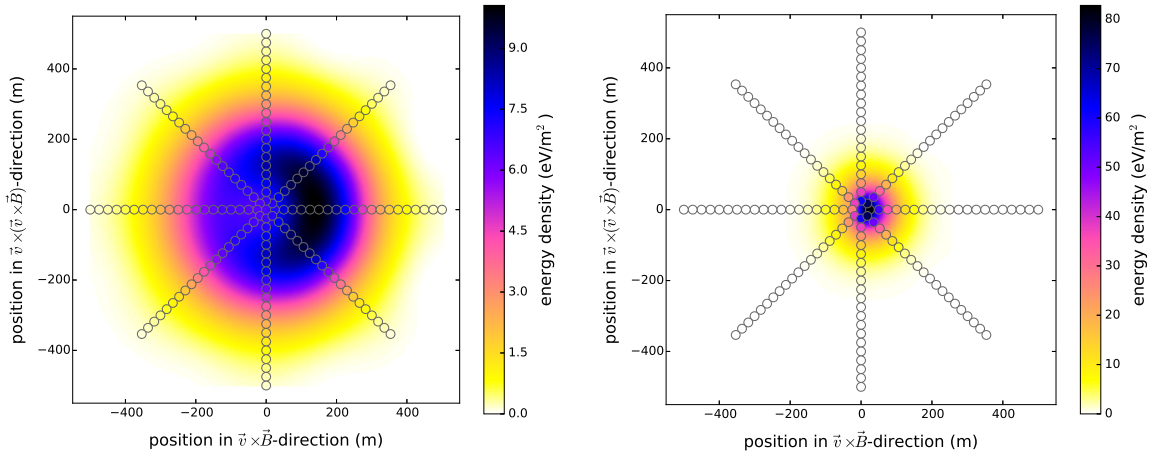

Figure 5.5: Simulations of the energy-density pattern of two extensive air showers with the same primary energy (0.44 EeV) and arrival direction (zenith angle: 55.7° azimuth angle: 5.9°). Left: Simulation with an $X_{\max}$ value of 592 g/cm^2 (iron). Right: Simulation with an $X_{\max}$ value of 1221 g/cm^2 (proton). The color scales differ by almost a factor of 10.

reference radiation energy of the following studies. When corrected for the geomagnetic angle ($S_{\text{radio}} = E_{\text{rad}}/\sin^2(\alpha)$), the correlation with the primary energy shows a small spread of 9.1% taken as the width of the distribution of relative differences for the used simulation set as shown in figure 5.6 (top row). The resolution has an intrinsic limit due to shower-to-shower fluctuations and second-order geometric effects. Determining the resolution only for showers initiated by iron nuclei yields a value of 6.0%. As air showers initiated by iron nuclei show in general significantly less intrinsic shower-to-shower fluctuations the contributions of these fluctuations is estimated to be comparable to the ones from geometric effects.
For the application to experimental data, the resolution of the cosmic-ray energy determination procedure using the integral over the energy-density distribution also depends on the accuracy with which the real energy density profile can be described by the LDF. Fitting the original equation 5.1 and the AERA specific parametrization in form of equation 5.2 to the star-shape simulations shows the impact of the simplified description on the resolution. For the original LDF description, the correlation between S_{radio} and the primary energy for the same shower simulations as used before is displayed in figure 5.6 (center row). Fitting the energy density distribution with the empirical parametrization in equation 5.1 introduces an additional scatter of 4% on the energy resolution. The reduction of fit parameters in the binned approach does not lead to a decrease in resolution compared to the full parameter fit. Even though the shower-by-shower determination of E_{rad} reveals differences arising from the two parametrizations, the overall resolution in terms of the energy reconstruction is almost the same in both cases as shown in figure 5.6 (bottom row) for the case of using the AERA parametrization.

In the next step, the influence of a sparse sampling of the energy-density profile on the ground

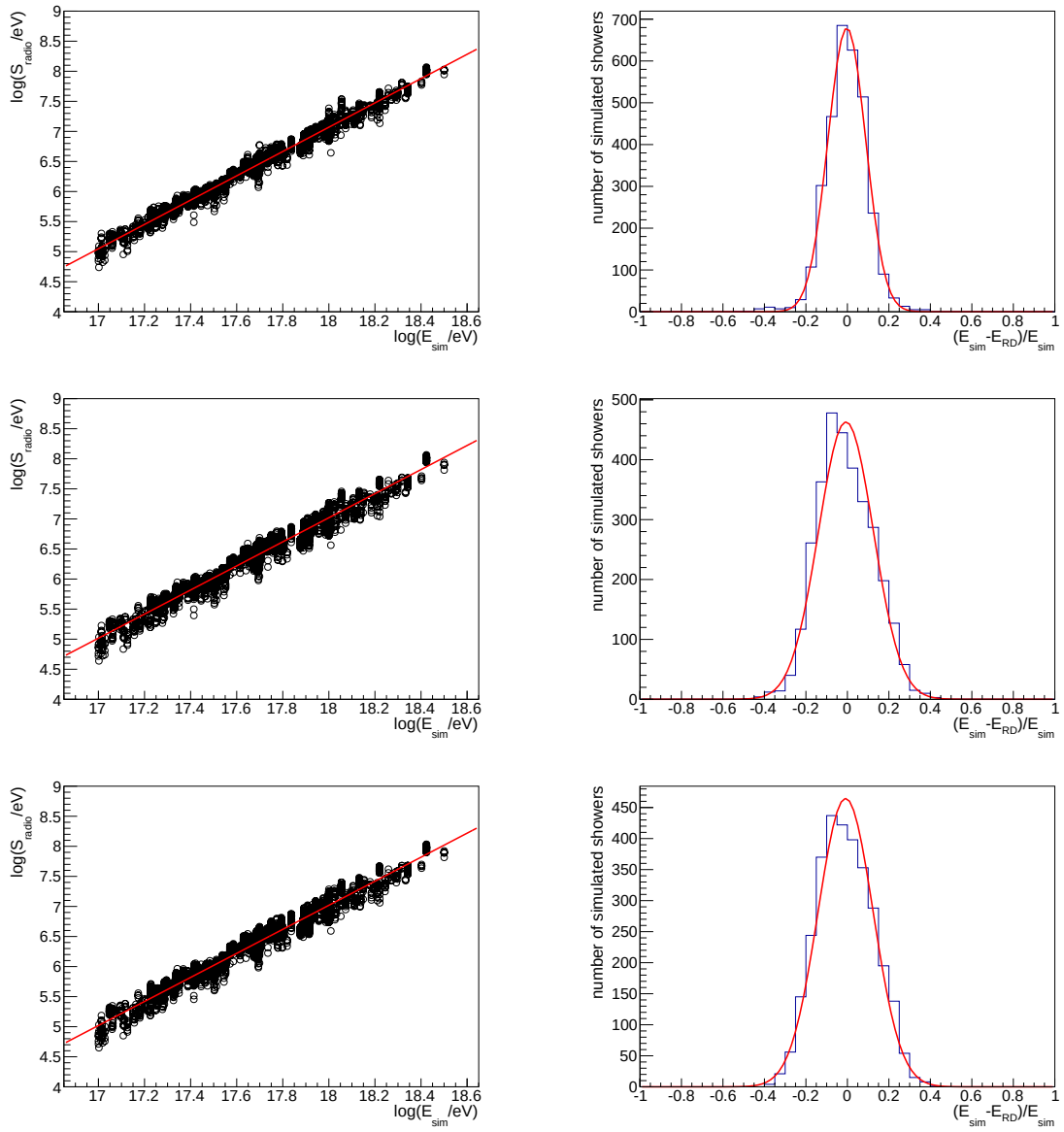

Figure 5.6: Correlations between S_{radio} based on the integral over the different versions of the LDF and the simulated primary energy. Left: Linear fit to the distribution. Right: Relative difference between the reconstructed energy based on S_{radio} and the simulated primary-particle energy. Top row: Numerical integration over the interpolated energy-densities of the star-shape simulations. Center row: Integration over the full parameter LDF given in equation 5.1. Bottom row: Integration over the LDF as adapted for AERA given in equation 5.2. The fit results as well as the obtained resolutions are listed in table 5.2.

as it is the case for an experimental setup is analysed. The sampling of the distribution depends on the grid of antenna stations as well as the core position and the arrival direction of the air shower. As it is computationally extremely expensive to re-simulate every air shower in the set with different core positions, a generic method is employed using the star-shape simulations. For every simulated air shower in the set, the AERA124 (and also AERA24 only) antenna-station positions are transformed into the $\vec{v} \times \vec{B}$ vs. $\vec{v} \times (\vec{v} \times \vec{B})$ plane. In this coordinate

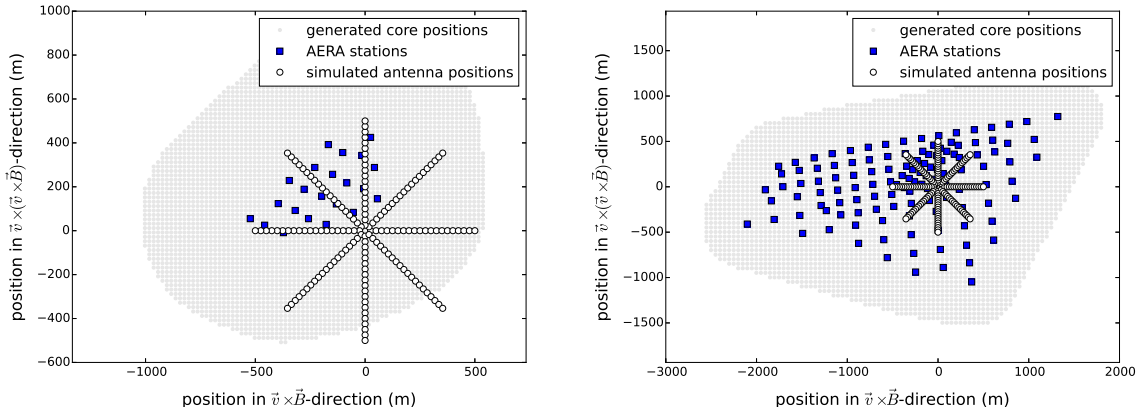

Figure 5.7: Example of the generated core positions for which a star-shape simulation is evaluated at the AERA antenna positions to test the influence of sampling on the LDF fit. Left: Core positions generated around the AERA24 RDS positions. Right: Core positions generated around the AERA124 RDS positions.

Table 5.2: Fitted slopes and corresponding resolutions of the correlations between the integrated energy density patterns and the primary particle energy using different parametrizations as shown in figure 5.6. In addition the values for the correlation for the usage of the corrected amplitude parameter A_+^* (see figure 5.4) are added.

used parametrization	slope	resolution (%)
A_+^* parameter	2.14 ± 0.02	30.2 (RMS)
interpolation	2.02 ± 0.01	9.1 ± 0.1
LDF original (equation 5.1)	2.00 ± 0.01	13.2 ± 0.2
LDF AERA (equation 5.2)	2.00 ± 0.01	13.3 ± 0.2

system, a convex hull with a distance of 500 m is defined around the array. Within the hull, core positions are generated on a regular grid with a spacing of 50 m (20 m for the AERA24 array) and transformed back to the East-North-vertical-coordinate system. An example of the generated shower-core positions for a given simulation is displayed in figure 5.7. For every core position, the energy density pattern taken from the interpolation of the simulated antenna positions is evaluated at the station positions corresponding to the chosen core position in the shower plane. In addition, also the simulated maximum amplitudes of the electric field at each simulated antenna station are interpolated and evaluated at the station positions of the AERA array. The interpolated amplitudes are used to define a lower limit below which the station would not have measured a signal in an experimental setup. This minimum amplitude is defined as 100 μV/m [158]. If the evaluation of the interpolation of less than three station positions on the AERA grid reveals an amplitude above this threshold, the procedure is aborted. As the parametrization of the LDF for AERA has 4 free parameters, at least five antenna stations with signal are needed to constrain the fit. However, in case of the experi-

Table 5.3: Values for mean and width of the Gaussian fits shown in figure 5.8. Additionally, the values for the total distributions are given. The fit uncertainties are of the order of 10^{-4} and thereby smaller than the stated precision.

array	# stations	contained	mean (Gaussian)	σ (Gaussian)	mean	std. dev.
configuration						
AERA24						
	$3-4$	yes	-0.159	0.110	-0.127	0.160
	$3-4$	no	-0.038	0.127	-0.174	0.240
	$5+$	yes	-0.042	0.068	-0.039	0.125
	$5+$	no	-0.052	0.123	-0.032	0.218
	all	all	-0.051	0.080	-0.071	0.212
AERA124						
	$3-4$	yes	-0.054	0.087	-0.106	0.203
	$3-4$	no	-0.009	0.063	-0.051	0.178
	$5+$	yes	-0.008	0.046	-0.022	0.119
	$5+$	no	-0.035	0.087	-0.029	0.136
	all	all	-0.020	0.060	-0.051	0.161

mental hybrid detection of air showers the two core-position parameters can be fixed to the core position as reconstructed externally, e.g., by the SD. For this analysis, the core position is fixed to the simulated core position in these cases. Stations below the amplitude threshold are included in the procedure as it is also the case for externally triggered data, where all stations are readout. The energy densities for stations further than 500 m away from the shower axis are set to 0 eV/m^2. The generated values for the energy density are fitted with the AERA parametrization of the LDF. The resulting radiation energy E_{rad} can then be compared to the one yielded from the numerical integral over the interpolation of the original simulation. The relative differences are distinguished for the cases of fixed and free core-position parameters (for $3-4$ or five and more signal stations) as well as for the core position being contained and not contained within the antenna array. In total, this method yields 4223690 reconstructed LDFs on the AERA24 array and 4686092 on the AERA124 array. For both arrays, the relative differences in radiation energy are shown in figure 5.8. The distributions in the varying cases are fitted with Gaussian functions to approximate the mean and the width of the distributions. The results are summarized in table 5.3. The widths of the distributions are of the order of 10%. Combined with the intrinsic energy resolution of E_{rad} taken from the integrated interpolation, the resulting resolution is about 14% which is in good agreement with the earlier findings for fitting the AERA parametrization directly to the energy density on the star shape pattern. The distributions especially for the cases of 3 and 4 signal stations are not Gaussian shaped in the tails. This has two reasons, one is that the shown distributions are superpositions of Gaussian

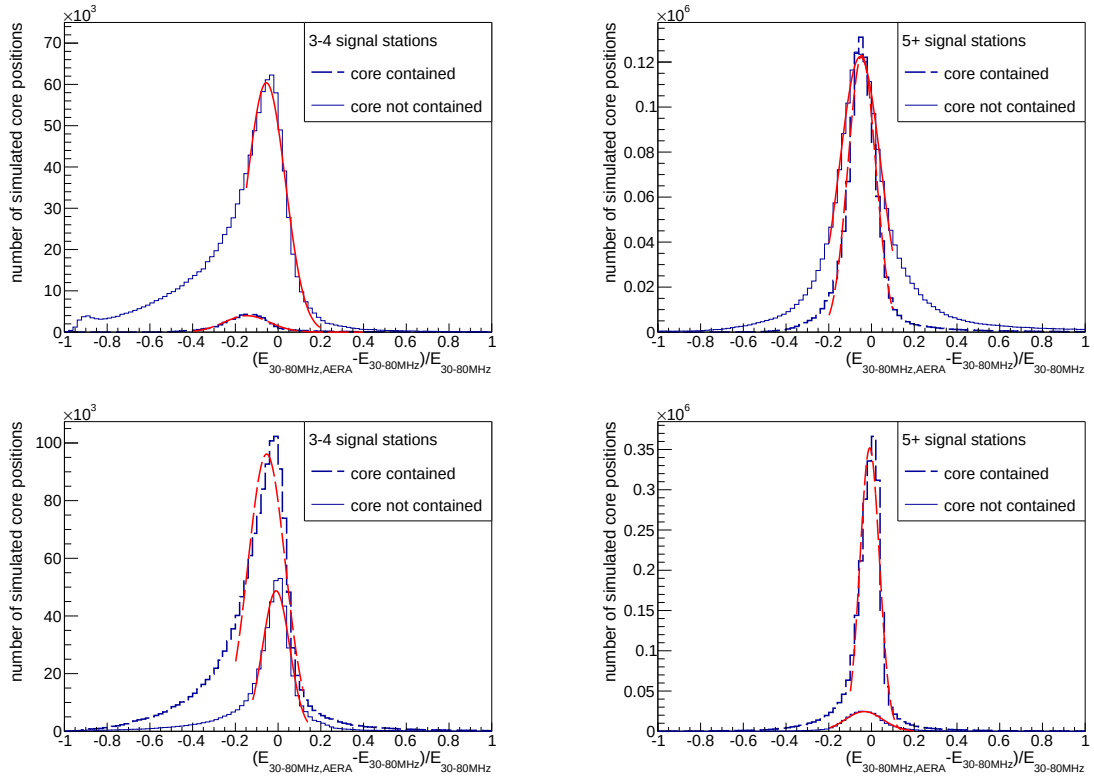

Figure 5.8: Comparison between the radiation energy E_{rad} taken from the interpolated energy density pattern and the one taken from the integration over the fit of the AERA LDF (equation 5.2) to the energy density evaluated at the AERA station positions (top row AERA24, bottom row AERA124). See text for further details on the procedure. Left: Relative difference in E_{rad} for three or four signal stations (evaluated amplitude $> 100\,\mu\mathrm{V/m}$). The parameters of the core position in the LDF are fixed to the true core position. Right: Relative difference in E_{rad} for 5 and more signal stations where the core position is a free fit parameter. The parameters of Gaussian fits to all distributions in the plotted range are given in table 5.3 together with the mean and the standard deviation of the whole distribution.

distributions of the relative differences in radiated energy of one air shower simulation under variation of the core position. Therefore, the total distribution is by construction not Gaussian in the tails. The second reason is the lower degree to which the LDF is constrained for certain geometries, e.g., when the signal station positions are very close together in the shower plane or the sampling is only on one site of the actual energy-density profile giving only very rough indications for the total amplitude or width. This effect gets bigger in the case of only 3 or 4 signal-stations despite the fixed core position. To also take the tail of the distributions into account the mean and the standard deviation are also calculated and given in table 5.3. From the standard deviations of the order of $15 - 20\%$ a total energy resolution of $17 - 22\%$ is determined which is in good agreement with experimental results discussed in chapter 6.
All distributions show a small negative offset of the order of 5% which corresponds to an underestimation of the radiation energy. The exact value however depends on the geometry of the air showers in the dataset. Taking subsets for only one type of primary or a small zenith

angle range, changes the absolute numbers. Therefore, a general correction for a bias introduced by the simplified description is not indicated. For the case of the AERA24 grid and 3 or 4 signal-station showers, the offset is significantly larger. For contained core positions, this constellation is suppressed as the AERA24 grid is rather dense and therefore only air showers with a very small footprint lead to the small number of signal stations. Mainly air showers with small zenith angles are in this subset which are known to be described by the LDF less accurately. On a large data sample, the influence of these effects on the overall resolution is however negligible as the fraction of these cases is suppressed since the radio footprint is small compared to the distance between the antennas. For not contained core-positions, the sampling on only one side of the axis is not sufficient to constrain the fit in all cases. This leads to an underestimation of the radiation energy. A possible bias in the reconstructed radiation energy from measured data is in general not expected to exceed 10% but the exact number can only be determined using simulations explicitly re-sampling the measured showers in geometry, energy, and shower development. Compared to the typical experimental systematic uncertainties in the radio detection of cosmic rays of the order of 30%, the possible contribution arising from the LDF parametrisation is in any case small.

5.2.3 Core Position

For air showers that were detected in five or more antenna stations, the LDF is used to reconstruct the core position. For this purpose, the resulting $\vec{r}_{\mathrm{core}}$ parameters are transformed from the shower plane to the ground plane. For the case where the AERA parametrization is fitted directly to the simulated energy densities on the star shaped grid, the spread of the reconstructed core position is of the order of 10 m in the $\vec{v} \times \vec{B}$-direction and about 5 m in the $\vec{v} \times (\vec{v} \times \vec{B})$-direction. The asymmetry in the spread arises from the construction of the LDF as the sum of a positive and a negative Gaussian which are displaced against each other in the $\vec{v} \times \vec{B}$-direction. After the transformation to the ground coordinated system, the tail of the distribution gets fanned out. The distributions in both coordinate systems are shown in figure 5.9 (top row). Most of the positions on the ground are also distributed along the horizontal axis which is due to the geomagnetic field pointing almost northwards at the location of AERA. From the generated energy density dataset with varying core positions and five or more signal stations, the core resolution of fitting the AERA LDF to data sampled on a realistically sparse grid can be evaluated. For this purpose, the two datasets generated for the AERA24 and the AERA124 arrays are re-used. The containment requirement of the shower core which means that the core position is surrounded by antenna stations on all sides is expected to have a major influence on the core position reconstruction. Therefore, the sets are split up in two subsets each with contained and not contained core positions. The initial value of the core parameter $\vec{r}_{\mathrm{core}}$ in the fit is set to (50 m, 50 m) in the shower plane. The reconstructed core positions for the AERA24 (center row) and the AERA124 (bottom row) array simulation datasets

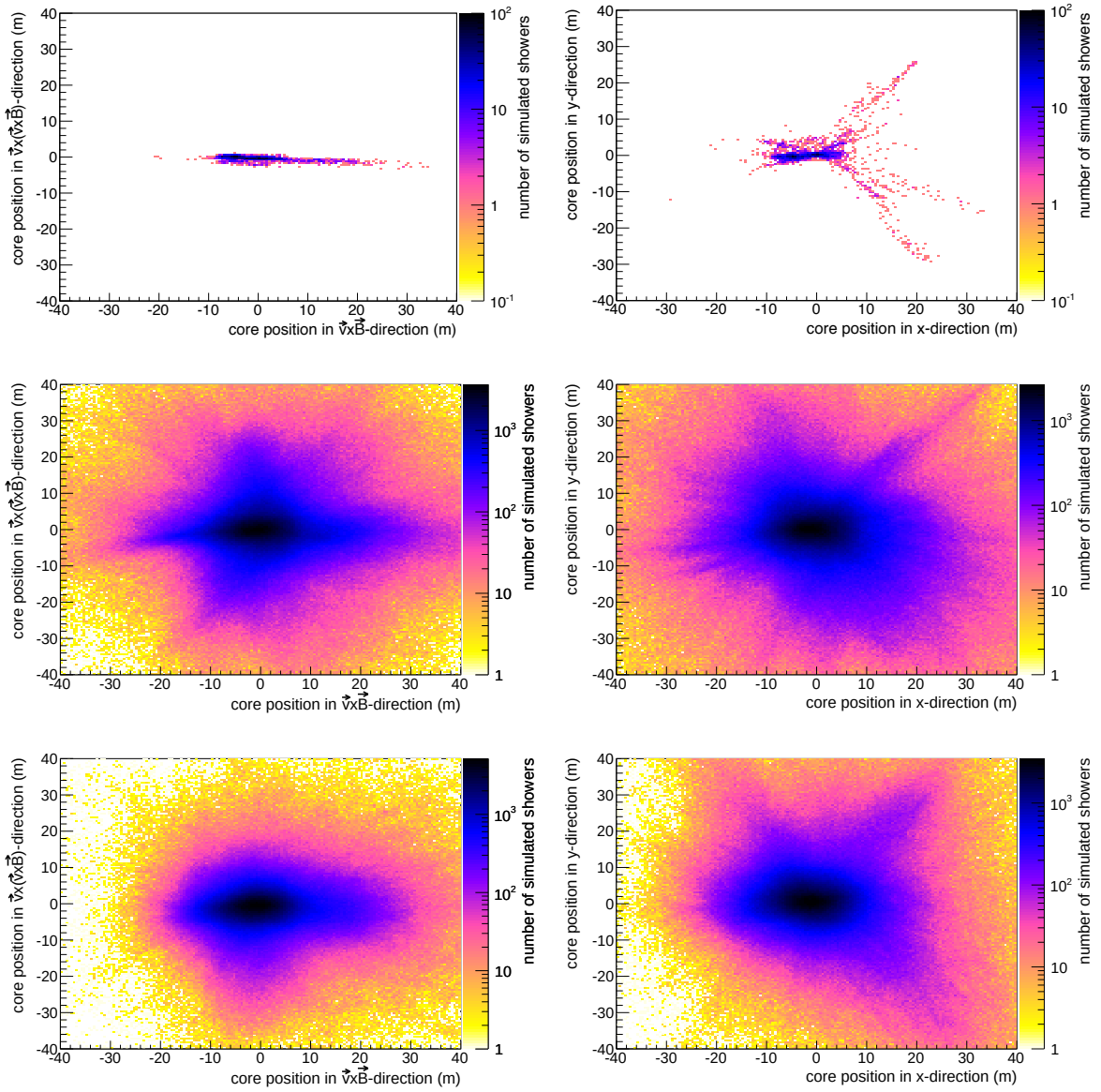

Figure 5.9: Reconstructed shower-core positions by fitting the AERA parametrization of the LDF (equation 5.2) to simulated data on the star-shape grid (top row), to simulations evaluated on the AERA24 array (center row), and to simulations evaluated on the AERA124 array (bottom row). The true core-position is set to $(0\,\mathrm{m}, 0\,\mathrm{m})$. Left: Distribution of the core positions in the $\vec{v}\times\vec{B}$ vs. $\vec{v}\times(\vec{v}\times\vec{B})$ plane. Right: Projection of the reconstructed core-position onto the ground plane (y-axis pointing northwards).

are shown in figure 5.9 in the shower as well as in the ground plane. Compared to the case of fitting the whole star shaped antenna position pattern, the distributions extend further in the $\vec{v}\times\vec{B}$-direction and also show a spread along the $\vec{v}\times(\vec{v}\times\vec{B})$-axis. The distribution is not radially symmetric due to the spread introduced from shifting the two Gaussian functions also seen in figure 5.9. After the transformation into the ground plane, the spread is more uniformly distributed around the true core position extending slightly further out. This

Table 5.4: Core resolution taken as the width of the distributions shown in figure 5.9. The means of the distributions are less than 1 m offset for all distributions. The fit uncertainties are of the order of 10^{-3} m and thereby smaller than the stated precision.

array	contained	$\sigma_{\vec{v}\times\vec{B}}$ (m)	$\sigma_{\vec{v}\times(\vec{v}\times\vec{B})}$ (m)	σ_x (m)	σ_y(m)
AERA24					
	yes	6.6	4.1	7.2	5.2
	no	9.7	11.3	13.1	13.0
	all	8.6	7.3	10.8	9.4
AERA124					
	yes	6.8	4.2	7.7	5.8
	no	7.1	11.3	9.5	15.1
	all	7.1	4.6	7.9	6.1

broadening is however only visible due to the chosen log-scale and has no major impact on the overall resolution which is approximated by fitting a two-dimensional Gaussian function to the distributions for the contained, the not contained, and the combined cases as given in table 5.4. The resolution is highest for the contained core positions inside the AERA24 array as it allows the densest sampling. For cores outside of the instrumented area, the resolution decreases and is even worse than for the case of the AERA124 array. This is due to the dense grid as it allows to reach five or more signal stations distributed on a smaller area and therefore also sampling a smaller part of the energy density distribution. It is worth noticing that the total resolution on the core position is not easily comparable between the two distributions as the number of contained and not contained showers differs by construction of the method. The fraction of contained showers is significantly lower for the AERA24 array and thereby the total resolution is strongly influenced towards the not-contained cases. This however should represent the situation as it is in the actual experimental dataset. In addition to the theoretical studies presented here, the influence of background noise on the fitting procedure needs to be analysed separately. It can however be concluded, that the principle resolution power from the method itself is comparable to the one of particle detector arrays with a similar detector spacing e.g., KASCADE-Grande with 5 m core resolution [82].

5.2.4 Depth of the Shower Maximum

The correlation of the width of the LDF σ_+ of the original LDF parametrization (equation 5.1) with the atmospheric distance (column density [g/cm^2]) to the shower maximum $D_{\max}^{\mathrm{atm}}$ has been studied on star-shape antenna-array simulations produced for the AERA site in [156]. It was found that the distribution can be described reasonably well by a third-degree polynomial function with a combined overall resolution of 23 g/cm^2. The 1572 simulations of the analysed set had values of $D_{\max}^{\mathrm{atm}}$ ranging up to 1200 g/cm^2. With the simulation set presented in

section 5.2.1, the same range in $D_{\max}^{\mathrm{atm}}$ is covered whereas the number of simulations is doubled. Furthermore, the set also includes showers induced by iron nuclei. Using a third degree polynomial leads to an unsatisfying description of the obtained distribution for the presented set of simulations. Therefore, a fifth degree polynomial is used to describe the distribution as shown in figure 5.10 (top left). The resolution obtained over the whole range of σ_+ is $13.9 \pm 0.3\,\mathrm{g/cm^2}$ and thereby is greatly improved compared to the earlier findings. As the slope of the distribution changes with increasing width, the resolution is not constant for all σ_+. Therefore, the resolution as function of the footprint width is calculated for bins with a width of 5 m and shown in figure 5.10 (top right). For large atmospheric distances to the shower maximum, mainly corresponding to inclined air showers, the spread of the distribution increases which results in a decrease in resolution. If $X_{\max}$ is close to ground and the footprint is very small, the resolution is also decreased.

In the next step, it is tested whether the simplified AERA parametrization has an impact on the resolution. This is expected to some extent due to the binning of function parameters in zenith angle bins. The distribution of the σ parameter, using equation 5.2 for the LDF fit and the resulting binned resolution using again a fifth-degree polynomial fit are shown in figure 5.10 (bottom row). The resolution over the whole range of σ is $17.8 \pm 0.3\,\mathrm{g/cm^2}$ in this case. The resolution is decreased and the effect of the binning becomes visible in terms of line-like structures in the distribution for larger values of $D_{\max}^{\mathrm{atm}}$. The spread as function of σ however decreases for the largest bins, as the distribution is extended to larger σ values. Correlating the $\sigma_{(+)}$ parameter to the atmospheric distance to $X_{\max}$ as shown here and also used in earlier work, reveals a very competitive limit on the resolution compared to other methods such as the air fluorescence technique.

In a simple theoretical model, the relation between $\sigma_{(+)}$ and the point of emission can be described with the intercept theorem, see figure 5.2. Therefore the width of the LDF should be correlated with the geometric rather than the atmospheric distance to the point of emission. The geometric distance to the shower maximum is introduced here as $D_{\max}^{\mathrm{geo}}$ calculated from equation 5.4 using geometrical distances for X_{total} and $X_{\max}$ instead of column densities. The correlation between $D_{\max}^{\mathrm{geo}}$ and σ_+ (equation 5.1) is shown in figure 5.11 (top row). The spread in this case is slightly smaller compared to $D_{\max}^{\mathrm{atm}}$. The resolution is given in units of kilometers and needs to be transformed into the atmospheric depth of the shower maximum per shower using the individual zenith angle and the respective atmospheric profile. The resolution over the whole range of σ_+ is $0.167 \pm 0.003\,\mathrm{km}$. Using the AERA parametrization a similar effect is visible in the distribution compared to what is seen when looking at $D_{\max}^{\mathrm{atm}}$. Using the AERA parametrization of the LDF with parameters binned in zenith angles limits the freedom of the function. This limitation results in a larger σ for larger zenith angles and thereby gives a smaller spread in this region. The overall spread however increases for σ bins up to about 180 m. The corresponding distributions are shown in figure 5.11 (bottom row). The resolution over the whole range of σ slightly increases to $0.217 \pm 0.004\,\mathrm{km}$. The parameters for the poly-

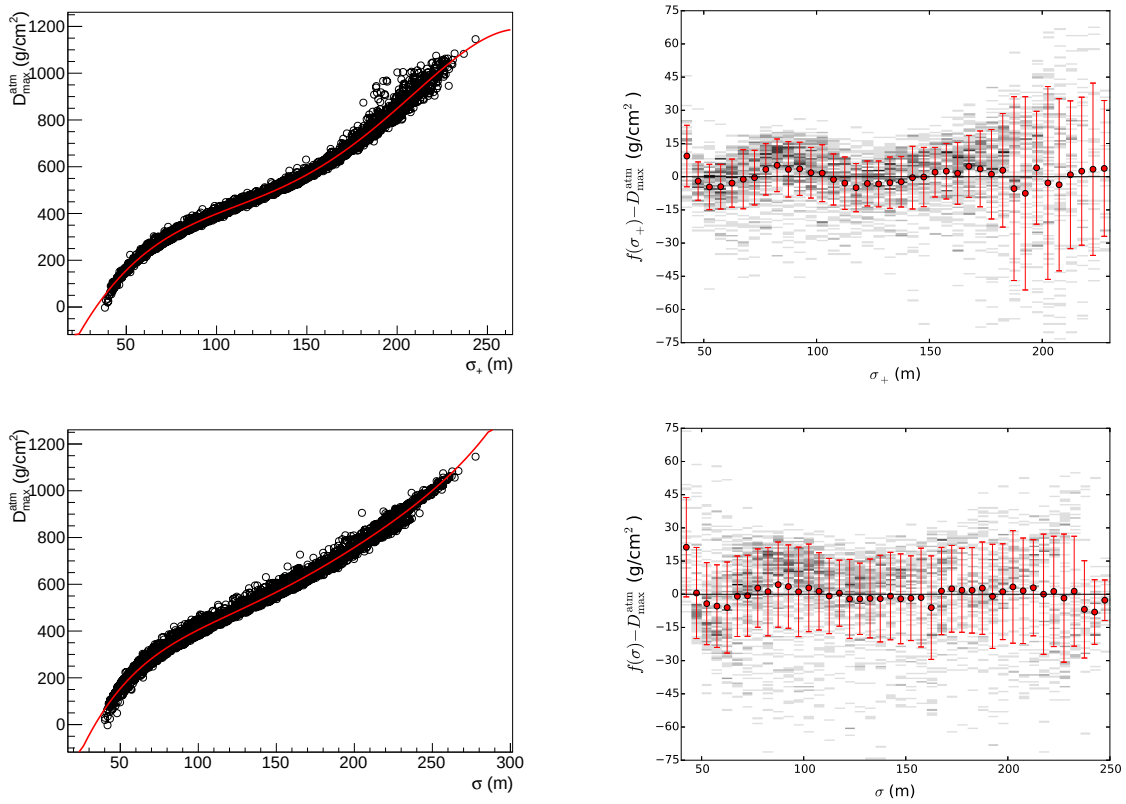

Figure 5.10: Correlation between the width of the footprint $\sigma_{(+)}$ and the atmospheric distance to the shower maximum $D^{\mathrm{atm}}_{\mathrm{max}}$ for the original LDF parametrization (equation 5.1) in the top row and the AERA LDF parametrization (equation 5.2) in the bottom row. Left: Fifth degree polynomial fit f to the distribution. Right: Resolution calculated for different bins in $\sigma_{(+)}$ with a width of 5 m. The points indicate the mean of the differences between $f(\sigma)$ and the true $D^{\mathrm{geo}}_{\mathrm{max}}$, the errorbar represents the standard deviation.

nomial fits of all shown distributions are given in the appendix A.5.

The resulting resolution on X_{max} can in this case not be taken from the distribution of residuals due to the ambiguity between the geometrical distance to X_{max} and the atmospheric density around that point. Therefore, the reconstructed values of $D^{\mathrm{geo}}_{\mathrm{max}}$ are transformed to X_{max} according to the zenith angles of the air showers and then compared to the X_{max} value as taken from the simulations. The resulting resolutions are $12.2\,\mathrm{g/cm^2}$ for the full fit of the original LDF parametrization and $15.4\,\mathrm{g/cm^2}$ for the AERA LDF parametrization which is an improvement of $1 - 2\,\mathrm{g/cm^2}$ compared to using $D^{\mathrm{atm}}_{\mathrm{max}}$. As before, the resolution in X_{max} is not constant over the range of $\sigma_{(+)}$-values. The corresponding profiles for the resolution as function of bins in $\sigma_{(+)}$ are shown in figure 5.12. The resolution of X_{max} achievable in this way is very competitive. It can be seen as a limit for the proposed method and will be influenced by experimental effects depending on the exact condition of the measurement.

The relation between the footprint width and the distance to the shower maximum is mainly dominated by the zenith angle and in second order by X_{max}. The dependency on the zenith

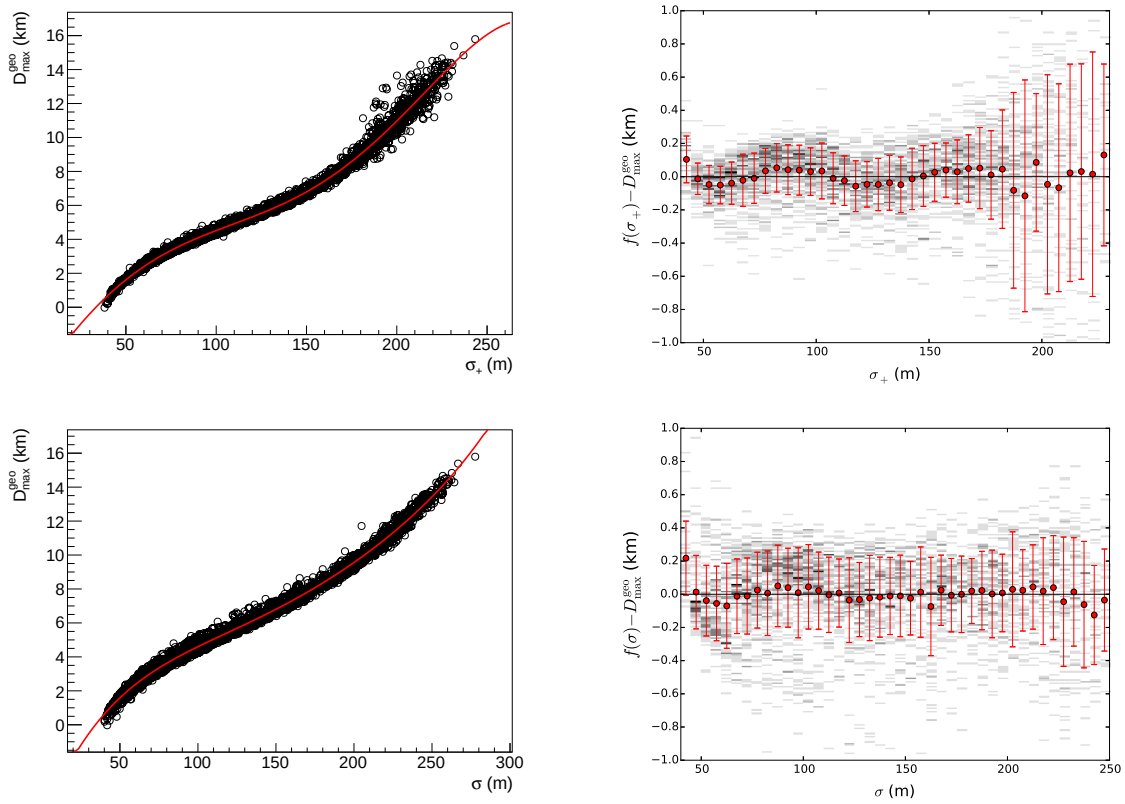

Figure 5.11: Correlation between the width of the footprint $\sigma_{(+)}$ and the geometric distance to the shower maximum $D^{\mathrm{geo}}_{\mathrm{max}}$ for the original parametrization (equation 5.1) in the top row and the AERA parametrization (equation 5.2) in the bottom row. Left: Fifth degree polynomial fit f to the distribution. Right: Resolution calculated for different bins in $\sigma_{(+)}$ with a width of 5 m. The points indicate the mean of the differences between $f(\sigma)$ and the true $D^{\mathrm{atm}}_{\mathrm{max}}$ and the errorbar represents the standard deviation.

angle is however not constant over the range of covered angles and the used polynomial function is a compromise for the description of the entire set of simulations. Figure 5.13 shows the different shapes of the correlation between $D^{\mathrm{geo}}_{\mathrm{max}}$ and σ_+ for various zenith angle bins. From the separated distributions, it is possible to see how the shape of the overall distribution is built up. It can be seen that the shape of the individual distributions is not completely re-sampled by the polynomial fit. For the application to state-of-the-art experiments like AERA or LOFAR, the detector characteristics introduce uncertainties which outrange these second order effects. For a next-generation radio experiment such as the Square Kilometer Array (SKA) with more than 60 000 antennas on a square kilometer, such effects will play a role and should be considered when developing new reconstruction tools. The resolution e.g., can be improved by fitting distinct ranges of zenith angles separately. For the given simulation set and the single polynomial fit function, the resolution can also be expressed as a function of the zenith angle of the air shower. The resulting profiles are shown in figure 5.14.

Analogue to the resolution of the energy and the core position reconstruction, also the resolution achievable for reconstructing X_{max} using the AERA LDF parametrization has been

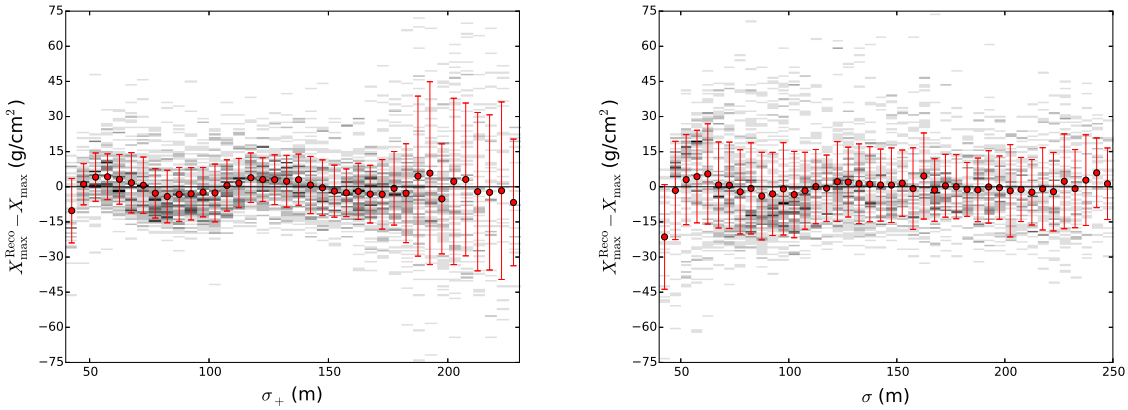

Figure 5.12: Resolution of the reconstructed value of $X_{\max}$ using the fitted relation between the width of the footprint $\sigma_{(+)}$ and the geometric distance to the shower maximum $D_{\max}^{\mathrm{geo}}$ transformed to atmospheric depth according to the individual zenith angles of the showers. The resolution is given for 5 m bins of $\sigma_{(+)}$. Left: Resolution when using the original LDF parametrization (equation 5.1). Right: Resolution obtained when fitting with the AERA parametrization of the LDF (equation 5.2).

evaluated for the station positions of the AERA array. Therefore, the same two datasets (one for AERA24 and one for AERA124) as described before with the generated core positions are used. In this case, the situation for the AERA124 array is especially interesting as for AERA124 the statistics on multi-hybrid data containing radio and FD detections of the same air showers are increasing rapidly which brings the experimental extraction of the correlation between the footprint width and the distance to $X_{\max}$ into reach. The experimentally determined relation can then be compared to the simulation results. Therefore, the results presented in the following are focussing on the AERA124 simulation set. As shown above, the resolution improves when using $D_{\max}^{\mathrm{geo}}$ which will be employed for the intermediate step to reconstruct $X_{\max}$ in all following analyses.

As air showers with an arrival direction close to the zenith only show a small footprint. With a sparse antenna grid, the sampling for these showers is sometimes not sufficient to reconstruct the exact shape of the density pattern and the fitted LDF is too broad and has a smaller amplitude. The effects of smaller amplitude and larger width mainly compensate each other when looking at the integral over the LDF. Concerning the footprint width however, these air showers have a significant impact on the spread, but also lead to a systematic shift in terms of σ. The correlation between σ and $D_{\max}^{\mathrm{geo}}$ for the AERA124 array is shown in figure 5.15. For small values of σ, the distribution shows a shift and therefore the data cannot be described with the polynomial function taken from the fit in figure 5.11 (bottom row) for values below $\sigma = 150\,\mathrm{m}$. The distribution is re-fitted by polynomials of different degrees, however the differences in resolution compared to a linear fit are negligible. Thus, only the linear fit is discussed in the following which shows an $X_{\max}$ resolution of $32.4 \pm 0.1\,\mathrm{g/cm^2}$. The resolution as function of σ using the fitted relation for the sub-range $\sigma = [95\,\mathrm{m}, 255\,\mathrm{m}]$ is displayed in

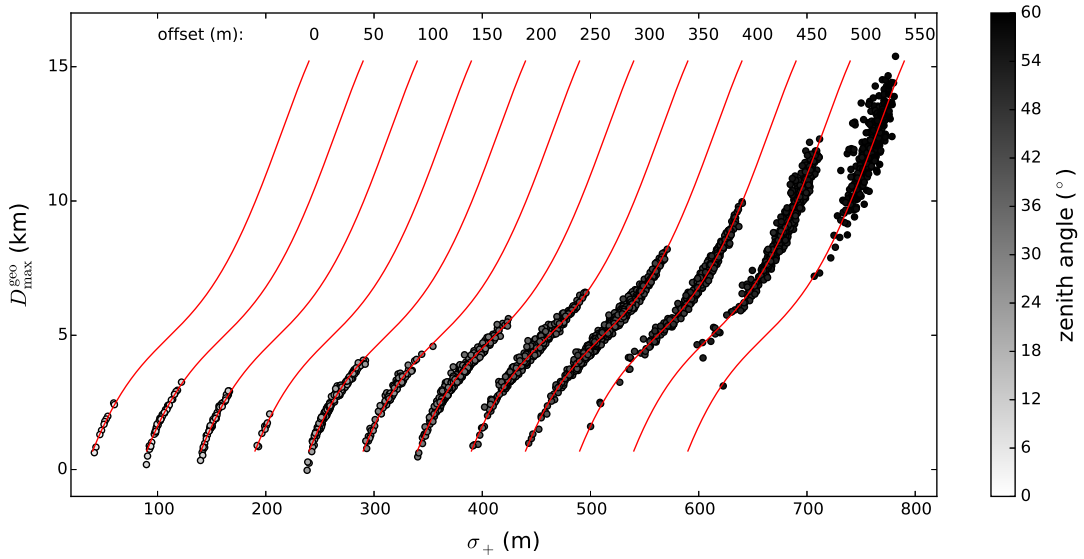

Figure 5.13: Distribution of $D^{\mathrm{geo}}_{\mathrm{max}}$ as function of σ_+ for zenith angle bins of 5° width. Every zenith angle bin is offset by 50 m in σ_+ with respect to the precursor bin. The color coding is continuously. The lines represent the polynomial function obtained from the fit to the distribution in figure 5.11 using equation 5.1 for the LDF fit. All lines represent the same function but are also offset for every zenith angle bin.

figure 5.16. In addition, the resolution obtained from applying the same method to a subset of showers for which 5 or more stations were evaluated with a signal amplitude above the detection threshold is also shown. In this case, the overall resolution improves to 27.4±0.1 g/cm^2 for the linear relation. Taking all together, the resolution is limited for small footprint widths and improves with growing width. This is an indication that the method requires a sufficiently dense array to sample the energy density distribution with high precision. The situation can also be improved when the detector array is at low altitude as $D^{\mathrm{geo}}_{\mathrm{max}}$ gets larger for all air showers in this case. But also for AERA, with increasing size of σ the in principle achievable resolution rapidly approaches a level comparable to the resolution of about $20 - 30\,\mathrm{g/cm^2}$ achieved with established techniques like the fluorescence [29] or the air Cherenkov detection [90]. The obtained resolutions for all studied constellations of LDF parametrizations and antenna arrays are summarized in table 5.5. The offset of the reconstructed values of X_{max} is smaller than 3 g/cm^2 for all constellations except using the AERA LDF on the AERA124 array including 3 and 4 signal-station showers where an offset of $7.7 \pm 0.1\,\mathrm{g/cm^2}$ is observed.

For the reconstruction of X_{max} with AERA, a direct calibration against the FD measurements in multi-hybrid air showers is the goal. The number of multi-hybrid RD-FD showers increases but is still limited for the frame of this work, therefore the determination of the calibration function on simulations is important to be able to reconstruct information about X_{max} for all air showers detected with AERA.

The general analyses presented in this chapter have shown the feasibility of using the method

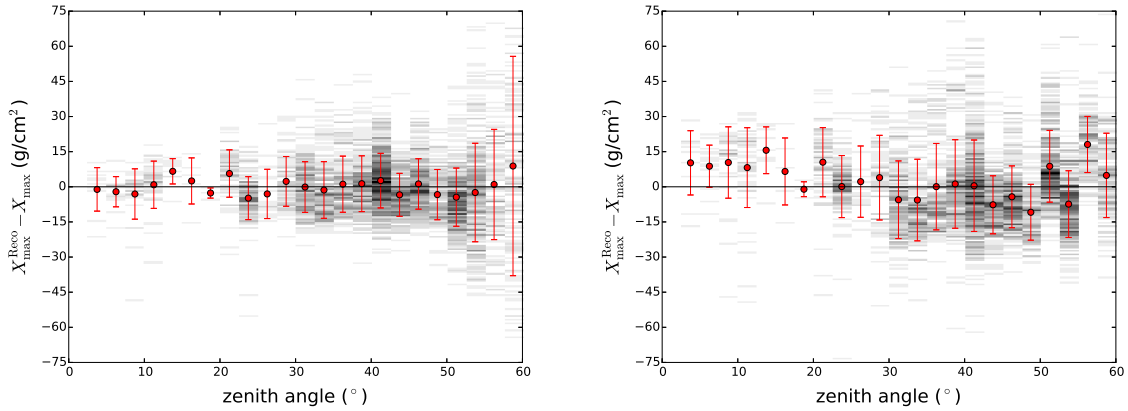

Figure 5.14: Resolution of the $X_{\max}$ determination analogue to figure 5.12 but for 2.5° bins in zenith angle. Left: Resolution for the application of the original LDF parametrization (equation 5.1). Right: Resolution for the application of the AERA LDF parametrization (equation 5.2).

Table 5.5: Resolutions of the reconstruction of the depth of the shower maximum. Two different LDF parametrizations, the original one from equation 5.1 and the one modified for AERA (equation 5.2) are used and applied to data sampled with the star-shape array and the AERA124 array. See text for further details on the method.

LDF	array	$\sigma(D_{\max}^{\mathrm{atm}})$ (g/cm^2)	$\sigma(D_{\max}^{\mathrm{geo}})$ (km)	$\sigma(X_{\max})$ (g/cm^2)
original	star-shape	13.9 ± 0.3	-	13.9 ± 0.3
AERA	star-shape	17.8 ± 0.3	-	17.8 ± 0.3
original	star-shape	-	0.167 ± 0.003	12.2 ± 0.2
AERA	star-shape	-	0.217 ± 0.004	15.4 ± 0.3
AERA	AERA124		0.509 ± 0.001	32.4 ± 0.1
AERA	AERA124	-	0.447 ± 0.001	27.4 ± 0.1
	5+ stations			

for the AERA124 array. The influence of the characteristics of the specific dataset under study (i.e., energy and direction ranges, geometry of the antenna array) on the correlation and resolution is however not negligible. For the reconstruction of $X_{\max}$ from the AERA124 data as presented in chapter 7, an additional simulation set which is exactly re-sampling the measured air showers and also includes measured noise is analysed for further studies of the influence of geometry and background noise. Before that, the determination of the energy of extensive air showers measured by AERA24 in coincidence with the Surface Detector array based on the AERA LDF is presented in the next chapter.

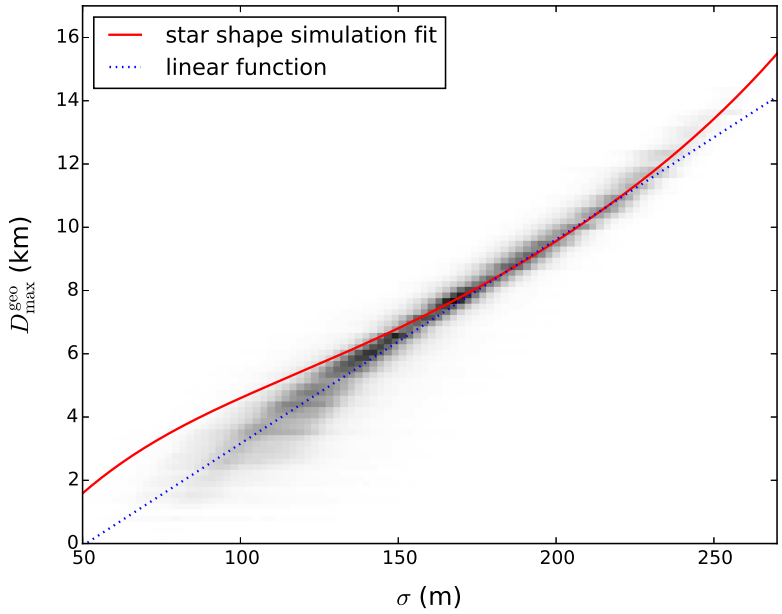

Figure 5.15: Correlation between the width of the LDF σ (equation 5.2) and the geometric distance to X_{max} $D^{\mathrm{geo}}_{\mathrm{max}}$ for the AERA124 array. The gray scale gives the number of entries in the background histogram from white to black. The solid line indicates the polynomial fit to the distribution obtained by fitting the AERA parametrization to the energy density at the star-shape antenna positions (see figure 5.11 (bottom row)). The dotted line represents a linear fit to the distribution.

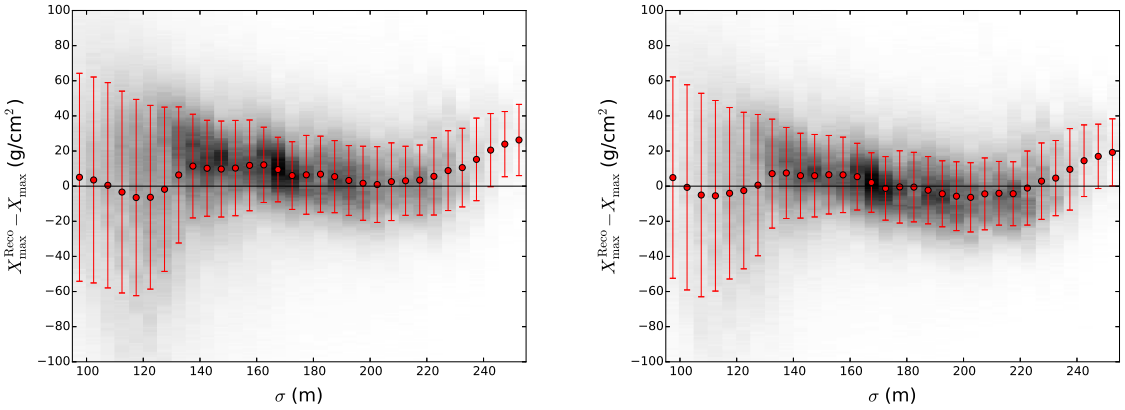

Figure 5.16: Resolution of the reconstructed X_{max} when sampling the energy density pattern with the array of AERA124 and fitting the parametrization of the LDF (equation 5.2). Left: Binned resolution for all showers. Right: Subset with 5 or more stations evaluated to be above the signal amplitude threshold.

6

Radio Energy Reconstruction

This chapter has been published as Auger Full Author List Publications:

The Pierre Auger Collaboration, A. Aab et al.,
Energy Estimation of Cosmic Rays with the Engineering Radio Array of the Pierre Auger Observatory
Submitted to Physical Review D, arXiv:1508.04267

The Pierre Auger Collaboration, A. Aab et al.,
The energy in the radio signal of extensive air showers
Submitted to Physical Review Letters

In this analysis we present an absolute calibration of cosmic-ray energies around 1 EeV using the energy radiated between 30 and 80 MHz as an estimator. The radiated energy is determined based on the integral over the 2D lateral distribution of the energy density as discussed in the preceding chapter.

6.1 Data Selection and Event Reconstruction

For this study we are using RD and SD data recorded between April 2011 and March 2013 when AERA was operating in its first commissioning phase. For this analysis, both self-triggered and externally triggered events are used.

6.1.1 Preselection of Cosmic Ray Candidates

In the case of the self-triggered events, a preselection is performed offline by searching for coincidences with the SD events. A radio event has to agree in time and location with an SD event to be considered as cosmic-ray candidate. The radio-trigger time and the time when the air shower core hits the ground have to agree within $\pm 20\,\mu s$. Such a conservative coincidence window also accounts for horizontal events, for which the time difference is expected to be larger. For both trigger types, only events with a clear radio pulse in at least three stations are considered, to allow for a reconstruction of the incoming direction of the signal. For externally triggered events the requirement is a signal-to-noise ratio (SNR) greater than ten.

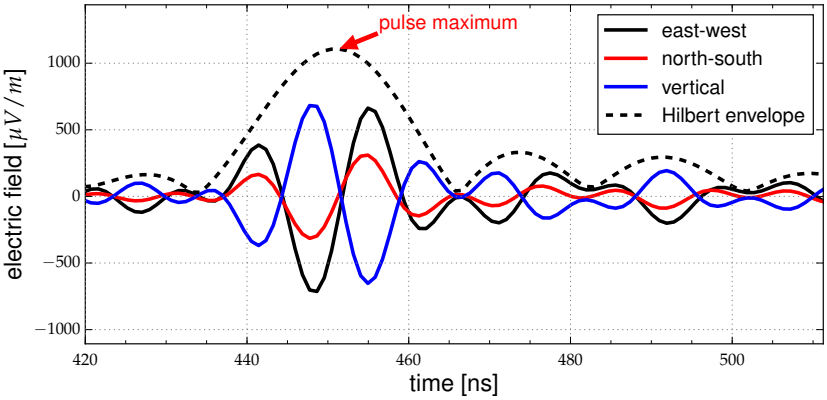

Figure 6.1: Reconstructed electric-field trace of one of the measured air showers. An upsampling by a factor of five was applied. The shown Hilbert envelope (dashed line) is the square root of the quadratic sum of the Hilbert envelopes of the three polarization components.

For self-triggered events the signal threshold is dynamically adjusted to the noise level to keep the trigger rate at a constant level of 100 Hz. We require that the reconstructed incoming directions from the radio and the Surface Detectors array agree within 20° to be accepted as a cosmic-ray candidate. The 20° cut does not reflect the angular resolution of the SD nor that of the radio detector. This preselection cut retains the maximum number of cosmic-ray signals and significantly reduces the number of anthropogenic noise pulses, which originate mainly from the horizon. In addition, we apply quality cuts on the data of the Surface Detector array as described in [67]. The most important cuts are that the core position be surrounded by a hexagon of active stations and that the zenith angle of the incoming direction be less than 55°. A total of 181 cosmic-ray candidates with energies above 10^{17} eV remain.

6.1.2 Reconstruction of Radio Data

We use a similar reconstruction scheme for the hybrid data as described in chapter 3. For this analysis we also apply the RFI cleaning procedure discussed in section 3.5.3. The energy density u of the incoming electromagnetic radio pulse at each radio station is determined by calculating the time integral over the absolute value of the Poynting vector as described in section 3.5.4. As the radio detector effects are corrected for in the data reconstruction, the obtained energy density can be directly compared to air-shower simulations. We also calculate the direction of the electric-field vector, i.e., the polarization direction of the signal. In the full width half maximum (FWHM) interval around the pulse maximum of the Hilbert envelope we observe that the reconstructed electric-field vectors are aligned approximately along the same direction for every time bin. To accurately determine the mean direction of the electric-field vector, we average over all vectors in the FWHM interval of the Hilbert envelope (see figure 6.1).

6.1.3 Selection of Radio Signals Induced by Cosmic Rays

Given the presents of pulsed background noise at the AERA site, the preselected events are likely to contain non cosmic ray signals that mimic cosmic-ray pulses. There are two scenarios possible: Signals in one or more stations are not caused by the air shower or an event contains only noise pulses that by chance led to a reconstructed incoming direction similar to that of the SD. In order to reject background signals, we take advantage of the expected polarization of the radio signal. The polarization of the radio pulse is only used for this purpose and not considered for the energy estimation. In the frequency range of AERA geomagnetic emission is dominant compared to the charge-excess emission process. The expected direction of the electric-field vector is therefore calculated from the geomagnetic and the charge-excess contributions

$$\vec{E}_{\text{exp}} \propto \sin\alpha\, \vec{e}_{\text{geo}} + a\, \vec{e}_{\text{CE}}\,, \tag{6.1}$$

where α is the angle between shower axis and magnetic field of the Earth, and a is the average relative charge-excess strength (0.14 ± 0.02 at AERA). Details on the emission mechanisms and the polarization of the radio signal are given in section 1.2.4. In this approach, the direction of the geomagnetic contribution depends only on the incoming direction of the air shower whereas the charge-excess contribution depends in addition on the position of the radio station relative to the shower axis. In figure 6.2, all stations with signal of a cosmic ray candidate are shown, and the measured polarization is compared with the expectations of the two radio-emission mechanisms. The overall agreement between measured and expected field polarizations is quantified using the angular difference

$$\beta_i = \angle(\vec{E}_{\text{meas},i}, \vec{E}_{\text{exp},i}) \tag{6.2}$$

at each station i. For each event, the average deviation $\bar{\beta}$ of the individual deviations β_i of the stations with signal is calculated and will be used as criterion for a quality cut. Relevant uncertainties are taken into account as follows:

- The relative strength a of the charge-excess can vary due to shower-to-shower fluctuations, and additional dependencies on the geometry of the air shower. Therefore, for each possible value of a between 0 and 0.5 the average deviation $\bar{\beta}$ is calculated and only the smallest value of $\bar{\beta}$ is considered.

- The uncertainty of the SD shower core position is taken into account by variation of the core within its estimated uncertainties. In our dataset the uncertainty varies between 10 m and 80 m depending on the energy and zenith angle. For each trial of the core position $\bar{\beta}$ is calculated. Again, only the smallest value of $\bar{\beta}$ is considered.

- Interference of the cosmic-ray radio signal with noise pulses can alter the polarization. Simulation studies showed that for a single radio station the uncertainty in β due to noise is below 8° at detection threshold, and decreases to 1° at high signal-to-noise

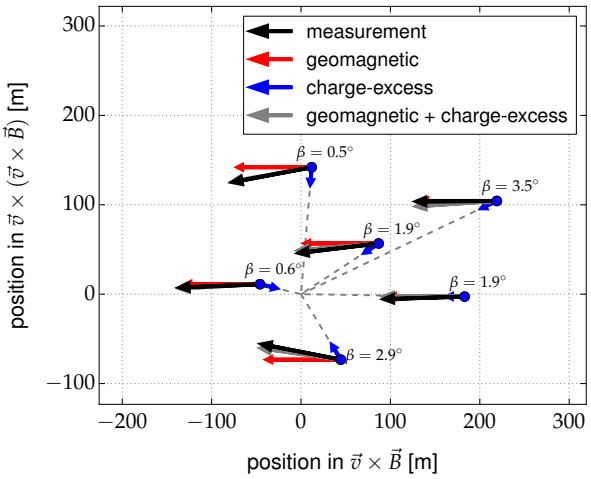

Figure 6.2: Polarization map of a single air shower. The SD shower core is at the coordinate origin. The measured polarizations are shown as black arrows. The gray arrows are the model expectations, and the red and blue arrows are the geomagnetic and the charge-excess components, respectively. The definition of β is described in the text. The properties of this air shower are: energy: 0.9 EeV, zenith angle: 36°, azimuth angle: 207°. For the emission model of equation 6.1, the optimal value of the relative charge-excess strength is $a = 0.18$.

ratios. To obtain the average value of β for all radio stations in the event we compute a weighted mean with weights $w_i = 1/\sigma^2_{\beta_i}$ with σ_{β_i} being the expected uncertainty from the simulation.

We impose a limit on the average deviation $\bar{\beta}$ of the polarization direction. This maximum deviation is fixed at a value of 3°. This value is slightly above the combination of the following effects. The incoming direction of an air shower reconstructed with the Surface Detector array has an uncertainty between 1.3° and 0.7° depending on the cosmic ray energy and the zenith angle [159]. Hence, the expected direction of the electric-field vector will have the same uncertainty. All antennas are aligned to the magnetic north (or perpendicularly to the magnetic north in case of the other polarization direction) with a precision of better than 1° [160]. All antennas are uniformly constructed and the two antennas of a radio station are identical. Asymmetries in the ground conditions have only negligible influence as the LPDA antenna is mostly insensitive towards the ground. A measurement at AERA has shown that the responses of all antennas differ by less than 0.3% [161]. A difference in the amplification of the signal chain of the north-south and east-west polarized antenna will influence the polarization measurement. From an individual measurement of the signal chain of all antennas the uncertainty is estimated to be 2.5% which results in a polarization uncertainty below 0.7°. In addition, we neglect the dependence of the relative strength a of the charge-excess on the distance between observer position and shower axis. For a single station this effect is relevant. However, in our approach we only use the average deviation of all stations with signal also taking into account the uncertainty in the core position. Therefore the distance dependence will mostly average

Table 6.1: Overview of selection cuts and the number of showers surviving these cuts. Preselection means: $E_{SD} \geq 0.1\,\mathrm{EeV}$, standard SD quality cuts, ≥ 3 radio stations with signal, SD and RD reconstructed incoming directions agree within 20°. See text for details.

cut	number of showers after cut
preselection (section 6.1.1)	181
polarization cut ($\bar{\beta} < 3°$, section 6.1.3)	136
no thunderstorm conditions (section 6.1.3)	134
LDF fit converged ($\sigma < 300\,\mathrm{m}$, section 6.2)	126
≥ 5 stations with signal (only high quality dataset, section 6.3)	47

out. We estimate that the remaining additional scatter is 1.5°. We account for individual radio stations being contaminated with substantial noise signals by iterating through all configurations with only one and then more stations removed, down to the minimum of three stations. An event where the weighted average deviation $\bar{\beta}$ is greater than 3° for all station combinations is rejected. If $\bar{\beta}$ is less than 3° for any station combination and the fraction of selected stations is larger than 50% of the total number of stations with signal, the shower candidate is considered a cosmic-ray event and only the stations from this particular combination are used. After this cut 136 showers remain. The number of excluded single stations and complete events is compatible with the measured rate of noise pulses. Most of the events recorded during thunderstorm conditions appear to be rejected by this selection procedure as the strong atmospheric electric-fields of a thunderstorm influence the radio emission and alter the polarization of the radio signals [162, 163]. For two thirds of the showers, a measurement of the atmospheric electric field is available. These showers are checked for thunderstorm conditions using an algorithm described in [164]. Based on this check, two additional showers were rejected. All cuts are summarized in table 6.1.

6.1.4 Uncertainties on the Energy Density in a Single Radio Station

In addition to the uncertainties on the amplification of the signal chain of 2.5% discussed above, no further uncertainties are expected that would result in a different response of stations within one event. To first order, the frequency content and the incoming direction of the radio pulse are similar at all observer positions. Therefore, an uncertainty of the antenna-response pattern has a negligible influence as it is evaluated for the same direction at all stations. Possible different ground conditions at different station positions that result in a different reflectivity of the soil are negligible due to the insensitivity of the antenna towards the ground. The 2.5% amplification uncertainty results in 5% uncertainty on the energy density u, as u scales quadratically with the electric-field amplitude. This uncertainty is added in quadrature to the signal uncertainty resulting from noise.

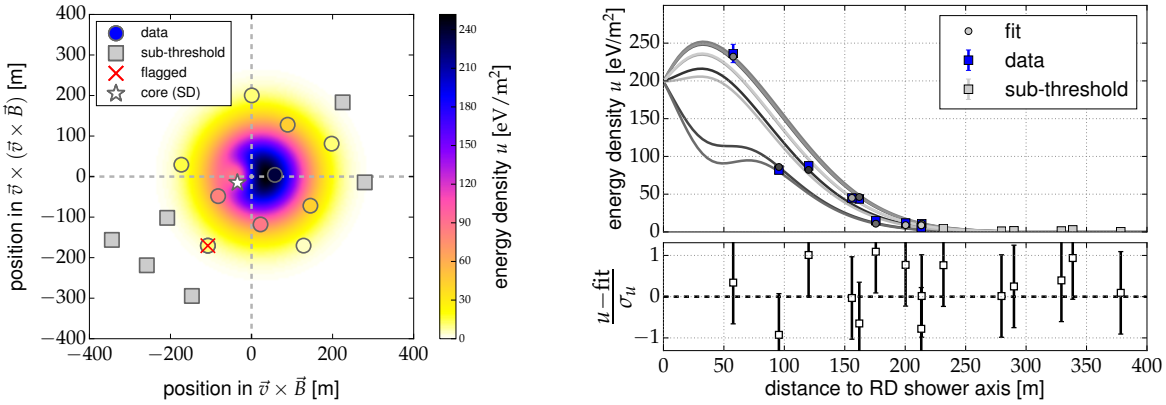

Figure 6.3: Lateral signal distribution of an air shower. The properties of this air shower are: energy: 0.75 EeV, zenith angle: 37°, azimuth angle: 44°. Left: The energy density in the shower plane. The measurements are indicated as circles where the color shows the energy density. Grey squares are stations with signal below threshold and the red cross marks a station that is rejected due to a mismatch in the signal polarization. The background map shows the LDF parametrization (equation 5.2). The coordinate origin is the reconstructed core position of the radio LDF fit. Right: The radio energy density is shown as a function of the perpendicular distance to the shower axis. Blue squares are the measurements and the circular symbols indicate the value of the LDF parametrization at the position of the measurement. Gray curves show the projection of the two-dimensional LDF onto a line connecting the radio-core position with each station position. Also shown are the residuals in units of the uncertainty of the measurement.

6.2 Energy Estimator

To obtain an absolute energy estimator from the signals at the different distances to the shower axis (energy density u in units of eV/m^2) the AERA LDF introduced in equation 5.2 in section 5.1 is used. The LDF is fitted to the data using a chi-square minimization. An example of one air shower within our dataset is shown in figure 6.3. Some shower data do not contain sufficient information to fit the LDF, such as when only three stations with signal are present that have roughly the same signal strength. This results in an unphysically broad LDF. To reject these events we impose the quality cut $\sigma < 300\,\text{m}$ (table 6.1). An analysis of simulations for the AERA geometry showed that the σ parameter of the LDF is never larger than 300 m (see section 5.2.4). In the following, only the 126 events that pass the quality cuts are considered and will be referred to as the full dataset. To derive the accuracy of the energy estimation method, the dataset will be further divided in a high-quality dataset containing only events with at least five stations with signal where the core position is reconstructed in the LDF fit.

6.2.1 Definition

The spatial integral of the lateral distribution function gives the amount of energy that is transferred from the primary cosmic ray into radio emission in the AERA frequency band during

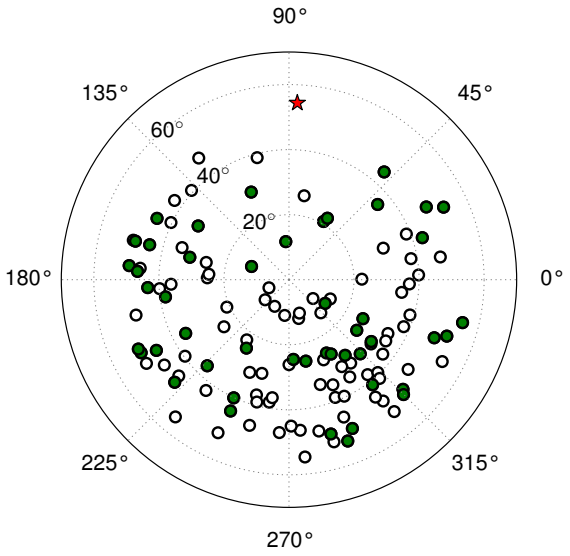

Figure 6.4: Skymap of the 126 selected cosmic rays. Green filled circles denote air showers with at least five stations with signal and open circles denote air showers with less than five stations with signal. The red star denotes the direction of the magnetic-field axis at AERA. All measured cosmic rays are at least 20° away from the magnetic-field axis. Therefore, the geomagnetic emission gives the dominant contribution to the radiation energy for all showers.

the air-shower development. We use the energy estimator S_{radio} as introduced in section 5.2.2 which is the radiation energy divided by $\sin^2(\alpha)$ to account for different emission strengths at different angles between shower axis and magnetic field,

$$\begin{aligned} S_{\text{radio}} &= \frac{1}{\sin^2\alpha} \int_{\mathbb{R}^2} u(\vec{r})\, \mathrm{d}^2\vec{r} \\ &= \frac{A\pi}{\sin^2(\alpha)} \left(\sigma^2 - C_0 C_3^2\, e^{2C_4\sigma}\right) , \end{aligned} \tag{6.3}$$

where $\mathbb{R}^2$ denotes the shower plane. The positive σ^2 term dominates by far over the negative second term resulting in a positive value of S_{radio}. The $\sin^2(\alpha)$ correction only holds if the geomagnetic emission is the dominant contribution which is the case for $\alpha > 10°$ at AERA. Due to the reduced emission strength the number of detections for arrival directions within 10° of the geomagnetic field axis is suppressed. The angular distribution of the air showers is shown in figure 6.4.

6.2.2 Shower-by-Shower Uncertainties

The following uncertainties are relevant for the energy estimator due to shower-by-shower fluctuations and summarized in table 6.2:

- The gains of the low-noise amplifiers and filter amplifiers exhibit a temperature dependence. The effect has been measured and amounts to $-42\,\mathrm{mdB/K}$. Each air shower

Table 6.2: Overview of uncertainties of the electric field amplitude $\sigma_{|\vec{E}|}$ and the energy estimator S_{radio}. "$\oplus$" denotes a quadratic sum. The average fit uncertainty of S_{radio} is 46% and 24% for the high quality subset of showers with at least five stations with signal.

source of uncertainty	$\sigma_{\lvert\vec{E}\rvert}$	$\sigma_{S_{\text{radio}}}$
shower-by-shower		
temperature dependence	4%	8%
angular dependence of antenna response pattern	5%	10%
reconstructed direction	negligible	negligible
LDF fit uncertainty	-	error propagation of fit parameters
total shower-by-shower uncertainty	6.4%	12.8% $\oplus$ **fit uncertainty**
absolute scale		
absolute scale of antenna response pattern	12.5%	25%
analogue signal chain	6%	12%
total absolute scale uncertainty	14%	28%

is measured under specific environmental conditions. In particular this implies that we have a random distribution of ambient temperatures which exhibit a Gaussian distribution with a standard deviation of 8.3° C. This corresponds to a fluctuation of the gain of 4%.

- An uncertainty of the simulated antenna response that depends on the incoming direction of the radio signal will lead to an shower-by-shower uncertainty as each shower has a different incoming direction. The effect is determined to be 5% by comparison of the simulated antenna response with a measurement at AERA [111].

- The reconstructed direction of the air shower obtained with the SD has an uncertainty of less than 1.3°. This has negligible influence on the antenna response pattern, since it can be considered uniform over such a small change of angle.

As the different uncertainties are independent, the total uncertainty of the electric field amplitude is $\sqrt{4\%^2 + 5\%^2} \approx 6.4\%$ and therefore 12.8% on S_{radio}. The uncertainty of α can be neglected. The fit uncertainties of A and σ including their correlation are propagated into S_{radio} using Gaussian error propagation. In the case of showers with less than five stations with signal, the core position of the SD reconstruction is used and its uncertainty is propagated into the fit uncertainty of S_{radio}. This fit uncertainty is added in quadrature to the statistical uncertainty of 12.8% of the energy estimator. The average fit uncertainty of S_{radio} is 46%. For showers with at least five stations with signal the average uncertainty reduces to 24%.

6.2.3 Absolute Scale Uncertainties

The dominant systematic uncertainties of the reconstructed electric-field amplitudes are the calibration of the analog signal chain and the antenna response pattern. The analog signal chain consists of the low-noise amplifier, the filter amplifier and all cables between the antenna and the analog-to-digital converter. The analog signal chain has been measured for each channel of each radio station separately in the field and differences are corrected for. The systematic uncertainty of the analog chain amounts to 6%. The simulated antenna response pattern has been confirmed by measurements at an overall level of 4%. The systematic uncertainty of the measurement is 12.5% in the vector effective length [165]. Conservatively, the systematic uncertainty of the antenna-response pattern is therefore estimated as 12.5%. Combining both uncertainties in quadrature, the systematic uncertainty of the electric-field amplitude is 14%. The radio energy density and the energy estimator scale with the amplitude squared. Therefore, the systematic uncertainty of the absolute scale of the radiation energy is 28%. We note that, as the cosmic ray energy is proportional to the square root of the radiation energy (see next section), the systematic uncertainty of a radio cosmic-ray energy scale would remain at 14%.

6.3 Energy Calibration

The radio-energy estimator S_{radio} is shown as a function of the cosmic ray energy measured with the Surface Detector array in figure 6.5 (top). A clear correlation is observed. For the calibration function we follow the same method as used for the calibration of the Surface Detector array with the Fluorescence Detector (see section 3.4.3). The calibration function

$$S_{\text{radio}} = A \times 10^7\,\text{eV}\,(E_{\text{SD}}/10^{18}\,\text{eV})^B \tag{6.4}$$

is obtained by maximizing a likelihood function that takes into account all measurement uncertainties, detector efficiencies and the steeply falling energy spectrum (the functional form of the likelihood function can be found in appendix A.6). The result of the calibration fit is $A = 1.58 \pm 0.07$ and $B = 1.98 \pm 0.04$. The resulting slope is compatible with an exponent of $B = 2$ implying that the energy deposited in radio emission increases quadratically with the cosmic ray energy. We can infer from equation 6.4 that, for a 1 EeV air shower perpendicular to the magnetic field axis, 15.8 MeV are deposited on average in radio emission in the frequency range of 30 to 80 MHz. In the lower left panel of figure 6.5 the scatter around the calibration curve for all air showers in our dataset is shown. This amounts to 29%. We also tested a high-quality dataset containing only air showers with at least five stations with signal, where a determination of the core position in the radio LDF fit is possible. These air showers are marked by green filled circles in figure 6.5. The fit of the calibration curve gives a compatible result ($A = 1.60 \pm 0.08,\ B = 1.99 \pm 0.05$) and the scatter around the calibration curve reduces to 24% (lower right panel of figure 6.5). To obtain a goodness-of-fit estimator,

the measured distribution is compared to the expected distribution which is computed from the likelihood function, i.e., from the probability model that describes the fluctuations. The comparison yields a reduced chi-square value of $\chi^2/\mathrm{ndf} = 13.8/12$ for the full dataset and $\chi^2/\mathrm{ndf} = 8.43/6$ for the high-quality dataset. In particular, it shows that the estimated uncertainties of the energy estimator in section 6.2.2 are compatible with the observed scatter around the calibration curve.

6.3.1 Uncertainties of the Reconstructed Cosmic-Ray Energy

To determine the energy resolution of the radio detector, the known resolution of the Surface Detector array needs to be subtracted from the combined scatter. The average (statistical) SD energy resolution for all air showers in our dataset is 18%. To obtain an estimate of the radio-energy resolution we use a Monte Carlo study which takes into account the energy and zenith angle dependence of the SD energy resolution. The combined scatter is simulated for different radio-energy resolutions, according to the number of air showers and the energy and zenith distribution of the dataset. We find that the energy resolution of the radio detector is 22% for the full dataset and 17% for the air showers where the core position could be determined in the radio LDF fit, when five or more radio stations have a significant signal. In the above calculation we assumed that the energy estimates from the SD and radio reconstruction are uncorrelated for a fixed energy. However, an anti-correlation is expected as radio emission originates from the electromagnetic part of the air shower whereas the SD signal is mostly due to muons resulting from the hadronic shower component [166] and which are anti-correlated shower parameters for a fixed cosmic ray energy. In case of an anti-correlation, the estimated radio-energy resolution would be even smaller making the above values conservative estimates. Furthermore, we studied the effect of a possible bias in the SD reconstructed energy for different primaries where the detector is not fully efficient ($0.1 - 0.3\,\mathrm{EeV}$) and has a slightly different efficiency curve for the two extreme scenarios of proton and iron primaries [159]. We found that the effect is negligible for our dataset. The uncertainty on the absolute scale of the energy estimator as discussed in section 6.2.3 is calibrated out by correlating S_{radio} with E_{SD}. The method, however, inherits the uncertainties of the SD energy scale. This scale uncertainty is dominated by the FD scale uncertainty, which is used to calibrate the SD. It is 16% at $10^{17.5}$ eV and decreases to 14% at energies $\geq 10^{18}$ eV [103].

6.3.2 Precision and Possible Improvements of the Reconstruction

We have found that the instrumental noise and the environmental influences are not the dominant contributions to our energy resolution. Applying the method described to a CoREAS Monte Carlo dataset, including a representative set of shower geometries as well as shower-to-shower fluctuations, but no instrumental or environmental uncertainties, a similar energy resolution is obtained for the same detector layout. The intrinsic limitation in the energy resolution

due to shower-to-shower fluctuations of the electromagnetic part of the shower is predicted to be smaller than 10% [93, 167] and we expect that the current energy resolution can be further improved. Under the condition that the LDF samples the relevant part of the signal distribution on the ground correctly for all geometries, the energy estimator should only be affected by the shower-to-shower fluctuations in the electromagnetic part of the shower. The dominant additional geometric dependence is due to the fact that the air shower might not be fully developed when reaching the ground, i.e., some part of the shower is clipped away. As the atmospheric depth increases with the secant of the zenith angle, clipping mostly affects high-energy vertical showers. Hence, we expect an additional dependence on the zenith angle. In the future, with larger statistics, this effect will be parametrized from data and will further improve the energy resolution. Also, a better understanding of the detector and the environmental effects, such as temperature dependencies, will help to improve the energy reconstruction. Combined measurements, such as they are possible at the Pierre Auger Observatory, hold great potential for future improvements of the energy resolution due to the anti-correlation of the energy reconstructed with the radio and Surface Detector array.

6.3.3 The Energy Content of Extensive Air Showers in MHz Radiation

So far, the energy content of extensive air showers in the radio frequency range of 30 to 80 MHz has only been measured at the Pierre Auger Observatory in Argentina. However, our findings can be generalized by the following consideration. To obtain a prediction that is independent of the location of the experiment, i.e., a universal formula to calculate the radiation energy from the cosmic-ray energy, the calibration function in equation 6.4 can be normalized to the local magnetic field. We found that it is sufficient to correct only for the dominant geomagnetic part of the radio emission. This is because the increase of radiation energy due to the charge-excess emission is small, as constructive and destructive interference with the geomagnetic emission mostly cancel out in the integration of the energy densities over the shower plane, see equation 6.3. For the average relative charge-excess strength of 14% at AERA the increase in radiation energy is only 2%. As most locations on Earth have a stronger magnetic field than the AERA site the effect of the charge-excess emission on the radiation energy will be even smaller. Within the statistical accuracy of the calibration function this effect can be neglected which leads to the universal prediction of the radiation energy

$$E_{30-80\,\mathrm{MHz}} = (15.8 \pm 0.7(\mathrm{stat}) \pm 6.7(\mathrm{sys}))\,\mathrm{MeV} \times \left(\sin\alpha\,\frac{E}{10^{18}\,\mathrm{eV}}\,\frac{B_{\mathrm{Earth}}}{0.24\,\mathrm{G}}\right)^2, \qquad (6.5)$$

where E is the cosmic ray energy, B_{Earth} denotes the local magnetic-field strength and 0.24 G is the magnetic-field strength at the AERA site. The systematic uncertainty quoted here is the combined uncertainty of S_{radio} (28%) and the SD energy scale (16% at $10^{17.5}$ eV). This formula will become invalid for radio detectors at high altitudes because the amount of radiation energy

decreases as – depending on the zenith angle – a significant part of the air shower is clipped away at the ground.

6.4 Relevance for the Absolute Energy Scale Determination

The energy in the radio signal can be used for a cross-calibration of different experiments and detection techniques. Alternatively, it can be used for an independent determination of the absolute energy scale of a cosmic-ray observatory. Such an absolute calibration requires input from the experimental and theoretical side, where the procedure for measuring the radiation energy has already been outlined above. On the theoretical side, the radiation energy emitted by an extensive air shower with a given energy in the electromagnetic component can be predicted from first principles using classical electrodynamics. Uncertainties in the propagation of the radio signal are insignificant since the atmosphere is transparent to radio waves in this frequency range. Using the sophisticated simulation codes discussed in section 1.2.4 the radio emission from extensive air showers can be calculated on the basis of Monte Carlo simulations. Electromagnetic radiation from the acceleration of charged particles in the electromagnetic component of the air shower, coherence effects due to the spatial particle distribution, and propagation effects in the refractive index gradient of the atmosphere fully determine the radio emission. These simulations thus involve no free parameters. There are no scaling uncertainties or "yield" factors. Work is still needed to compare the predictions of existing simulation codes in more detail, but no insurmountable problems have been identified. To relate the radiation energy emitted by the electromagnetic component of an extensive air shower to the energy of the primary cosmic ray, a correction for the invisible energy, i.e., the energy carried away by high-energy muons and neutrinos, needs to be applied. This correction can be obtained by a data-driven method exploiting the correlation between the invisible energy and the muon number at the ground [168], and only adds a small contribution to the overall energy scale uncertainty [103].
Combining accurate measurements of the energy in the radio signal and predictions from first-principle calculations, an independent determination of the absolute energy scale using radio detection of cosmic rays becomes possible.

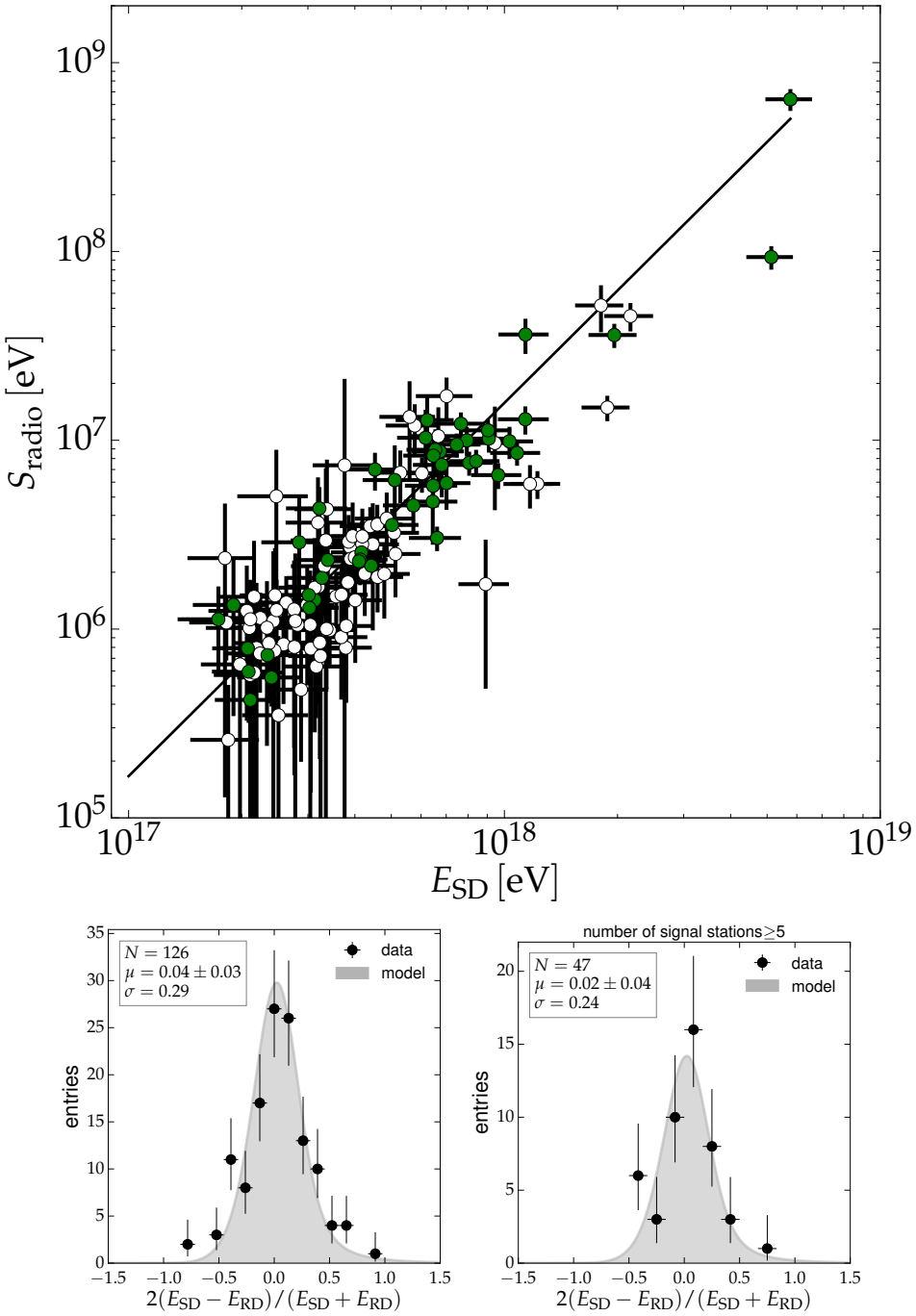

Figure 6.5: Top: The radio energy estimator S_{radio} as a function of the cosmic-ray energy measured with the Surface Detector array. A power law is fitted to the data using a likelihood approach which takes all uncertainties and detection efficiencies into account. Green filled circles denote air showers where the core position has been determined in the radio LDF fit, i.e., all air showers with at least five stations with signal. Open circles denote events with less than five stations with signal and use the SD core position. Bottom: Relative energy resolution: The energy of the radio detector is obtained using the fit in the top figure. The left histogram contains all air showers, and the right histogram contains the air showers with at least five stations with signal (green filled circles). The expected distribution is shown as a gray shaded area which is computed from the fitted probability model that describes the fluctuations.

7

Radio X_{max} Reconstruction

For the reconstruction of the depth of the shower maximum X_{max}, two different methods are presented in this chapter and applied to AERA124 multi-hybrid data, performing a comparison to the measurements of the Fluorescence Detector. Both methods are based on the radio energy-density pattern measured on the ground. In one approach, the width of the 2D LDF as discussed in chapter 5 is used. In the other approach, sets of simulations for different shower developments are generated and X_{max} is determined from the agreement between the individual simulations and the measured data. Both methods are also compared to each other. Finally, the width of the LDF is reconstructed for the thousands of showers in the RD-SD hybrid dataset and the average value of X_{max} as function of energy is determined and compared to other experimental data and predictions from different hadronic interaction models.

7.1 X_{max} from the 2D Radio LDF

The radio lateral distribution function can be used to reconstruct X_{max} with AERA124, as discussed in chapter 5. To apply the method to measured data, the correlation found for the generic simulations is redetermined for the real detector geometry and also including measured noise. This correlation is verified using the RD-SD-FD multi-hybrid showers.

7.1.1 Calibration with Full Detector Simulations

The correlation between the width of the LDF σ and the geometric distance to X_{max} $D^{\mathrm{geo}}_{\mathrm{max}}$ depends on the layout of the antenna array (see section 5.2.4). Furthermore, the influence of real background noise on the reconstruction of the width parameter needs to be investigated. This however cannot be easily determined from the generic simulation set for the real AERA antenna grid. Therefore the specific simulations purpose-made for the AERA layout and the properties (energy and arrival direction) of the reconstructed showers in the AERA dataset are used (see section 3.7).

In the presence of noise and considering the uncertainties introduced by the detector setup, the reconstruction of the radio signals and the determination of the LDF becomes more challenging. The uncertainty associated with the signal chain has a significant influence on the largest signals whereas the noise mainly impacts stations with signals around or below the signal-to-noise threshold. Both effects together influence the reconstruction quality and result

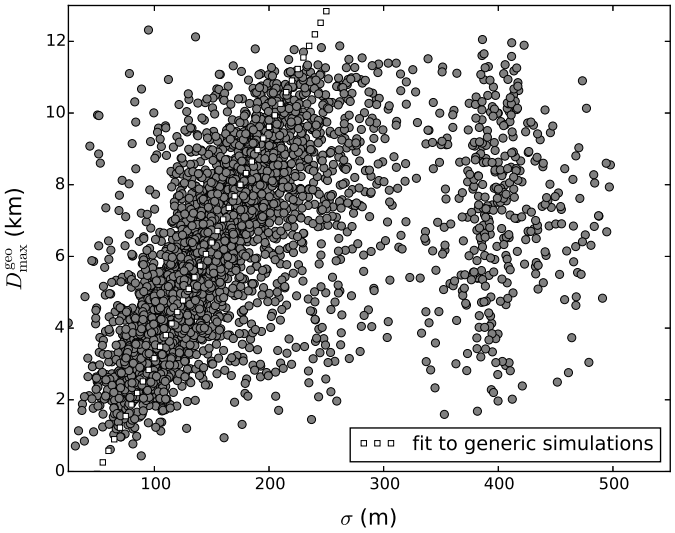

Figure 7.1: Correlation between the geometric distance to X_{max} $D^{\mathrm{geo}}_{\mathrm{max}}$ and the width of the LDF σ obtained from all successfully reconstructed simulations (with zenith angle $< 55°$) which are purpose-made for AERA124. The simulations are re-sampling the measured air showers and include measured background noise. No quality cuts are applied to the shown dataset. The line indicates the linear correlations obtained from the generic simulations in figure 5.15.

in cases for which the reconstruction is not successful. Altogether, 5832 simulated showers were successfully reconstructed. The distributions of σ and $D^{\mathrm{geo}}_{\mathrm{max}}$, for the 4479 reconstructed air showers for which the zenith angle of the arrival directions is smaller than 55°, are shown in figure 7.1. In addition, the linear dependency obtained from the fit shown in figure 5.15 is plotted as an indicator of the expected correlation. The bulk of the data points is located around the line predicted from the generic simulations. The distribution however has a rather broad spread and a number of points are located in a separated region vertically oriented around $\sigma = 400\,\mathrm{m}$. For further analysis, quality cuts are enforced on the reconstructed data as summarized in table 7.1. Due to the relatively large spread in the distribution, rather strict quality cuts are imposed on the events for this X_{max} analysis to obtain a high-quality sample. These cuts can be loosened or otherwise optimized depending on the target of the specific analysis. A cut on the number of signal stations (above SNR threshold) is not necessary in this case, as for these simulations, the core position parameters are fixed to the real core position for showers with less than 5 signal stations. For real data this however is not the case and a cut might be needed. The distribution is fitted with a linear function revealing a χ^2/ndf of 7.68. This indicates that the uncertainty on σ taken directly from the LDF fit are either underestimated or that there are additional influences playing a role, e.g., the background noise. To correct for this, the uncertainties on σ are increased by quadratically adding $11.15\,\mathrm{g/cm^2}$ resulting in a χ^2/ndf of 1.0. The modified uncertainties can then be propagated into the uncertainty of X_{max}. The distribution is shown together with the linear fit to the data and the linear re-

Table 7.1: Overview of selection cuts and the number of showers surviving these cuts starting with 5832 simulated showers. For the robustness against value variation, the values of the measured or simulated energy densities are varied according to their uncertainties and the LDF is re-fitted 1000 times. If less than half of these fit attempts are successful, the shower is rejected.

cut	number of showers after cut
zenith angle $> 55°$	4479
geomagnetic angle $\alpha > 10°$	4479
$\sigma < 270\,\mathrm{m}$	4004
$\chi^2/ndf < 2$	2662
uncertainty of $\sigma < 10\%$	957
robustness against value variation	950

lation obtained from the generic simulations in figure 7.2. The width of the distribution of $\sigma = 53.5 \pm 1.7\,\mathrm{g/cm^2}$ is taken as the resolution on X_{max}. The similarity between the relation found in the two independent simulation sets indicates that the added background noise has no significant systematic influence on the reconstructed σ. The spread however increases as the noise varies the reconstructed energy density at the individual station positions and also the uncertainties of the energy density introduce more freedom for the minimization process.

7.1.2 Comparison of Simulations and Multi-Hybrid Data

For the reconstruction of X_{max} using the lateral distribution function, the Pierre Auger Observatory provides a unique ensemble of detectors. On the one hand multi-hybrid RD-SD-FD showers can be used to perform a calibration between radio and the FD independently of simulation results and on the other hand the large RD-SD hybrid dataset allows to reconstruct the values of X_{max} of measured air showers for which no FD information is available. To compare the results obtained from simulations to hybrid data, a selection is made from the dataset of multi-hybrid RD-SD-FD showers described in chapter 3.
For simulated air-showers, the value of X_{max} as well as the value of $D^{\mathrm{geo}}_{\mathrm{max}}$ is based on a parametrized atmospheric model. During the reconstruction of measured data, the atmospheric overburden at the time of the shower is extracted from GDAS (see section 2.2). This information is used when fitting the Gaisser-Hillas function to the FD data and thereby determining X_{max}. It is also used for its transformation into a geometric distance using

$$D^{\mathrm{geo}}_{\mathrm{max}}(X_{\mathrm{max}}, \theta) = \frac{(h_{\mathrm{GDAS}}(X_{\mathrm{max}}/\cos\theta) - h_{\mathrm{Auger}})}{\cos\theta}. \tag{7.1}$$

Here, $h_{\mathrm{GDAS}}(X_{\mathrm{max}})$ is the vertical geometrical height above sea level for a given GDAS profile and a given shower with a certain X_{max} and zenith angle θ. h_{Auger} is thereby the elevation of the AERA site above sea level.

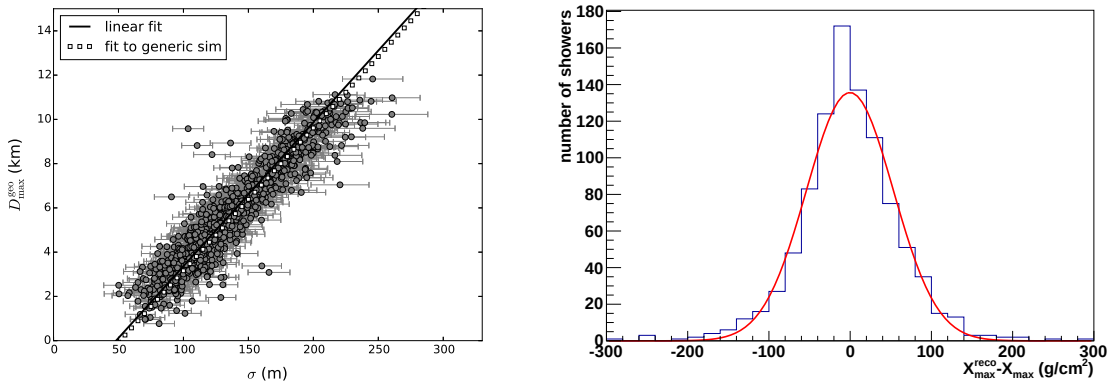

Figure 7.2: $X_{\max}$ determination from the purpose-made AERA124 simulations including measured noise. Left: Correlation between the geometric distance to $X_{\max}$ $D^{\mathrm{geo}}_{\max}$ and the width of the LDF σ together with the best linear fit (solid line) and the linear relation obtained from the generic simulations in figure 5.15 (dashed line). Right: Absolute differences between the reconstructed and the true value of $X_{\max}$. The distribution is fitted with a Gaussian function with $\mu = -0.3 \pm 1.7\,\mathrm{g/cm^2}$ and $\sigma = 53.5 \pm 1.7\,\mathrm{g/cm^2}$.

Table 7.2: Overview of selection cuts and the number of showers surviving these cuts starting with 105 RD-SD-FD multi-hybrid showers.

cut	number of showers after cut
LDF fit not successful	102
≥ 5 stations with signal	30
geomagnetic angle $\alpha > 10°$	30
$\sigma < 270\,\mathrm{m}$	30
uncertainty of $\sigma < 20\%$	28

The RD-SD-FD multi-hybrid dataset contains 105 showers of which 52 have 3 signal stations (above SNR threshold), 23 showers have 4 signal stations and 30 showers have 5 or more signal stations. Three showers with 3 signal stations do not have a successful LDF fit. To ensure a high reconstruction quality and to stay independent of influences of the SD reconstruction in terms of the shower core position, only showers with 5 or more signal stations are used for the following analysis. From this subset, showers are selected based on the radio quality cuts introduced in table 7.2. These cuts are less strict than the ones applied to the simulation dataset in order to increase the number of showers. In addition it is checked, that the atmospheric electric fields are not enhanced by thunderstorm conditions. A detailed description on this criterion can be found in [164]. Nineteen of the selected showers are found to be not associated with thunderstorm conditions, whereas for 9 of the selected showers no atmospheric electric field data are available. The distribution of the arrival directions of the selected cosmic rays as well as the distributions of the energy and $X_{\max}$ as measured with the Surface Detector and

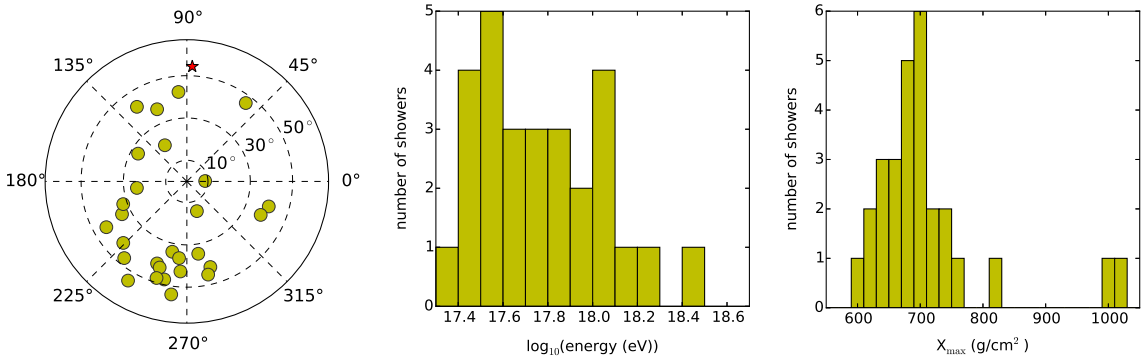

Figure 7.3: Parameters of the shower set for the comparison of the reconstructed values of $X_{\max}$ using the width of the LDF and the FD measurement. Left: Arrival directions taken from the SD. Center: Energy distribution taken from the SD. Right: $X_{\max}$ distribution taken from the FD.

the Fluorescence Detector, respectively, are shown in figure 7.3. The selected air showers are mainly arriving from the south-west. This is related to three aspects. First, the domination of the geomagnetic emission mechanism leads to a suppression of showers being detected from the North i.e., parallel to the geomagnetic field. Second, the Fluorescence Detector quality criteria do not allow showers coming directly towards the telescopes which suppresses showers from the East. And third, the antenna spacing of AERA favours inclined showers with larger footprints to be detected by multiple stations. The distributions of energy and $X_{\max}$ resample those for the whole dataset (see figure 3.10) except for a higher minimum energy of $10^{17.2}\,\mathrm{eV}$ caused by the applied selection criteria.

The selected dataset is used to experimentally verify the results of the simulation studies. Therefore, the correlation between σ and $D^{\mathrm{geo}}_{\max}$ is determined for this set analogue to the procedure for the simulations. The uncertainties of $X_{\max}$ based on the radio LDF are propagated from the modified uncertainties of the LDF fit. The uncertainties of $X_{\max}$ measured with the FD are taken as discussed in section 3.6. The corresponding correlation is shown in figure 7.4 on top of the results from the generic and the purpose-made AERA124 simulation studies. The measured showers show a similar correlation compared to the AERA124 simulations and the generic ones. The exact parameters of the linear fits are given in table 7.3 also indicating the agreement of the results obtained from both simulation sets compared to the measured data. The much larger number of showers in the purpose-made AERA124 simulation dataset results in smaller uncertainties of the fit parameters. Therefore, the calibration obtained from this simulation set is used to reconstruct the value of $X_{\max}$ from the width of the LDF. The resolution on $X_{\max}$ which can be obtained from the measured air shower set is $59.3 \pm 15.7\,\mathrm{g/cm^2}$ and thereby increased compared to the simulations. This can be attributed to the less strict cuts applied to the set. Applying the same cuts to the AERA simulation set results in a comparable resolution. The reconstructed $X_{\max}$ values as function of the $X_{\max}$ values measured with the FD are shown in figure 7.5 together with the corresponding residuals. The correla-

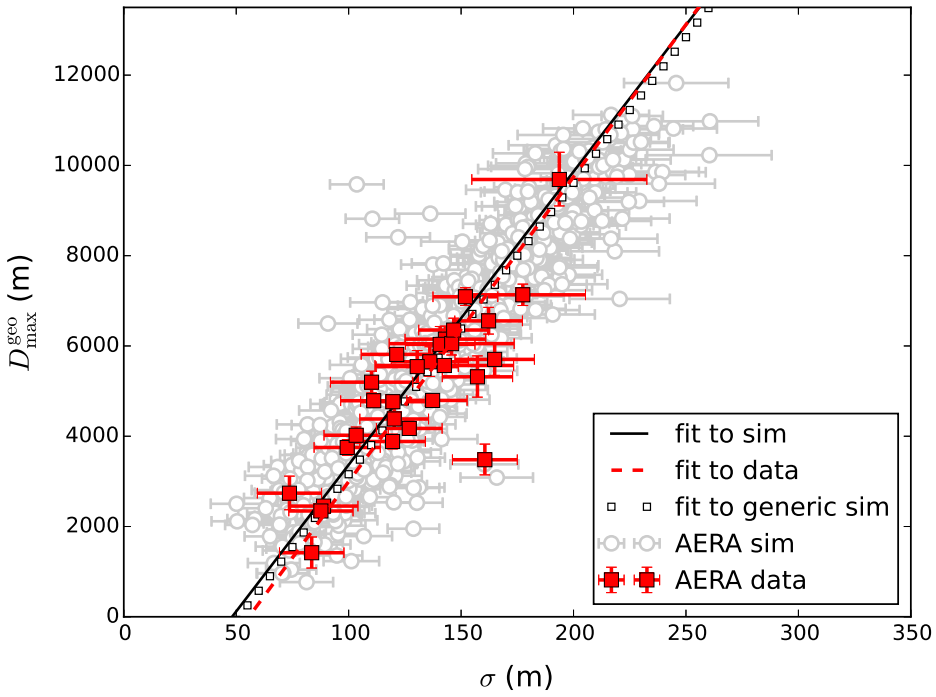

Figure 7.4: The distance to the shower maximum $D^{\mathrm{geo}}_{\mathrm{max}}$ as a function of the with of the radio footprint σ, based on RD-SD-FD multi-hybrid showers (red squares and red dashed line). In the background the data obtained from simulations as shown in figure 7.2 are plotted.

Table 7.3: Fit parameters obtained for the linear correlation $D^{\mathrm{geo}}_{\mathrm{max}} = p_0\sigma + p_1$ for the different simulated and measured datasets.

dataset	p_0	p_1 (m)
generic Sim	64.6 ± 0.1	-3297 ± 2
AERA124 Sim	65.0 ± 0.8	-3129 ± 121
AERA124 measurement	67.5 ± 9.6	-3755 ± 1217

tion of the data points is 0.76. The values of X_{max} based on the radio LDF show an offset of $-12.0 \pm 13.4\,\mathrm{g/cm^2}$ compared to the FD measurements. Even though the value is still compatible with 0, investigating possible systematic effects is subject of ongoing studies.

7.2 $X_{\mathbf{max}}$ from Simulated Energy-Density Profiles

In addition to the reconstruction of X_{max} based on the fit of the parametrized LDF description, a more fundamental approach was developed by the LOFAR-collaboration by fitting detailed Monte Carlo simulations to the measured data [71]. For this method a typical resolution for the determination of X_{max} of about 17 g/cm^2 is stated for LOFAR with its high antenna density

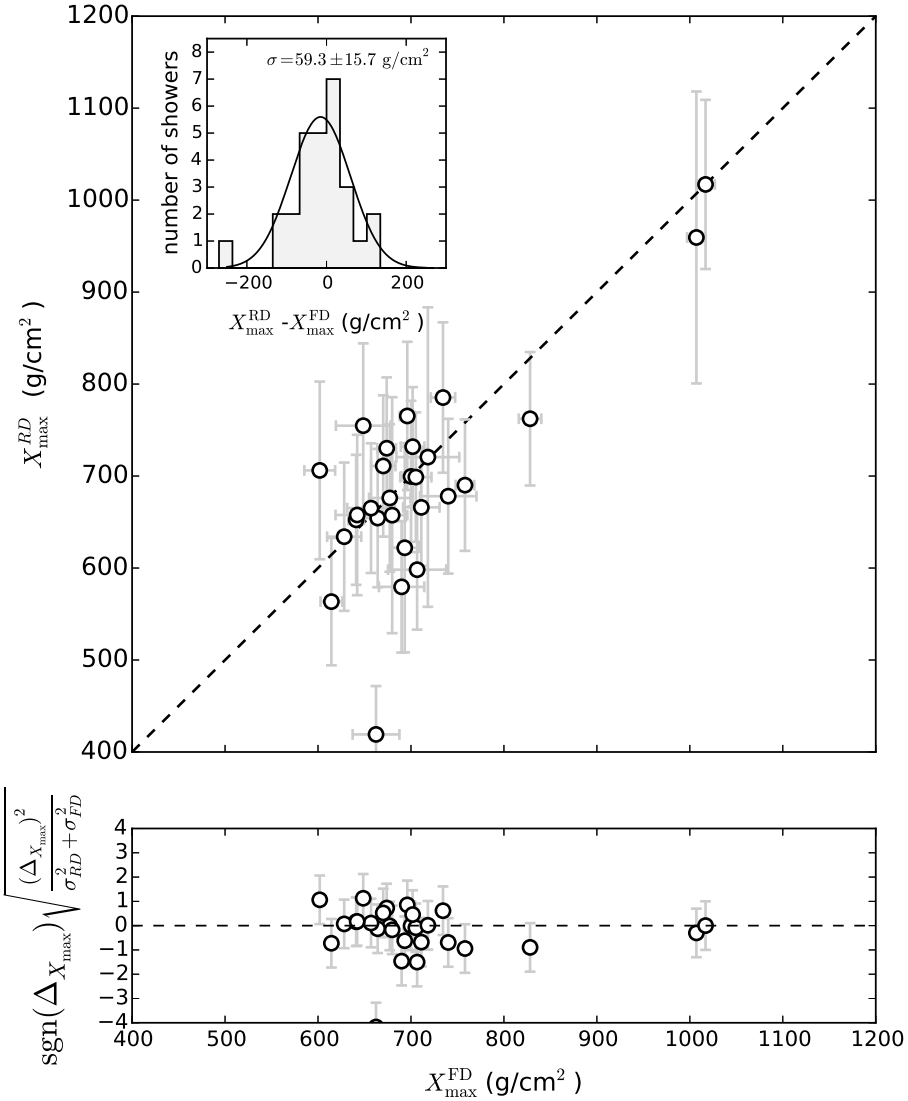

Figure 7.5: Comparison between the reconstructed depth of the shower maximum X_{max} based on the width of the radio LDF and the measurements of the Fluorescence Detector. The dashed line represents the bisecting line. In the bottom panel, the residuals are shown. The uncertainties do not include the systematic uncertainties of the standard FD measurement. In the inset, the distribution of the differences of the reconstructed values is shown. The solid line represents a fit with a Gaussian function with $\mu = -12.0 \pm 13.4\,\mathrm{g/cm^2}$ and $\sigma = 59.3 \pm 15.7\,\mathrm{g/cm^2}$.

with a theoretical duty cycle of almost 100%. The application of the method to AERA data allows high-resolution X_{max} measurements and the results are compared to FD data.

7.2.1 Basic Principle of the Method

The basic idea behind the method is to produce a set of air shower simulations resampling the measured air-shower. The simulations are produced with the generic star-shape antenna

pattern, as discussed in section 3.8. For these simulations, the calculated energy density in the shower plane is interpolated on a two-dimensional map and fitted to the measured energy density by varying the core positions and the scaling. For better accuracy, information acquired with the Surface Detector array is included and compared to the simulated particle distribution at ground level in a similar way, using a one-dimensional particle LDF. The best value for X_{max} is then taken from the fitted minimum of the reduced chi-square distribution from the entire simulation set. A detailed description of the individual steps of the method, modified for AERA is outlined in the following.

7.2.2 Individual Shower Simulations

For every measured air shower, 20 simulations for showers induced by protons and 10 simulations for showers induced by iron nuclei are produced with CORSIKA and CoREAS, based on the energy and direction reconstructed from the SD data. In the simulations, the height of the first interaction of the cosmic ray in the atmosphere is determined by the hadronic interaction model using different reproducible random seeds for different showers. Thereby, a broad but realistic (under the assumption that the interaction models are correct) range of heights of first interactions and further shower developments is achieved. The X_{max} values from a simulation set of 30 showers cover the value of X_{max} measured by the FD in most cases. If this is not the case, CONEX (see section 1.2.3) is used to find the random seeds for which the simulated showers are likely to have a X_{max} value in the region measured by the FD. These seeds are used as input for the production of additional simulations. For this analysis, the CONEX option is only used in case the original distribution of simulated X_{max} values is not covering the value of X_{max} measured by the FD. All showers are simulated using the US standard atmosphere parametrized according to Lindsey [53].

Simulated Electric Field and Energy Density

The simulated electric-field traces are processed to be comparable to measured data. Therefore, the traces are down sampled to the experimental time resolution and filtered between 30 and $80\,\mathrm{MHz}$. The peak position is defined as the maximum of the Hilbert envelope of the magnitude trace of the electric field. Around this peak position, a 100 ns broad window is used to determine the total energy density of the three-dimensional electric field as well as the energy density in the individual polarizations. The total energy density is then interpolated in the $\vec{v} \times \vec{B}$ vs. $\vec{v} \times (\vec{v} \times \vec{B})$ plane.

Simulated Lateral Particle Distribution

In addition to the radio information, particle information can optionally be included in the procedure if available. The method is in principle similar to the one for the radio data, but uses a different reconstruction procedure. To be able to compare particle simulations to measured

data, a common quantity (such as the energy density for the radio emission) needs to be chosen and reconstructed for simulations and measurements. For the SD, the standard quantity for particle signals is the number of vertical equivalent muons (VEM) as it is discussed in chapter 4. To determine the number of VEM from simulations, the detector response is applied to the simulated particles on the ground. Due to the thinning mechanism used during the air-shower simulation, a de-thinning procedure [169] is performed before applying the detector simulation for the SD stations [170]. The full GEANT4 simulation for a large number of water Cherenkov detector stations is very computational expensive and therefore look up tables are used for the detector simulation[1].

The classical particle LDF has a one-dimensional form (see NKG function 1.23) and does not account for geometrical effects for inclined showers where on one side of the axis the shower develops further in the atmosphere before reaching the ground than on the other side. This breaks the rotational symmetry of the LDF and leads to a biased reconstruction of the core position for inclined showers. To lower the impact of the asymmetry, a ground pattern of simulated detector stations is used that forms a regular 18-arm star in the shower plane. The arms have an angular spacing of 20° and an increasing radial distance. As the number of particles decreases with the distance to the shower axis, the area which is used to resample the particles has to be increased. Here, a value of $\mathrm{d}R = \pm 10\%$ of the radial distance of the stations to the shower axis defines the resampling area together with a central angle of $\pm 10^\circ$. The radial spacing between two neighbouring stations with $R_1 < R_2$ is then set by $R_2 = 1.23 R_1$. After the simulation of the response of all stations in this dense array to the simulated particles, a trigger simulation is made and sub-threshold stations are rejected. The generated data for the remaining stations are used to reconstruct an one-dimensional LDF. This is done by using the standard SD reconstruction module sequence (see section 3.4.1), where for the special case of a dense array individual reconstruction modules need to be modified to not reject these stations. An example LDF including all stations from the dense star-shape grid is shown in figure 7.6. The LDFs of all simulations can then be included in a combined fit mechanism as explained in the following. It should be noted that the reconstructed standard LDF for the Surface Detector array is only valid for air showers with zenith angles smaller than 55°. Therefore, the particle information will only be included in the fitting procedure for showers with zenith angles below this limit.

7.2.3 Data Selection

From the whole RD-SD-FD multi-hybrid dataset presented in section 3.6, 80 air showers are reconstructed. The showers are required to have more than 4 radio signal stations, a successful radio LDF fit (without applying the additional quality cuts), and an uncertainty of the value of $X_{\max}$ obtained from the FD of less than $40\,\mathrm{g/cm^2}$. In addition to the standard RdObserver

[1] TabulatedTankSimulator module of the $\overline{\mathrm{Off}}\underline{\mathrm{line}}$ framework

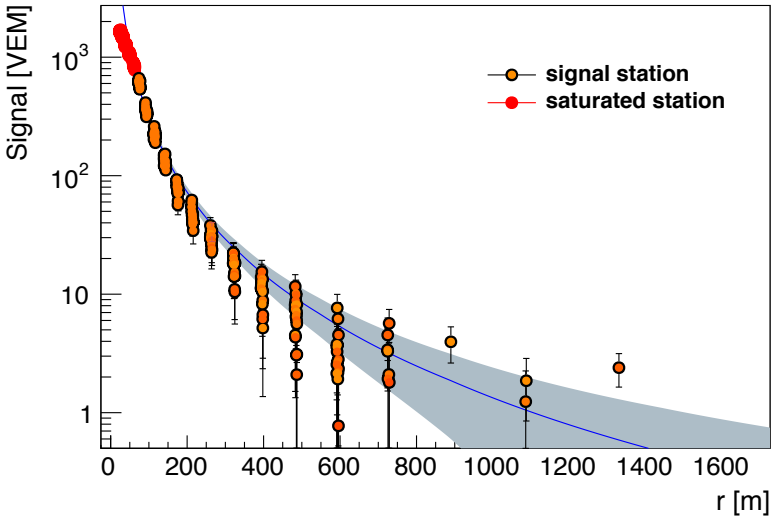

Figure 7.6: Lateral particle distribution reconstructed from a CORSIKA air shower simulation processed in $\overline{\text{Off}}\underline{\text{line}}$. The simulated signal is plotted in units of vertical equivalent muons (VEM) as a function of the distance to the shower axis. As simulated detector array, an idealized 18-arm star grid with increasing radial distances between the stations is used. The saturated stations are recovered during the reconstruction. See text for details on the simulations.

reconstruction, the RFI cleaning method as discussed in section 3.5.3 is applied. Only a part of the selected showers are actual high-quality multi-hybrid events, the other air showers are additionally selected for test purposes. The direction and energy needed as input for the simulation is taken from the SD reconstruction to test the method already for the case that no FD information is available. Due to the low number of candidate showers, no further selection on the zenith angle is made here, even though for 13 inclined showers in the set the particle information cannot be included in the fit as the zenith angle exceeds 55°.

For the fit procedure itself, a station selection is applied on a shower-by-shower basis. Hereby, all stations with a signal pulse (SNR of ≥ 10, as defined in chapter 3), are selected together with a number of sub-threshold stations that were up and running but registered no signal above the threshold. The sub-threshold stations are only considered if their position is less than 500 m away from the shower axis and included for the same reason as in chapter 6 for the topic of the 2D LDF fit which becomes unreasonably flat and broad for showers, where all signal stations measured roughly the same energy density. For the simulation based $X_{\max}$ reconstruction, this case leads to misleading best fits of the broadest simulated energy density profile. Furthermore, the possible shift of the core position to optimize the fit is limited in case the signal stations are surrounded by sub-threshold stations. The uncertainty of the measured energy density is calculated from the energy density of the noise in a correspondingly long time window added in quadrature to the uncertainty introduced from the signal chain of 5% (see also chapter 6). Saturated radio detection stations are excluded from the analysis. Together with further quality cuts summarized in table 7.4, an event rejection based on the

atmospheric electric field conditions is applied at a later stage. For the data from the SD, the signal stations are taken as they are reconstructed in $\overline{\text{Off}}\underline{\text{line}}$ for the Infill array, in addition stations marked as accidental are discarded and for saturated stations the recovered signal values are used.

7.2.4 Fit Procedure for the Reconstruction of $X_{\max}$

Following the procedure in [71], the two-dimensional energy-density profile and the particle LDF are fitted simultaneously to the RD and the SD data in a least χ^2 fit, using:

$$\begin{aligned}\chi^2 = &\sum_{\text{RD stations}} \left(\frac{u_{\text{RDS}} - S_{\text{r}}\, u_{\text{sim}}(\vec{r}_{\text{RDS}} - \vec{r}_{\text{core}})}{\sigma_{\text{RDS}}} \right)^2 \\ &+ \sum_{\text{SD stations}} \left(\frac{p_{\text{SDS}} - S_{\text{p}}\, p_{\text{sim}}(\vec{r}_{\text{SDS}} - \vec{r}_{\text{core}})}{\sigma_{\text{SDS}}} \right)^2 .\end{aligned} \tag{7.2}$$

Here, u_{RDS} is the measured energy-density of a radio detection station (as defined in equation 3.9) at ground position $\vec{r}_{\text{RDS}}$ with its uncertainty σ_{RDS} as discussed above and a scaling parameter S_{r} to account for the uncertainty of the input energy, possible offsets in the absolute antenna calibration, and the absolute scale of the simulations. Analogue, p_{SDS} is the measured particle signal of a Surface Detector station at ground position $\vec{r}_{\text{SDS}}$ with uncertainty σ_{SDS} and a scaling factor S_p to account for the uncertainty of the input energy and the overall offset of the reconstructed LDF from simulation due to missing muons. For the fit procedure, the core position $\vec{r}_{\text{core}}$ is varied on the ground plane in every step and the system is then transformed to the $\vec{v} \times \vec{B}$ vs. $\vec{v} \times (\vec{v} \times \vec{B})$ frame to calculate the χ^2. In case of inclined showers with zenith angles above 55°, the fit is performed based on the radio data only which reduces equation 7.2 to its first summand. For every simulation the procedure is repeated resulting in a χ^2/ndf-distribution as function of the Monte Carlo $X_{\max}$ value. To obtain the final $X_{\max}$ value from this distribution, a parabola is fitted to the data points within $\pm 200\,\text{g/cm}^2$ around the simulation with the lowest χ^2/ndf value. If the fit does not converge or returns a negative parabola, the range is gradually extended in steps of $\pm 50\,\text{g/cm}^2$ until the fit is successful or a total range of 500 g/cm^2 is reached where the procedure is aborted. The minimum of the fit is taken as the best $X_{\max}$ estimate from this method.

7.2.5 Application to Multi-Hybrid Data

The outlined method is applied to the selected set of 80 air showers and exemplary, the fit results for two air showers are discussed in detail in the following. The measured radio data together with the best fitting simulation for these two showers are displayed in figure 7.7. The footprints as spatially sampled with AERA are indicated by the large coloured circles together with the interpolation (background colour) of the best fitting (lowest χ^2/ndf) simulation (small circles). For one of the shown air showers the initial cosmic ray has an arrival direction from

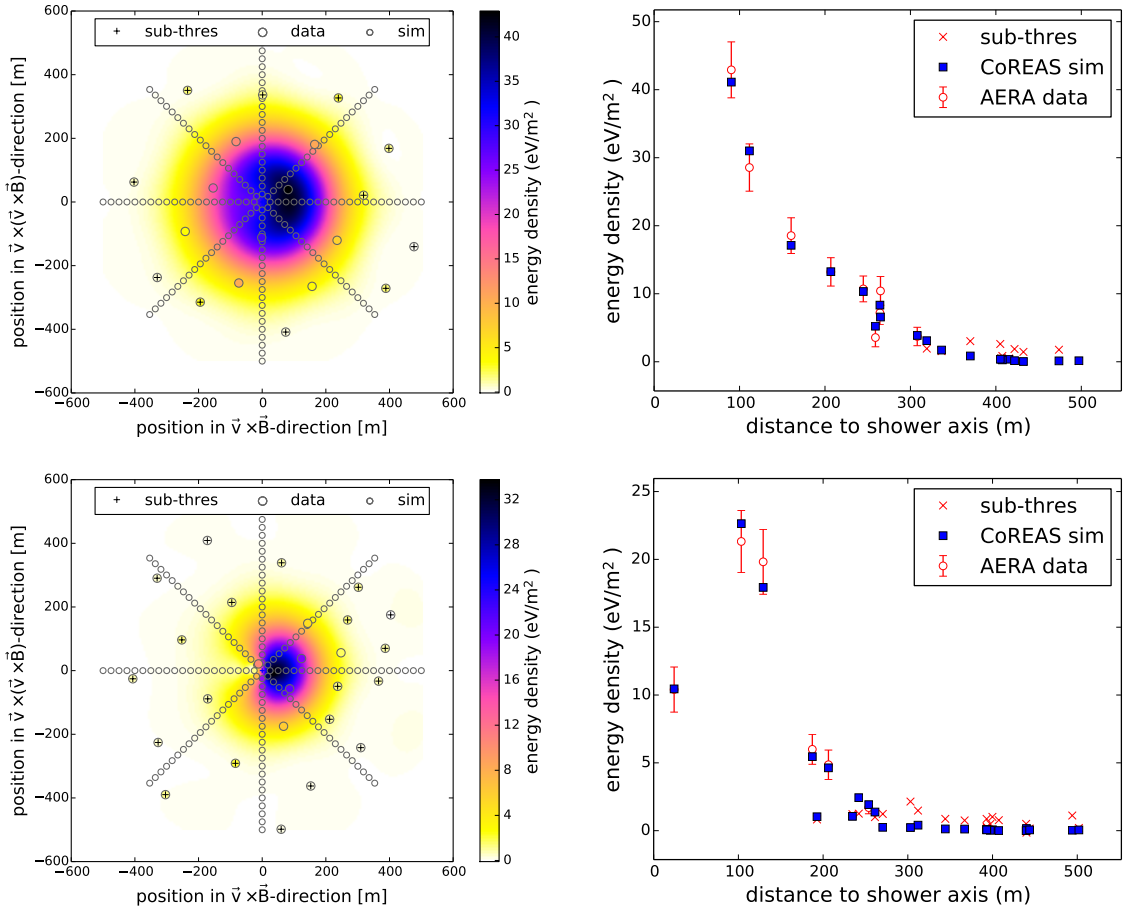

Figure 7.7: Reconstructed radio lateral distribution function for two example showers. Left: The best fitting CoREAS simulation (small circles) interpolated in the shower plane (background color map) as fitted to the measured energy densities by the AERA stations (large circle), sub-threshold stations are additionally marked by a "+". The reconstructed position of the shower axis is shown by a small "×" at (0,0). Right: One-dimensional representation of the simulated and measured LDF. The sub-threshold stations are marked by crosses.

the South (zenith angle: 49.6°, azimuth angle: 292.6°) and for the other one from the North (zenith angle: 42.5°, azimuth angle: 95.4°). Thereby, the second shower developed almost parallel to the geomagnetic field which results in the very distinct footprint shape. The one-dimensional representation of the LDF has in this case the maximum of the energy-density pattern about 100 m away from the shower axis and the station closest to the shower axis has measured a significantly lower energy density. Using simulated energy-density patterns to fit the data automatically takes these effects into account and no further restrictions on the shower geometry are necessary for this method. Only when using the method in hybrid mode, a restriction might originate from e.g., the particle detector reconstruction.

In addition to the radio measurement, also the particle data are used in the fit procedure for presented events. In figure 7.8 (left), the particle counterparts to the radio measurements shown

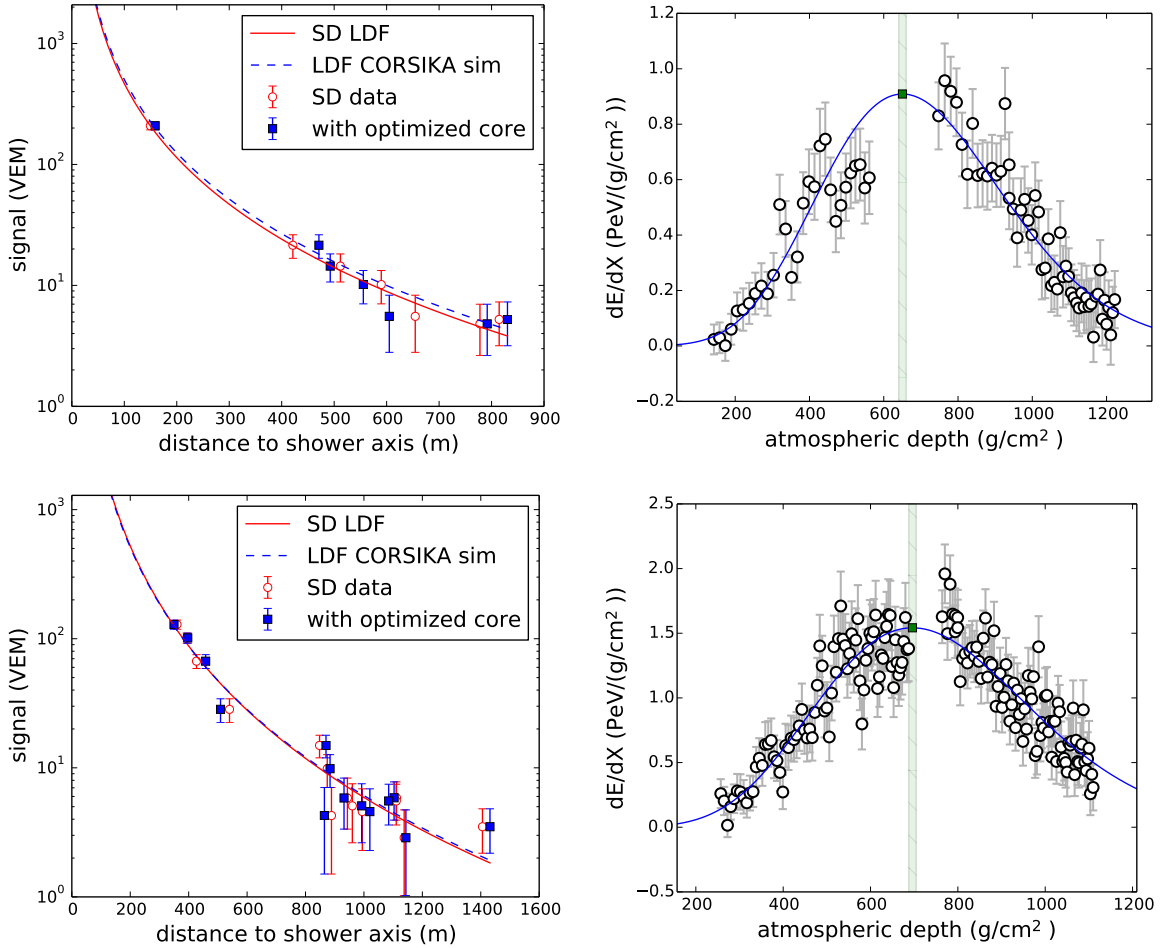

Figure 7.8: Auger baseline measurements of the two air showers shown in figure 7.7. Left: Particle signal in vertical equivalent muons (VEM) as function of the measured (circles) and fitted (squares) distance to the shower axis together with the original reconstructed LDF (red solid) and the LDF based on the best fitting simulation (blue dashed). Right: Longitudinal shower-profile as measured with the Fluorescence Detector (see section 1.2.5 for details on the technique). The energy deposition in the atmosphere is depicted as function of the atmospheric depth. The vertical band represents the reconstructed value of X_{max} together with the corresponding uncertainty.

in figure 7.7 are plotted including the result from the combined fit regarding the core position and the particle LDF. Depending on the size of the particle footprint and thereby the number of triggered SD stations, the influence of the particle distribution on the sensitivity to X_{max} is in general limited. In some cases the fit procedure is however dominated by the influence of the particle signal. For these cases the fit can be performed in a radio-only mode. In general it is however beneficial to include the information in a combined fit as it helps to constrain the geometry e.g., when the shower core position is outside of the radio array. As the particle SD array is larger than AERA, the core in this cases is always confined in the particle array. In figure 7.8 (right), the longitudinal profiles of the corresponding air showers as measured with the Fluorescence Detector are shown. The atmospheric depth of the maximum shower de-

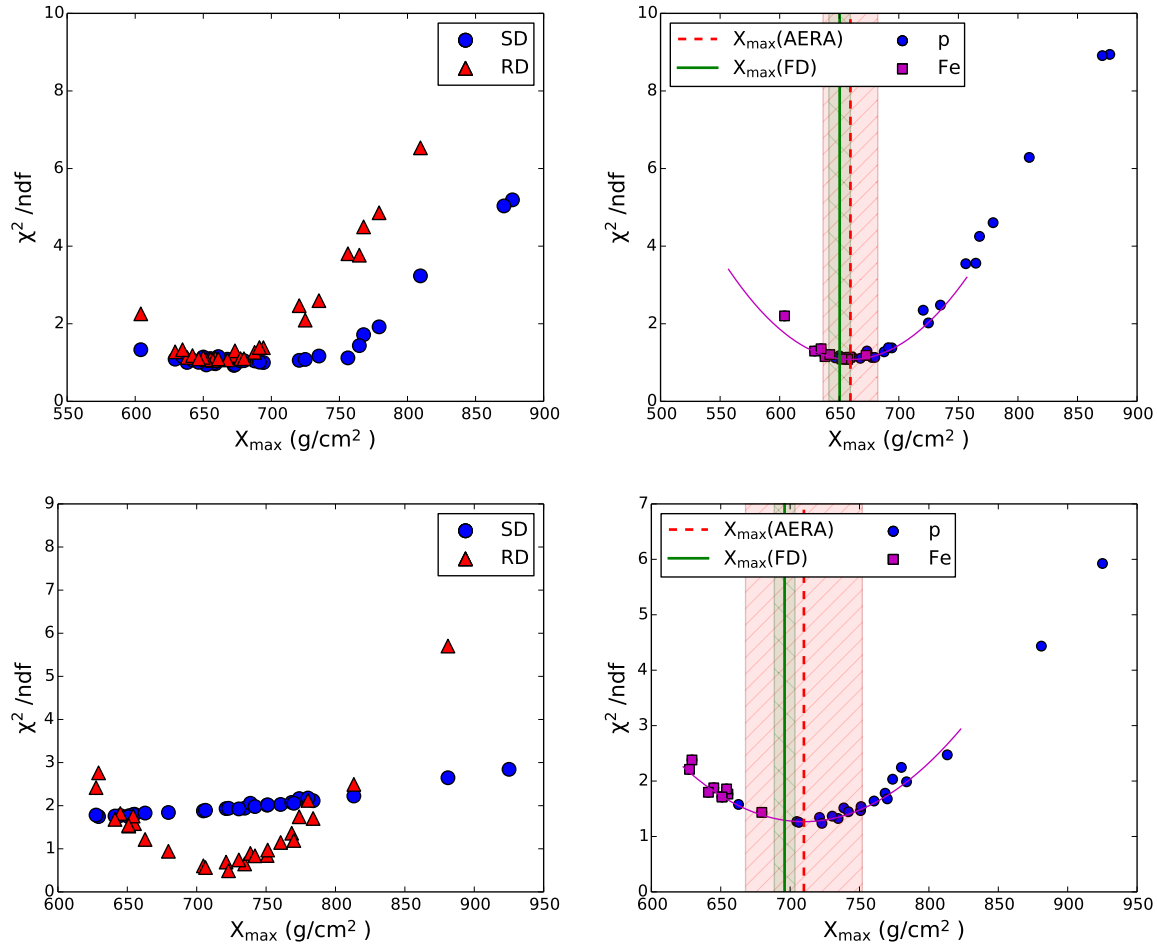

Figure 7.9: Distribution of the fit quality for the simulated showers against the depth of the shower maximum $X_{\max}$ as taken from the simulations. Left: Fit qualities of the radio (triangles) and particle (squares) parts separated for the two showers presented in 7.8. Right: Reconstructed value of $X_{\max}$ from the combined radio and particle fit. The dots (proton primaries) and squares (primary iron nuclei) represent the simulations. The solid line is a parabolic fit to the data points around the simulation which yields the lowest χ^2/ndf. The dashed vertical line represents $X_{\max}$ taken as the minimum of the parabola together with the one sigma uncertainty on this value. The solid vertical line represents $X_{\max}$ as measured with the FD together with its uncertainty.

velopment is obtained by fitting the Gaisser-Hillas function (see equation 1.24) to the shower profiles.

The resulting χ^2/ndf distributions for all simulations for the two example showers are plotted against the true $X_{\max}$ value and shown in figure 7.9. Here the results for the particle as well as the radio χ^2/ndf are shown together with the combined distribution including the fitted parabola and the determined value for $X_{\max}$. The uncertainty is calculated as described in section 7.2.6. In both cases the reconstructed value of $X_{\max}$ agrees with the FD measurement within the uncertainties.

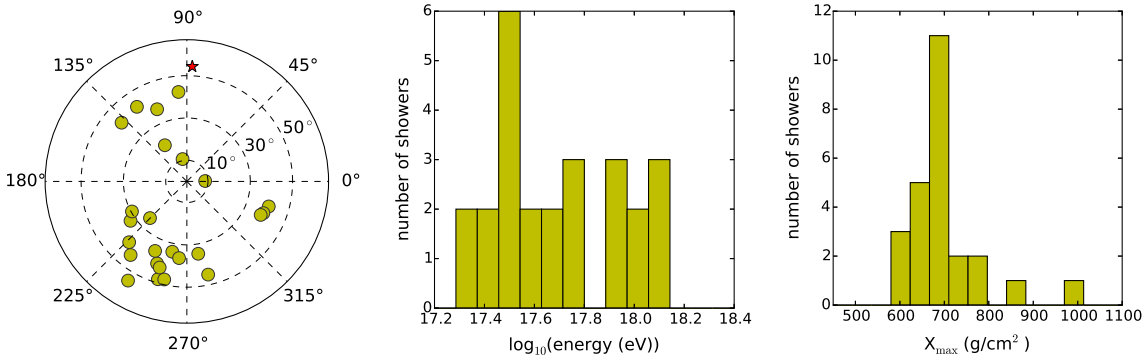

Figure 7.10: Parameters of the shower set for the comparison of the reconstructed values of $X_{\max}$, using the simulated radio energy-density profiles and the FD measurement. Left: Arrival directions taken from the SD. Center: Energy distribution taken from the SD. Right: $X_{\max}$ distribution taken from the FD.

Table 7.4: Overview of the quality cuts for the comparison between the reconstructed $X_{\max}$ values based on the fit of simulated radio energy-density profiles and the FD measurement. The selection starts with a set of 80 showers.

cut	number of showers after cut
SD-FD energy calibration quality cuts	32
minimum in χ^2/ndf-distribution	26
more than 75% of the simulations converge in the fitting	25

For the comparison of the reconstructed values of $X_{\max}$ with the Fluorescence Detector data, additional quality cuts targeting the baseline reconstruction need to be applied to the set. For the 80 showers for which simulations were run, 32 fulfil the quality criteria for the SD-FD energy calibration as described in section 3.6. For these 32 showers, the χ^2/ndf-distribution of 6 of them does not show a minimum but keeps continuously de- or increasing over the whole covered $X_{\max}$ range. One additional shower is deselected as in the fitting procedure for more than half of the simulated profiles no minimum could be found. Table 7.4 summarizes the selection criteria of the considered showers. The distribution of the arrival directions of the 25 cosmic rays in the final selection as well as the distributions of the energy, and $X_{\max}$ as measured with the Surface Detector and the Fluorescence Detector, respectively, are shown in figure 7.10. The asymmetry in the distribution of the arrival directions of the selected showers is similar to the one discussed in section 7.1.2.

Using the presented dataset, the individually reconstructed values of $X_{\max}$ obtained from the FD and the radio measurements are compared. The resulting scatter plot of $X_{\max}^{\mathrm{RD}}$ vs. $X_{\max}^{\mathrm{FD}}$ is shown together with the corresponding residuals in figure 7.11. A correlation with a correlation coefficient of 0.83 is found and the values from the radio reconstruction are consistent with the measurements of the Fluorescence Detector. The resolution taken as the width of

the distribution of $X_{\max}^{\mathrm{RD}} - X_{\max}^{\mathrm{FD}}$ is $\sigma = 47.0 \pm 16.9\,\mathrm{g/cm^2}$. The mean of the distribution is $\mu = 4.4 \pm 13.9\,\mathrm{g/cm^2}$ and thereby compatible with 0.
The method should be finally verified as soon as more multi-hybrid data that fulfil the quality cuts of the various detector components are available. Especially showers were the whole longitudinal shower-profile is observed by the Fluorescence Detector are rare. This might also be a geometrical effect similar as for the arrival directions of the selected shower set. Even though all of the selected showers fulfil the SD-FD energy calibration quality cuts, for some showers only a fraction of the longitudinal shower-profile was observed by the Fluorescence Detectors. An example for such a shower is shown in figure 7.12 which also represents the shower with the largest residual in the used set. In addition, the shower with the second largest residual is also shown for which the profile is measured with a higher quality.

7.2.6 Uncertainty of the Reconstructed Value

The uncertainty on the reconstructed value of $X_{\max}$ is not taken from the χ^2/ndf-distribution but determined by applying the method to shower data generated from the simulations. For each simulated air shower, artificial radio data are produced by evaluating the interpolated energy density map at the selected AERA station positions with respect to the measured shower core positions. Therefore, the signals are varied according to Gaussian fluctuations as given by the original signal uncertainties. Similarly, particle data are produced by evaluating the simulation-based lateral distribution function (reconstructed as described in section 7.2.2) at the participating SD station positions. The generated SD signals are also varied according to Gaussian fluctuations as given by the original signal uncertainties. The produced shower data are then reconstructed analogue to real data by fitting all simulated energy-density profiles except for the one used to produce the artificial shower data. As the $X_{\max}$ value is known for the simulated data, it can be compared to the reconstructed $X_{\max}$. Repeating the procedure for all simulations, a distribution of the differences is obtained and the uncertainty on the reconstructed value of $X_{\max}$ for measured data is taken as the 68% quantile of this distribution.
An overall correction needs to be applied for the difference between the atmospheric profile used in the simulation and the actual profile of the atmosphere in which the air shower developed. The atmospheric conditions at the time of measurement are obtained from the GDAS. Figure 7.13 gives an example for the differences in the atmospheric profile between GDAS and the US standard parametrization for one of the showers in the dataset. The difference of $X_{\max}$ is then determined as

$$\Delta X(h) = \frac{1}{\cos\theta} X_{\mathrm{GDAS}}(h), \tag{7.3}$$

using the zenith angle of the air shower, the atmospheric depth of a given altitude extracted from GDAS $X_{\mathrm{GDAS}}(h)$, and the geometrical hight h calculated from combining the Monte Carlo $X_{\max}$ with the atmospheric profile used in the simulation. This correction is possible because the overall size of the energy density pattern on the ground is determined by the geo-

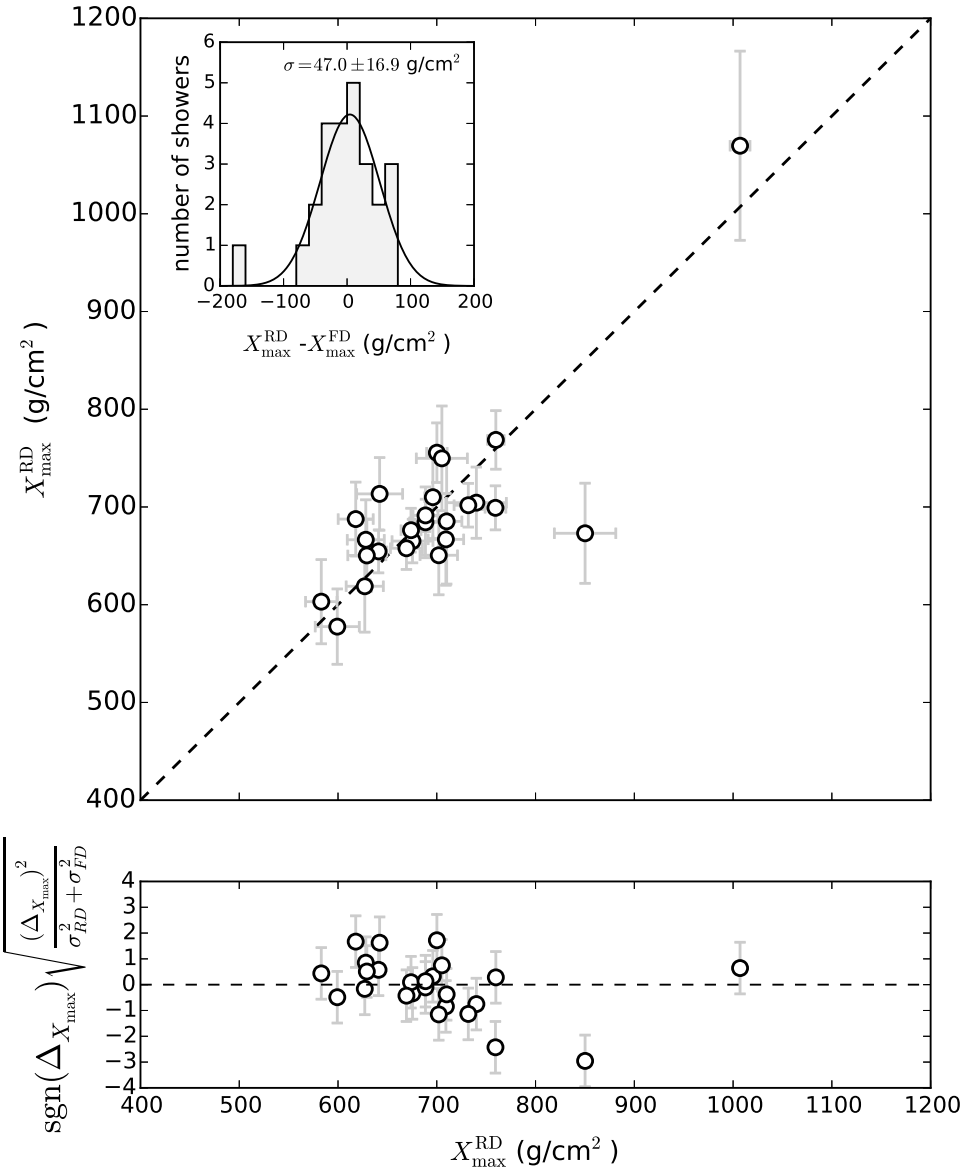

Figure 7.11: Comparison between the reconstructed X_{max} based on the simulated energy-density profiles and the measurements of the Fluorescence Detector. The dashed line represents the bisecting line. In the bottom panel, the residuals are shown. The uncertainties do not include systematic uncertainties of the FD measurement. In the inset, the distribution of the differences of the reconstructed values is shown. The solid line represents a fit with a Gaussian function with $\mu = 4.4 \pm 13.9\,\mathrm{g/cm^2}$ and $\sigma = 46.7 \pm 16.9\,\mathrm{g/cm^2}$.

metrical distance to X_{max} (see section 5.2.4). The typical correction is of the order of 20 g/cm^2. The uncertainty associated with this correction is less than 1 g/cm^2. However, a difference in the atmospheric profile also effects the whole shower development. From re-simulating a subset of showers with an adapted atmosphere and thereby different deviations compared to the GDAS profile, the reconstructed value of X_{max} is affected by less than 3 g/cm^2. For the

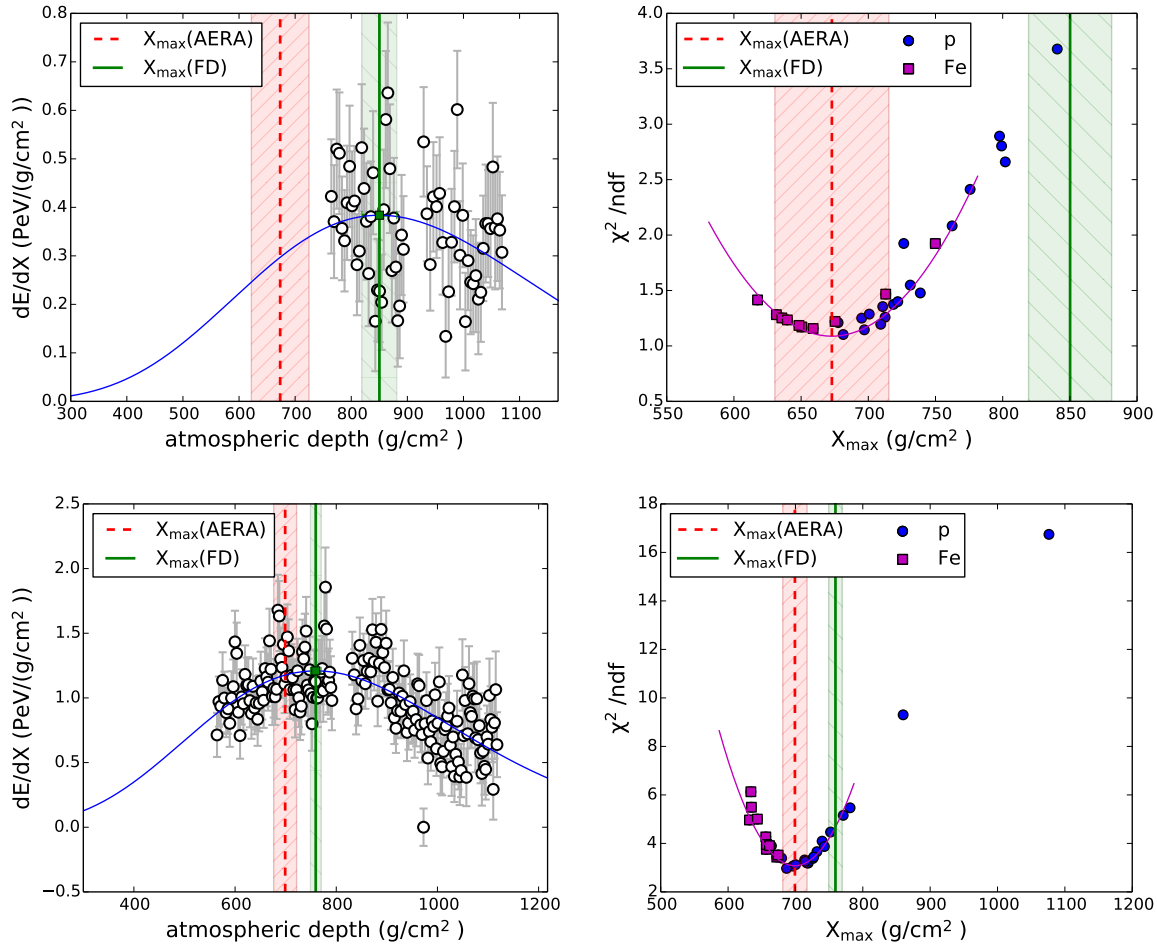

Figure 7.12: χ^2/ndf-distributions and longitudinal profiles for the two showers with the largest residuals in the subset used for the direct $X_{\max}$ comparison.

correction of the atmospheric density profile, the arrival direction is used which also introduces an uncertainty that depends on the value of $X_{\max}$ itself and due to the secant relation given in equation 7.3 also on the shower geometry. The contribution of this uncertainty depends on the angular resolution and is determined during reconstruction for every individual shower. The determination of the uncertainty originating from simulating the shower only for the reconstructed arrival direction not taking the angular resolution into account is pending. Uncertainties for the FD measurements are taken as presented in section 3.6. A summary of the discussed uncertainties is given in table 7.5. In addition, the used simulation codes and therein especially the hadronic interaction models introduce uncertainties as they are based on extrapolations from values for lower energies. These uncertainties are not included in the presented analyses. It is up to future work to extend the simulation sets to also include and compare the different interaction models. The analysis is also only performed with simulations based on CoREAS. Efforts to compare the results with a similar but not identical kind of analysis based on ZHAires simulations are ongoing and no principle problems have been

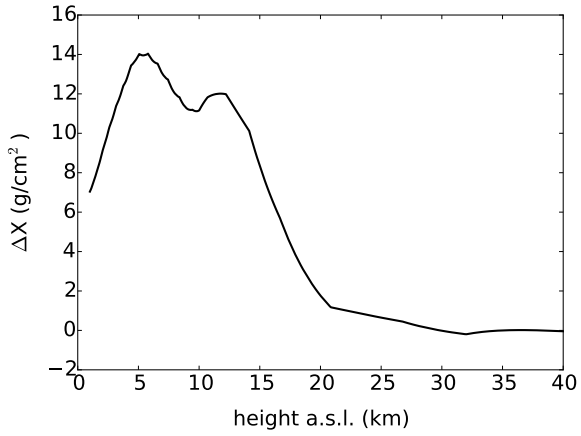

Figure 7.13: Difference in atmospheric depth as a function of the height above sea level between GDAS and the US standard parametrization of the atmosphere. The GDAS profile is evaluated for March 6th, 2014 at 5:34 UTC.

Table 7.5: Overview of uncertainties on the reconstructed value of $X_{\max}$ for the radio as well as for the Fluorescence Detector reconstruction.

	source of uncertainty	$\sigma_{X_{\max}}$
RD		
	GDAS profile	$< 1\,\mathrm{g/cm^2}$
	correction for the simulated atmosphere	$< 3\,\mathrm{g/cm^2}$
	angular resolution	propagated from the SD reconstruction
	minimum in χ^2/ndf-distribution	determined from sim set
FD		
	missing Mie data (for a subset of the data)	6.2 g/cm^2
	photonstatistics, geometry, atmosphere, timing	taken from FD reconstruction
	FD systematic uncertainty	$8 - 11\,\mathrm{g/cm^2}$

identified so far. Also no indication for large discrepancies due to different simulation codes is given by the authors in [71] describing the original application of the method to LOFAR data. The average uncertainty of $X_{\max}$ taken from all 55 successfully reconstructed showers is 34 g/cm^2. The increased average uncertainty compared to the results from LOFAR can mainly be attributed to the sparser antenna station grid which results in only a handful of signal stations per event compared to hundreds of antennas measuring the radio signal per shower for the LOFAR experiment. Nevertheless, the technique improves the achievable resolution for $X_{\max}$ measurements with AERA compared to other methods developed so far.

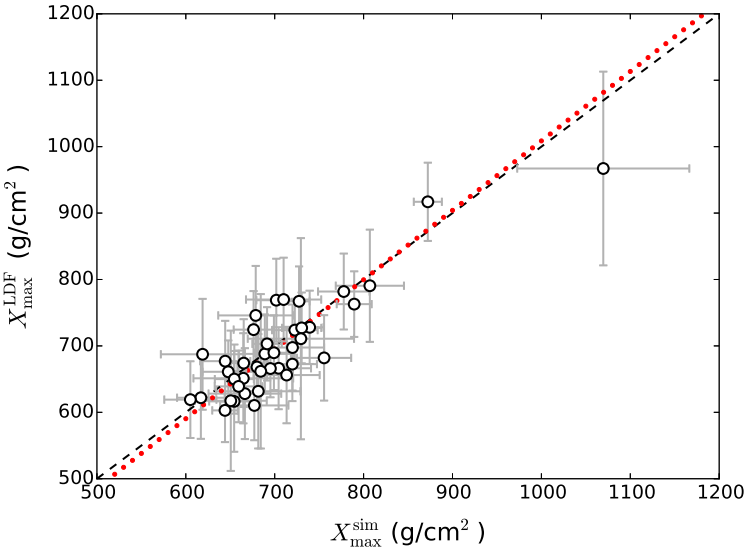

Figure 7.14: Comparison of the reconstructed X_{max} from the simulated energy-density profiles and from the 2D LDF fit. The black dashed line represents the bisecting line, the red dotted line is the best fit to the data ($X_{\mathrm{max}}^{\mathrm{LDF}} = (1.05 \pm 0.20)\, X_{\mathrm{max}}^{\mathrm{sim}} - (37 \pm 137)$ (g/cm^2)).

7.2.7 Direct Comparison between both Methods

The two presented methods to determine X_{max} can be cross checked against each other. It should be noted, that the methods are not completely independent, as the parametrization of the 2D LDF is based in the same type of simulations as directly fitted to the data and both approaches use the same measured quantity, the energy density, for the reconstruction. For the check, 40 showers from the set which also survive the quality criteria associated with the LDF fit given in table 7.6 are selected. For the other showers either the simulation-based reconstruction does not succeed or the LDF reconstruction quality cuts are not fulfilled. The correlation is shown in figure 7.14. Within the uncertainties, a linear fit to the data is in agreement with the bisecting line. The scatter around the line has a mean of $\mu = 14.7 \pm 6.0\,\mathrm{g/cm^2}$ and a width of $\sigma = 32 \pm 8\,\mathrm{g/cm^2}$. The seen offset is thereby compatible with the combination of the offsets of the two radio reconstructions when compared to the FD measurement (see figure 7.5 and figure 7.11). The width has a comparable value as seen in a similar comparison for LOFAR data where the resolution is 38 g/cm^2 [39].

7.3 X_{max} Reconstruction using RD-SD Hybrid Data

Based on the calibration presented in section 7.1, X_{max} is reconstructed for the whole RD-SD hybrid dataset for which mainly no FD observations are available. All events observed with three or more RDSs are potentially usable for the reconstruction of X_{max}. For showers detected with three and four RDS however, the core position needs to be taken from the SD

Table 7.6: Overview of selection cuts and the number of showers surviving these cuts starting with 6569 RD-SD hybrid showers.

cut	number of showers after cut
successful 2D LDF fit (equation 5.2)	6192
zenith angle $< 55°$	4708
geomagnetic angle $\alpha > 10°$	4701
≥ 5 stations with signal	1543
$\sigma < 270\,\mathrm{m}$	1410
uncertainty of $\sigma < 20\%$	1203
no thunderstorm conditions	1074
(no data available for 230 events)	

reconstruction which in many cases introduces additional scatter due to the uncertainties in the SD core position reconstruction. Therefore, these events are not taken into account for the following analysis. This hard cut has an impact on the energy distribution as well as the distribution of arrival directions as it requires the lateral distribution of the electric field with an amplitude above the SNR to be wide enough. Thereby, the low-energy showers are cut away and at the same time showers with a small zenith angles are disfavoured as their footprints are small due to the small distances to $X_{\max}$. As before, a cut on the maximum zenith angle is set to 55°. Furthermore, the same radio quality cuts as applied to the multi-hybrid dataset are used for this set. The cut statistics are shown in table 7.6. The distributions of energy and arrival direction in the resulting dataset are shown in figure 7.15. Remarkable is the horseshoe like population in the skyplot. This is due to the combination of the suppression of radio emission for air showers arriving parallel to the geomagnetic field and the fact that for vertical air showers, the distance to the emission region is small and therefore detections with high radio station multiplicity are suppressed. The energy distribution of the selected showers has a higher energy threshold compared to the total set. This is also due to the effects mentioned before in combination with the minimum number of signal stations set to five.

Besides these influences on the distributions of energy and arrival direction, there is also a possible influence on the measured distribution of $X_{\max}$. Deeply penetrating vertical (proton) primaries induce an extensive air shower at lower altitude and thereby the air shower is not fully developed before reaching ground. This on one hand leads to less energy in the radiation as discussed in chapters 5 and 6 and on the other hand gives a lower detection probability with a radio array due to the smaller footprint and the lower amplitudes. The full efficiency for the radio detector depends on multiple air-shower parameters which are energy, zenith angle, geomagnetic angle and $X_{\max}$, and also on which part of AERA the air shower was detected in as the antenna spacing is not homogeneous. On top, it also needs to be kept track of the uptime of the individual RDSs. Taking all these influences together further data reduction and

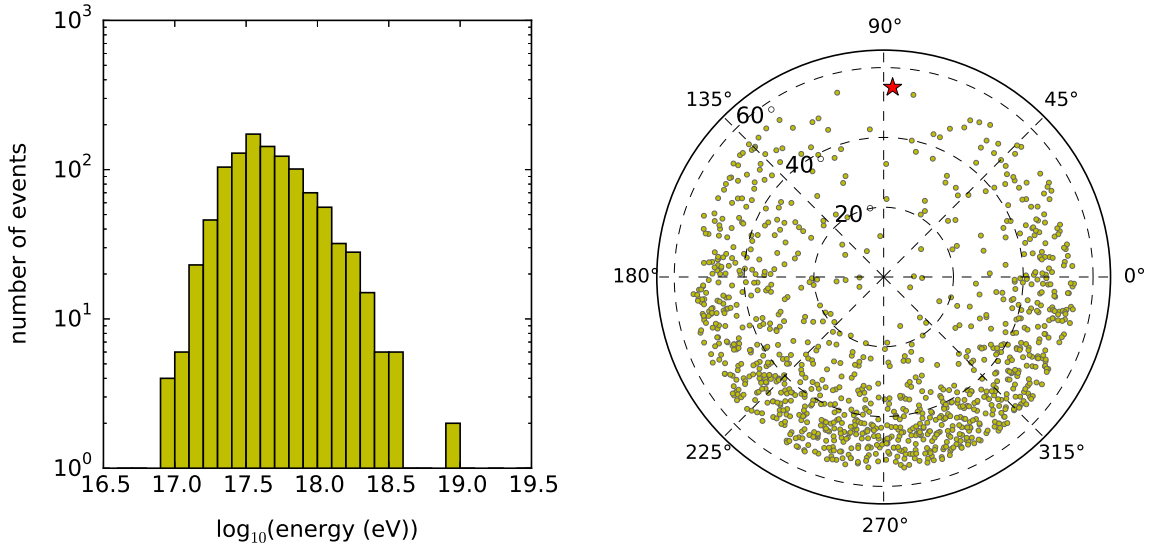

Figure 7.15: Distributions of energy (left) and arrival direction (right) for all air showers detected with a signal above SNR threshold in five or more RDSs. The star in the skyplot indicates the direction of the geomagnetic field at the site of AERA.

extended simulation studies are necessary to determine a fully unbiased dataset. For now, only a plain representation of the reconstructed X_{max} distribution is shown in the following as a preliminary result, not including bias corrections and systematic uncertainties.
The comparison between the measured average value of the depth of the shower maximum $\langle X_{\mathrm{max}} \rangle$ and the predictions from simulation studies for different hadronic interaction models gives an indication of the composition of the cosmic rays. To extract this information, the reconstructed and selected air showers in the hybrid dataset presented above are used to determine $\langle X_{\mathrm{max}} \rangle$ and the elongation rate for the AERA data. A histogram of the X_{max} distribution as well as a scatter plot of the reconstructed values of X_{max} using AERA as function of the cosmic-ray energy as measured with the SD for all selected events is shown in figure 7.16. The overall distribution of X_{max} is similar to the one obtained from the RD-SD-FD multi-hybrid events (see figure 3.10). The shown uncertainties are determined by propagating the modified fit uncertainties of the LDF width parameter. The general shape indicates the increase in X_{max} with increasing energy and a decreasing overall spread. To compare the obtained distribution with other experimental results and model predictions, the reconstructed X_{max} values are binned in energy and summarized in a profile histogram. The chosen energy range spans over one decade from $10^{17.2}$ eV to $10^{18.2}$ eV and is split up in 5 bins which are equally spaced in the common logarithm of the energy. The obtained values are directly compared to results from experiments using optical detectors to determine X_{max} like Tunka, Yakutsk, or the Auger Fluorescence Detector. The corresponding plot is shown in figure 7.17 and also contains simulation results for proton and iron nuclei based on the hadronic interaction models EPOS-LHC and QGSJET-II-04 (see section 1.2.3). The simulated lines should be interpreted as indicators

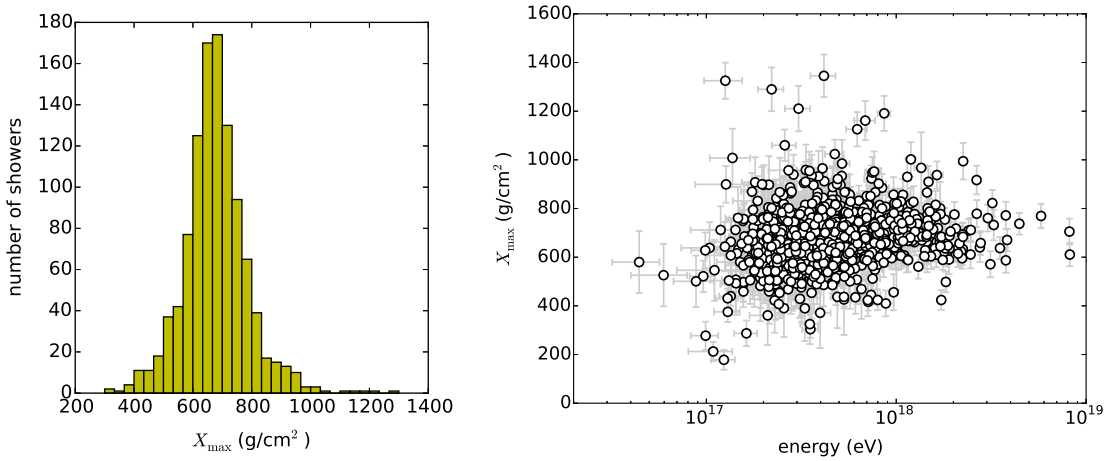

Figure 7.16: Reconstructed values of $X_{\max}$ using the width of the LDF and the calibration presented in section 7.1. Left: Distribution of the reconstructed $X_{\max}$ values. Right: Scatter plot of $X_{\max}$ as function of the cosmic ray energy.

for the two extreme cases in terms of single cosmic-ray species. For the investigated energy range, the $\langle X_{\max} \rangle$ as determined from the AERA data is in agreement with the measurements of the other experiments shown and also indicates the trend from a heavier towards a lighter composition with increasing energy. The values determined with AERA are smaller than the ones obtained with the Fluorescence Detector (Auger) which is in line with the offset seen in figure 7.5. Correcting for this offset would shift the values upwards very close to the ones obtained from the Fluorescence Detector. The relation between the average depth of the maximum shower development $\langle X_{\max} \rangle$ for a given primary type and cosmic-ray energy is described by the elongation rate (see section 1.2.2). It has been determined by extensive simulation studies for different hadronic interaction models and has a literature value of $50 - 60\,\mathrm{g/cm^2}$ per decade of energy for a single cosmic-ray species in the energy range investigated by AERA (e.g., [175]). Using a linear fit to the presented average values results in an elongation rate of $89 \pm 14\,\mathrm{g/cm^2}$ per decade of energy which is very similar to the value obtained for example from the Auger Fluorescence Detector of $85.0\,\mathrm{g/cm^2}$ per decade of energy [171] for the energy range from 10^{17} eV to $10^{18.3}$ eV.

These results are to be seen as a first effort to reconstruct $X_{\max}$ and from their the composition of the measured cosmic rays using the lateral distribution of the radio emission with AERA. Further studies of the detection efficiencies and the systematic uncertainties are pending. The obtained result is nevertheless a promising step on the way to composition measurements with radio detectors.

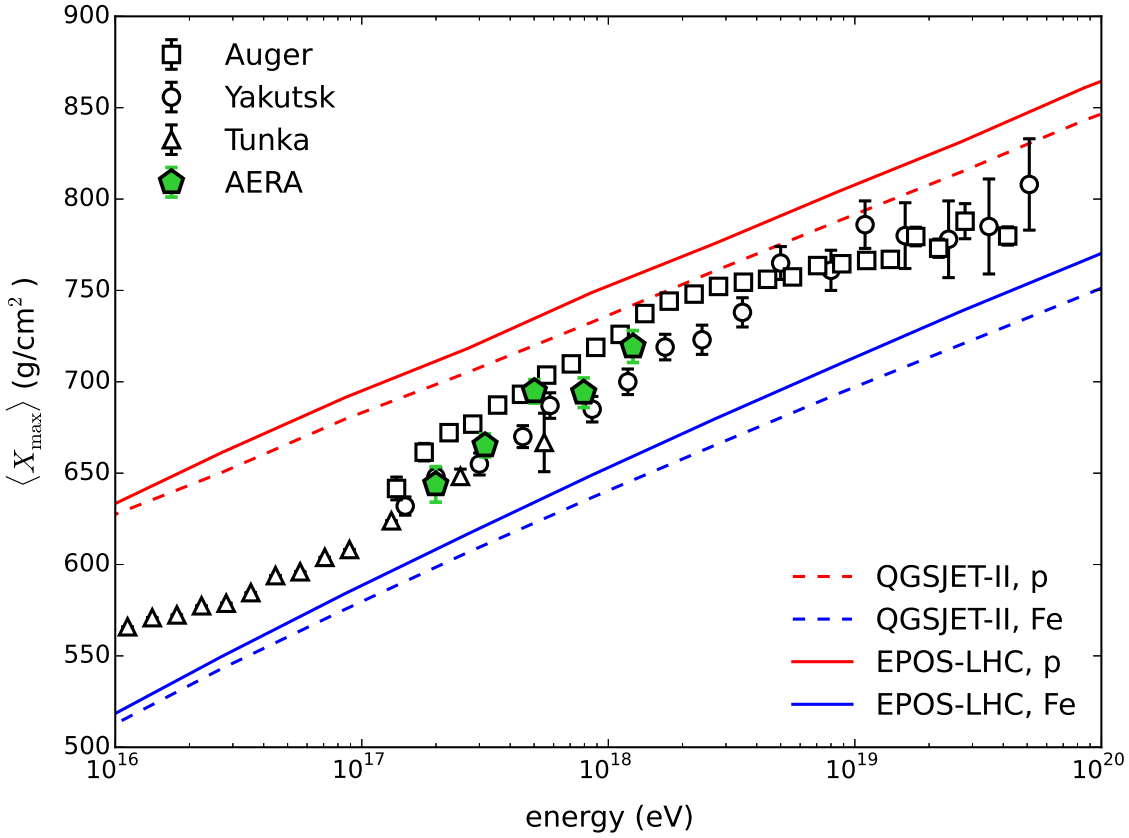

Figure 7.17: Average depth of the shower maximum $\langle X_{\mathrm{max}} \rangle$ as function of the energy as measured with AERA. In addition, the data from the Auger Fluorescence Detector [171], Tunka [172], and the Yakutsk array [173, 174] are shown. The lines indicate $\langle X_{\mathrm{max}} \rangle$ values obtained from simulations for protons and for iron nuclei using the hadronic interaction models EPOS-LHC [49] and QGSJET-II-04 [148]. It should be noted here that the AERA dataset is not corrected for possible efficiency biases and other systematic effects.

8

Conclusions and Outlook

Rapid developments of the experimental as well as the theoretical aspects of the radio detection of extensive air-showers have drawn the attention from the cosmic-ray research community towards the recent results of experiments like AERA, LOFAR, and Tunka-Rex. The radio technique not only offers a competitive sensitivity to the three observables, **direction**, **energy**, and **particle type** but also a duty cycle of 100%. Thereby, it is suited to become the key tool to unriddle the nature and the origin of ultra high-energy cosmic rays. With an improved understanding of the microscopic and the macroscopic effects responsible for the radio emission and propagation taking place in extensive air showers, big improvements became possible in the theoretical prediction and also in the experimental reconstruction of the measured signals and their interpretation (chapter 1). The high-quality multi-hybrid data from AERA and the baseline detectors of the Pierre Auger Observatory thereby allow a precise calibration of properties reconstructed from the radio signals with complementary detection techniques.

The work presented in this thesis is contributing to the field of radio detection by targeting the three observables, especially the particle type with AERA. On the way to this goal, hardware and field work were carried out to extent the existing engineering array becoming the world's largest radio cosmic ray detector which AERA is today (chapter 2). A revised station design and the enlarged array required testing the solar power system as well as the electromagnetic compatibility of the electronics to be suitable for the planed application. Additionally, the communication of the radio detection stations has been extended from an optical fibre to a wireless network to bridge the large distances. All together the system integration efforts have contributed to two efficient deployment campaigns and a smooth operation of AERA in its extended stages with 124 and later 153 radio detection stations. The gained experience is also valuable input for future hardware development. The small internal particle detectors deployed with a number of radio detection stations are a reliable trigger source. Based on the measurements with these detectors, information about the shower is obtained and can be included in the data reconstruction (chapter 4). The size of the detectors is however small and the trigger efficiency as well as the sensitivity to shower parameters would benefit from larger units.
Since 2011 and especially after the extension of AERA in 2013, thousands of air showers have been measured in coincidence with the Surface Detector array and partly also with the Fluorescence Detector. The acquired dataset represents the largest number of cosmic rays measured through there radio emission and simultaneously with a classical detection technique so far.

The development of a standardized reconstruction pipeline for these data is a major effort of the whole AERA group and contributions were made in this thesis (chapter 3). The resulting dataset also contains several hundred reconstructed multi-hybrid measurements of air showers which is unique in its kind and is used for various analyses. From a basic comparison between the arrival directions as reconstructed from the radio signal times and the arrival directions as measured with the Surface Detector array, a resolution of better than 0.5° is obtained.
On the simulation side, great progress has been made by generating two large sets of simulations for AERA. One set is based on the properties of the measured air showers using realistic antenna positions on the ground. Combined with noise data from the time of the measurement, this set is used for realistic studies and further development of the reconstruction of air shower parameters. The other set is using a generic antenna array forming a regular star in the shower plane. The special alignment of the simulated antenna positions allows to resample the 2D energy-density pattern in great detail. Based on this set, observables are tested for their correlation with shower parameters and second order effects in the radio emission processes have been investigated.
The lateral distribution of the radio signal cannot be described in one dimension only. Therefore, the parametrization of the lateral distribution was a long-standing challenge. With the recent developments on the simulation site e.g., the star-shape antenna grid, and the detailed measurements from the LOFAR telescope, this challenge has been tackled and an empirical two-dimensional description is now available. A detailed simulation study reveals an unseen sensitivity to the energy, the position of the shower axis, and the depth of the shower maximum (chapter 5). A new observable which is the total energy in the radio signal taken as the integral over the 2D lateral distribution function (LDF) is strongly correlated with the total energy in the shower. Using this quantity yields a better resolution than using the maximum intensity of the lateral distribution. Based on the general description of the LDF, a revised version has been formulated for AERA, optimized for a less densely populated antenna station array. The influences of this simplified model on the reconstructed parameters are investigated and found to be small compared to the influence of the number of antennas and their spacing. The AERA spacing is however dense enough to use the 2D LDF as a basis for the reconstruction of shower parameters with a higher resolution than other methods available so far.
Employing the 2D LDF to reconstruct the energy radiated in the MHz frequency band for measured hybrid data has been used by the AERA group for a calibration with the energy measured with the Surface Detector array which in turn is calibrated with the Fluorescence Detector (chapter 6). The radio energy shows a quadratic dependency on the shower energy when corrected for geometric influences on the strength of the emission processes. This relation is expected for the coherent emission of the radiation. The reached energy resolution is 22% for the used dataset and is improved to 17% by using a high-quality subset. The energy in radiation is only a small fraction of the total energy in the shower and a value of 15.8 MeV for a shower with 1 EeV is found when the shower arrives perpendicular to the geomagnetic

field. The energy in the radiation is not only a very good energy indicator, but also a quantity that can be determined from first principles based on the laws of electro-magnetism. Thereby it can be used to determine the energy scale of cosmic rays and to calibrate other detection techniques.

Based on the results of simulation studies using the generic and the purpose-made simulations for AERA, a calibration of the width of the lateral distribution as function of the distance to the shower maximum has been performed for AERA for the first time (chapter 7). This calibration allows for the unique opportunity to compare the results obtained from radio data to the measurements of the Fluorescence Detector. The amount of high quality RD-SD-FD multi-hybrid data is at the moment unfortunately still too limited for a purely data driven calibration, the simulation-based calibration is however in agreement with the available measurements of the Fluorescence Detector. The confirmation of the method is important for AERA as well as for other radio experiments which can not be cross checked with an independent detection technique. The resolution on the depth of the shower maximum obtained from the calibration is $53.5 \pm 1.7\,\mathrm{g/cm^2}$ and limited by the relatively sparse antenna array. The application of the method to the whole AERA RD-SD hybrid dataset has been used to measure the average depth of the shower maximum for 5 bins in the energy range from $10^{17.2} - 10^{18.2}\,\mathrm{eV}$. Thereby, an independently confirmed method to measure the depth of the shower maximum is used for the first time to extract information about the cosmic ray composition from the radio signals. The measurements exhibit a trend towards a lighter composition as a function of energy. The obtained results are in perfect agreement with results from other experiments using classical techniques operating in the same energy range. It is up to future work to incorporate the effects on the measured distribution by means of efficiency, preferred shower geometries, and other aspects which can influence the resulting average values.

A second technique to reconstruct the depth of the maximum shower development proposed by the LOFAR collaboration is based on the agreement between simulations for the measured energy and arrival direction of the cosmic rays and the measured data. Sets of simulations covering the whole range of possible depths of the shower maximum are compared to the measured values and the interpolated depth for which the best agreement is achieved, is taken as the reconstructed value. The procedure has been adapted and developed further for the application to data acquired by AERA and also the Surface Detector array. The resulting values of the depth of the shower maximum are compared to the measurements with the Fluorescence Detector (chapter 7). This comparison is of great importance to validate the method also for other experiments. It has been shown here that the method works for AERA despite the limited number of signal stations and provides a measurement of the depth of shower maximum with an average uncertainty of $34\,\mathrm{g/cm^2}$. A subset has been compared to data from the Fluorescence Detector and the reconstructed values are in agreement within their uncertainties. Comparing both method the reconstruct the depth of maximum shower development with AERA, a linear correlation is found compatible with a slope of 1 and a spread of $32 \pm 8\,\mathrm{g/cm^2}$.

Altogether, the presented work contains answers to the questions of how to reconstruct air shower parameters with a radio cosmic-ray observatory. Competitive resolution is achieved for the measured **arrival direction** and the **energy**. The central scientific results of this thesis are the two methods to determine the **depth of the maximum shower development**. The methods are discussed in detail and the obtained values from AERA are validated by the direct comparison to the measurements of the Fluorescence Detector. In addition, the results are compared on a statistical basis to other experiments for the first time.

The next generation of radio cosmic-ray observatories will benefit from the achieved technological and methodical developments. Cost efficient, robust, and self sufficient radio detection stations are essential for the construction of a large-scale detector-array targeting the highest energies. For these stations, thorough system integration is of extreme importance and the hardware developers will need to go new ways in the station design.
With the already very precise energy reconstruction of AERA, the focus of related work shifts towards the determination of second order effects. This is a necessary step on the way towards the determination of the energy scale of cosmic rays from first principles. Future work will also target improvements on the parametrization of the lateral distribution function. Here, a description based on the now well understood emission mechanisms and their interplay building up the observed density patterns could improve the agreement between data and model even further. First efforts in these directions have already been carried out and early results will be available soon.
On the shorter time scale, the focus of research at radio cosmic ray observatories is heading towards the precise determination of the depth of the maximum shower development. Mainly the combination of various shower development sensitive parameters offers great potential to improve the sensitivity even further. The timing information and also the frequency content of the pulses were found to be sensitive to the depth of the maximum shower development. Combined with the lateral distribution function, these observables will be included in joined analyses. The same holds true for the simulation-based reconstruction of the depth of the shower maximum for which these information is also available from the simulations and can be included in the fitting procedure.
The ongoing efforts in the radio detection of cosmic rays will allow to better understand the origin of ultra high-energy cosmic rays. Right now, the foundations are laid but further work is needed to pin point the objects responsible for these fascinating particles. As a final future prospect of the contribution of the radio detection of cosmic rays to this challenge, the average values of the depth of the shower maximum measured with AERA (figure 7.17) are converted to the mean logarithmic mass number and shown together with compiled data from various experiments in figure 8.1. The AERA measurements are in good agreement with the world data. In addition, predictions of the average mass number from a small selection of proposed astrophysical models are shown. The ankle model for example is based on the assumption that the

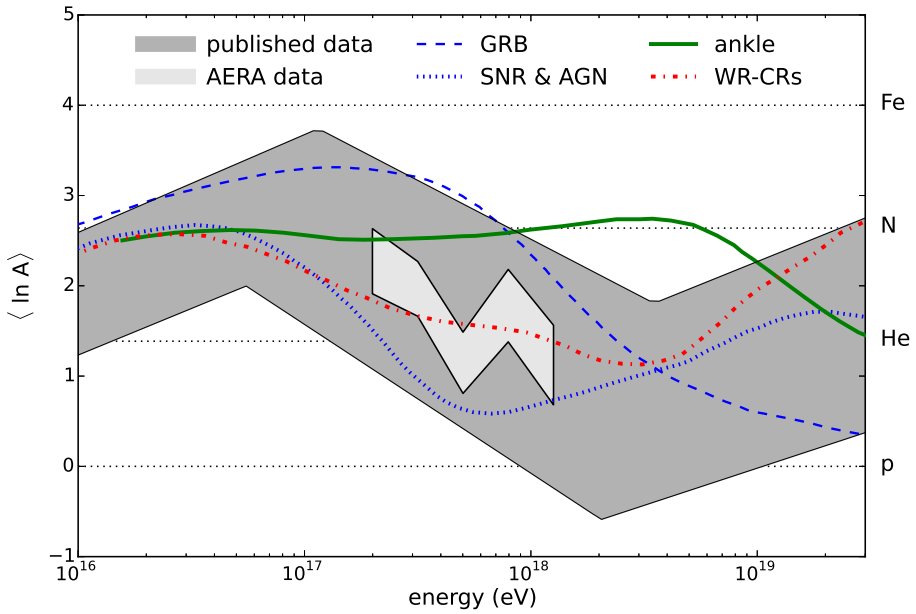

Figure 8.1: Values of the mean logarithmic mass number $\langle \ln \mathrm{A} \rangle$ from the experimental data and astrophysical models as a function of energy. The bands of published experimental data as well as the AERA data are computed using the two hadronic interaction models QGSJET-II-04 [148] and EPOS-LHC [49]. The collection of published data is taken from [25]. The values for the different models (ankle, GRB, SNR & AGN, and WR-CRs) are based on the work presented in [32, 176, 177, 178] and taken partly from [25].

composition and the origin of the cosmic rays changes around the ankle at $4 \times 10^{18}\,\mathrm{eV}$ from being mainly galactic iron nuclei towards extragalactic protons [32]. Also focussing on the transition from galactic to extragalactic cosmic rays is the SNR & AGN model which assumes that the lower energetic component of the cosmic radiation ($E < 10^{17}\,\mathrm{eV}$) is accelerated by supernova remnants and the highest energetic cosmic rays are of extragalactic origin, accelerated by active galactic nuclei [176]. The GRB model in contrast to that assumes cosmic rays are accelerated in highly relativistic jets originating from gamma ray bursts [177]. The last model shown is the WR-CRs model which proposes the sources of high energy cosmic rays to be Wolf-Rayet star explosions [178]. Further details on the shown models are given in the corresponding references. The WR-CRs model shows the best agreement with the AERA data and is also compatible with the compiled data of various experiments (taken from [25]) over the whole energy range presented. In general also the other models are in agreement with this compiled data but less favourable concerning the results from AERA. The presented AERA data are preliminary and investigations of systematic effects are not yet considered. Nevertheless, the presented result shows the great potential of the radio technique to help answering the fundamental questions about the nature of ultra high-energy cosmic rays.

A

Appendix

A.1 Wireless Communication Hardware and Settings

Information about the installed hardware and the used settings for frequency, channel width, and firmware for the AERA wireless communication network presented in chapter 2.

Table A.1: RDS with Ubiquiti COMs

Hardware	Bullet M5 HP
Channel width	40 MHz
Polarization	vertical
Firmware	XM.v5.5.4
Antenna	L-COM HG5827EG

Table A.2: Ubiquiti point-to-point CRS-Coihueco I

Hardware	Bullet M5 HP (Titanium @ CO)
SSID	AERACoihueco-CRS
Frequency	5.660 GHz
Channel width	40 MHz
Polarization	vertical
Firmware	XM.v5.5.4
Antenna	Poynting Antennas K-GRID-003-06

Table A.3: Ubiquiti point-to-point CRS-Coihueco II

Hardware	Bullet M5 HP (Titanium @ CO)
SSID	AERACoihueco-CRS#2
Frequency	5.600 GHz
Channel width	40 MHz
Polarization	vertical
Firmware	XM.v5.5.6
Antenna	Poynting Antennas K-GRID-003-06

Table A.4: Access Points CRS

AP	CRS-East	CRS-West
Hardware	Rocket M5 GPS	Rocket M5
SSID	AERAsectorE_CRS	AERAsectorW_CRS
Frequency	5.785 GHz	5.805 GHz
Channel width	40 MHz	40 MHz
Polarization	vertical	vertical
Firmware	XM.v5.5.4	XM.v5.5.4
Antenna	Airmax Sector 5G-90-20	Airmax Sector 5G-90-20

Table A.5: Access Points Coihueco

Hardware	Rocket M5 GPS Titanium	Rocket M5 GPS
SSID	AERAsector_Coihueco	AERAsector_Coihueco2
Frequency	5.745 GHz	5.560 GHz
Channel width	40 MHz	40 MHz
Polarization	vertical	vertical
Firmware	XM.v5.5.4	XM.v5.5.4
Antenna	Airmax Sector 5G-90-20	Airmax Sector 5G-90-20

A.2 Module Sequence RdObserver

Module sequence of the RdObserver which is used to reconstruct the RD-SD hybrid and RD-SD-FD multi-hybrid datasets presented in chapter 3 and used in the analyses in chapter 7.

```
<loop numTimes="unbounded">
  <module> EventFileReaderOG                    </module>
  <module> RdEventPreSelector                   </module>
  <module> EventCheckerOG                       </module>
  <module> SdQualityCutTaggerOG                 </module>
  <module> SdPMTQualityCheckerKG                </module>
  <module> TriggerTimeCorrection                </module>
  <module> SdCalibratorOG                       </module>
  <module> SdBadStationRejectorKG               </module>
  <module> SdSignalRecoveryKLT                  </module>
  <module> SdEventSelectorOG                    </module>
  <module> SdPlaneFitOG                         </module>
  <module> LDFFinderKG                          </module>
  <try>
    <module> SdHorizontalReconstruction         </module>
  </try>
  <module> RdEventInitializer                   </module>
  <module> RdStationPositionCorrection          </module>
  <module> RdStationRejector                    </module>
  <module> RdChannelADCToVoltageConverter       </module>
  <module> RdChannelSelector                    </module>
  <module> RdChannelPedestalRemover             </module>
  <module> RdChannelResponseIncorporator        </module>
  <module> RdChannelBeaconTimingCalibrator      </module>
  <module> RdChannelBeaconSuppressor            </module>
  <module> RdStationTimingCalibrator            </module>
  <module> RdStationTimeWindowConsolidator      </module>
  <module> RdChannelTimeSeriesTaperer           </module>
  <module> RdChannelBandstopFilter              </module>
  <module> RdChannelUpsampler                   </module>
  <module> RdChannelRiseTimeCalculator          </module>
  <module> RdAntennaChannelToStationConverter   </module>
  <module> RdStationSignalReconstructor         </module>
  <module> RdStationEFieldVectorCalculator      </module>
  <loop numTimes="unbounded">
```

```
      <module> RdTopDownStationSelector </module>
      <module> RdPlaneFit               </module>
    </loop>
    <module> RdClusterFinder                    </module>
    <module> RdPlaneFit                         </module>
    <module> RdStationRiseTimeCalculator        </module>
    <module> RdEventPostSelector                </module>
    <module> RdLDFMultiFitter                   </module>
    <module> Rd2dLDFFitter                      </module>
    <try>
      <module> FdCalibratorOG                   </module>
      <module> FdEyeMergerKG                    </module>
      <module> FdPulseFinderOG                  </module>
      <module> FdSDPFinderOG                    </module>
      <module> FdAxisFinderOG                   </module>
      <module> HybridGeometryFinderOG           </module>
      <module> HybridGeometryFinderWG           </module>
      <module> FdApertureLightKG                </module>
      <module> FdEnergyDepositFinderKG          </module>
      <module> FdProfileReconstructorKG         </module>
    </try>
    <module> RdStationTimeSeriesWindowCutter    </module>
    <module> RdStationTimeSeriesTaperer         </module>
    <module> RdREASSimPreparator                </module>
    <module> EventFileExporterOG                </module>
    <module> RecDataWriterNG                    </module>
  </loop>
```

A.3 Quality Cuts for the RD-SD-FD Multi-Hybrid Dataset

Quality cuts used for the energy calibration of the Surface Detector Infill array using SD-FD hybrid events. These cuts are applied to the RD-SD-FD multi-hybrid data to extract high quality $X_{\max}$ measurements. The selected showers are used in the analysis in chapter 7.

Table A.6: SD-FD energy calibration cuts for the Infill array.

cut	value
!lightning	
minRecLevel	3
maxZenithSD	55°
T4Trigger	2
T5Trigger	2
heatOrientationUp	
eyeCut	101111
minLgEnergyFD	1e-20
skipSaturated	
badFDPeriodRejection	
maxVAOD	0.1
LidarCloudRemoval	25
MinCloudDepthDistance	params: -50 50
MaxCloudThickness	100
!badPixels	1
xMaxObsInExpectedFOV	params: 40 20
xMaxError	40.0
energyTotError	0.18
profileChi2Sigma	2.5 -1.1
maxDepthHole	20.
maxCoreTankDist	750m

A.4 Scintillator Calibration

Values of the upper limits of the particle density for sub-threshold scintillator detectors and calibration values for the deposited energy in the scintillator detectors by single muons. Both quantities are calculated as discussed in chapter 4.

Table A.7: Upper limits (UL) for the integrated signal in sub-threshold stations.

No.	UL Top (VEM)	UL Bottom (VEM)	No.	UL Top (VEM)	UL Bottom (VEM)
34	0.60	0.60	110	0.64	0.96
35	0.66	0.84	111	0.66	0.58
36	0.62	0.68	112	0.82	0.74
43	0.60	0.62	113	0.62	0.60
44	0.52	0.56	122	0.46	0.62
49	0.70	0.60	123	0.50	0.60
58	0.64	0.64	124	0.58	0.64
59	0.54	0.64	125	0.58	0.84
60	0.52	0.58	135	0.52	0.52
69	0.62	0.92	136	0.50	0.48
70	0.42	0.50	137	0.60	0.64
83	0.56	0.66	144	0.54	0.56
84	0.50	0.66	145	0.40	0.70
85	0.62	1.14	151	0.50	1.52
92	0.62	0.64	152	0.56	0.58
93	0.60	0.80	88	0.58	-
94	0.64	0.66	103	0.58	-
100	0.58	0.78	126	0.58	-
101	0.62	0.82	146	0.58	-
102	0.64	0.84	157	0.58	-

Table A.8: Values in units of fC extracted from the single muon calibration for the individual scintillators. The values for a combined distribution of all scintillators are displayed under <average>.

No.	$\text{width}_{L,\,T}$	peak_{T}	$\text{width}_{G,\,T}$	$\text{width}_{L,\,B}$	peak_{B}	$\text{width}_{G,\,B}$
<average>	0.08±0.01	0.91±0.01	0.35±0.01	0.09±0.01	0.76±0.01	0.34±0.01
34	0.07±0.01	0.87±0.01	0.30±0.02	0.07±0.01	0.87±0.02	0.34±0.02
35	0.06±0.01	0.81±0.02	0.30±0.02	0.08±0.01	0.68±0.01	0.26±0.02
36	0.07±0.01	0.85±0.01	0.28±0.02	0.08±0.01	0.80±0.01	0.29±0.02
43	0.09±0.01	0.93±0.01	0.29±0.02	0.07±0.01	0.84±0.01	0.31±0.02
44	0.06±0.01	0.99±0.02	0.44±0.02	0.08±0.01	0.92±0.01	0.30±0.02
49	0.05±0.01	0.98±0.02	0.49±0.03	0.07±0.01	0.84±0.02	0.31±0.02
58	0.06±0.01	0.94±0.02	0.30±0.02	0.08±0.01	0.78±0.01	0.28±0.02
59	0.10±0.01	0.99±0.02	0.33±0.02	0.06±0.01	0.76±0.01	0.28±0.01
60	0.07±0.01	0.99±0.01	0.30±0.01	0.06±0.01	0.84±0.01	0.30±0.02
69	0.06±0.01	0.88±0.01	0.30±0.02	0.06±0.01	0.55±0.03	0.45±0.04
70	0.08±0.01	1.25±0.02	0.41±0.02	0.07±0.01	1.13±0.02	0.43±0.02
83	0.07±0.01	0.92±0.02	0.34±0.02	0.09±0.01	0.79±0.02	0.43±0.03
84	0.08±0.01	1.06±0.01	0.33±0.02	0.08±0.01	0.76±0.01	0.30±0.02
85	0.08±0.01	0.99±0.02	0.35±0.02	0.09±0.01	0.63±0.02	0.28±0.02
92	0.08±0.01	0.84±0.01	0.29±0.02	0.09±0.01	0.82±0.01	0.31±0.02
93	0.08±0.01	0.85±0.01	0.27±0.02	0.07±0.01	0.73±0.01	0.31±0.02
94	0.05±0.01	0.80±0.02	0.34±0.02	0.09±0.01	0.74±0.01	0.23±0.02
100	0.08±0.01	0.93±0.02	0.31±0.02	0.09±0.01	0.79±0.01	0.27±0.02
101	0.05±0.01	0.88±0.02	0.34±0.02	0.09±0.01	0.67±0.01	0.26±0.02
102	0.07±0.01	0.84±0.01	0.27±0.01	0.06±0.01	0.58±0.01	0.25±0.02
110	0.06±0.01	0.90±0.02	0.30±0.02	0.08±0.01	0.56±0.01	0.27±0.02
111	0.05±0.01	0.78±0.02	0.36±0.02	0.07±0.01	0.85±0.02	0.33±0.02
112	0.08±0.01	0.65±0.01	0.24±0.02	0.13±0.01	0.73±0.01	0.25±0.03
113	0.07±0.01	0.78±0.01	0.27±0.02	0.05±0.01	0.86±0.02	0.34±0.02
122	0.07±0.01	1.11±0.02	0.42±0.02	0.07±0.01	0.80±0.01	0.28±0.02
123	0.06±0.01	1.04±0.01	0.31±0.01	0.09±0.01	0.86±0.01	0.29±0.02
124	0.07±0.01	0.90±0.02	0.34±0.02	0.08±0.01	0.76±0.01	0.26±0.02
125	0.06±0.01	0.88±0.02	0.32±0.02	0.06±0.01	0.71±0.01	0.31±0.02
135	0.05±0.01	0.99±0.02	0.36±0.02	0.06±0.01	0.96±0.02	0.39±0.02
136	0.08±0.01	1.04±0.02	0.39±0.02	0.15±0.02	1.05±0.02	0.39±0.03
137	0.07±0.01	0.83±0.01	0.26±0.01	0.07±0.01	0.79±0.01	0.27±0.02
144	0.06±0.01	0.99±0.02	0.35±0.02	0.10±0.01	0.89±0.01	0.31±0.02
145	0.13±0.02	1.28±0.03	0.49±0.04	0.09±0.01	0.72±0.01	0.25±0.02
151	0.14±0.02	1.03±0.02	0.33±0.04	0.09±0.01	0.26±0.01	0.00±0.03
152	0.07±0.01	0.95±0.02	0.32±0.02	0.08±0.01	0.87±0.02	0.33±0.02

A.5 LDF Width Parameter Correlation

Parameters for the fifth-degree polynomial fit to the distribution of the atmospheric and the geometric distance to $X_{\max}$ as function of the width of the LDF $\sigma_{(+)}$ as discussed in chapter 5. The fit parameters are obtained by either using the original LDF function (equation 5.1) or the AERA parametrization (equation 5.2).

Table A.9: Atmospheric distance to $X_{\max}$ - $D^{\mathrm{atm}}_{\max}$

parameter	full fit	AERA
p0	-516.27	-571.323
p1	20.5449	23.8009
p2	-0.16958	-0.248084
p3	0.000545931	0.00143211
p4	4.06132e-07	-3.99593e-06
p5	-3.05614e-09	4.46421e-09

Table A.10: Geometric distance to $X_{\max}$ - $D^{\mathrm{geo}}_{\max}$

parameter	full fit	AERA
p0	-4.53748	-5.74906
p1	0.159968	0.229873
p2	-0.000627602	-0.00219756
p3	-4.21959e-06	1.22506e-05
p4	4.4592e-08	-3.28206e-08
p5	-9.05486e-11	3.67051e-11

A.6 Likelihood Function of the Energy Calibration

Likelihood function as used in chapter 6 for the energy calibration of AERA. The likelihood function (for one pair of radio signal S_{radio} and SD cosmic-ray energy estimate E_{SD}) has the following form

$$
\begin{aligned}
f(S_{\mathrm{radio}}, E_{\mathrm{SD}}) = \quad & \frac{1}{\mathrm{N}} \sum_i \frac{\varepsilon_{\mathrm{SD}}(E_{SD}, \Theta_i)\, \varepsilon_{\mathrm{RD}}(E_{\mathrm{SD}}, \Theta_i, \Phi_i)}{\varepsilon_{\mathrm{SD}}(E_{\mathrm{SD},i}, \Theta_i)\, \varepsilon_{\mathrm{RD}}(E_{\mathrm{SD},i}, \Theta_i, \Phi_i)} \times \\
& g_{\mathrm{RD}}(S_{\mathrm{radio}} | S(E_{\mathrm{SD},i}), ...) \times \\
& g_{\mathrm{SD-sh}}(E_{\mathrm{SD}} | E_{\mathrm{SD},i}, \Theta_i)\,. \qquad \text{(A.1)}
\end{aligned}
$$

The summation is performed over all events in the selected dataset. $g_{\mathrm{RD}}(S_{\mathrm{radio}}|S, ...)$ and $g_{\mathrm{SD-sh}}(E_{\mathrm{SD}}|E, \Theta)$ are the conditional probability density functions, which describe the probability to measure a radio signal S_{radio} or energy E_{SD} if the true radio signal, energy and zenith angle are S, E and Θ. Φ denotes the azimuth angle. $g_{\mathrm{RD}}(S_{\mathrm{radio}})$ is obtained for each event in a Monte Carlo simulation where all reconstructed parameters that influence the radio-energy estimator are varied within their uncertainties. $\varepsilon_{\mathrm{SD}}(E_{\mathrm{SD}}, \Theta)$ and $\varepsilon_{\mathrm{RD}}(E_{\mathrm{SD}}, \Theta, \Phi)$ are the efficiencies of the surface and the radio detector. The radio efficiency has been determined with Monte Carlo air-shower simulations and a full-detector simulation and depends on the energy, the zenith and the azimuth angle. N is the normalization of the function to an integral of one.

Bibliography

[1] B. ABELEV *et al.*, ALICE COLLABORATION, *Performance of the ALICE experiment at the CERN LHC*, International Journal of Modern Physics A, 29 (2014), p. 30044.

[2] J. LINSLEY, *Evidence for a Primary Cosmic-Ray Particle with Energy* 10^{20} *eV*, Physical Review Letters, 10 (1963), pp. 146–148.

[3] V. F. HESS, *Über Beobachtungen der durchdringenden Strahlung bei sieben Freiballonfahrten*, Physikalische Zeitschrift, 13 (1912), pp. 1084–1091.

[4] P. AUGER *et al.*, *Extensive Cosmic-Ray Showers*, Reviews of Modern Physics, 11 (1939), pp. 288–291.

[5] W. KOLHÖRSTER *et al.*, *Gekoppelte Höhenstrahlen*, Naturwissenschaften, 26 (1938), pp. 576–576.

[6] V. BONVICINI *et al.*, PAMELA COLLABORATION, *The PAMELA experiment in space*, Nuclear Instruments and Methods in Physics Research A, 461 (2001), pp. 262–268.

[7] M. AGUILAR *et al.*, AMS COLLABORATION, *First Result from the Alpha Magnetic Spectrometer on the International Space Station: Precision Measurement of the Positron Fraction in Primary Cosmic Rays of 0.5-350 GeV*, Physical Review Letters, 110 (2013), p. 141102.

[8] T. SANUKI *et al.*, BESS COLLABORATION, *Precise Measurement of Cosmic-Ray Proton and Helium Spectra with the BESS Spectrometer*, Astrophysical Journal, 545 (2000), pp. 1135–1142.

[9] M. AVE *et al.*, *The TRACER instrument: A balloon-borne cosmic-ray detector*, Nuclear Instruments and Methods in Physics Research A, 654 (2011), pp. 140–156.

[10] H. S. AHN *et al.*, CREAM COLLABORATION, *The Cosmic Ray Energetics And Mass (CREAM) instrument*, Nuclear Instruments and Methods in Physics Research A, 579 (2007), pp. 1034–1053.

[11] P. AUGER *et al.*, *Les grandes gerbes cosmiques de l'atmosphère*, Proceedings of the Academy of Sciences, 207 (1938), pp. 228–230.

[12] J. A. SIMPSON, *Elemental and isotopic composition of the galactic cosmic rays*, Annual Review of Nuclear and Particle Science, 33 (1983), pp. 323–382.

[13] W. D. APEL *et al.*, KASCADE-GRANDE COLLABORATION, *Kneelike Structure in the Spectrum of the Heavy Component of Cosmic Rays Observed with KASCADE-Grande*, Physical Review Letters, 107 (2011), p. 171104.

[14] J. R. HÖRANDEL, *On the knee in the energy spectrum of cosmic rays*, Astroparticle Physics, 19 (2003), pp. 193–220.

[15] J. R. HÖRANDEL *et al.*, *The Knee in the Energy Spectrum of Cosmic Rays in the Framework of the Poly-Gonato and Diffusion Models*, in Proceedings of the 28th International Cosmic Ray Conference, Tsukuba, Japan, 2003.

[16] Y. S. YOON *et al.*, CREAM COLLABORATION, *Cosmic-ray Proton and Helium Spectra from the First CREAM Flight*, Astrophysical Journal, 728 (2011), p. 122.

[17] A. D. PANOV *et al.*, *Elemental energy spectra of cosmic rays from the data of the ATIC-2 experiment*, Bulletin of the Russian Academy of Science, Physics, 71 (2007), pp. 494–497.

[18] O. ADRIANI *et al.*, PAMELA COLLABORATION, *PAMELA Measurements of Cosmic-Ray Proton and Helium Spectra*, Science, 332 (2011), p. 69.

[19] R. U. ABBASI *et al.*, HIGH RESOLUTION FLY'S EYE COLLABORATION, *First Observation of the Greisen-Zatsepin-Kuzmin Suppression*, Physical Review Letters, 100 (2008), p. 101101.

[20] W. D. APEL *et al.*, KASCADE-GRANDE COLLABORATION, *The spectrum of high-energy cosmic rays measured with KASCADE-Grande*, Astroparticle Physics, 36 (2012), pp. 183–194.

[21] M. AMENOMORI *et al.*, TIBET ASγ COLLABORATION, *The All-Particle Spectrum of Primary Cosmic Rays in the Wide Energy Range from 10^{14} to 10^{17} eV Observed with the Tibet-III Air-Shower Array*, Astrophysical Journal, 678 (2008), pp. 1165–1179.

[22] A. SCHULZ FOR THE PIERRE AUGER COLLABORATION, *The measurement of the energy spectrum of cosmic rays above 3×10^{17} eV with the Pierre Auger Observatory*, in Proceedings of the 33rd International Cosmic Ray Conference, Rio de Janeiro, Brazil, 2013.

[23] P. SCHELLART, *Measuring Radio Emission from air showers with LOFAR*, PhD thesis, Radboud University Nijmegen, 2015.

[24] J. BLÜMER *et al.*, *Cosmic rays from the knee to the highest energies*, Progress in Particle and Nuclear Physics, 63 (2009), pp. 293–338.

[25] K.-H. KAMPERT *et al.*, *Measurements of the cosmic ray composition with air shower experiments*, Astroparticle Physics, 35 (2012), pp. 660–678.

[26] T. ANTONI *et al.*, KASCADE COLLABORATION, *KASCADE measurements of energy spectra for elemental groups of cosmic rays: Results and open problems*, Astroparticle Physics, 24 (2005), pp. 1–25.

[27] D. D'ENTERRIA *et al.*, *Constraints from the first LHC data on hadronic event generators for ultra-high energy cosmic-ray physics*, Astroparticle Physics, 35 (2011), pp. 98–113.

[28] T. K. GAISSER, *The Cosmic-ray Spectrum: from the knee to the ankle*, Journal of Physics Conference Series, 47 (2006), pp. 15–20.

[29] A. AAB *et al.*, PIERRE AUGER COLLABORATION, *The Pierre Auger Cosmic Ray Observatory*, Nuclear Instruments and Methods, A798 (2015), pp. 172–213.

[30] W. H. BAUMGARTNER *et al.*, *The 70 Month Swift-BAT All-sky Hard X-Ray Survey*, Astrophysical Journal Supplement, 207 (2013), p. 19.

[31] A. AAB *et al.*, PIERRE AUGER COLLABORATION, *Searches for Anisotropies in the Arrival Directions of the Highest Energy Cosmic Rays Detected by the Pierre Auger Observatory*, Astrophysical Journal, 804 (2015), p. 15.

[32] V. BEREZINSKY *et al.*, *On astrophysical solution to ultrahigh energy cosmic rays*, Physical Review D, 74 (2006), p. 043005.

[33] K. GREISEN, *End to the Cosmic-Ray Spectrum?*, Physical Review Letters, 16 (1966), pp. 748–750.

[34] G. T. ZATSEPIN *et al.*, *Upper Limit of the Spectrum of Cosmic Rays*, Soviet Journal of Experimental and Theoretical Physics Letters, 4 (1966), p. 78.

[35] R. ALVES BATISTA *et al.*, *Effects of uncertainties in simulations of extragalactic UHECR propagation, using CRPropa and SimProp*, ArXiv e-prints, (2015).

[36] E. FERMI, *On the Origin of the Cosmic Radiation*, Physical Review, 75 (1949), pp. 1169–1174.

[37] A. M. HILLAS, *The Origin of Ultra-High-Energy Cosmic Rays*, Annual Review of Astronomy and Astrophysics, 22 (1984), pp. 425–444.

[38] J. CANDIA *et al.*, *Turbulent diffusion and drift in galactic magnetic fields and the explanation of the knee in the cosmic ray spectrum*, Journal of High Energy Physics, 12 (2002), p. 33.

[39] A. NELLES, *Radio emission from air showers*, PhD thesis, Radboud University Nijmegen, 2014.

[40] A. M. HILLAS, *TOPICAL REVIEW: Can diffusive shock acceleration in supernova remnants account for high-energy galactic cosmic rays?*, Journal of Physics G Nuclear Physics, 31 (2005), p. 95.

[41] A. ABRAMOWSKI *et al.*, HESS COLLABORATION, *HESS J1640-465 - an exceptionally luminous TeV gamma-ray supernova remnant*, Monthly Notices of the Royal Astronomical Society, 439 (2014), pp. 2828–2836.

[42] M. ACKERMANN *et al.*, FERMIN-LAT COLLABORATION, *Detection of the characteristic pion-decay signature in supernova remnants*, Science, 339 (2013), pp. 807–811.

[43] M. G. AARTSEN *et al.*, ICECUBE COLLABORATION, *Evidence for High-Energy Extraterrestrial Neutrinos at the IceCube Detector*, Science, 342 (2013), p. 1.

[44] M. G. AARTSEN *et al.*, ICECUBE COLLABORATION, *First Observation of PeV-Energy Neutrinos with IceCube*, Physical Review Letters, 111 (2013), p. 021103.

[45] W. HEITLER, *Quantum theory of radiation*, 1954.

[46] J. MATTHEWS, *A Heitler model of extensive air showers*, Astroparticle Physics, 22 (2005), pp. 387–397.

[47] J. R. HÖRANDEL, *Cosmic Rays from the Knee to the Second Knee:. 10^{14} to 10^{18} eV*, Modern Physics Letters A, 22 (2007), pp. 1533–1551.

[48] J. ENGEL *et al.*, *Nucleus-nucleus collisions and interpretation of cosmic-ray cascades*, Physical Review D, 46 (1992), pp. 5013–5025.

[49] T. PIEROG *et al.*, *EPOS LHC : test of collective hadronization with LHC data*, ArXiv e-prints, (2013).

[50] G. BATTISTONI *et al.*, *The FLUKA code: description and benchmarking*, in Hadronic Shower Simulation Workshop, M. Albrow *et al.*, eds., vol. 896 of American Institute of Physics Conference Series, 2007, pp. 31–49.

[51] S. OSTAPCHENKO, *QGSJET-II: towards reliable description of very high energy hadronic interactions*, Nuclear Physics B Proceedings Supplements, 151 (2006), pp. 143–146.

[52] E.-J. AHN *et al.*, *Cosmic ray interaction event generator SIBYLL 2.1*, Physical Review D, 80 (2009), p. 094003.

[53] D. HECK *et al.*, *CORSIKA: A Monte Carlo Code to Simulate Extensive Air Showers*, FZKA–6019, FZKA, 1998.

[54] S. J. SCIUTTO, *AIRES: A system for air shower simulations (Version 2.2.0)*, ArXiv e-prints, (1999).

[55] T. PIEROG *et al.*, *First results of fast one-dimensional hybrid simulation of EAS using CONEX*, Nuclear Physics B Proceedings Supplements, 151 (2006), pp. 159–162.

[56] L. G. DEDENKO, *A new method of solving the nuclear cascade equation*, in Proceedings of the 9th International Cosmic Ray Conference, London, UK, 1965.

[57] A. M. HILLAS, *Calculations on the propagation of mesons in extensive air showers*, in Proceedings of the 9th International Cosmic Ray Conference, London, UK, 1965.

[58] G. BOSSARD *et al.*, *Cosmic ray air shower characteristics in the framework of the parton-based Gribov-Regge model NEXUS*, PRD, 63 (2001), p. 054030.

[59] G. A. ASKARYAN, *Excess Negative Charge of the Electron-Photon Shower and Coherent Radiation Originating from It. Radio Recording of Showers under the Ground and on the Moon*, Journal of the Physical Society of Japan Supplement, 17 (1962), p. C257.

[60] F. D. KAHN *et al.*, *Radiation from Cosmic Ray Air Showers*, Royal Society of London Proceedings Series A, 289 (1966), pp. 206–213.

[61] S. GREBE, *Finger on the pulse of cosmic rays - dependence of the radio pulse shape on the air shower geometry*, PhD thesis, Radboud University Nijmegen, 2013.

[62] J. V. JELLEY *et al.*, *Radio Pulses from Extensive Cosmic-Ray Air Showers*, Nature, 205 (1965), pp. 327–328.

[63] F. G. SMITH *et al.*, *The detection of radio pulses of wavelength 6. 8 m, in coincidence with extensive air showers, in the energy region 10^{16}-10^{17} eV*, in Proceedings of the 9th International Cosmic Ray Conference, London, UK, 1965.

[64] H. R. ALLAN, *Radio Emission From Extensive Air Showers*, Progress in Elementary Particle and Cosmic Ray Physics, 10 (1971), pp. 171–302.

[65] O. RAVEL FOR THE CODALEMA COLLABORATION, *The CODALEMA experiment*, Nuclear Instruments and Methods in Physics Research A, 662 (2012), p. 89.

[66] P. LAUTRIDOU *et al.*, *Some possible interpretations from data of the CODALEMA experiment*, in American Institute of Physics Conference Series, R. Lahmann *et al.*, eds., vol. 1535 of American Institute of Physics Conference Series, 2013, pp. 99–104.

[67] J. SCHULZ FOR THE PIERRE AUGER COLLABORATION, *Status and prospects of the Auger Engineering Radio Array*, in Proceedings of the 34th International Cosmic Ray Conference, The Hague, The Netherlands, 2015.

[68] A. AAB *et al.*, PIERRE AUGER COLLABORATION, *Probing the radio emission from air showers with polarization measurements*, Physical Review D, 89 (2014), p. 052002.

[69] P. SCHELLART *et al.*, LOFAR COLLABORATION, *Detecting cosmic rays with the LOFAR radio telescope*, Astronomy & Astrophysics, 560 (2013), p. A98.

[70] P. SCHELLART *et al.*, *Polarized radio emission from extensive air showers measured with LOFAR*, Journal of Cosmology and Astroparticle Physics, 10 (2014), p. 14.

[71] S. BUITINK *et al.*, *Method for high precision reconstruction of air shower X_{max} using two-dimensional radio intensity profiles*, Physical Review D, 90 (2014), p. 082003.

[72] O. SCHOLTEN *et al.*, *A Macroscopic Description of Coherent Geo-Magnetic Radiation from Cosmic Rays*, in Proceedings of the 30th International Cosmic Ray Conference, Merida, Mexico, 2008.

[73] K. WERNER *et al.*, *A realistic treatment of geomagnetic Cherenkov radiation from cosmic ray air showers*, Astroparticle Physics, 37 (2012), pp. 5–16.

[74] J. ALVAREZ-MUÑIZ *et al.*, *Monte Carlo simulations of radio pulses in atmospheric showers using ZHAireS*, Astroparticle Physics, 35 (2012), pp. 325–341.

[75] T. HUEGE *et al.*, *Simulating radio emission from air showers with CoREAS*, in American Institute of Physics Conference Series, R. Lahmann *et al.*, eds., vol. 1535 of American Institute of Physics Conference Series, 2013, pp. 128–132.

[76] C. W. JAMES *et al.*, *General description of electromagnetic radiation processes based on instantaneous charge acceleration in endpoints*, Physical Review E, 84 (2011), p. 056602.

[77] J. ALVAREZ-MUÑIZ *et al.*, *Radio pulses from ultra-high energy atmospheric showers as the superposition of Askaryan and geomagnetic mechanisms*, Astroparticle Physics, 59 (2014), pp. 29–38.

[78] K. KAMATA *et al.*, *The Lateral and the Angular Structure Functions of Electron Showers*, Progress of Theoretical Physics Supplement, 6 (1958), pp. 93–155.

[79] K. GREISEN, *Cosmic Ray Showers*, Annual Review of Nuclear and Particle Science, 10 (1960), pp. 63–108.

[80] A. HAUNGS *et al.*, *Energy spectrum and mass composition of high-energy cosmic rays*, Reports on Progress in Physics, 66 (2003), pp. 1145–1206.

[81] T. ANTONI *et al.*, KASCADE COLLABORATION, *The cosmic-ray experiment KASCADE*, Nuclear Instruments and Methods in Physics Research A, 513 (2003), pp. 490–510.

[82] W. D. APEL *et al.*, KASCADE-GRANDE COLLABORATION, *The KASCADE-Grande experiment*, Nuclear Instruments and Methods in Physics Research A, 620 (2010), pp. 202–216.

[83] G. VAN AAR *et al.*, $\langle x_{\max} \rangle$ *measured with the surface detector*. Auger Internal Publication (GAP2015_032), April 2015.

[84] M. AVE *et al.*, AIRFLY COLLABORATION, *Measurement of the pressure dependence of air fluorescence emission induced by electrons*, Astroparticle Physics, 28 (2007), pp. 41–57.

[85] T. K. GAISSER *et al.*, *Reliability of the method of constant intensity cuts for reconstructing the average development of vertical showers*, in Proceedings of the 17th International Cosmic Ray Conference, Plovdiv, Bulgaria, 1977.

[86] M. UNGER *et al.*, *Reconstruction of longitudinal profiles of ultra-high energy cosmic ray showers from fluorescence and Cherenkov light measurements*, Nuclear Instruments and Methods in Physics Research A, 588 (2008), pp. 433–441.

[87] T. ABU-ZAYYAD *et al.*, *The prototype high-resolution Fly's Eye cosmic ray detector*, Nuclear Instruments and Methods in Physics Research A, 450 (2000), pp. 253–269.

[88] H. KAWAI *et al.*, TELESCOPE ARRAY COLLABORATION, *Telescope Array Experiment*, Nuclear Physics B - Proceedings Supplements, 175-176 (2008), pp. 221–226.

[89] J. ABRAHAM *et al.*, PIERRE AUGER COLLABORATION, *The fluorescence detector of the Pierre Auger Observatory*, Nuclear Instruments and Methods in Physics Research A, 620 (2010), pp. 227–251.

[90] N. BUDNEV *et al.*, *Tunka-25 Air Shower Cherenkov array: The main results*, Astroparticle Physics, 50 (2013), pp. 18–25.

[91] A. HORNEFFER FOR THE LOPES COLLABORATION, *LOPES Detecting Radio Emission from Cosmic Ray Air Showers*, ArXiv Astrophysics e-prints, (2004).

[92] F. G. SCHRÖDER *et al.*, *Tunka-Rex: A radio antenna array for the Tunka experiment*, in American Institute of Physics Conference Series, R. Lahmann *et al.*, eds., vol. 1535 of American Institute of Physics Conference Series, 2013, pp. 111–115.

[93] W. D. APEL *et al.*, LOPES COLLABORATION, *Reconstruction of the energy and depth of maximum of cosmic-ray air showers from LOPES radio measurements*, Physical Review D, 90 (2014), p. 062001.

[94] A. CORSTANJE *et al.*, LOFAR COLLABORATION, *The shape of the radio wavefront of extensive air showers as measured with LOFAR*, Astroparticle Physics, 61 (2015), pp. 22–31.

[95] Q. DOROSTI HASANKIADEH FOR THE PIERRE AUGER COLLABORATION, *Advanced Reconstruction Strategies for the Auger Engineering Radio Array*, 6th Conference on Acoustic and Radio EeV Neutrino Detection, Annapolis, Maryland, USA, (2014).

[96] A. NELLES *et al.*, *A parameterization for the radio emission of air showers as predicted by CoREAS simulations and applied to LOFAR measurements*, Astroparticle Physics, 60 (2015), pp. 13–24.

[97] J. SCHULZ *et al.*, *EMC-test of the AERA124 reference station*. Auger Internal Publication (GAP2013_063), November 2013.

[98] R. M. TENNENT, *The Haverah Park extensive air shower array*, Proceedings of the Physical Society, 92 (1967), pp. 622–631.

[99] I. ALLEKOTTE *et al.*, PIERRE AUGER COLLABORATION, *The surface detector system of the Pierre Auger Observatory*, Nuclear Instruments and Methods in Physics Research A, 586 (2008), pp. 409–420.

[100] J. ABRAHAM *et al.*, PIERRE AUGER COLLABORATION, *Properties and performance of the prototype instrument for the Pierre Auger Observatory*, Nuclear Instruments and Methods in Physics Research A, 523 (2004), pp. 50–95.

[101] J. ABRAHAM *et al.*, PIERRE AUGER COLLABORATION, *Trigger and aperture of the surface detector array of the Pierre Auger Observatory*, Nuclear Instruments and Methods in Physics Research A, 613 (2010), pp. 29–39.

[102] S. ARGIRÒ *et al.*, PIERRE AUGER COLLABORATION, *The offline software framework of the Pierre Auger Observatory*, Nuclear Instruments and Methods in Physics Research A, 580 (2007), pp. 1485–1496.

[103] V. VERZI FOR THE PIERRE AUGER COLLABORATION, *The Energy Scale of the Pierre Auger Observatory*, in Proceedings of the 33rd International Cosmic Ray Conference, Rio de Janeiro, Brazil, July 2013.

[104] J. T. BRACK *et al.*, *Absolute calibration of a large-diameter light source*, Journal of Instrumentation, 8 (2013), p. 5014P.

[105] A. C. ROVERO *et al.*, *Multi-wavelength calibration procedure for the pierre Auger Observatory Fluorescence Detectors*, Astroparticle Physics, 31 (2009), pp. 305–311.

[106] J. ABRAHAM *et al.*, PIERRE AUGER COLLABORATION, *A study of the effect of molecular and aerosol conditions in the atmosphere on air fluorescence measurements at the Pierre Auger Observatory*, Astroparticle Physics, 33 (2010), pp. 108–129.

[107] B. KEILHAUER FOR THE PIERRE AUGER COLLABORATION, *The Balloon-the-Shower programme of the Pierre Auger Observatory*, Astrophysics and Space Sciences Transactions, 6 (2010), pp. 27–30.

[108] P. ABREU *et al.*, PIERRE AUGER COLLABORATION, *Description of atmospheric conditions at the Pierre Auger Observatory using the Global Data Assimilation System (GDAS)*, Astroparticle Physics, 35 (2012), pp. 591–607.

[109] F. SANCHEZ FOR THE PIERRE AUGER COLLABORATION, *The AMIGA detector of the Pierre Auger Observatory: overview*, in Proceedings of the 32nd International Cosmic Ray Conference, Beijing, China, 2011.

[110] H. KLAGES FOR THE PIERRE AUGER COLLABORATION, *Enhancements to the Southern Pierre Auger Observatory*, Journal of Physics Conference Series, 375 (2012), p. 052006.

[111] P. ABREU *et al.*, PIERRE AUGER COLLABORATION, *Antennas for the detection of radio emission pulses from cosmic-ray induced air showers at the Pierre Auger Observatory*, Journal of Instrumentation, 7 (2012), p. 11P.

[112] M. ERDMANN *et al.*, *Antenna Alignment for the first 24 Stations of AERA*. Auger Internal Publication (GAP2010_083), July 2010.

[113] A. NELLES *et al.*, *A Survey of Narrowband and Broadband Radio-frequency Interference at AERA*. Auger Internal Publication (GAP2011_062), 2011.

[114] A. VAN DEN BERG *et al.*, *Fiber Communication System for the Auger Engineering Radio Array at the Southern Auger Observatory*. Auger Internal Publication (GAP2011_035), March 2011.

[115] D. CHARRIER, CODALEMA COLLABORATION, *Antenna development for astroparticle and radioastronomy experiments*, Nuclear Instruments and Methods in Physics Research A, 662 (2012), p. 142.

[116] B. REVENU FOR THE PIERRE AUGER COLLABORATION AND THE CODALEMA COLLABORATION, *Radio detection of cosmic ray air showers by the RAuger experiment, a fully autonomous and self-triggered system installed at the Pierre Auger Observatory*, Nuclear Instruments and Methods in Physics Research A, 662 (2012), p. 130.

[117] C. TIMMERMANS *et al.*, *Description of the scintillator triggered AERA-II stations*. Auger Internal Publication (GAP2013_074), August 2013.

[118] F. G. SCHRÖDER *et al.*, *New method for the time calibration of an interferometric radio antenna array*, Nuclear Instruments and Methods in Physics Research A, 615 (2010), pp. 277–284.

[119] Y. ZHU FOR THE PIERRE AUGER COLLABORATION, *A flexible FPGA-based module for wireless communications in astroparticle physics experiments*, in Proc. of the 9th Internationl Symposium on Telecommunications, Piscataway, N.J., October 2012, Behlilovic, N.

[120] J. KELLEY *et al.*, *Design and Testing of a 5 GHz Commercial Wireless Network for AERA*. Auger Internal Publication (GAP2012_054), April 2012.

[121] M. HEVINGA *et al.*, *Photo-Voltaic System for the Auger Engineering Radio Array*. Auger Internal Publication (GAP2011_034), March 2011.

[122] PVSYST SOFTWARE PACKAGE, *http://www.pvsyst.com*.

[123] A. VAN DEN BERG, *private communication*.

[124] HTTPS://EOSWEB.LARC.NASA.GOV/, *Atmospheric Science Data Center*.

[125] VICTRON ENERGY, *http://www.victronenergy.nl/batteries/Gel-and-AGM-batteries*, http://www.victronenergy.nl/batteries/Gel-and-AGM-batteries.

[126] J. KELLEY *et al.*, *AERA EMC Tests at ASTRON*. February 2010.

[127] J. L. KELLEY FOR THE PIERRE AUGER COLLABORATION, *Data acquisition, triggering, and filtering at the Auger Engineering Radio Array*, Nuclear Instruments and Methods in Physics Research A, 725 (2013), pp. 133–136.

[128] B. F. REVENU, *AERA Central Trigger*. Auger Internal Publication (GAP2012_115), 2012.

[129] J. MALLER FOR THE PIERRE AUGER COLLABORATION, *Radio detection of extensive air showers at the Pierre Auger Observatory*, Nuclear Instruments and Methods in Physics Research A, 742 (2014), pp. 232–236.

[130] J. MALLER *et al.*, *Two methods for rejecting background radio traces in RAuger data at the level of a single station (T1 or T2)*. Auger Internal Publication (GAP2012_087), November 2013.

[131] S. JANSEN *et al.*, *Towards standardizes selection criteria for AERA data*. Auger Internal Publication (GAP2015_007), January 2015.

[132] FEDERAL AVIATION ADMINISTRATION, *Automatic Dependent Surveillance Braodcast (ADS-B) Out Performance Requirements to Support Air Traffic Control (ATC) Service*, Federal Register, 75 (2010).

[133] R. BRUN *et al.*, *ROOT - An object oriented data analysis framework*, Nuclear Instruments and Methods in Physics Research A, 389 (1997), pp. 81–86.

[134] S. MATHYS *et al.*, *Development and applications of a ROOT based IO library for AERA*. Auger Internal Publication (GAP2015_01), January 2015.

[135] P. ABREU *et al.*, PIERRE AUGER COLLABORATION, *Advanced functionality for radio analysis in the Offline software framework of the Pierre Auger Observatory*, Nuclear Instruments and Methods in Physics Research A, 635 (2011), pp. 92–102.

[136] D. VEBERIC *et al.*, *SD Reconstruction - Offline Reference Manual*. Auger Internal Publication (GAP2005_035), 2005.

[137] M. SETTIMO, *Measurement of the cosmic ray energy spectrum using hybrid events of the Pierre Auger Observatory*, European Physical Journal Plus, 127 (2012), p. 87.

[138] A. PORCELLI, *Measurement of the Depth of Shower Maximum in the Transition Region between Galactic and Extragalactic Cosmic Rays with the Pierre Auger Observatory*, PhD thesis, Karlsruher Insitute of Technology, 2014.

[139] A. AAB *et al.*, PIERRE AUGER COLLABORATION, *Depth of maximum of air-shower profiles at the Pierre Auger Observatory. I. Measurements at energies above* $10^{17.8}$ *eV*, Physical Review D, 90 (2014), p. 122005.

[140] I. C. MARIS FOR THE PIERRE AUGER COLLABORATION, *Measurement of the Energy Spectrum of Cosmic Rays above* 3×10^{17} *eV at the Pierre Auger Observatory*, vol. EPS-HEP2013, 2013, p. 405.

[141] S. GREBE *et al.*, *Suppression of self-introduced narrowband RFI in the time domain*. Auger Internal Publication (GAP2013_012), November 2013.

[142] R. C. JONES, *A new calculus for the treatment of optical systems*, Journal of the Optical Society of America, 31 (1941), pp. 488–493.

[143] G. BURKE *et al.*, *Numerical electromagnetics code (nec) method of moments, part ii and iii*. tech.rep., 1981.

[144] D. CHARRIER, *Calculating the vector equivalent length of the butterfly antenna from nec2 by simulating the antenna in transmitting mode*. Auger Internal Publication (GAP2014_025), 2014.

[145] S. JANSEN, *private communication*.

[146] K. LINK *et al.*, LOPES COLLABORATION, *Revised absolute amplitude calibration of the LOPES experiment*, ArXiv e-prints, (2015).

[147] A. NELLES *et al.*, *Calibrating the absolute amplitude scale for air showers measured at lofar*, Journal of Instrumentation, 10 (2015), p. P11005.

[148] S. OSTAPCHENKO, *QGSJET-II: physics, recent improvements, and results for air showers*, in European Physical Journal Web of Conferences, vol. 52 of European Physical Journal Web of Conferences, 2013, p. 2001.

[149] M. KOBAL FOR THE PIERRE AUGER COLLABORATION, *A thinning method using weight limitation for air-shower simulations*, Astroparticle Physics, 15 (2001), pp. 259–273.

[150] A. AAB *et al.*, PIERRE AUGER COLLABORATION, *Reconstruction of inclined air showers detected with the Pierre Auger Observatory*, Journal of Cosmology and Astroparticle Physics, 8 (2014), p. 19.

[151] S. AGOSTINELLI *et al.*, *GEANT4 – a simulation toolkit*, Nuclear Instruments and Methods in Physics Research A, 506 (2003), pp. 250–303.

[152] J. BERINGER *et al.*, PARTICLE DATA GROUP, *Review of Particle Physics*, Physical Review D, 86 (2012), p. 010001.

[153] T. ANTONI *et al.*, KASCADE COLLABORATION, *Electron, muon, and hadron lateral distributions measured in air showers by the KASCADE experiment*, Astroparticle Physics, 14 (2001), pp. 245–260.

[154] S. THOUDAM *et al.*, *LORA: A scintillator array for LOFAR to measure extensive air showers*, Nuclear Instruments and Methods in Physics Research A, 767 (2014), pp. 339–346.

[155] P. K. F. GRIEDER, *Extensive Air Showers*, 2010.

[156] A. NELLES *et al.*, *A parameterization for the radio signal measured with AERA*. Auger Internal Publication (GAP2014_073), September 2014.

[157] A. NELLES *et al.*, *The radio emission pattern of air showers as measured with LOFAR - a tool for the reconstruction of the energy and the shower maximum*, Journal of Cosmology and Astroparticle Physics, 5 (2015), p. 18.

[158] T. HUEGE, *private communication*.

[159] I. MARIŞ FOR THE PIERRE AUGER COLLABORATION, *The amiga infill detector of the Pierre Auger Observatory: performance and first data*, in Proceedings of the 32nd International Cosmic Ray Conference, Beijing, China, 2011.

[160] S. FLIESCHER, *Antenna Devices and Measurement of Radio Emission from Cosmic Ray induced Air Showers at the Pierre Auger Observatory*, PhD thesis, RWTH Aachen University, 2011.

[161] M. STEPHAN FOR THE PIERRE AUGER COLLABORATION, *Antennas, Filters and Preamplifiers designed for the Radio Detection of Ultra-High-Energy Cosmic Rays*, Proceedings of the Asia Pacific Microwave Conference, TH3G-49 (2010).

[162] M. ENDER *et al.*, *Radio Emission of Extensive Air Showers during Thunderstorms*, in Proceedings of the 31st International Cosmic Ray Conference, Lodz, Poland, 2009.

[163] P. SCHELLART *et al.*, *Probing atmospheric electric fields in thunderstorms through radio emission from cosmic-ray-induced air showers*, Physical Review Letters, 114 (2015), p. 165001.

[164] S. NEHLS, *Calibrated Measurements of the Radio Emission of Cosmic Ray Air Showers*, PhD thesis, Institut für Kernphysik, Universität Karlsruhe, 2008.

[165] K. WEIDENHAUPT, *Antenna Calibration and Energy Measurement of Ultra-High Energy Cosmic Rays with the Auger Engineering Radio Array*, PhD thesis, RWTH Aachen University, 2014.

[166] G. FARRAR FOR THE PIERRE AUGER COLLABORATION, *The muon content of hybrid events recorded at the Pierre Auger Observatory*, in Proceedings of the 33rd International Cosmic Ray Conference, Rio de Janeiro, Brazil, July 2013.

[167] T. HUEGE *et al.*, *Dependence of geosynchrotron radio emission on the energy and depth of maximum of cosmic ray showers*, Astroparticle Physics, 30 (2008), pp. 96–104.

[168] M. TUEROS FOR THE PIERRE AUGER COLLABORATION, *Estimate of the non-calorimetric energy of showers observed with the fluorescence and surface detectors of the Pierre Auger Observatory*, in Proceedings of the 33rd International Cosmic Ray Conference, Rio de Janeiro, Brazil, 2013.

[169] P. BILLOIR, *A sampling procedure to regenerate particles in a ground detector from a thinned air shower simulation output*, Astroparticle Physics, 30 (2008), pp. 270–285.

[170] T. MCCAULEY *et al.*, *GEANT4 simulation of the surface detectors*. Auger Internal Publication (GAP2000_055), 2000.

[171] A. PORCELLI FOR THE PIERRE AUGER COLLABORATION, *Measurements of $X_{\max}$ above 10^17 eV with the fluorescence detector of the Pierre Auger Observatory*, in Proceedings of the 34th International Cosmic Ray Conference, The Hague, The Netherlands, 2015.

[172] S. EPIMAKHOV FOR THE TUNKA COLLABORATION, *Elemental Composition of Cosmic Rays above the Knee from X_{max} measurements of the Tunka Array*, in Proceedings of the 33rd International Cosmic Ray Conference, Rio de Janeiro, Brazil, 2013.

[173] S. P. KNURENKO *et al.*, *The depth of maximum shower development and its fluctuations: cosmic ray mass composition at E_0>10^{17} eV*, Astrophysics and Space Sciences Transactions, 7 (2011), pp. 251–255.

[174] S. P. KNURENKO *et al.*, *Study of cosmic rays at the Yakutsk EAS array: energy spectrum and mass composition*, Nuclear Physics B Proceedings Supplements, 212 (2011), pp. 241–251.

[175] M. UNGER *et al.*, PIERRE AUGER COLLABORATION, *Study of the Cosmic Ray Composition above 0.4 EeV using the Longitudinal Profiles of Showers observed at the Pierre Auger Observatory*, Astronomische Nachrichten, 328 (2007), p. 614.

[176] E. G. BEREZHKO, *Composition of Cosmic Rays Accelerated in Active Galactic Nuclei*, Astrophysical Journal, Letters, 698 (2009), pp. L138–L141.

[177] A. DAR *et al.*, *A theory of cosmic rays*, Physics Reports, 466 (2008), pp. 179–241.

[178] S. THOUDAM *et al.*, *Study of the energy spectrum and composition of cosmic rays up to the highest energies*, in preperation.

Index

Summary

The Earth is continuously exposed to a flux of particles coming from outer space. These particles are called *cosmic rays* and their existence has been known for more than a century. The beginning of the life-cycle of the most energetic ones among them is however still unexplained. Especially the sources able to accelerate particles to the observed energies have not been identified yet. One of the reasons for the still open questions about the nature of the highest energetic cosmic rays is their low flux. Over long ranges of the known spectrum of cosmic rays, the flux decreases according to a power law ($\propto E^{-2.7}$). At the end of the measured spectrum at about $10^{20}\,\mathrm{eV}$, only one cosmic ray is observed per square-kilometer per century. Therefore, air- or space-borne experiments cannot be employed for their direct detection. Experiments that measure enough of these rare particles to infer information about their origin must be large and can only be built on the ground. There however, only secondary particles such as muons, photons, electrons, positrons, and other products of the collisions of the cosmic rays with nuclei in the Earth's atmosphere can be measured. During their propagation through the atmosphere, these particles are likely to also interact, creating new particles which subsequently also interact and create new particles and so on. Thereby, the initial energy of the cosmic ray is transferred to millions of secondary particles in a particle cascade which is called *extensive air shower*. From the observation of the extensive air shower, the properties of the cosmic ray which are the energy, the arrival direction, and the type of the original particle need to be reconstructed to learn about its origin and propagation towards the Earth.

The first two properties are in general reconstructed from the secondary particles measured on the ground. This technique has been used since the first description of the phenomenon of extensive air showers and yields high resolution for both observables. The measurement of the particle type of the cosmic rays is still challenging. Without the direct measurement of the primary particle, information about its kind is only indirectly available via the development of the air shower which differs for different primary particles on a statistical basis. At the highest energies, mainly optical methods are employed to directly or indirectly detected light induced by the secondary particles in the air shower. These techniques are however limited to a duty cycle of about 10% by environmental conditions as they can only operate during clear moonless nights.

Already proposed in the 1960's, the detection of radio signals originating from the charged particles in the air showers is an alternative to the established techniques. The radio emission originates from two mechanisms which are both based on the separation of positive and negative charges during the air shower development. One mechanism is the *charge excess mechanism*. It is based on the effect that during the air shower development electrons are knocked out

of atmospheric molecules and join the front of the air shower whereas the positively charged ions are left behind. The other mechanism is the *geomagnetic emission mechanism* which is based on the separation of electrons and positrons in the shower front due to the Lorentz-force in the geomagnetic field. On the ground, the emission can be detected in the MHz-regime which shows a characteristic interference pattern.

After the experimental investigation of the emission mechanisms, and also improvements of the theoretical understanding and modelling of the underlying processes, the sensitivity of the radio technique to air-shower and thereby cosmic-ray parameters is in the focus of today's research. A reliable way is the comparison to established detection techniques when measuring the same air showers simultaneously which is the subject of this thesis and carried out at the Pierre Auger Observatory in Argentina. There, the Auger Engineering Radio Array (AERA) is operated together with a fluorescence light detector and a particle detector array. The presented work focuses on the simultaneous detection of extensive air-showers with the different detector types and the comparisons of the radio measurements to the other techniques. The basic idea of multi-hybrid air shower detection is sketched on page 195. During the air shower development, fluorescence light is emitted from excited nitrogen molecules in the atmosphere. This light is used to image the shower development. Furthermore, MHz radiation is emitted and detected on the ground. The distribution of the energy density in the radiation has a complex shape as indicated by the color coding in the sketch. Together with the radio pulses, the particles of the air shower are detected with particle detectors on the surface and sometimes also with additional buried muon counters. The reconstruction of the arrival direction of a cosmic ray is based on the arrival times of the pulses or particles. The resolution of the measurement is similar for both, particle and radio detectors. For the reconstruction of the cosmic ray energy, the radio energy yield, which is the amount of energy transferred in MHz-radiation (the integral over the sketched color map) is introduced and calibrated with the particle detector measurement in this work and the resolution is shown to be competitive to the other techniques. Finally, the sensitivity of the radio technique to the shower development is investigated in simulation studies and demonstrated on data of simultaneous observations of the radio emission and the fluorescence light. A cross calibration is performed between the two methods, based on the measured energy density of the radio signals on the ground. One method is based on sets of Monte Carlo simulations performed for protons and iron nuclei using the measured arrival direction and energy as input. The sets cover a broad range of possible shower developments and the better the prediction of the energy density pattern fits the measurement, the more likely the simulated shower development corresponds to the one of the actual shower. The other method employs an empiric parametrization of the lateral energy density distribution which is fitted to the data. The width of the distribution is sensitive to the shower development. After the calibration with the fluorescence light measurements, this method is applied to a much larger dataset for which no fluorescence light data are available to also infer information about the shower development for these showers. This results in the first

measurement of the depth of the shower maximum from radio data that has been calibrated with an independent detection technique and thus the mass (type) of cosmic rays as a function of energy.

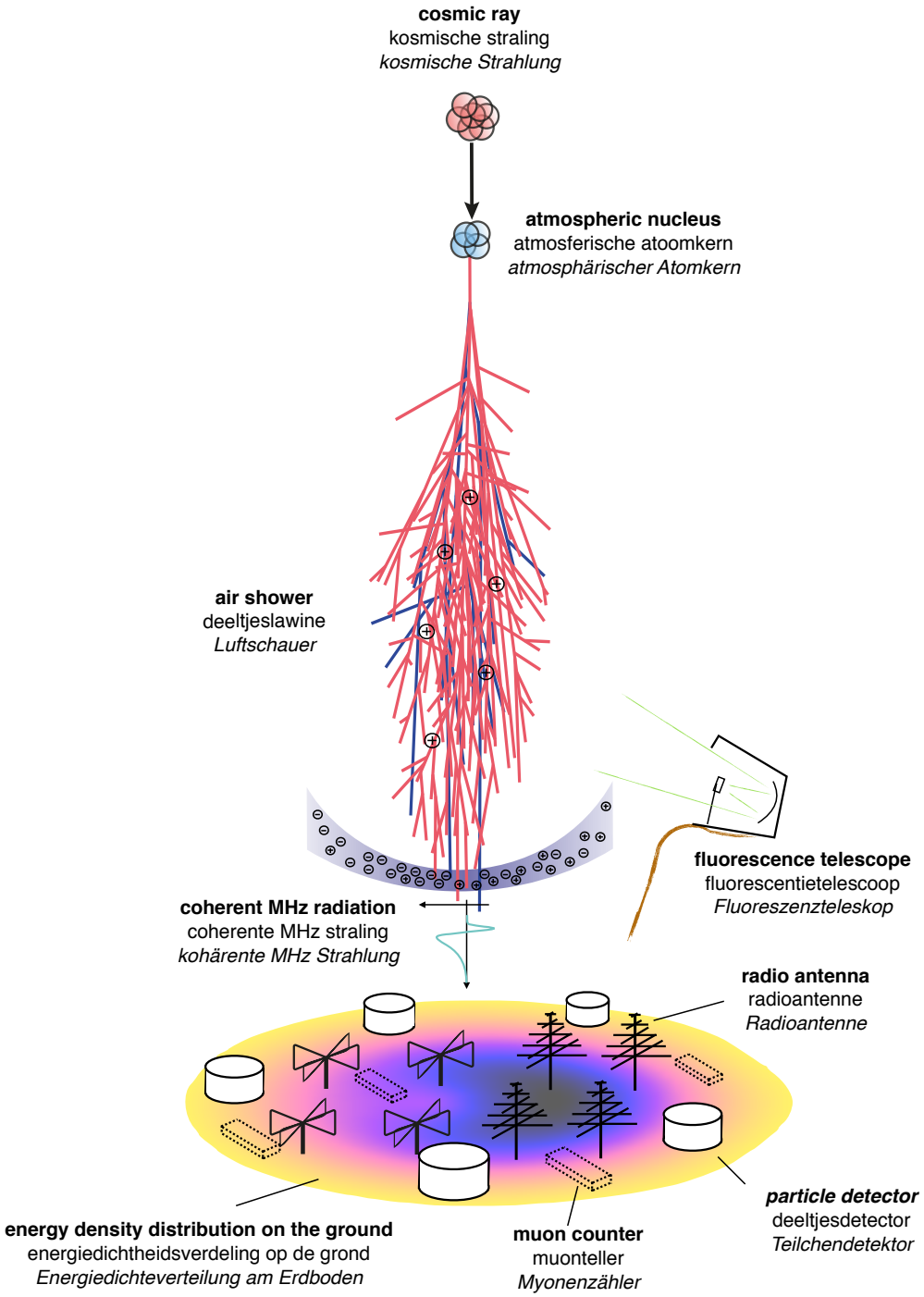

Sketch of the multi-hybrid air shower detection at the Pierre Auger Observatory.
Illustratie van de waarneming van een deeltjes lawine bij het Pierre Auger Observatorium.
Schematische Darstellung der Hybridmessungen von Luftschauern am Pierre Auger Observatorium.

Samenvatting

De aarde is blootgesteld aan een voortdurend bombardement van subatomaire deeltjes vanuit de ruimte. Deze deeltjes worden *kosmische straling* genoemd, en hun bestaan is al meer dan een eeuw bekend. De oorsprong van de meest energetische van deze deeltjes is echter nog steeds niet verklaard. Om meer specifiek te zijn, zijn de bronnen die in staat zijn om de deeltjes tot de waargenomen hoge energieën te versnellen nog niet geïdentificeerd. Een van de redenen waarom vragen over de oorsprong van hoogenergetische kosmische straling nog steeds open staan is de zeer lage *flux*. Over een groot deel van het bekende spectrum van kosmische straling neemt de flux af met toenemende energie volgens een machtsfunctie ($\propto E^{-2.7}$). Aan het einde van het gemeten spectrum, op ongeveer $10^{20}\,\mathrm{eV}$, wordt slechts één kosmisch deeltje waargenomen per vierkante kilometer per eeuw. Daarom kunnen ballon- en satellietexperimenten niet gebruikt worden voor detectie van kosmische straling met deze energieën. Experimenten die genoeg van deze zeldzame deeltjes kunnen meten om informatie over hun oorsprong te verzamelen zijn daarom noodzakelijkerwijs groot, en worden op de grond gebouwd. Op de grond kunnen echter alleen secundaire deeltjes zoals muonen, fotonen, elektronen, positronen en andere producten van de botsingen tussen kosmische deeltjes en atomen in de atmosfeer van de aarde worden gemeten. Tijdens de propagatie van kosmische straling door de atmosfeer van de aarde is er een grote kans op interactie. De daarbij ontstane deeltjes gaan op hun beurt ook weer interacties aan, enzovoort. Hierdoor wordt de initiële energie van het kosmische deeltje verdeeld over miljoenen secundaire deeltjes in een *deeltjeslawine*. Door middel van waarnemingen van deeltjeslawines moeten eigenschappen van het oorspronkelijke kosmische deeltje, zoals de energie, de aankomstrichting en het type deeltje, worden gereconstrueerd om kennis te verkrijgen over hun bronnen en de processen die plaats vinden tijdens hun reis door de ruimte op weg naar de aarde.

De eerste twee van de bovengenoemde eigenschappen worden typisch gereconstrueerd vanuit metingen van de secundaire deeltjes op de grond. Deze techniek wordt gebruikt sinds de eerste beschrijving van deeltjeslawines en geeft een hoge resolutie in zowel energie als aankomstrichting. Het reconstrueren van het type deeltje is nog steeds een grote uitdaging. Zonder een directe meting van het primaire deeltje is informatie over de aard van het deeltje alleen indirect beschikbaar, via statistische verschillen tussen de ontwikkeling van deeltjeslawines voor verschillende soorten primaire deeltjes. Op de hoogste energieën worden voornamelijk optische methoden gebruikt om licht op te vangen dat direct of indirect wordt geproduceerd door de secundaire deeltjes in de lawine. Deze technieken zijn echter beperkt tot een lage "*duty cycle*" van ongeveer 10% doordat deze waarnemingen alleen kunnen plaatsvinden gedurende heldere, maanloze nachten.

De detectie van radiostraling afkomstig van de geladen deeltjes in de deeltjeslawine is al in

de jaren ‘60 voorgesteld als alternatief voor de bovengenoemde methoden. Deze radiostraling wordt geproduceerd door twee mechanismen, die beide gebaseerd zijn op ladingsscheiding van de positieve en negatieve lading in de deeltjeslawine. Een van deze twee mechanismen is het ladingsoverschot-mechanisme. Hierbij worden elektronen losgeslagen uit atmosferische moleculen, waarna ze meebewegen met de deeltjeslawine en waarbij de positief geladen ionen achtergelaten worden. Daarnaast is er het *geomagnetische* mechanisme waarbij de ladingsscheiding tussen elektronen en positronen in de deeltjeslawine veroorzaakt wordt door de Lorentz-kracht in het magnetisch veld van de aarde. Bij beide mechanismen verandert tevens het aantal vrije deeltjes in de lawine als functie van de tijd, hetgeen ook weer resulteert in radiostraling. Interferentie tussen de radiostraling van deze mechanismen geeft een karakteristiek intensiteitspatroon, dat op de grond gedetecteerd kan worden in het megahertz-frequentiebereik.

Volgend op experimentele verificatie van de emissiemechanismen, en verbeteringen in het theoretisch begrip van de onderliggende processen, is het huidig onderzoek gericht op het bepalen van de gevoeligheid van radiostralingsmetingen van eigenschappen van de deeltjeslawine en de kosmische straling zelf. Een betrouwbare methode hiervoor is een rechtstreekse vergelijking met bestaande meettechnieken wanneer dezelfde deeltjeslawine tegelijkertijd met meerdere meettechnieken wordt waargenomen. Deze methode is het onderwerp van dit proefschrift. Dit onderzoek is uitgevoerd bij het Pierre Auger Observatorium in Argentinië. Daar opereert de Auger Engineering Radio Array (AERA) samen met optische fluorescentietelescopen en deeltjesdetectoren. Het werk dat in dit proefschrift gepresenteerd wordt richt zich op de gelijktijdige detectie van deeltjeslawines met de verschillende meetinstrumenten en een vergelijking van de meettechnieken. Het concept van een dergelijke multi-hybride waarneming is geschetst op pagina 195. Gedurende de ontwikkeling van een deeltjeslawine wordt fluorescentielicht uitgestraald door aangeslagen stikstofmoleculen in de atmosfeer. Dit licht wordt gebruikt om met de fluorescentietelescopen een foto te maken van de ontwikkeling van de deeltjesregen. Daarnaast komt er radiostraling vrij in het megahertz-frequentiebereik die met AERA gedetecteerd wordt op de grond. De distributie van de energiedichtheid in deze radiostraling heeft een complexe vorm, zoals aangegeven door de kleur in de schets. Naast de radiopulsen worden ook de secundaire deeltjes gedetecteerd met deeltjesdetectoren op de grond, en soms met ingegraven muonendetectoren. De reconstructie van de aankomstrichting van het kosmische deeltje is gebaseerd op metingen van de aankomsttijd van de radiopulsen of van de secundaire deeltjes. De resolutie van beide meettechnieken is vergelijkbaar. Voor de reconstructie van de energie van het kosmische deeltje wordt de *radio-opbrengst*, de hoeveelheid energie aanwezig in de megahertz-radiostraling (ofwel de integraal over het geschetste patroon), bepaald. Deze wordt gemeten, en gekalibreerd met de waarnemingen van de deeltjesdetectoren. De resolutie van deze nieuwe methode is vergelijkbaar met die van eerder ontwikkelde technieken. Als laatste wordt de nauwkeurigheid van de radiodetectietechniek voor de ontwikkeling van de deeltjesregen onderzocht. Aanvankelijk aan de hand van simulatiestudies, en vervol-

gens door directe vergelijkingen tussen radio- en fluorescentiewaarnemingen. Een kalibratie is uitgevoerd tussen deze twee methodes, gebaseerd op de gemeten energiedichtheid van het radiosignaal op de grond. Vervolgens zijn er twee methoden gebruikt voor de reconstructie van de ontwikkeling van de deeltjeslawine. Voor de eerste methode zijn Monte Carlo-simulaties uitgevoerd met protonen en ijzerkernen als primaire deeltjes, met de gemeten aankomstrichting en energie als invoerparameters. Deze simulaties beslaan een groot bereik aan mogelijke deeltjeslawine-ontwikkelingen. Hoe beter het gesimuleerde energiedichtheidspatroon van de radiostraling overeenkomt met het gemeten patroon, hoe groter de kans dat het gesimuleerde ontwikkelingspatroon van de deeltjeslawine overeenkomt met het ontwikkelingspatroon van de gemeten deeltjeslawine. De tweede methode gebruikt een empirische parametrisatie van de laterale energiedichtheidsdistributie, die vervolgens zo gekozen wordt dat hij overeen komt met de gemeten waarden. De breedte van de distributie is afhankelijk van de ontwikkeling van de deeltjeslawine. Na een calibratie met fluorescentiewaarnemingen is deze methode toegepast op een veel grotere set waarnemingen, waarvoor geen fluorescentiewaarnemingen beschikbaar zijn. Dit resulteert in de eerste meting van de atmosferische diepte van het maximum van de deeltjeslawine, en dus de massa (ofwel het deeltjestype) van kosmische straling, als functie van de energie op behulp van radiometingen die zijn gekalibreerd met een onafhankelijke detectiemethode.

Zusammenfassung

Die Erde wird kontinuierlich von kleinen Teilchen und größeren Objekten aus dem Weltall getroffen. Das Licht der Sonne oder der Sterne und die kleinen Meteoren, die als Sternschnuppen in unserer Atmosphäre glühen sind zum Beispiel allgemein bekannte Vertreter. Neben den masselosen Lichtteilchen und den teils massiven Meteoren befinden sich auch viele massebehaftete Elementarteilchen und Atomkerne unter den eintreffenden Teilchen. Diese werden als kosmische Strahlung bezeichnet und ihre Existenz fasziniert die Wissenschaft seit nunmehr über 100 Jahren. Seit der ersten Beschreibung dieses Phänomens durch Victor Hess in der er seine Entdeckung Höhenstrahlung nennt, konnte das Verständnis dieser Teilchen weiter und weiter verbessert werden. Die gesammelten Erkenntnisse basieren dabei hauptsächlich auf Messungen der Energie, der Ankunftsrichtung und der Art der Teilchen in der kosmischen Strahlung. Aus diesen Observablen können Rückschlüsse auf die Natur der individuellen Teilchen gezogen werden. Besonderes Interesse gilt dabei den höchstenergetischen Teilchen und der Frage nach den Quellen, die in der Lage sind Teilchen auf diese Energien zu beschleunigen. Heutzutage wissen wir, dass die Anzahl der Teilchen in der kosmischen Strahlung die die Erde erreichen stark abhänging von ihrer Energie ist. Grundsätzlich gilt, je höher die Energie desto weniger Teilchen werden beobachtet. Dies hat zur Folge, dass direkte Messungen oberhalb der Erdatmosphäre an Bord von Satelliten oder Ballonen auf Grund der begrenzten Größe der Detektoren nur bis zu einer gewissen Energie genügend Teilchen nachweisen können um sichere Rückschlüsse über deren Charakteristik zu ziehen. Diese maximale Energie für direkte Messungen der Kosmischen Strahlung ist etwa 100 TeV, was ungefähr dem hundertfachen der Energie einer fliegenden Mücke entspricht. Für höhere Energien und damit kleinere Teilchenzahlen sind größere Detektorflächen nötig wie sie hauptsächlich auf der Erdoberfläche gebaut werden können. Messungen mit Detektoren auf der Erdoberfläche können jedoch nur indirekt Aufschluss über das Primärteilchen geben, da dies mit der Erdatmosphäre wechselwirkt und auf dem Erdboden nicht mehr nachweisbar ist. Die Wechselwirkung der Teilchen der kosmischen Strahlung mit Atomkernen der Atmosphärenmoleküle ähnelt den Ereignissen in einem Teilchenbeschleuniger wie dem Large Hadron Collider am CERN. Durch die während der Kollision freiwerdende Energie werden unzählige neue Teilchen erzeugt, die ihrerseits wieder wechselwirken und auch zerfallen können und dabei jeweils neue Teilchen erzeugen. Diese Entwicklung führt zu einer Teilchenkaskade und einer Zunahme der Teilchenzahl bis die primäre Energie auf so viele Teilchen aufgeteilt ist, dass diese im Durchschnitt zu klein ist um neue Teilchen zu erzeugen und die Kaskade langsam wieder ausstirbt. Die Teilchenkaskade in der Erdatmosphäre wird als (ausgedehnter) Luftschauer bezeichnet und wurde zu erst von Pierre Auger, Bruno Rossi und Werner Kolhörster beschrieben. Nur ein kleiner Teil der erzeugten Teilchen erreicht dabei den Erdboden und kann dort nachgewiesen werden. Zum

Nachweis werden häufig regelmäßig angeordnete Teilchendetektoren benutzt. Basierend auf der Messung der sekundären Teilchen am Boden können Rückschlüsse über die Bewegungsrichtung und die Energie des ursprünglichen primären Teilchens gewonnen werden. Aktuell entwickelte Analysemethoden versprechen außerdem Rückschlüsse auf die (durchschnittliche) Massenzahl über die Rekonstruktion der Luftschauerentwicklung. Je größer die Massenzahl des primären Teilchens, desto höher in der Atmosphäre beginnt der Luftschauer im Durchschnitt. Die Bestimmung der Massenzahl ist ein essenzieller Aspekt für die Beantwortung der Frage nach den Quellen der höchstenergetischen kosmischen Strahlung. Eine weitere bewährte, wenn auch herausfordernde Messmethode ist die Detektion von Fluoreszenzlicht, welches von atmosphärischen Stickstoffmolekülen emittiert wird, nachdem diese durch die Teilchen in der Luftschauerkaskade angeregt wurden. Die Menge an Licht ist dabei abhängig von der Teilchenzahl, die wiederum mit der Energie des primären Teilchens zusammenhängt. Zusätzlich lässt sich die Entwicklung des Luftschauers mit dieser Technik sehr genau verfolgen und es können damit Rückschlüsse auf die primäre Massenzahl gezogen werden. Da die betreffende Lichtmenge jedoch extrem gering ist und nur bei klaren und mondlosen Nächten detektiert werden kann, ergeben sich kurze Betriebszyklen von nur etwa 10% der gesamten Zeit. Auf Grund der erreichten Präzision ist die Fluoreszenztechnik trotzdem nach wie vor das Zugpferd im Bereich der Vermessung der höchstenergetischen kosmischen Strahlung und wird meist in einem hybriden Ansatz in Kombination mit einem Teilchendetektor eingesetzt. Die beiden Techniken können dann gegeneinander kalibriert werden. Somit kann der Teilchendetektor, der einen Betriebszyklus von 100% aufweist auch während der Zeiten zu denen keine Fluoreszenzlichtmessungen möglich sind, hochwertige Informationen über die Eigenschaften der kosmische Strahlung liefern. Diese Kombination von Detektionstechniken wird unter anderem am Pierre Auger Observatorium in Argentinien eingesetzt. Auf einer Fläche von über $3000\,\mathrm{km}^2$ sind hier 1600 Teilchendetektoren in einem regelmäßigen Muster angeordnet und werden von 27 Fluoreszenzteleskopen komplementiert. Damit bildet das Pierre Auger Observatorium das weltgrößte Instrument zur Untersuchung der kosmischen Strahlung und liefert gleichzeitig einzigartige Voraussetzungen um neue Technologien zu testen und mit den beiden Hauptdetektoren zu kalibrieren. Eine dieser Technologien ist die Detektion von extrem kurzen Radiopulsen die während der Luftschauerentwicklung entstehen und am Boden mit Radioantennen detektiert werden können. Die Detektion solcher Pulse und deren Interpretation ist Thema dieser Arbeit. Erste Versuche auf dem Gebiet wurden bereits in den 1960er Jahren durchgeführt. Wenn auch vielversprechend, wurde die Methode auf Grund der technischen Limitationen der damaligen Zeit nicht weiter verfolgt. Seit Beginn des neuen Jahrtausends sind diese Limitationen nun mit heutiger Elektronik überwunden und die Radiodetektion von kosmischer Strahlung ist mittlerweile etabliert. Durch die modernen Radiodetektoren war es möglich Theorien zu den Emissionsmechanismen der Radiostrahlung zu überprüfen und das Verständnis dieses Phänomens weiter zu vertiefen. Es hat sich dabei gezeigt, dass die Radioemission auf zwei verschiedenen Mechanismen beruht, die in Kombination zu den auf dem Erdboden beobach-

teten Pulsen führen. Die Mechanismen basieren auf der zeitlich veränderlichen Trennung von Ladungen während der Luftschauerentwicklung. Einerseits werden positive und negative Ladungen durch die Lorenzkraft im Erdmagnetfeld getrennt. Andererseits tritt eine Trennung von positiven Ladungen ein, wenn bewegliche negative Elektronen aus Luftmolekülen ausgelöst werden und ein positives Ion hinter sich zurück lassen. Die Ladungstrennung und die sich gleichzeitig durch die Luftschauerentwicklung ändernde Teilchenzahl führen zu einem sich ändernden Dipolmoment welches die Emission von elektromagnetischer Strahlung verursacht. Da dieses Dipolmoment räumlich begrenzt ist, ergibt sich eine kohärente Überlagerung der einzelnen Beiträge die zu den beobachteten Nanosekundenpulsen führt. Neben den experimentellen Erkenntnissen ist damit heutzutage auch das theoretische Verständnis und damit die Möglichkeit für Vorhersagen zur Radioemssion von ausgedehnten Luftschauern vorhanden. Die Vorhersagen stimmen mittlerweile gut mit den Beobachtungen überein und haben dadurch ihrerseits zur besseren Interpretation der Messdaten beitragen können. Die Radiodetektion von ausgedehnten Luftschauern bietet wie auch die Detektion der Teilchen, die Möglichkeit eines kontinuierlichen Betriebszyklus und ist nur eingeschränkt durch das Auftreten atmosphärischer elektrischer Felder, wie sie z.B. in Gewitterwolken vorkommen. Dadurch bietet die Radiotechnik bei entsprechender Sensitivität für die entscheidenden Eigenschaften Energie, Ankunftsrichtung und Massenzahl (Luftschauerentwicklung) der gemessenen Teilchen ein sehr mächtiges Werkzeug zur Erforschung der kosmischen Strahlung. Die Bestimmung der Sensitivität im Hinblick auf diese drei Eigenschaften ist Hauptthema dieser Arbeit. Hierzu wurden Daten des größten Radiodetektors für kosmische Strahlung, dem Auger Engineering Radio Array, kurz AERA, analysiert. AERA ist ein Bestandteil des Pierre Auger Observatoriums und wird in Kombination mit den dort etablierten schon beschriebenen Detektoren betrieben. Um die Anzahl der detektierten Luftschauer zu vergrößern wurde AERA 2014 von $0.5\,\mathrm{km}^2$ auf $12\,\mathrm{km}^2$ und 2015 nochmals auf $17\,\mathrm{km}^2$ erweitert und umfasst nun 153 Radiodetektorstationen. Die technischen Vorbereitungen und die Durchführung zur Erweiterung des Antennenfeldes sind ebenso Teil dieser Arbeit. Auf Grund der gleichzeitigen Messung der ausgedehnten Luftschauer mit sowohl den Radio-, als auch den Fluoreszenz- und den Teilchendetektoren können die gewonnen Ergebnisse untereinander kalibriert und verglichen werden. Dadurch ist es möglich die Sensitivität der Radiomessungen mit den etablierten Detektortypen zu vergleichen, die Technik weiter zu entwickeln und für zukünftige Forschungsprojekte als Haupttechnik zu positionieren. Eine illustrierte Darstellung der hybriden Detektion von Luftschauern am Pierre Auger Observatorium ist auf Seite 195 gezeigt in der die wichtigsten Bestandteile sowohl des Luftschauers als auch der Detektoren zusammengefasst sind. Der gezeigten Energiedichteverteilung des Radiosignals am Erdboden (farbig gekennzeichnet) kommt für die Analysen im Rahmen dieser Arbeit eine besondere Bedeutung zu. Anders als die Rekonstruktion der Ankunftsrichtung des primären Teilchens die auf den Signalankunftszeiten beruht, wird für die Energiemessung und die Rekonstruktion der Luftschauerentwicklung die Verteilung der Energiedichte herangezogen. Auf Grund der Interferenz der Radiostrahlung der zwei Emis-

sionsmechanismen kann diese nicht durch eine rotationssymmetrische Funktion beschrieben werden und eine analytische Beschreibung konnte erst kürzlich gefunden werden. Das Integral über die Energiedichtefunktion entspricht der totalen Energie in der Radiostrahlung. Diese ist proportional zur Energie des primären Teilchens, wie durch eine Kalibrierung mit dem Teilchendetektor des Observatoriums gezeigt werden kann. Die resultierende Energieauflösung ist dabei vergleichbar mit der Energieauflösung von etablierten Detektionsmethoden. Auch für die Rekonstruktion der Luftschauerentwicklung kann die Energiedichtefunktion herangezogen werden. Dazu werden in dieser Arbeit zwei Methoden vorgestellt und auf AERA Daten angewendet. Einerseits kann die Breite der Energiedichtefunktion als Indikator für die Entfernung zum Ort der Radioemission, der wiederum von der Luftschauerentwicklung abhängt, genutzt werden. Andererseits ermöglichen aktuelle Simulationsprogramme für gegebene Energie und Ankunftsrichtung (z.B. durch Messung mit den Teilchendetektoren) eine Vorhersage der Energiedichteverteilung für verschiedene Luftschauerentwicklungen. Durch den Vergleich der Vorhersagen mit den Messungen kann dann das wahrscheinlichste Szenario bestimmt werden. Beide Methoden wurden im Rahmen dieser Arbeit zum ersten Mal überhaupt mit Ergebnissen einer anderen, unabhängigen Detektionsmethode, in diesem Fall der Messung des Fluoreszenzlichtes verglichen. Die Ergebnisse sind daher von Bedeutung für die aktuelle Forschung und gleichzeitig auch für die Etablierung von Radiodetektoren als Hauptbestandteil zukünftiger Observatorien für höchstenergetische kosmische Strahlung.

Acknowledgments

During the work for this thesis, I was supported by many people, directly and indirectly, scientifically and privately and I would like to thank these people.

I will start here with my supervisor Jörg Hörandel whom I met in the middle of nowhere and who offered me to join his group for this PhD project. Jörg, thank you for having me work in Nijmegen and for all the support and discussions during the last four years. I learned so many new things and got in touch with many interesting people. Thanks for all the opportunities you created during this time.
I would also like to thank my Promotor Heino Falcke for his comments on tricky scientific questions and his general advices.
In addition to these two senior scientists from the department of astrophysics, I want to thank Sijbrand de Jong and Charles Timmermans from the department of high energy physics for their commitment to the AERA group in Nijmegen and their feedback and ideas related to my work. Many thanks also go to John Kelley for introducing me to the subject of radio detection of cosmic rays and to Stijn Buitink for all the discussions and help along the way of my thesis. I learned a lot about electrical engineering from Peter Dolron with whom I worked on the subject of system integration.

Within the radio cosmic ray group in Nijmegen, I benefited a lot from the younger generation. Anna Nelles and Pim Schellart often made my day either from the scientific or the social point of view. With the two of them, our office became the hot spot for a special kind of humour. I also enjoyed travelling with Anna to South and North America and having many fruitful brainstorming occasions with Pim e.g., about selection criteria. I would further like to thank all the PhD students from the Auger group at EHEF, Harm Schoorlemmer, Stefan Grebe, Stefan Jansen, Guus van Aar, Giuseppe De Mauro and Fabrizia Canfora for their collaboration and teamwork. A special thanks goes to Stefan Jansen for forcing me to speak Dutch in the middle of the Argentinian Pampa. A big thank you also to my colleagues Laura Rossetto and Antonio Bonardi for scientific discussions and an introduction to Italian gestures. Arjen van Vliet deserves my thanks for answering all my in-between questions and also for making our office vital again.

My office mates Marianne Heida and Thomas Kupfer created a warm and pleasant atmosphere and introduced me to many new things on various subjects. I enjoyed the discussions about soccer with Thomas despite his Bavarian opinion and fed Gianni under Marianne's supervision on a daily basis. Unfortunately only visiting irregularly, I enjoyed the company of Jan Kuijpers

in our office and benefited from his experience and profound knowledge of astrophysics.
Already during my first visit to the department of astrophysics I felt at home and this feeling never left me again. Therefore, I would like to thank all members and ex-members of the department for generating this great spirit making the department such a nice place to work. It was often interesting to see how different the approaches between astrophysics and astroparticle physics sometimes are and what one can learn from each other.

Working within the Pierre Auger Collaboration set up the framework for many fruitful discussions with colleagues from all over the world. Thanks to everyone how made this project possible! Especially within AERA, I got in contact with many interesting people and I want to thank them all for their collaborativeness. My closest foreign collaborator Christian Glaser I would like to thank for all the inspiring discussions and teamwork and for becoming a friend during many hours of scientific conversations and especially common travels to meetings, conferences and the AERA site.

Before starting my PhD-project, numerous people from my former institute in Münster encouraged me to take this step forward. Thank you!

Despite the many great people from my scientific environment, I got the most important support from my family and friends. Thanks to all of those who helped me to be able to make it to this point. Thanks for the incredible support during the most difficult times and for never doubting that there is sunshine after the rain.
Without the great people I met and became friends with over the years I wouldn't feel the same way I do today. Thank you!

Ganz besonders möchte ich meiner Familie danken, dass sie mich immer bedingungslos unterstützt hat. Mama und Papa, ohne euch wäre es nie so weit gekommen. Danke für alles!

Was würde ich ohne dich machen? Du bist immer für mich da, danke Jenni.

About the Author

Johannes was born in Lemgo (Germany) in October 1986. He attended the Christian-Dietrich-Grabbe Gymnasium and specialized in physics and mathematics in the final years. During his school time, he was active in the local swim team both as a swimmer and as a coach. In 2006, he graduated and went to the University of Münster to study Physics. As an undergraduate student he got in contact with the various facets of the subject of physics. In the following he decided to specialize in the two fields of "nuclear and astroparticle physics" as well as "medical physics and biophysics". For his Diploma thesis, he got the opportunity to work in the group of Prof. Dr. C. Weinheimer on the topic of direct dark matter searches within the XENON-project. He designed, constructed, and tested a 2-phase time projection chamber for electron drift length measurements in liquid Xenon. Throughout this project, he worked in close collaboration with physicists, engineers and technicians further strengthening his interest in the combination of science and engineering.

To broaden his scientific as well as his personal horizon, Johannes switched subjects and moved to the Netherlands to work with Dr. J. Hörandel on the radio detection of cosmic rays at the Radboud University in Nijmegen. The scientific results of his work are discussed in this manuscript. Besides the presented topics, he was also actively involved in the deployment of the second stage of the Auger Engineering Radio Array.

During his Diploma and PhD project, Johannes worked in an international collaboration and presented his work at various conferences. He was also actively involved in teaching problem sessions and lab classes for Bachelor and Master students.